Modelling of Dilution of Thermal Discharges in Enclosed Coastal Waters

Article *in* RESEARCH JOURNAL OF CHEMISTRY AND ENVIRONMENT · October 2013

CITATION
1

READS
261

3 authors:

Lale Balas
Gazi University
54 PUBLICATIONS **243** CITATIONS
SEE PROFILE

Asu Inan
Gazi University
27 PUBLICATIONS **65** CITATIONS
SEE PROFILE

Asli Numanoglu Genc
Atilim University
7 PUBLICATIONS **10** CITATIONS
SEE PROFILE

Research Journal of Chemistry and Environment

Vol. 17(10) October 2013

Journal is indexed by Chemical Abstracts, SCOPUS and SCIE having impact factor 0.636

E-ISSN No.: 2278 – 4527

RESEARCH JOURNAL OF CHEMISTRY AND ENVIRONMENT

An International Research Journal of Chemical Sciences and Environmental Sciences

Res. J. Chem. Environ., Volume **17**, No. **(10)**, Pages 1-104, October **(2013), SCI Impact Factor 0.636**

Editor- in- Chief (Hon.)
Dr. SHANKAR LAL GARGH
M. Sc., Ph.D., M.B.A., LL.B., FICCE, FISBT, A. Inst. Pet.
Phone: +91-731-4004000 Mobile: 094250-56228

Correspondence Address:
Research Journal of Chemistry and Environment
Sector AG/80, Scheme No. 54, **Indore** 452 010 (M.P.) **INDIA**
Phones: 2552837, 4004000 Fax: 0731-2552837

Website<**www.shankargargh.org**> E-mail: **infoshankargargh@gmail.com**

CONTENTS

❖ EDITORIAL BOARD: P II ❖ INSTRUCTIONS TO AUTHORS: P III ❖ MEMBERSHIP FORM: P VI

General Instruction:

Please see that manuscript submitted by you is as per our standard format and as per Instructions to Authors. Authors are requested to check the latest issue of any of our journals for our standard format.

Select the journal where you wish to submit your paper for example journal "Research Journal of Chemistry and Environment" , then go to menu "paper submission". Follow the instructions and you can upload your paper online. Please submit manuscripts, tables, figures, references all together in one shot. It is a must to agree to terms and conditions of declaration given there. Please send declaration/copyright form along with manuscript. One can download this form from menu "downloads".

After submitting the paper, go to menu "paper received" and you will find your paper there. Please see that all entries are correct otherwise submit again. In case you find any problem in uploading, please send your paper by email as attachment at papershankargargh@gmail.com Write name of the journal in the subject when you send manuscript by email. If you send paper by email, then please attach the declaration/copyright form as well.

Rules for Membership and Processing fees:

Please see that you submit processing fees within 10 days of submission of manuscript otherwise it will not be possible for us to process your manuscript. Your manuscript will be sent for blind review to two experts anywhere in the world and their decision will be final and binding. The editorial board reserves the right to condense or make changes in the paper.

Please note that processing fees will not be refunded by us whether your manuscript is accepted or rejected by the experts. Decision of experts will be informed within 45 days of receipt of processing fees and manuscript. If your manuscript is accepted, it will be published within 6 months from date of acceptance of manuscript in coming issues. If your manuscript is rejected, you will be permitted to submit to another journal. While submitting the manuscript, please attach processing fees form as well. One can download this form from menu "downloads".

When you receive the acceptance of manuscript by email, all the authors are requested to be members of journal- annual or life or fellow. Only after receipt of membership subscription, papers will be published otherwise not. It is compulsory for authors to be members of journal after approval and acceptance of manuscripts by experts. In case authors do not wish to be members of journal, they should contact Editor-in-Chief for approval at his email sgargh@gmail.comand his decision regarding membership or no membership will be final and binding.

Authors and co-authors must be members of Journal- Annual or Life or Fellow. Fellow membership is the best because preference is given to fellow members or life members in early publication otherwise waiting time may be even six months. Fellow members are also given preference in appointment as members of editorial board. Further fellow members need not pay registration fees of the conference being organized by the journal for which they are fellow members. Please note that membership of authors should be submitted only when you get the confirmation of acceptance of your manuscript.

Instructions for preparing the manuscript:

All our journals publish research papers containing original research work of good standard, case studies, short communications and review papers of contemporary relevance from all over the world.

Following types of contributions are considered for publication:

RESEARCH PAPERS (Full Length - Maximum of 12 pages-A/4 size)
CASE STUDIES
SHORT COMMUNICATIONS
REVIEW PAPERS including Mini Reviews

We also publish about latest products in Industry, Recent Research, Information about Awards/Prizes, Scholarships, News and Views, Advertisements about Seminars, Conferences, Appointments etc.

1. Papers are accepted only in English. English spelling and punctuation is preferred. All the matter and information should be submitted online by uploading at website www.shankargargh.org at the menu "Paper Submission". If one finds difficulty in uploading, then one can send manuscript as attachment on email papershankargargh@gmail.com Manuscript format should be in

MS word only. Charts, Tables and Diagrams should be in MS Excel or MS Word and images in JPG format using maximum possible 72dpi resolution. All the matter should be typed in Times New Roman Font size - 11 point with single spacing.

2. Full length Research Papers (Maximum of 12 pages in A/4 size) should be divided as follows : Title, Authors names (family names/surnames first in bold) with institutional address and corresponding author email (One author should be identified as the Corresponding Author with asterisk), Abstract in Italics, Keywords, Introduction, Material and Methods, Results and Discussion, Conclusion, Acknowledgement and References. Pages should be properly numbered. Tables and Figures must be in separate sheet. Mathematical data should be strictly provided. References should be in alphabetical order.

3. References must be in separate sheet alphabetically in serial order in name of authors-family name/surname first and typed in the following order:
Family name first and then initials or first name followed by title of paper, name of journal in abbreviated form in Italics (name of book in normal), volume no. in Bold, page no. in normal and publication year in Bold in bracket e.g.

1. Patel R.M., Patel D.M., Shah K.P. and Patel D.A., Synthesis of Polyketones and their Antimicrobial Study, *Res. J. Chem. Environ.*, **3 (2),** 47**(1999)**

2. Rao C.N.R., Chemical Applications of IR Spectroscopy, Academic Press, London, 250 **(1963)**

4. References must be serially numbered and should be arranged alphabetically by family name (surname) first. References must be quoted compulsorily in the text as numerals either at name of author or at the end of the sentence e.g. .....solution.[1]

5. Manuscripts should be strictly in accordance with prescribed FORMAT of the journal. They will not be returned in any case whether accepted or rejected. Manuscripts and all other correspondence should be addressed to Editor. Acceptance communication will be sent to authors in 45 days of submission of manuscript and processing fees. Rejected manuscripts can be sent by authors to other journals only after our prior permission. Please note that membership subscription and processing fees will not be refunded in any case whether your paper is rejected or accepted.

6. **Declaration to be given by authors: The** facts and views in the manuscript are ours and we are totally responsible for authenticity, validity and originality etc. I / We undertake and agree that the manuscripts submitted to your journal have not been published elsewhere and have not been simultaneously submitted to other journals. I / We also declare that manuscripts are our original work and we have not copied from anywhere else. There is no plagiarism in our manuscripts. Our manuscripts whether accepted or rejected will be property of the publisher of the journal and all the copyrights will be with the publisher of the journal.

7. Please correspond by email and always mention title of manuscript, name of the journal, number of authors, name of corresponding author (It will be preferable if only corresponding author makes the enquiry), date of submission of manuscript and payment details of membership and processing fees. Please write the name of the journal in subject.

Instructions for Manuscript-format

a) Page Layout: A4 (21cm × 28 cm) leaving 2 cm margin on all sides of the text. All the text should be single spaced and the pages should be numbered consecutively. Alignment should be Left.
b) Use MS word (2003-2007) for text and TIFF, JPEG or Paint for figures.
c) The first page should contain:

Title-bold, 18 point size
Name/s of author/s-bold, 10 point size (Surname or Family name first in bold)
Affiliation/s-address of all the author/s followed by email of corresponding author in 8.5 point size
Abstract in italics up to 200 words in 12 point size
Keywords- at least 5 keywords in 11 point size

d) Main Text-The paper should be divided into the following sections:

Introduction, Material and Methods, Results and Discussion, Conclusion, Acknowledgement and References.
Tables and Figures of good resolution (72 dpi) should be numbered consecutively and given alphabetically by surname or family name in the order of their appearance in the text.

e) References-References should be cited in the text as superscript on persons name[1, 2] or at the end of the sentence[3].

Acceptance

As soon as one submits the paper online, it will appear in heading "Papers Received". When we receive the paper along with "Declaration of Authors", processing fees form as well as processing fees, we will send your paper to two experts for comments anywhere in the world. After acceptance by both the experts, we will inform you regarding acceptance within 45 days of submission of manuscript and processing fees. If it is accepted, we will send you acceptance letter and your paper will be published within 6 months in coming issues. After acceptance of paper, all the authors should be members of journal. If your paper is rejected, you can submit to other journal with our prior permission. Please note that your membership subscription or processing fees will not be refunded in any case whether your paper is rejected or accepted.

Proofs

Proofs will be sent to the corresponding author via e-mail as an Acrobat PDF (Portable Document Format) which should be returned to the Editorial office within 3 working days. Acrobat Reader will be required in order to read the PDF.

✂-

GOD IS

Govt. of India Regn. No.: 68381/98 E-ISSN No.: 2278 - 4527
Phone & Fax: +91- 731- 2552837 **Website:** www.shankargargh.org
E-mail :infoshankargargh@gmail.com

17th Year of Publication, **SCI Impact Factor 0.636;**
Journal is indexed by Chemical Abstracts, SCIE, SCOPUS

RESEARCH JOURNAL OF CHEMISTRY AND ENVIRONMENT

Sector AG/80, Scheme No. 54, Vijay Nagar, A.B.Road, Indore 452010 (M.P.) INDIA

MEMBERSHIP FORM

Dear Editor,

I / We wish to be an Annual Member/ Life Member/ Fellow Member of **"Research Journal of Chemistry and Environment"** and agree to abide by your rules and regulations.

1. Name in Full : _____ Male☐ Female☐
   (In Block Letters)
2. Nationality : _____ 3. Date of Birth_____
4. Correspondence Address :_____
   _____
5. Institutional/Business Address :_____
   _____
6. Mobile_____ E-Mail_____
7. Academic Qualifications : _____
8. Profession and Experience : _____
9. Present Position/Post : _____
10. Chemistry Interest : _____
11. How you came to know of Journal : _____

Membership Fees	Fellow	Life	Annual
Individual	Rs. 20,000/-, US $ 2000	Rs. 15,000/-, US $ 1500	Rs. 3000/-, US $ 300
Institutional	Rs. 30,000/-, US $ 3000	Rs. 20,000/-, US $ 2000	Rs. 4000/-, US $ 400

(Processing fees upto Four authors: Rs. 2000/-, US $ 200.)

Fellow Members can use the title "**FICCE**", (Fellow, International Congress of Chemistry and Environment) and **Associate Members (Life)** can use the title "**AICCE**" (Associate, International Congress of Chemistry and Environment) after their names, after approval by the editors.

Rs./$ _____remitted by Bank Draft No./Cheque No./Cash/M.O. Receipt No._____Date_____Banker's Name _____.

[For Cheques, please add Rs. 125/-(US $ 25) extra towards collection charges. Drafts/ Cheques should be in name of "**Research Journal of Chemistry and Environment**"]

Place : _____
Date : _____ (Signature of the applicant)

From the Editor's Desk

Vermicomposting as an environment friendly Bio-fertilizer

Sinha Jayanta
Our Guest Editor from Department of Zoology, B.B. College, Asansol, West Bengal, INDIA
jayantasinha_02@yahoo.co.in

With the dawn of the first Green revolution which came during the 1950s and 60s of the twentieth century, there has been a widespread usage of various agrochemicals such as fertilizers and chemical pesticides. This green revolution have been quite successful in increasing the quantity of food item but in turn reduced the nutrient levels and also had a detrimental effect on the soil fertility through years. Thus the soil became ravenous of these chemical inputs to sustain its crop yield. There has been an augment of crop yield between the times periods of 1950 to mid 1980s, but after that plateau was reached. Further usage of chemical fertilizers triggered a wide spread destruction of soil friendly microbes which had a huge role in renewing and rejuvenating natural fertility.

Chemical fertilizers again impaired the ability of 'biological resistance' in crops making them susceptible to pests and diseases. Thus agro-chemicals acted as a slow poison for the soil having serious withdrawal symptoms. Studies point to a bitter but obvious fact that continued use of chemical pesticides as a prime input and vital requirement of 1st green revolution, there is good amount of 'residual pesticides' that contaminate crops and remain after their post harvest processing and ultimately enter the human and other animals after they are bought and/or consumed. Edible samples have been contaminated with 100% with HCH and 50% with DDT. Scientific reports proved that pesticide residues were found in meat, fish, egg, milk and milk product and also in mother's milk and human fat. There was cent percent contamination with HCH, nearly 70% with DDT and 43% with aldrin, which is quite alarming.

Extoxnet data revealed in 1996 that Chloropyrifos is a very common contaminant that mixes with urban streams. Plants depend upon the variety of soil microbes to transform the atmosphere nitrogen into nitrites and nitrates which plants can utilize. Glyphosate reduces the growth and also the activity of nitrogen fixing bacteria in soil and also in root nodules. In India, excessive use of chemical fertilizers and pesticides was studied under Greenpeace in 2009, they conducted research in 50 villages in various districts of Punjab and revealed chemical, radiation and biological toxicity in Punjab.

Backlashes of the first green revolution have impelled agricultural scientist and other biologist to think for certain other alternatives for a much safer and environment friendly agricultural process and practice. Brundtland Commission Report (United Nations, 1987) advocated for '*Sustainable Development*' i.e. development (both social and economic) to meet the needs of present generation keeping in mind that the future generation are also to be accounted for their needs. Such development should also aim towards the advancement of total quality of life (i.e. the whole biosphere), therefore stewardship of both natural and human resource is of prime importance.

Searching for an alternative of the conventional agricultural practices, today scientists are genuinely searching for an economically stable, socially acceptable and environmentally sustainable alternative of the chemical aided agricultural practice.

One of the important approaches of sustainable agriculture is Organic farming or agriculture. This was developed as holistic and through an ecosystem based approach and is visualized as a feasible alternative to ecologically unsound conventional agriculture.

In India certified organic farming has enormous scope. About 30,000 ha of farmland were under certified agricultural production. In sustainable agriculture, especially organic farming there is employment of various novel methods that have been improvised from traditional knowledge. One of the most important methods of organic farming is the use of biofertilizers. The necessity of biofertilizers application has evolved primarily due to certain reasons i.e. despite the fact that chemical fertilizers boost soil fertility, crop productivity and production, but large scale / severe use of chemical fertilizers has caused grave concern of soil texture, soil fertility and other environmental backlashes, thus use of biofertilizers is both economical as well as environment friendly.

Vermicomposting is one of the most important biofertilizer that has a wide spread application. Vermicomposting is one of the age old traditions for generation of organic compost. Today use of this vermicompost as means for generation of organic fertilizer as a part of organic farming drive meets several requirement of sustainable agriculture. With the increment of 3Ps i.e. Population, Pollution and Poverty along with rapid industrialization and speedy urbanization, there is ever mounting problem of solid waste generation and disposal. These wastes pollute soil and damage it. So conversion of this solid waste into a nutrient rich material may be very important solution to such problems. This role can be played by an earthworm. Earthworms have been in

the process of waste and land management, soil improvement and farm production for 600 million years. That is why Charles Darwin referred them as 'Unheralded soldier of mankind and farmers', a friend working day and night under the soil.

Vermicomposting is a much uncomplicated biotech-nological procedure in which certain earthworm species are utilized to enhance and augment the process of solid waste conversion and produce a better and useful end product. Vermicomposting is very much different from conventional composting procedure. Fundamentally, it is a mesophillic process that utilizes microbes and earthworm being active at 10^oC - 32^oC. The process is much faster than conventional composting and is rich in pant growth regulators, microbial activity and is supported with pest deterrent properties.

Being a decomposition process and involving a combined activity of earthworm and microbes; they act as mechanical strainers modifying the physical and chemical properties, slowly reducing C: N ratio and augmenting the surface area which is exposed to microbes helping higher microbial activity and also decomposition. Vermicomposting is found to be successful with variety of raw materials such as solids from waste water, effluent from breweries, paper wastes and urban residues and also from horticultural residues, processed potatoes and mushroom identity. Vermicompost are known to be as 'miracle' for plant growth.

Very importantly vermicompost functions as a 'soil conditioner' and its continued use year after year shows the way to total improvement and recovery in the quality of soil and farmland, even the degraded and sodic soils. They act as a supplier of nutrients to plant roots and trigger growth and increase soil organic matter that includes humus and humic acid and thus affect nutrient storage and supports root growth, which soil takes many years to produce through decomposition of organic matter. Humic acid in soil helps fertilizers to work more efficiently. Further, leaves in vermicast also help in scrubbing 'toxins', harmful fungi and bacteria from soil and protect plant.

Vermicompost has obtained 'hormone-induced activity' which is related to high quantity of nutrients. Vermi-compost increased the rate of seed germination, growth of seedling and augmented certain growth promoting hormones viz. auxin, cytokinin, gibberlin being secreted by earthworm. Vermicompost is also very rich in microorganism and thus plays a pivotal role in improving soil fertility and increasing crop productivity and they are quite capable of atmospheric nitrogen fixation, solubilization of insoluble phosphorus and release of locked plant nutrents. It includes *Azotobacter*, *Actinomycetes*, *Nitrobacter*, *Rhizobium* and certain phosphate solubilizing bacteria.
The organic carbon present in the vermicompost helps in the release of nutrients slowly and steadily into the soil which helps the plants to absorb the nutrients available. Vermicompost was found to improve the trace element of the soil. Vermicompost has higher nitrate (more available form of nitrogen) where as conventional compost is higher in ammonium, it also supplies several other plant nutrients viz. phosphorus (P), potassium (K), sulfur (S) and magnesium (Mg). Soil treated with vermicompost has a significant augmentation in soil enzyme activities viz. urease, phophomonoesterase, phosphoodiesterase and arylsulphatase. Vermicompost is rich with enzymes such as lipase, amylase, chitinase and cellulose which help in break down of organic matter to the plant roots which are not feasible through the use of conventional chemical fertilizers.

Vermicompost acts as plant growth regulator and is a favoured nutrient supplier employed in organic farming. Vermicompost, especially those produced from various animal waste sources, generally have extra mineral elements than commercial plant growth media and many of these elements were transformed to forms which can be easily and readily taken up by the plants, such as nitrates, exchangeable phosphorus, and soluble potassium, calcium, and magnesium. In India, when vermicompost is applied during sorghum cultivation, crop exhibited appreciably increased growth morphological parameters viz. plant height, shoot biomass, root length, root biomass, leaf number and area in the mixtures of vermicompost and soil compared to the mixtures of normal compost and soil. It has been reported that earthworms and their excreta augmented the growth of different plants such as clover, rye, spinach, peas, oat, barley and wheat and also in paddy. Soil enriched with vermicompost improved the chlorophyll content of leaves and fresh and dry weight of plants.

One can achieve quality production of tomato as reflected through increase in total soluble solids, titratable acidity, pH and fruit dry matter and nutrient concentration (K, Fe, Zn, Cu and Mn) in tomato shoot. It is also proved that use of different levels of vermicompost to *Chrysanthemum chinensis* affected in increased fresh weight of flowers, number of flowers per plant, flower diameter and yield with the application at the rate of 10 t / hectare of vermicompost. A study was made in Griffith University during 2006-2007 where corn plants grown with vermicompost in soil accomplished quick and outstanding growth and reached maturity (reflected through the appearance of male and female reproductive organs) very quickly whereas plants on conventional compost could not mature until the period of study i.e. 14 weeks.

Further, plants on beds enriched with worms that are provided with 'feeding materials' work better than those on conventional compost at the completion of study period of 14 weeks. So it was inferred that worms require adequate 'organic residues' in soil to nourish upon and change into vermicast which functions as a 'storehouse' of nutrients and the growth promoting factors of biochemical nature.

Due to application of vermicompost higher germination, growth and yield of mung bean (*Vigna radiate* L.) compared with the control have been achieved. The use of vermicompost in the contribution of Ca and Mg macronutrients in lettuce production represented more availability of the above mentioned nutrients in relation to compost. Vermicompost application increased photo-synthetic pigments and leaf gas exchange in red pepper (*Capsicum annum* L.). When *Vinca rosea* and *Oryza sativa* were grown in 50:50 soil to vermicompost mixtures, it was noticed that length, weight, number of seeds, number of shoots in *Vinca* and tillers in *Oryzae* increased.

Sometimes vermicompost is used in combination with chemical fertilizers (NPK-90:75:60), it has been observed that there is a substantial increase in growth and yield in wheat crop where diminished dose i.e. three quarter dose of chemical fertilizer was adjuncted with full dose of vermicompost @ 2.5 t/ha. Even though vermicompost alone can work as 'driving force' but when chemical fertilizers are appended as 'helping hand', it can perform little better.

In recent years one can find many evidences regarding the ability of earthworms and its vermicompost to act as a plant protection agent against various pests and diseases either by suppressing or repelling them or by inducing biological resistance in plants to fight them or by killing them through pesticidal action. Relatively small applications of commercially-produced vermicomposts resisted or suppressed attacks by *Pythium*(fungus) on cucumbers, *Rhizoctonia* on radishes in the greenhouse and by *Verticillium* on strawberries and *Phomopsis* and *Sphaerotheca fulginae* on grapes in the field. This was due to microbial antagonism by the microbes present in vermicompost.

Moreover, earthworm excreted actinomycetes fungus in their vermicast produce chemicals that destroy parasitic fungi, such as *Pythium* and *Fusarium*. Stripted cucumber beetle (*Acalymma vittatum*), spotted cucumber beetle (*Diabotrica undecimpunctata*) and larval hornworms (*Manduca quinquemaculata*) damage on tomatoes can be reduced by application of vermicompost, both in greenhouse and field experiments. According to a study of aphids, mealy bug, spider mite populations decreased significantly, along with a subsequent reduction in plant damage in tomato, pepper and cabbage trials with 20% and 40% vermicompost additions. Field treatments of soil with vermicomposts reduced the incidence of leaf miner *Aproaerema* on groundnuts. Jassids (*Empoasca verri*) and aphid (*Aphis* sp.) attacks were decreased in response to field applications of vermicompost.

Vermicompost is an eco- friendly, economical and non-toxic biofertilizer that uses low energy input for composting and is a recycled biological material.

******

Design, synthesis and interaction with Cu^{2+} ions of ice templated composite hydrogels

Dragan Ecaterina Stela* and Dinu Maria Valentina
"Petru Poni" Institute of Macromolecular Chemistry, Aleea Grigore Ghica 41A, 700487 Iasi, ROMANIA
*sdragan@icmpp.ro

Abstract
Semi-interpenetrating polymer networks (semi-IPN) composite hydrogels based on polyacrylamide (PAAm) and chitosan (CS) were prepared either at room temperature (22 ^oC) or at -18 ^oC. The swelling kinetics and gels morphology were strongly influenced by the synthesis temperature. Full-IPN hydrogels were prepared by the cross-linking of CS entrapped in PAAm matrix with epichlorohydrin in alkaline medium. The sorption capacity for Cu^{2+} ions was strongly influenced by the generation of the second network at high pH because a partial hydrolysis of the PAAm matrix simultaneously occurred. The synthesis temperature of semi-IPN hydrogel had also an influence, the conventional hydrogels synthesized at 22 ^oC having a lower sorption capacity than those synthesized at -18 ^oC.

Keywords: Chitosan, composite, cryogels, interpenetrating polymer networks, copper, dye.

Introduction

Hydrogels are usually described as hydrophilic polymers which swollen in water without dissolving, their integrity being stabilized by physical or chemical linkages. Hydrogels absorb water due to the presence of numerous hydrophile chemical groups (such as –OH, $-CONH_2$, – CONH, –COOH and $-SO_3H$), capillary effects and osmotic pressure. Stimuli responsive hydrogels change their volume/shape in response to small variations of the external environment such as pH, ionic strength, temperature, or electromagnetic radiation.[1-4]

For many applications, multicomponent hydrogels as semi- or interpenetrating polymer networks (IPN) show improved response rate and diffusion of solutes.[5-8] IPNs represent an intimate association of two independently cross-linked polymers, at least one of which being cross-linked or synthesized in the presence of the other. Semi-IPNs hydrogels are typically produced in a "single step" by synthesizing a hydrophilic polymer matrix around the pre-existing water soluble polymer chains considering the trapped polymer.

Due to the characteristic properties such as high hydrophylicity, biocompatibility and lack of toxicity, hydrogels have a wide range of biological, medical and pharmaceutical applications,[9,10] as well as in agriculture, as soil conditioners, to decrease soil erosion or to control the release of herbicides[11,12] and in hydrometallurgy as adsorbents in waste water remediation. The ability of a hydrogel to adsorb ionic species is depending on some of its intrinsic characteristics like: hydrophilic/hydrophobic balance, swelling degree, chemical and mechanical stability.

Many types of hydrogels based sorbents are effective in removing heavy metal ions from aqueous effluents.[13-15] Natural polymeric materials are gaining more and more interest for application as adsorbents in waste water treatment due to their biodegradability and non-toxic nature.[16-20] However, the structural versatility of synthetic polymers makes them very attractive for the removal of various organic compounds.[19,20] A combination of natural and synthetic polymers in the preparation of multicomponent hydrogels can enhance the properties of the gel or even induce novel characteristics for the gels.[11,21]

The macroporous hydrogels, characterized by a faster response at the external stimuli compared to the conventional hydrogels, received enhanced attention in last decade. One route to get macroporous hydrogels is to conduct cross-linking reactions below the freezing point of the reaction solutions, when the most part of water (free water) forms crystals, the bound water and the soluble substances (monomers, initiator, polymers) being concentrated in a non-frozen liquid microphase. [22-24] The ice crystals act as inert template, the microstructure of the gel being the negative replica of the ice crystals. Cryogels can withstand high levels of deformations, such as elongation and torsion, being characterized by superfast responsiveness at water absorption.[25-27]

Ionic multicomponent cryogels, having enhanced mechanical and chemical resistance, have been tested as novel sorbents in the separation processes of small ionic species.[28-32] Therefore, cryogelation technique was adopted to prepare super- macroporous ionic composite IPN gels consisting of cross-linked PAAm as the first matrix and chitosan (CS) as trapped polycation.

The synthesis of some ionic composite hydrogels based on CS as a physical entrapped polymer within polyacrylamide (PAAm) 3D network, as a function of the cross-linker ratio, CS molar massand pH of the reaction mixture has been recently reported.[29,33] The evaluation of the sorption properties of the semi-IPN and full-IPN composite

Author for Correspondence

hydrogels obtained at 22 ^{o}C and -18 ^{o}C for Cu^{2+} was developed in the present paper.

Material and Methods

Chitosan as powder, with molar mass of 235 kDa (CS1) and 467 kDa (CS2), purchased from Sigma-Aldrich, was used as received. The viscometric average molar mass was measured in 0.3 M CH_3COOH - 0.2 M CH_3COONa (1:1, v/v), at 25 ± 0.1 ^{o}C according to the method previously described.[18,34] Degree of acetylation (DA) of CS was evaluated by infrared spectroscopy in KBr pellets, using a Vertex 70 Bruker FTIR spectrometer as previously shown.[18,34] An average value of DA = 15% resulted from three measurements, was taken into account. Acrylamide (AAm, Fluka), N,N'-methylenebisacrylamide (BAAm), ammonium persulfate (APS), N,N,N',N'-tetramethyl ethylenediamine (TEMED), all purchased from Sigma-Aldrich, were used as received.

ECH purchased from Sigma-Aldrich, was double distilled on KOH before using. Stock solutions of APS and TEMED were prepared by dissolving 0.2 g of APS and 0.625 mL of TEMED, each in 25 mL of double distilled water. Stock solutions of BAAm were prepared by dissolving BAAm, calculated for a certain cross-linker ratio in 10 mL of double distilled water at 30^{o}C under magnetic stirringand used for cryogels synthesis after 24 h. $CuSO_4.5H_2O$ (from Aldrich) was used as metal ion source for the adsorption tests.

Composite hydrogels, based on PAAm and CS, were prepared by free radical cross-linking copolymerization in aqueous medium at two temperatures: at 22 ^{o}C to obtain conventional hydrogels (HG)and at -18 ^{o}C, to get cryogels (CG). The initial concentration of monomers (AAm + BAAm), C_o, was kept constant (5 wt.%). The redox initiator system used consisted of APS and TEMED. The concentrations of initiator (APS) and activator (TEMED) were kept constant in all experiments. The cross-linker ratio X (the mole ratio of the cross-linker BAAm to the monomer AAm) was fixed at 1:60. The synthesis procedure used in the preparation of semi-IPN composite hydrogels is briefly presented below:

Typically, 0.4825 g AAm, 6.3 g aqueous solution of CS1 (1 wt.-%), 0.7 mL double distilled water, 1 mL BAAm (0.436 g/25 mL) and 1 mL TEMED (0.625 mL/25 mL) were first mixed in a graduated flask of 10 mL. The solution was cooled at 0 ^{o}C in ice-water bath, purged with nitrogen gas for 20 min and then, 1 mL of APS stock aqueous solution was added and the whole mixture was further stirred about 20 sec. Portions of this solution, each 1 mL, were transferred to syringes of 4 mm in diameter; the syringes were sealed, immersed in a thermostated bath at either 22 ^{o}C or -18 ^{o}Cand the polymerization was conducted for 24 h. After polymerization, the gels were cut into pieces of about 10 mmand immersed in water for 48 h to wash out any soluble polymers, unreacted monomers and the initiator. Thereafter, the swollen gel samples were frozen in liquid nitrogenand freeze dried in a Martin Christ, ALPHA 1-2LD device (24 h, at -57 ^{o}C and 0.045 mbar), for 24 h.

For the synthesis of full-IPN composite hydrogels, the just synthesized semi-IPN gels, cut into pieces of about 10 mm, were immersed in a flask containing 0.6 mL ECH in 60 mL aqueous solution of 2 M NaOHand kept at 22 ^{o}C for 24 h, followed by 2 h at 37 ^{o}C.[29,33] After that, the gel pieces have been separated from the basic medium and intensively washed with distilled water up to neutral pH. The swollen gels were freeze dried in the same conditions like the semi-IPN cryogels. The sample code consists of IPN composite hydrogels consisting of semi-IPN or full-IPN followed by 1 or 2, for CS1 or CS2 used as trapped polymer respectively and a number with two figures, which represents the mole number of AAm per one mole of BAAm.

Surface morphology and internal structure of the dried composite gels were observed by an Environmental Scanning Electron Microscope (ESEM) type Quanta 200 operating at 20 kV with secondary electrons, in low vacuum mode. Swelling behavior of composite hydrogels in water was investigated using the conventional gravimetric procedure. The dried gels were immersed in water at pH 5.5, at 25 ^{o}C. Swollen gels were weighed by an electronic balance, at predetermined intervals, after wiping the excess surface liquid by filter paper. The swelling ratio (*SR*) was defined by eq. (1):

$$SR = (W_t - W_d)/W_d,\ g \cdot g^{-1} \quad (1)$$

where W_d is the weight (g) of the dried sample and W_t is the weight (g) of the swollen sample at time *t*.

Study of the metal ion sorption properties of the composite hydrogels was carried out using a batch equilibrium procedure. Thus, around 0.01 g of dried sample was placed in a flask and contacted with 10 mL of the aqueous solution of Cu^{2+}, with a concentration of 444.5 mg/L, at 25 ^{o}C and pH 5.5, at different contact durations (up to 3 h). The composite gels were filtered offand the residual concentration of Cu^{2+} remained in the filtrate was measured by the UV-VIS spectroscopy at 808 nm, on a SPECORD M42 Carl Zeiss Jena, Germany.

The amount of Cu^{2+} sorbed on the composite gels was calculated with eq. 2:

$$q_t = \frac{(C_0 - C_t)V}{W}, mg/g \quad (2)$$

where C_0 and C are the concentrations of the metal ion in aqueous solution (mg/L) before and after the interaction with composite gel respectively, V is the volume of the aqueous phase (L)and W is the amount of the dried

composite gel (g). For each adsorption experiments, the average of three replicates was reported.

Results and Discussion

The strong difference between the swelling kinetics of conventional hydrogels and cryogels is shown in fig. 1. As can be observed from fig. 1A, the time necessary to attain the equilibrium swollen state starting from the dry state was about 600 min for the conventional hydrogel. On the other hand, the corresponding cryogel is characterized by a superfast swelling, the equilibrium swellen state being attained in 2 - 3 sec (the inset of fig. 1A). The semi-IPN cryogel presents also the typical behavior for the macroporous morphologies with interconnected pores i.e. the most part of water adsorbed being driven out by squeezing and sucked up very fast when the pressure is removed.

The main differences between full-IPN and semi-IPN cryogels concerning the swelling kinetics (full-IPN1.60, fig. 1B, compared to semi-IPN1.60, fig. 1B) consist of the much higher values of the equilibrium swelling ratio (155 g/g compared with 33 g/g) and of the time necessary to reach the equilibrium swelling which was about 45 sec compared with 3 sec. The increase of the time necessary to reach the equilibrium swelling is explained by the changes in the morphology of the cryogels and by the presence of two networks which respond independently to environmental changes. The much higher swelling ratios of full-IPN cryogels are explained by the presence of the anionic matrix which is bearing -COO^- groups known for their high hydrophilicity.

The morphologies of freeze-dried gel samples were examined by SEM. Figs. 2A and 2B show the microstructure of the semi-IPN and full-IPN composite hydrogels as a function of CS molar mass, the cross-linker ratio being the same (1:60). As can be observed, the gel morphology was strongly influenced by the synthesis temperature (22 ^oC for conventional hydrogelsand -18 ^oC, for cryogels). Thus, the semi-IPN conventional hydrogel (Fig. 2A, left) has no visible pores, while the cryogels (Fig. 2A, middleand Fig. 2B, left) show interconnected macropores. The CS molar mass seems to influence mainly the pore walls, which are thicker in the case of cryogels prepared with CS2 (Fig. 2B) than in the case of cryogels prepared with CS1 (Fig. 2A).

Sorption kinetics of Cu^{2+} onto IPN PAAm/CS composite gels: First test on the adsorption of Cu^{2+} was performed on the semi-IPN1.60 but no significant adsorption occurred. Therefore, only full-IPN composite hydrogels were used in the next sorption experiments. The amount of metal ion adsorbed on the conventional hydrogels (HG-IPN1.60 and HG-IPN2.60) as a function of contact time at a temperature of 25 ^oC, at pH 5.5, are presented in fig. 3. As can be observed from fig. 3, the sorption equilibrium was established after about 100 min and that further increase of the contact duration did not influence the sorption process. The effect of the contact time on the Cu^{2+} sorption capacity of the composite cryogels is presented in fig. 4. As can be seen, in the case of cryogels, the sorption equilibrium was established in about 90 min and that the cryogels had a higher sorption capacity compared to conventional hydrogels. However, the amount of metal ions sorbed at equilibrium was almost independent on the CS molar mass for both conventional hydrogels and cryogels.

To get information about the sorption mechanism of Cu^{2+} ions on the composite hydrogels, the experimental kinetic data were analyzed by two kinetic models. The Lagergren rate equation, known as the pseudo-first-order (PFO) kinetic model, considers the adsorption rate proportional with the difference between the equilibrium adsorption capacity and the adsorbed amount, its nonlinear form being expressed by eq. 3[35]:

$$q_t = q_e\,(1 - e^{-k1t}) \tag{3}$$

where q_e and q_t are the amounts of metal ion sorbed at equilibrium (mg/g) and at time t respectively and k_1 is the rate constant of the PFO kinetic model (min^{-1}).

The pseudo-second-order (PSO) kinetic model is based on the assumption that the rate-limiting step is chemisorption involving valence forces through sharing or exchange electrons between adsorbent and sorbate, the nonlinear form being expressed by eq. 4[36]:

$$q_t = \frac{k_2 q_e^{\,2} t}{1 + k_2 q_e t} \tag{4}$$

where q_e and q_t have the same meaning as in eq. 3, k_2 being the rate constant of PSO kinetic model (g mg^{-1} min^{-1}).

All the kinetic parameters were evaluated by the non-linear regression method using an OriginPro 7.5 software. The nonlinear regression method was adopted because it was previously demonstrated that the calculated errors are reduced compared with the linear fitting.[32,37]

As table 1 shows, the theoretical $q_{e,calc}$ values estimated by fitting the PFO kinetic model are significantly different compared to experimental values, the correlation coefficients being also low. These results show that the PFO kinetic model does not describe well the sorption process. On the other hand, the values of $q_{e,calc}$ estimated by fitting the PSO kinetic model (Eq. 4) are very close to those experimentally found, irrespective of CS molar mass, the correlation coefficients being high for all full-IPN composite gels. Therefore, it could be assumed that the adsorption of Cu^{2+} onto the full-IPN composite gels obeys the PSO kinetic model better than the PSO kinetic modeland this supports the chemisorption would be the

rate-determining step controlling the adsorption process of metal ion.

The strong difference between semi-IPN and full-IPN concerning the interaction with Cu^{2+} which consists of the missing of the sorption capacity for metal ions of the semi-IPN and a significant sorption capacity of full-IPN, could be explained by the status of CS chains, which are embedded in the walls of semi-IPN cryogels, which were getting more accessible after the formation of the second network in full-IPN (Figs. 2A and 2B).

On the other hand, it has been already demonstrated that during the formation of the second network under alkaline conditions, a high number of $-COO^-$ groups were generated on the PAAm matrix, which contribute to the binding of metal ions.[29] As can be observed from the colored images in figs. 3A and 3B, a strong dehydration of the cryogel occurred after the interaction with Cu^{2+}, the diameter of the sample after this process being about ¼ and ½ from that of the initial gels, in the case of full-IPN conventional hydrogels (Fig. 3A)and in the case of full-IPN cryogels (Fig. 3B). This behavior is supporting a strong interaction between the functional groups of the gels and Cu^{2+} ions.

Conclusion

In this paper we described first the preparation and characterization of semi-IPN and full-IPN composite hydrogels as monoliths based on cross-linked PAAm as a matrix and CS as trapped polymer. The swelling kinetics and the gels morphology support the strong difference between the conventional hydrogels and cryogels.

It was found that while the semi-IPN had no adsorption capacity for Cu^{2+}, a significant sorption capacity of metal ions was found for full-IPN composite hydrogels which recommend them as potential sorbents for heavy metal ions. The strong difference between semi-IPN and full-IPN concerning their interaction with Cu^{2+} is attributed to the structural changes in the PAAm matrix which occur during the formation of the second network at high pH, when part of the amide groups was transformed in carboxylate groups.

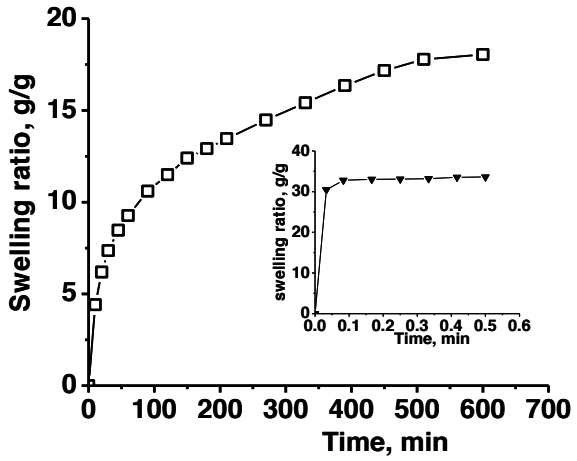

Fig. 1A: Swelling ratio as a function of contact time for semi-IPN composite hydrogel prepared with CS1 as entrapped polymer; the inset shows the swelling ratio as a function of contact time for the corresponding semi-IPN composite cryogel.

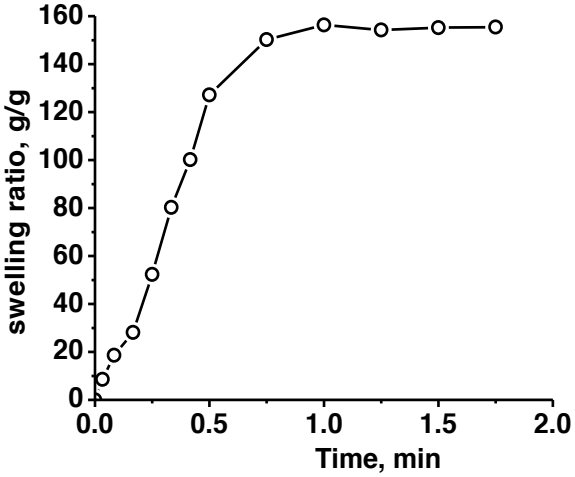

Fig. 1B: Swelling ratio as a function of contact time for semi-IPN composite cryogel prepared with CS1 as entrapped polymer.

Table 1
Kinetic parameters for the sorption of Cu^{2+} on the conventional hydrogels (HG) and cryogels (CG)

Full-IPN hydrogel sample	$q_{e,\,exp}$, mg/g	PFO kinetic model			PSO kinetic model		
		$q_{e,\,calc}$, mg/g	k_1, min^{-1}	R^2	$q_{e,\,calc}$, mg/g	k_2, g/mg x min	R^2
HG IPN1.60	24.32	31.34	2.43×10^{-2}	0.981	24.653	0.70×10^{-3}	0.990
CG IPN1.60	30.9	41.86	2.86×10^{-2}	0.974	32.36	0.65×10^{-3}	0.983
HG IPN2.60	23.25	28.25	2.96×10^{-2}	0.986	22.97	11.3×10^{-3}	0.993
CG IPN2.60	32.1	44.53	2.69×10^{-2}	0.987	32.237	0.6×10^{-3}	0.990

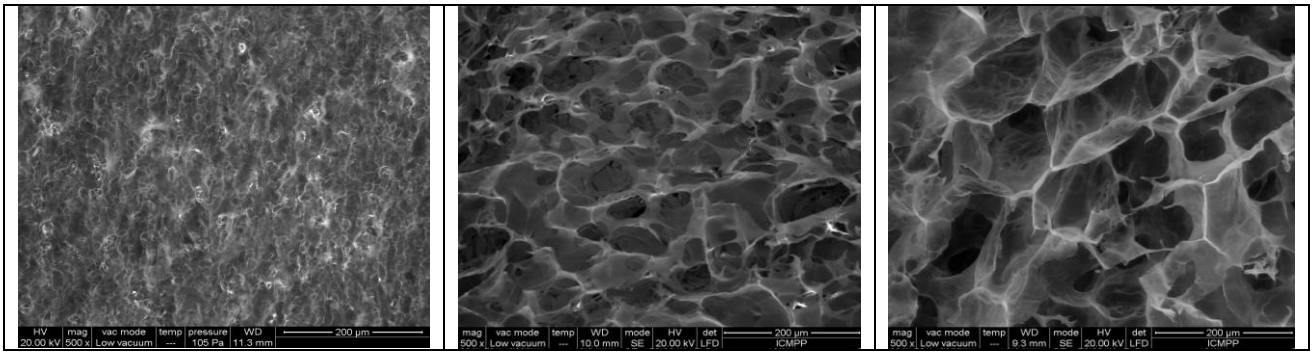

Fig. 2 A: SEM images of semi-IPNconventional hydrogel (left), semi-IPN cryogel (middle) and full-IPN cryogel (right) synthesized with CS1entrapped in PAAm matrix; scalling bar 200μm and Mag 500x

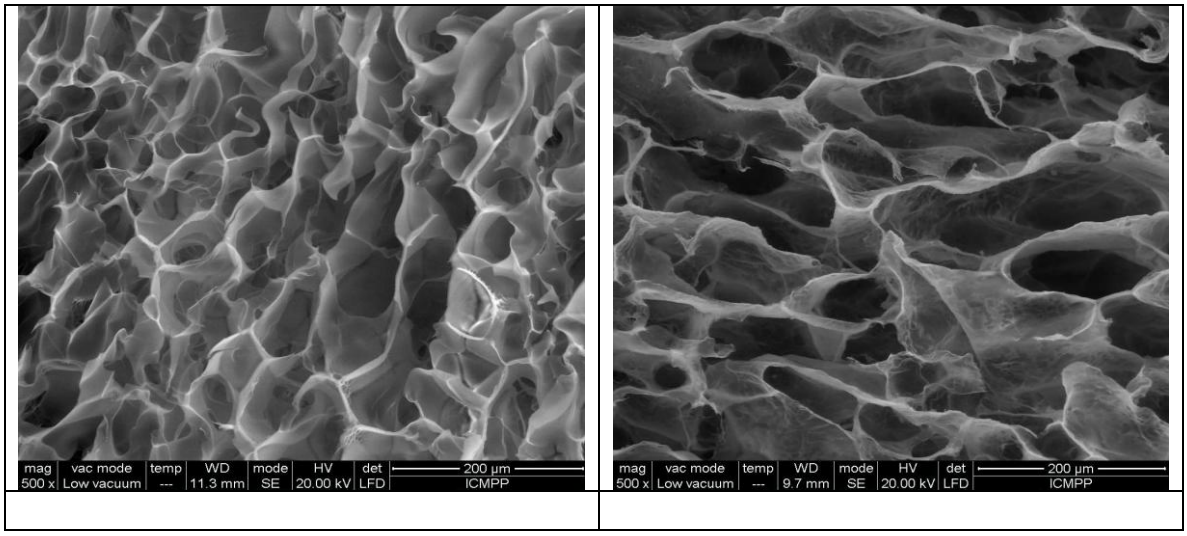

Fig. 2 B: SEM images of semi-IPN (left) and full-IPN (right) of the cryogels synthesized with CS2 entrapped in PAAm matrix; scalling bar 200μm and Mag 500x.

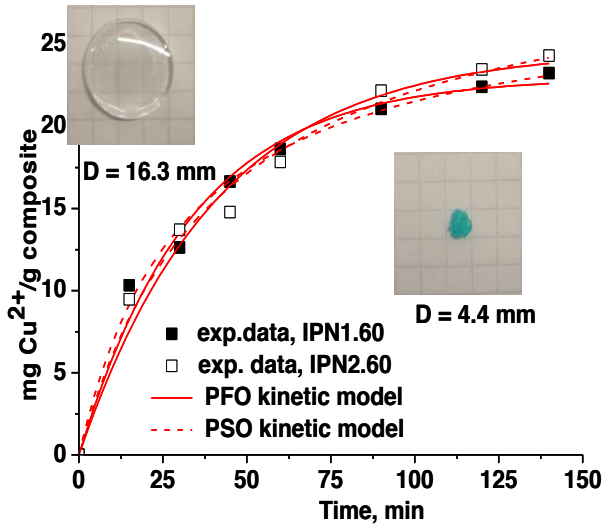

Fig. 3: Sorption kinetics of Cu^{2+} on two conventional full-IPN composite hydrogels prepared with CS1 (IPN1.60) and CS2 (IPN2.60); temperature 25 ^{o}C, sorbent dose 0.01 g, initial concentration of Cu^{2+} 444.5 mg/L.

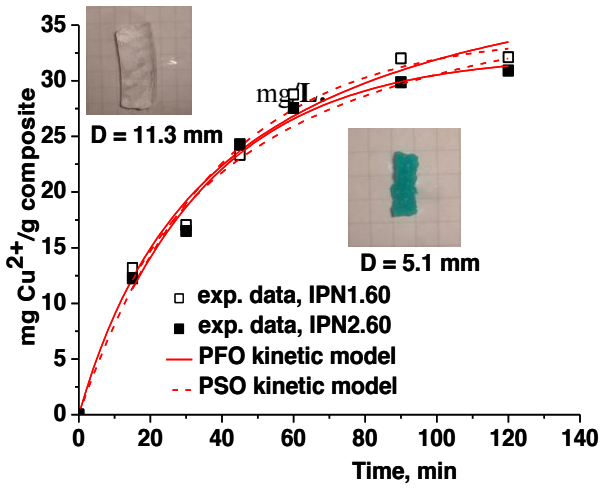

Fig. 4: Sorption kinetics of Cu^{2+} ions on two composite cryogels prepared with CS1 (IPN1.60) and CS2 (IPN2.60); temperature 25 ^{o}C, sorbent dose 0.01 g, initial concentration of Cu^{2+} 444.5 mg/L.

Acknowledgement
This work was supported by CNCSIS-UEFISCSU by the project PN-II-ID-PCE-2011-3-0300.

References
1. Chen J., Liu M. and Chen S., Synthesis and characterization of thermo- and pH-sensitive kappa-carrageenan-*g*-poly (methacrylic acid)/poly (N,N-diethylacrylamide) semi-IPN hydrogel, *Mat. Chem. Phys.*, **115**, 339 (**2009**)

2. Kim B. and Shin Y., pH-Sensitivity Swelling and Release Behaviors of Anionic Hydrogels for Intelligent Drug Delivery System, *Journal of Applied Polymer Science*, **105**, 3656 (**2007**)

3. Liu F. and Urban M.W., Recent advances and challenges in designing stimuli-responsive polymers, *Progress in Polymer Science*, **35**, 3 (**2010**)

4. Wang Q., Zhang J. and Wang A., pH-Responsive Carboxymethylcellulose-*g*-Poly (sodium acrylate)/ Polyvinyl pyrrolidone Semi-IPN Hydrogels with Enhanced Responsive and Swelling Properties, *Macromol. Res.*, **19**, 57 (**2011**)

5. Liang S., Liu L., Huang Q. and Yam K.L., Preparation of single or double-network chitosan/poly (vinyl alcohol) gel films through selectively cross-linking method, *Carbohydr. Polym.*, **77**, 718 (**2009**)

6. Murthy P.S.K., Mohan Y.M., Sreeramulu J. and Raju K.M., Semi-IPNs of starch and poly(acrylamide-co-sodium methacrylate): Preparation, swelling and diffusion characteristics evaluation, *React. Funct. Polym,* **66**, 1482 (**2006**)

7. Myung D., Waters D., Wiseman M., Duhamel P.E., Noolandi J., Ta C.N. and Frank C.W., Progress in the development of interpenetrating polymer network hydrogels, *Polym. Adv. Technol.*, **19**, 647 (**2008**)

8. Thimma Reddy T. and Takahara A., Simultaneous an squential micro-porous semi-interpenetrating polymer network hydrogel films for drug delivery and wound dressing applications, *Polymer*, **50**, 3537 (**2009**)

9. Muzzarelli R.A.A., Genipin-crosslinked chitosan hydrogels as biomedical and pharmaceutical aids, *Carbohydr. Polym.*, **77**, 1 (**2009**)

10. Peppas N.A., Hilt J.Z., Khademhosseini A. and Langer R., Hydrogels in Biology and Medicine: From Molecular Principles to Bionanotechnology, *Adv. Mater.*, **18**, 1345 (**2006**)

11. Abd El-Rehim H.A., Characterization and Possible Agricultural Application of Polyacrylamide/Sodium Alginate Crosslinked Hydrogels Prepared by Ionizing Radiation, *J. Appl. Polym. Sci.*, **101**, 3572 (**2006**)

12. Zohuriaan-Mehr M.J., Omidian H., Doroudiani S. and Kabiri K., Advances in non-hygienic applications of superabsorbent hydrogel materials, *J. Mater. Sci.*, **45**, 5711 (**2010**)

13. Bajpai S.K. and Johnson S., Superabsorbent hydrogels for removal of divalent toxic ions. Part I: Synthesis and swelling characterization, *React. Funct. Polym.*, **62**, 271 (**2005**)

14. Chauhan K., Chauhan G.S. and Ahn J.H., Synthesis and characterization of novel guar gum hydrogels and their use as Cu^{2+} sorbents, *Bioresour. Technol.*, **100**, 3599 (**2009**)

15. Zheng Y., Hua S. and Wang A., Adsorption behavior of Cu^{2+} from aqueous solutions onto starch-g-poly(acrylic acid)/sodium humate hydrogels, *Desalination*, **263**, 170 (**2010**)

16. Chen A.H., Liu S.C., Chen C.Y. and Chen C.Y., Comparative adsorption of Cu(II), Zn(II)and Pb(II) ions in aqueous solution on the crosslinked chitosan with epichlorohydrin, *J. Hazard. Mater.*, **154**, 184 (**2008**)

17. Copello G.J., Varela F., Martinez Vivot R. and Diaz L.E., Immobilized chitosan as biosorbent for the removal of Cd(II), Cr(III) and Cr(VI) from aqueous solutions, *Bioresour. Technol.*, **99**, 6538 (**2008**)

18. Dragan E.S., Dinu M.V. and Timpu D., Preparation and characterization of novel composites based on chitosan and clinoptilolite with enhanced adsorption properties for Cu^{2+}, *Bioresour. Technol.*, **101,** 812 (**2010**)

19. Dragan E.S. and Dinu I.A., Removal of Azo Dyes from Aqueous Solution by Coagulation/Flocculation with Strong Polycations, *Res. J. Chem. Environ.,* **12(3)**, 5 (**2008**)

20. Bucatariu F., Dragan E.S., Fundueanu Gh., Covaci A. and Dirtu A.C., Interaction of some persistent organic pollutants with oligopeptide chains formed onto silica microparticles, *Res. J. Chem. Environ.,* **17(1)**, 68-75 (**2013**)

21. Rodriguez D. E., Romero-Garcia J., Ramirez-Vargas E., Ledezma-Perez A. S. and Arias-Marin E., Synthesis and swelling characteristics of semi-interpenetrating polymer network hydrogels composed of poly(acrylamide) and poly(γ-glutamic acid), *Materials Letters*, **60**, 1390 (**2006**)

22. Lozinsky V.L., Plieva F.M., Galaev I.Y. and Mattiasson B., The potential of polymeric cryogels in bioseparation, *Bioseparation*, **10**, 163 (**2001**)

23. Dinu M.V., Ozmen M.M., Drăgan E.S. and Okay O., Freezing as a path to build macroporous structures: Superfast responsive polyacrylamide hydrogels, *Polymer*, **48**, 195 (**2007**)

24. Bucatariu Florin, Dragan Ecaterina Stela, Fundueanu Gheorghe,Covaci Adrian and Dirtu Alin Constantin , Interaction of some persistent organic pollutants with oligopeptide chains formed onto silica microparticles, *Res. J. Chem. Environ.*,**17(1)**, 68-75 (**2013**)

25. Zhao Q., Sun J., Wu X. and Lin Y., Macroporous double network cryogels: formation mechanism, enhanced mechanical strength and temperature/pH dual sensitivity, *Soft Matter*, **7**, 4284 (**2011**)

26. Dinu M.V., Perju M.M. and Dragan E.S., Composite IPN ionic hydrogels based on polyacrylamide and dextran sulfate, *React. Funct. Polym.*, **71**, 881 (**2011**)

27. Orakdogen N., Karacan P. and Okay O., Macroporous, responsive DNA cryogel beads, *React. Funct. Polym.*, **71**, 782 (**2011**)

28. Tekin K., Uzun L., Şahin C.A., Bektaş S. and Denizli A., Preparation and characterization of composite cryogels containing imidazole group and use in heavy metal removal, *React. Funct. Polym.*, **71**, 985 (**2011**)

29. Dragan E.S., Perju M.M. and Dinu M.V., Preparation and characterization of IPN composite hydrogels based on polyacrylamide and chitosan and their interaction with ionic dyes, *Carbohydr. Polym.*, **88**, 270 (**2012**)

30. Hajizadeh S., Kirsebom H., Galaev I.Y. and Mattiasson B., Evaluation of selective composite cryogel for bromate removal from drinking water, *J. Sep. Sci.*, **33**, 1752 (**2010**)

31. Liu M., Liu H., Bai L., Liu Y., Cheng J. and Yang G., Temperature swing adsorption of melamine on thermosensitive poly(N-isopropylacrylamide) cryogels, *J. Mater. Sci.*, **46**, 4820 (**2011**)

32. Apopei D.F., Dinu M.V., Trochimczuk A. and Dragan E.S., Sorption isotherms of heavy metal ions onto semi-IPN cryogels based on polyacrylamide and anionically modified potatoes starch, *Ind. Eng. Chem. Res.*, **51**, 10462 (**2012**)

33. Dragan E.S., Perju M.M., Dinu M.V. and Doroftei F., Macroporous composite IPN hydrogels based on poly(acrylamide) and chitosan with tuned swelling and sorption of cationic dyes, *Chem. Eng. J.*, **204-206**, 198 (**2012**)

34. Gamzazade A.I., Shimac V.M., Skljar A.M., Stykova E.V., Pavlova S.A. and Rogozin S.V., Investigation of the hydrodynamic properties of chitosan solutions, *Acta Polymerica*, **36**, 420 (**1985**)

35. Lagergren S., Kungliga Svenska Vetenskapsakademiens, *Handlingar*, **24**, 1 (**1898**)

36. Ho Y. S., Review of second-order models for adsorption systems, *J. Hazard. Mater.*, **136**, 681 (**2006**)

37. Foo K.Y. and Hameed B.H., Insights into the modeling adsorption isotherm systems, *Chem. Eng. J.*, **156**, 2 (**2010**).

(Received 20th May 2013, accepted 10th September 2013)

Syngas production by carbon dioxide reforming methane over carbonaceous catalyst and reaction kinetics of carbonaceous materials

Zhang Guojie[1*], Du Yannian[1], Xu Ying[1] and Shi Xiaoling[2]
1. Key Laboratory of Coal Science and Technology, Taiyuan University of Technology, Taiyuan 030024, CHINA
2. Research Institute of Changzhi Sports Bureau, Changzhi 046001, CHINA
*Zhgjdoc@126.com

Abstract
In this work, synthesis gas production by carbon dioxide reforming methane over carbonaceous catalyst and reaction kinetics of carbonaceous materials with carbon dioxide were investigated using a fixed bed reactor system operating at atmospheric pressure. Mass balance of reforming reaction studies was conducted by measuring C element. The gas was detected by FPD and PID equipped gas chromatography. The results showed that the carbonaceous materials have a profound catalytic effect on the CH_4 cracking and CH_4-CO_2 reforming, the initial reaction temperature decreased about 50^oC.

Beyond the simple material balance, it can be found that the mass of carbon content in phase gas increases during the carbon dioxide reforming methane. It indicated that the gasification of carbonaceous materials by CO_2 takes place during the synthesis production process by carbon dioxide reforming methane over carbonaceous catalyst. An overall unreacted shrinking core model is formulated to describe the rates of the reaction kinetics of carbonaceous materials with carbon dioxide processes. The apparent activation energy of the reaction of carbonaceous materials with CO_2 was more than 230kJ/mol during CH_4-CO_2 reforming.

Keywords: CH_4 cracking, CH_4-CO_2 reforming, Kinetics, Carbonaceous catalyst, Syngas.

Introduction

Methane is the most abundant organic molecule in the Earth's atmosphere and plays important role in both the planet's radiative energy budget and global atmospheric chemistry [1, 2].Global warming is primarily a problem of too much carbon dioxide in the atmosphere. This carbon overload is caused mainly when we burn fossil fuels like coal, oil and gas or cut down and burn forests [1-3].

On the one hand, CO_2 and CH_4 are the most important greenhouse gases after H_2O vapour, leading adverse effect in global warming [4-6], but on the other hand, CO_2 and CH_4 are precious resources. Any success in research and development of a feasible utilization of CO_2 and CH_4 will signify the attainment of objectives of slowing down a build-up of greenhouse gases in the atmosphere and better carbon resource utilization. The reforming of methane with carbon dioxide is a promising method for production of synthesis gas with a low H_2/CO ratio which are preferable feeds for F–T synthesis, dimethyl ether and methanol production [7, 8].

Many literature reports have focused on the catalytic reforming of CO_2-CH_4 over transition metals such as Ni, Fe and Co which can be easily deactivated by carbon deposition. Great efforts have been focused on the development of noble metals catalysts such as Ru, Rh, Pd, Ra, Ir which can be more resistant to coking, but higher cost and limited availability discouraged their industrial application [6, 9-11]. Due to the difficulty in the utilization of CO_2-CH_4 reforming via the conventional catalysis, a search for suitable new catalysts is still a research priority. A possible alternative and a new kind of cheap carbon-based catalysts for reforming of CO_2-CH_4 to produce syngas were proposed and have been developed in laboratories [9-13].

This catalyst showed not only a high resistance to carbon formation, but also a high activity and selectivity in the reforming. . However, there are still some unknowns such as the difference between the carbonaceous catalyst and carbon deposition, the carbonaceous consumption and so on. In this work, carbon dioxide reforming methane over carbonaceous catalyst and reaction kinetics of carbonaceous materials with carbon dioxide is discussed.

Material and Methods

Catalyst preparation and Catalytic activity test: The carbonaceous catalysts (C-catalyst) used in the experiment were prepared by pyrolysis of Datong coal at 1150 ^oC for 1.5h, crushing the catalyst mass to 30-60 mesh-size particles.

The catalytic activity measurements of reforming of CO_2-CH_4 reforming were carried out at the normal pressure in a continuous-flow quartz reactor (I.d. 20 mm) packed with 3.0g catalyst and provided with a thermocouple located in the center of the catalyst bed [5]. Before carrying out the reaction, the catalyst was heated in situ at 800^{0}C in a flow of moisture-free nitrogen for 1 h. After carrying out the reaction, the product gases (after condensation) were analyzed by gas chromatography (GC) [9-15]. All experiments with larger errors in the material balances were rejected.

The conversion of methane and carbon dioxide can be calculated using the following equation:

$$\text{Conversion } (CH_4)\ X_{CH4} = (V_{in}\ C_{CH4,in} - V_{out}\ C_{CH4,out}) / V_{in}\ C_{CH4,in} \quad (1)$$

$$\text{Conversion } (CO_2)\ X_{CO2} = (V_{in}\ C_{CO2,in} - V_{out}\ C_{CO2,out}) / V_{in}\ C_{CO2,in} \quad (2)$$

where "V" is the total volumetric flow rate, "C" is the concentration of CH_4 or CO_2 and the subscripts "in" and "out" refer to the reactor inlet and outlet conditions respectively. The flow rate at the exit of the reactor was determined using a soap bubble flow meter.

Balance Equation: A material balance is an accounting for material. Thus, material balances are often compared to the balancing of current accounts. They are used in industry to calculate mass flow rates of different streams entering or leaving chemical or physical processes. If there are no leaks and the measurements are correct, then the other possibilities that can account for this difference are that propane is either being generated, consumed or accumulated within the unit [16, 17].

This paper analyses the calculation of carbon atoms through material balance. The formula of carbon atoms material balance (CAMB) was as follows:

$$CAMB = (V_{out}\ C_{CO2,out} + V_{out}\ C_{CO,out} + V_{out}\ C_{CH4,out}) / (V_{in}\ C_{CO2,in} + V_{in}\ C_{CH4,in}) \quad (3)$$

If carbon atoms material balance value is more than 1, then it shows that CO_2 reacts with carbon and form CO gas. If carbon atoms material balance value is less than 1, it shows that CH_4 pyrolyzes and forms carbon deposition.

Results and Discussion

The effect of C- catalyst on CH_4 cracking: CH_4 cracking has been studied in a fixed bed reactor system operating at the atmospheric pressure over carbonaceous catalyst or in that catalyst. The methane cracking conversion at different reaction condition is shown in fig. 1 and fig. 2. It can be seen from the figure that the methane conversion over carbonaceous catalyst is higher than that of non-catalytic CH_4 cracking. The increased temperature results in higher methane cracking conversion. At temperature of 900^0C, 1000^0C and 1100^0C, non-catalytic methane cracking conversions are 0.7%, 4.5% and 38.5% respectively. Methane cracking conversion reached 9.5%, 22.7%, 62.7% over carbonaceous catalyst respectively. It indicates that the C-catalyst has a profound catalytic effect on the methane cracking.

Cracking of methane being a moderately endothermic reaction, a higher reaction temperature is conducive to methane decomposition.[10,18] In addition, it can be seen from fig. 2 that the methane cracking conversion can be divided into two steps. At the first stage, the catalyst has high catalytic activity, CH_4 cracking conversion is higher, the maximum conversion of methane at 1100^0C, 1000^0C and 900^0C is 76.1%, 33.4% and 17.6% respectively. By increasing the reaction time, the methane cracking conversion and activity of catalyst are quickly reduced and enter to the second stage. There are mainly two reasons:

(1) CH_4 cracking forming carbon deposition to cover catalyst internal pore and surface active sites which change surface composition and the active constituent electronic structure of the catalyst, resulting in decreased catalytic activity;

(2) Conversely, carbon deposition (new species carbon) from CH_4 cracking has a certain catalytic activity. When C-catalyst deactivation and new species carbon activity reached equilibrium, conversion of methane cracking remained unchanged. It indicates that CH_4 cracking forming new species carbon is different with C-catalyst structure.

The effect of C-catalyst on CH_4-CO_2 reforming: It can be seen from the fig. 3 that CH_4 conversion of CH_4 cracking and CH_4-CO_2 reforming has the same trend, the maximum difference of CH_4 conversion is less than 10%. CH_4 initial transformation temperature reaches 850^0C. It indicated that CH_4-CO_2 reforming is divided into two steps. First, CH_4 is decomposed to H_2 and carbon deposition, then carbon reacts with CO_2.

The comparison studies of CH_4-CO_2 reforming both uncatalyzed and catalyzed by C-catalyst are shown in fig. 4. It can be seen from fig. 4 that the initial methane transformation temperature reaches 850^0C on uncatalyzed condition. But, the initial methane transformation temperature reduces to 650^0C over C-catalyst. At the temperature of 1000^0C, the conversion of CH_4 and CO_2 achieves 66.9% and 90.6 % for the catalyzed reaction, respectively. 11.3 % CH_4 conversion and 5.5 % CO_2 conversion are achieved for the uncatalyzed reaction. These prove that the C-catalyst is an efficient catalyst to CH_4-CO_2 reforming.

Carbon balace: Material balance is first important step when designing a new process or analyzing an existing one. In industrial process plants, using the fact that the mass entering and leaving any portion of a process plant must balance, data validation and reconciliation algorithms may be employed to correct measured flows provided that enough redundancy of flow measurements exists to permit statistical reconciliation and exclusion of detectably erroneous measurements.

The C balance in CH_4-CO_2 reforming process is shown in table 1. From table 1 can be seen that the value of C balance is less than 1 when CO_2/CH_4 ratio is equal to 1. It indicates that carbon deposition is formed in the reaction

process. When CO_2/CH_4 is more than 1, the value of C balance is more than 1. It indicates that the reaction carbon elimination by CO_2 velocity is greater than carbon deposition. Thus, the value of H_2/CO is adjusted.[15]

Carbonaceous consumption kinetics: The gasification of C-catalyst and CO_2 takes place under the condition of excess amount of CO_2, the reaction model is followed:

$$A_{(g)} + B_{(s)} \rightarrow P \tag{4}$$

For gas phase A, it will be:

$$\varepsilon \frac{\partial C_A}{\partial t} = D_{eA} \frac{\partial^2 C_A}{\partial r^2} + \frac{2}{r} \frac{\partial C_A}{\partial r} \tag{5}$$

Let the process of the hypothesis be steady state process, that is $\varepsilon \frac{\partial C_A}{\partial t} = 0$. During the reactions, the surface reaction rate equation of individual particle unreacted-core shrinking is followed [19]:

$$\frac{-1}{4\pi r^2} \frac{dN_A}{dt} = \frac{-1}{4\pi r^2} \frac{dN_B}{dt} \tag{6}$$

$$\frac{dN_B}{dt} = \frac{\rho_B \square dv}{dt} = 4\pi r^2 \rho_B dr / dt \tag{7}$$

According to shrinking core model, the model equation to be controlled by chemical reaction is deduced. The experiment demonstrates that the gasification process follows the surface chemical reaction control kinetic law of "shrinking of unreacted core".

$$-\rho_B \frac{dr}{dt} = K_S \cdot C_{Ag} \tag{8}$$

By integrals:

$$1 - (1 - x)^{1/3} = \frac{K_S C_{Ag} t}{\rho_B R_0} = K \cdot t \tag{9}$$

where C_{Ag}: $p_{CO_2}^n$; K is the reaction rate constant of CO_2 gasification with C-catalyst, min^{-1}.

The time differential is performed.

$$\frac{dx}{dt} = \frac{3K_S}{\rho_B \square R_0} p_{CO_2}^n (1 - X)^{2/3} \tag{10}$$

Let $$\frac{3K_S}{\rho_B \square R_0} = K' = K_0 \exp(\frac{-E}{RT}) \tag{11}$$

The differential equation is described as follows:

$$\frac{dx}{dt} = K_0 \exp(\frac{-E}{RT}) p_{CO_2}^n (1 - X)^{2/3} \tag{12}$$

The data of the reaction kinetics parameters calculation by C-catalyst at high temperature are shown in table 2.

As can be seen from table 2, the activation energy of the CO_2 gasification with carbonaceous materials is more than 230 kJ /mol. According to the literature,[9,10, 20] the activation energy of carbon dioxide reforming methane over a different catalyst is 97.7-162.7 kJ/mol. The activation energy of the CH_4 cracking is about 82.6kJ/mol [20]. The sequences of C-catalyst reaction activation energy of the activation energy of CH_4 cracking, carbon dioxide reforming methane and CO_2 gasification with carbonaceous materials are CO_2 gasification with carbonaceous materials > carbon dioxide reforming methane > CH_4 cracking. It indicated that CH_4-CO_2 reforming is as follows: first, CH_4 is cracking to H_2 and carbon and then carbon reacting with CO_2 and CH_4-CO_2 reforming reaction occur simultaneously.

Conclusion

Syngas production by carbon dioxide reforming methane over carbonaceous catalyst and reaction kinetics of carbonaceous materials with carbon dioxide were investigated using a fixed bed reactor. The results showed that the carbonaceous materials have a profound catalytic effect on the CH_4 cracking and CH_4-CO_2 reforming. From the carbon balance, it can be found that the mass of carbonaceous catalyst reduced during the carbon dioxide reforming reaction of methane. It indicated that CH_4-CO_2 reforming processes not only include CH_4 cracking and CH_4-CO_2 reforming but also includes carbonaceous materials with CO_2 reaction. The apparent activation energy of carbonaceous materials with CO_2 reaction in CH_4-CO_2 reformation process was more than 230kJ/mol. The sequences of activation energy are CO_2 gasification with carbonaceous materials > carbon dioxide reforming methane > CH_4 cracking.

Acknowledgement

Project was supported by the National Basic Research Program of China (Grant No.2005CB221202), the Natural Science Foundation of China (Grant No. 21006066, 51274147) and Shanxi Provincial Natural Science Foundation (Grant No. 2011021009-2).

References

1. Brasseur G., Orlando J. and Tyndall G., Atmospheric Chemistry and Global Change, Topics in Environmental Chemistry, Oxford University Press, New York, 56 **(1999)**

2. Kazancioglu F., Assessment of greenhouse production performance of Turkey compared to use of her main energy sources, *Energy Educ. Sci. Technol.*, Part A, **29**, 851-858 **(2012)**

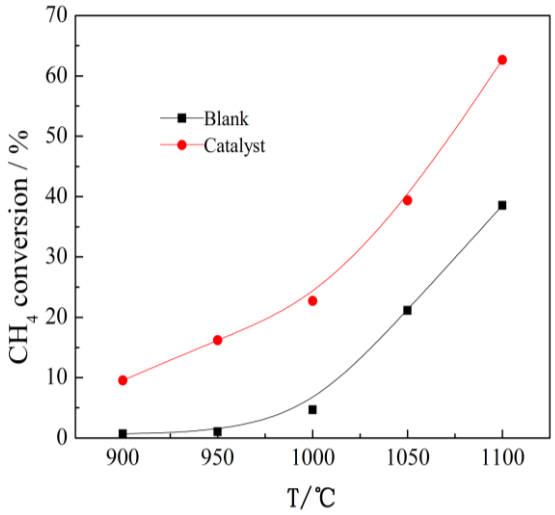

Fig. 1: CH_4 cracking with different catalyst

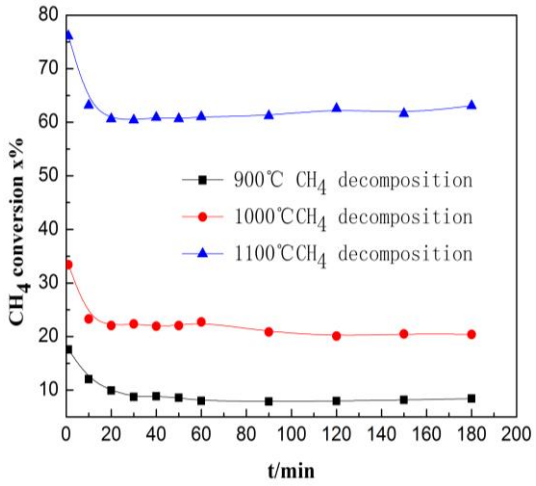

Fig. 2: CH_4 cracking conversion with time

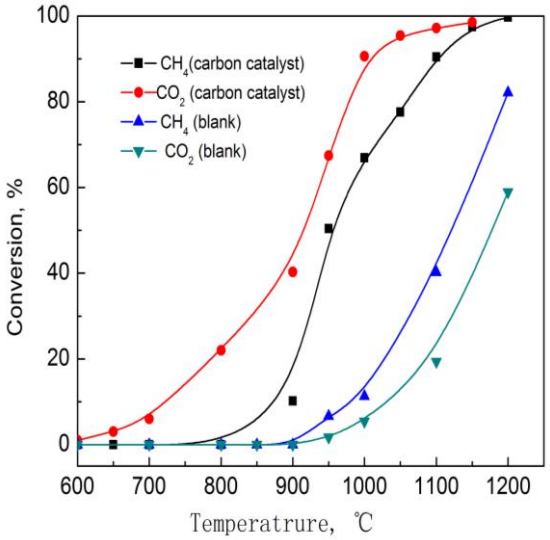

Fig. 3: CH_4 conversion in blank

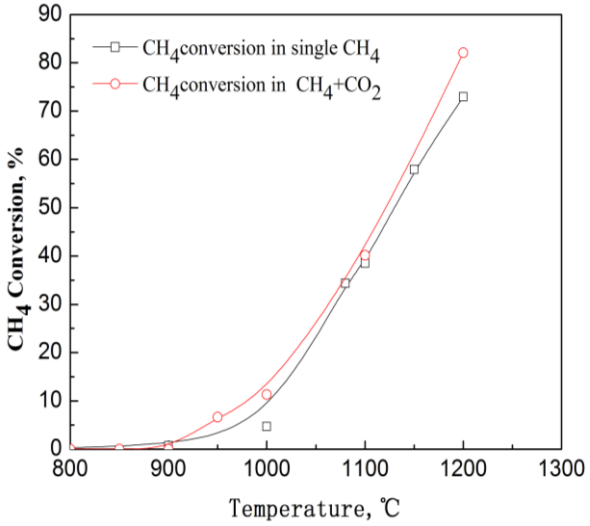

Fig. 4: The effect of C-catalyst on reforming

Table 1
The C balance in CH_4-CO_2 reforming process

CO_2/CH_4	Temp ,°C	C balance	CH_4 Conv.%	CO_2 Conv. %
0.0	1000	0.78	21.4	0.0
1.0	1029	0.93	71.6	94.5
1.0	1078	0.95	82.1	96.5
1.5	1131	1.29	95.5	98.6
2.0	1184	1.29	98.0	98.8

Table 2
The result of reaction kinetics parameters

Sample	950℃~1100℃	
	Activation energy, $kJ.mol^{-1}$	Pre-exponential factor, K_0
C-catalyst (1000℃)	232	3.32×10^6
C-catalyst (1050℃)	256	5.46×10^6
C-catalyst (1100℃)	265	6.68×10^6

3. Guha Sujata and Francisco Joseph S., Bromine-Catalyzed Oxidation of Methane in the Earth's Atmosphere: An Alternate Perspective, *Res. J. Chem. Environ.,* **8(3)**,11-14 **(2004)**

4. Tollefson J., Graphic detail countries with highest CO_2-emitting power sectors (tons per year), *Nature*, **450**, 327-327 **(2007)**

5. Keith P. S. and William T. S., Atmospheric science: CO_2 is not the only gas, *Science*, **315**, 1804-1805 **(2007)**

6. Kerr R. A., Climate change - Yes, it's been getting warmer in here since the CO_2 began to rise, *Science*, **312**, 1854-1854 **(2006)**

7. Barama S., Dupeyrat-Batiot C., Capron M., Bordes-Richard E. and Bakhti- Mohammedi O., Catalytic properties of Rh, Ni Pd and Ce supported on Al-pillared montmorillonites in dry reforming of methane, *Catal. Today*, **141**, 385–392 **(2009)**

8. Hao Z., Zhu Q. and Jiang Z., Characterization of aerogel Ni/Al_2O_3 catalysts and inves-tigation on their stability for CH_4–CO_2 reforming in a fluidized bed, *Fuel Process Technol*., **90**, 113–121 **(2009)**

9. Wei Y., Wang H., He F. and Xie J., Progress in methane catalytic reforming with carbon dioxide to syngas, *Appl. Chem. Ind.,* **34**, 721- 725 **(2005)**

10. Zhang G. , Dong Y., Feng M., Zhang Y., Zhao W. and Cao H., CO_2 reforming of CH_4 in coke oven gas over coal char catalyst, *Chem. Eng. J*., **156**, 519-523 **(2010)**

11. Zhang Y., Zhang G., Zhang B., Guo F. and Sun Y., Effects of pressure on CO_2 reforming of CH_4 over carbonaceous catalyst, *Chem Eng J*, **173**, 592-597 **(2011)**

12. Li Y., Zhang H., Zhao W. and Zhang Y., Effect of char on the conversion of methane to produce syngas-transfer and conversion of sulfur in char during the conversion of oven gas, *Coal. Conv*., **30**, 41-44 **(2007)**

13. Zhang Y., Zhang M., Zhang G. and Zhang H., The effect of carbon deposition over carbonaceous catalyst on CH_4 decomposition and CH_4-CO_2 reforming, *Front. Chem. Eng. China*, **4**, 481-485 **(2010)**

14. Zhang W. and Zhang Y., Study of CH_4–CO_2 reforming syngas with carbonaceous catalyst, *Shanxi Energy Conser***v, 4,** 34–37 **(2009)**

15. Zhang M., Zhang G. and Zhang Y., Research technique of carbon deposit in CH_4/CO_2 reforming reaction process, *Guangzhou Chem Ind*, **37,** 58–60 **(2009)**

16. Felder R. and Rousseau R., Elementary Principles of Chemical Processes, John Wily and Sons, 68 **(1986)**

17. Himmelblau D., Basic principles and calculations in chemical engineering, Prentice Hall, New Jersey, 96 **(1982)**

19. Pinilla J. L., Suelves I., Lazaro M. J. and Moliner R., Kinetic study of the thermal decomposition of methane using carbonaceous catalysts, *Chem. Eng. J*., **138**, 301-306 **(2008)**

20. Zhang G., Zhang Y., Zhang M. and Zhao W., Methane decomposition over carbonaceous catalyst and its kinetic characteristics, *Mod. Chem. Ind*., **29**, 29-32 **(2009)**.

(Received 20th April 2013 , accepted 25th July 2013)

Noise Impact Assessment due to Aircraft Operations in the surrounding Areas of an Upcoming Airport in India

Mishra Arun kumar [1 *] and Srivastava Prabhat [2]
1. Civil Engg. Deptt Govt. Engg. College, Gorakhpur,U.P., INDIA
2. Civil Engg. Deptt, S.P.College of Engg., Bombay, INDIA
*arun_gmishra@yahoo.co.in

Abstract
The main purpose of this study is to assess the impact and effect of noise emitted by aircrafts in the surrounding areas of an upcoming international airport at Navi-Mumbai ,India. This study presents on site noise level measurement at 10 locations situated at a distance of 20 km. radius from the Airport reference Point (ARP). Noise monitoring was carried out at all locations for 24 Hours (Leq) in residential, commercial, Industrial and silence zone location around the surrounding areas of Navi Mumbai (India) airport during November-February, 2009. The results show that noise pollution around the airport is wide spread on most of its areas. Noise in the surrounding areas of airport is composite in nature. Noise Propagation Model has been used to a assess the noise level at different receptor locations. The local standards implemented by the Central Pollution Control Board (CPCB) have been used to assess the actual field data and the predicted noise level has also been compared with standards prescribed by CPCB.

Keywords: Airport, Noise, Navi Mumbai, Noise Pollution , Noise Propagation Model.

Introduction

Noise can be defined as an unwanted sound[3]. Noise is one of the principle externalities of transportation specially air and road transportation and it mostly goes unpriced[9].The noise pollution produced by aircrafts during operations around airports represents serious social, ecological, technical and economic problem. The ability to assess and predict noise exposure accurately is an increasingly important factor in the design and implementation of any airport improvements. Aircrafts are complex noise sources. The number and intensity of noise sources vary with type of aircraft and in particular, with the type of engines incorporated in their power plants. Relationship between the acoustic characteristics of the main noise sources and the flight mode parameters (or engine mode parameters) must be known for the best evaluation of noise levels under the flight path for any type of aircraft at any stage of its flight.

It has been estimated that around 20 percent of the European population from the noise level that are considered unacceptable[8]. Environmental noise pollution has not been an entirely new phenomenon, but has been a problem that has grown steadily worse with time[4]. Noise perceived as an environmental stressor and nuisance. Increasing noise level exposure is today a serious problem for most cities and high focus is put into monitoring and calculating actual noise exposure to understand the size of the actual problem[2].

Noise is a prominent feature of the environment including noise from transport, aircrafts, industry and neighbors. Transport noise is an increasingly prominent feature of the urban environment making noise pollution an important environmental public health issue[2]. Noise pollution in urban cities is steadily increasing over the years[6].This has direct and indirect impact to the people that can lead to the health hazard[7]. Some of the major health hazards cause by the noise are permanent hearing loss and psychological disorder[10]. Other health problem may be high blood pressure, muscle tension, headache, migraine, irritability insomnia[5]. In India there were very few researchers on noise pollution being carried out. Even such surveys conducted in the past have revealed that noise level in urba areas are generally higher than the prescribed limit given by CPCB[11].

The main purpose of this study is to assess the noise quality in the surrounding areas of the airport due to vehicular traffic, aircraft traffic and other activities and to suggest the preventive measures to control and minimize the noise pollution.

Material and Methods

Study Area: The site of Navi Mumbai (India) airport is selected near Panvel town in an area admeasuring 2347 acres of land which is situated about 45 km away from the CBD of Mumbai/Santacruz airport. The airport is planned with two runways of 3700 M with parallel taxiways designed to suit the new generation large aircraft. The other facilities include the domestic terminal, international terminal, cargo terminal, airfield lighting, city side facilities etc. The phase wise development approach has been adopted to suit the air travel demand.

The study area shown in figure 1 covers the area around the airport falling within the radius of 10 km. The study area is further divided in two parts namely core area and fringe area. The core area covers the area within the radius of 10 km in which all the scooped environmental parameters have been studied to understand the magnitude of impact.

In the remaining area i.e. fringe area places of historical importance, aesthetics, cultural including environmentally sensitive have been studied.

Methodology for Noise level measurement: Noise quality monitoring stations were selected based on different noise generating sources and type of receptor environment in the project area. The list of sites selected for noise monitoring in the project area is given in table1. The noise equivalent level (Leq) was measured continuously at each monitoring sites using sound level meter Model (LUTREN, SL-4001). The sound level meter was placed 1.2 to 1.5m above ground level and at 3m away from sound reflecting sources like walls etc. in the outdoor environment. Measurements were taken for 24 hrs at twelve locations during the month of January 2009 (post monsoon season) to establish representative background (existing noise level) noise level. The Leq result of each location was statistically analyzed and the results were presented in terms of average $L_{10,}$ L_{50} and L_{90} for different locations and these values are given in table 2. Locations of noise monitoring stations are given in figure 2.

Noise Modeling for Aircrafts

Integrated Noise model (INM): The integrated noise model is a computer program developed by Federal Aviation Administration (FAA), United States. INM evaluates aircraft noise in the vicinity of the airport using flight traffic information, aircraft fleet mix, standards defined aircraft profiles, user define aircraft profiles and terrains. INM supports three different types of aircrafts : civil airplanes, military airplanes and helicopters. INM program requires the input of the physical and operational characteristics of the airports. Physical characteristics include runway co ordinates, airport altitude, temperature and optional topographical data. Operational characteristics refer to various types of aircraft data which include aircraft types and flight tracks, departure and arrival procedure of the aircrafts. INM is also used to generate noise contours around the airports.

Aircraft Mix: The forecast peak day profiles identified aircraft by their ICAO code groups. However each aircraft has different noise characteristics depending on the engine used or the configuration of the aircraft. For the purpose of the noise modeling, aircraft forecast in the five groups have been assigned representative types of noise modeling for example, Boing 737, Boing 747, Airbus A320, AB 310/ AB 330.

Flight Operations: The average daily number of flights was calculated in accordance to the following factors: Aircraft type, type of operation, runway used and flight path**.** Table 4 summarizes the average daily flight frequency at Navi Mumbai international airport.The operations were divided into three categories Day Operation (0700H- 1900H), Evening Operation (1900H-2200H) and Night Operation (2200H- 0700H) .

Meteorological data: The annual average, monthly average weather conditions were collected from the Panvel Meteorological Station. Table 3 summarizes the temperature, wind speed and atmospheric pressure at the Navi- Mumbai airport.

Results and Discussion

Noise level at different locations due to aircraft operation along with ambient noise level is shown table 7.

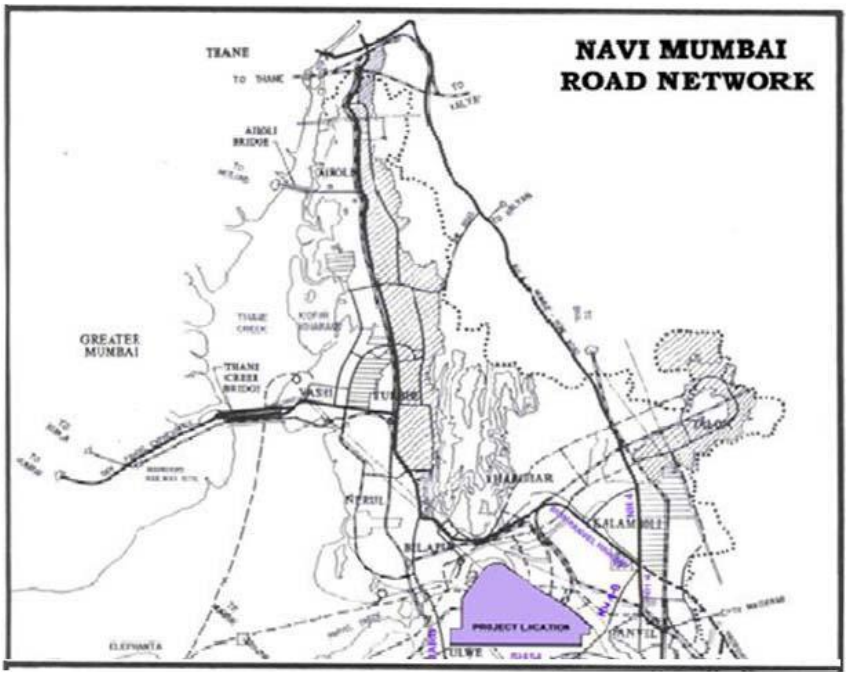

Figure 1: Study area along with Road Network Plan of Navi- Mumbai Region

Table 1
Ambient noise quality monitoring stations around the project area

S. No.	Station Name	Category of area
1	Ambuja Cement Limited	Industrial area
2	CIDCO Bhavan, CBD Belapur	Commercial area
3	Palaspa Junction	Commercial area
4	Teen Tank Gavanphata	Commercial area
5	Panvel CIDCO Office	Residential Area (Mixed category[a])
6	Kharghar Nodal Office	Residential Area
7	Panchsheel Guest House	Residential Area
8	Pargaon School	Sensitive area (Mixed category[a])
9	MES School	Sensitive area(Mixed category[a])
10	MGM Hospital, Kalamboli	Sensitive area(Mixed category[a])
11	Swapna Nagri	Residential Area (Mixed category[a])
12	Karnala Bird Sanctuary	Sensitive area

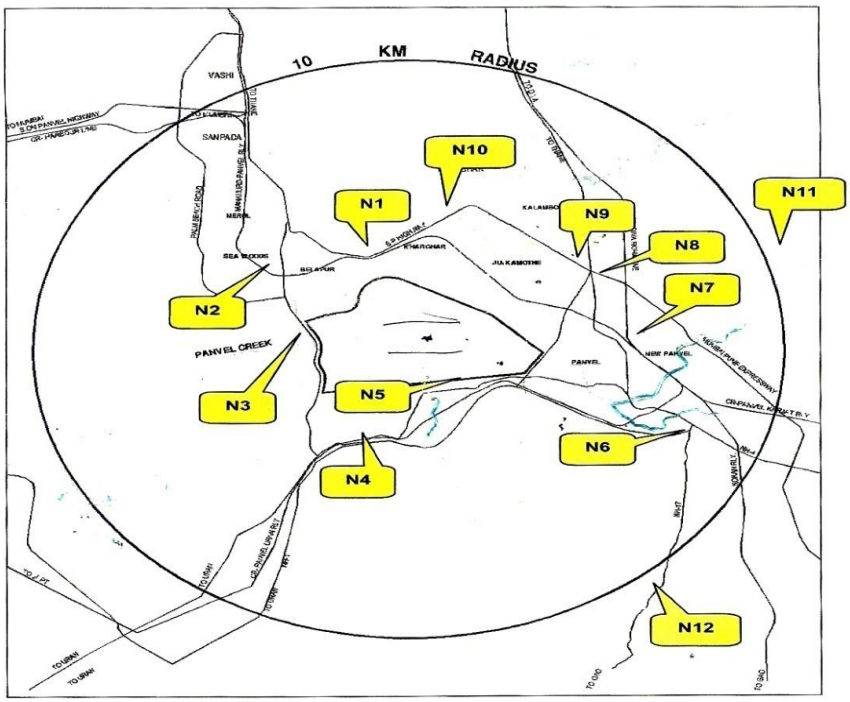

Figure 2: Plan showing Noise Monitoring station

Conclusion

- Leq recorded for industrial area during day time was 61.6 dBA and during night time was 59.2 dBA which are well within the prescribed limit for industrial area.

- Leq values recorded for commercial areas during day time were in the range of 56.6 dBA to 72.2 dBA and during night time Leq are in the range of 53.3 dBA to 72.4 dBA. Noise levels at traffic junction Palaspa and Gavanphata are higher than the prescribed limit because of the movement of heavy vehicles. Road construction activities further increase the noise levels at these junctions.

- Noise levels recorded for residential areas during day time are in the range of 48.7 dBA to 65dBA and during night time it was recorded 46.4 dBA to 59.1 dBA. Noise level in Swapna Nagari is more than the prescribed limit. This increase in noise level is due to film shooting etc. Noise level at Panvel, Kharghar and Panchsheel are exceeding due to domestic and traffic noise in these areas.

Table 2
Ambient Noise Level At Various Location Of The Project Area During Post Monsoon Season

S. N	Station	Ldn dB(A)	Leq (d) dB(A)	Leq (n) dB(A)	L10 dB(A)	L50 dB(A)	L90 dB(A)	Lmax dB(A)	Lmin dB(A)
Industria Area									
1.	Ambuja Cement Limited	66.0	61.6	59.2	61.7	57.7	53.8	75.0	49.8
Commercial Areas									
2.	CBD Belapur	60.6	56.6	53.3	58.2	55.5	47.2	62.6	45.1
3.	Palaspa Junction	79.1	72.2	72.4	76.3	69.1	62.2	82.0	54.9
4.	Teen Tank Gavanphata	69.5	64.1	62.9	67.1	61.8	56.8	73.2	50.4
Residential Areas									
5.	Panvel CIDCO Office	65.3	65.7	54.5	67.3	60.6	51.6	73.7	51.6
6.	Kharghar Nodal office	65.9	62.2	58.7	63.8	59.9	55.8	69.3	51.2
7.	Panchsheel Guest House	65.9	61.0	59.1	63.6	57.6	51.6	70.4	51.6
8.	Swapna Nagri	53.8	48.7	46.4	49.2	46.2	45.1	51.6	48.5
Sensitive Areas									
9.	Pargaon School	69.6	71.0	56.0	71.1	60.7	52.2	82.4	47.8
10.	MES School, New Panvel	65.2	65.4	54.8	65.4	57.8	49.8	81.9	46.6
11	MGM Hospital, Kalamboli	67.2	63.6	60.1	64.9	61.2	57.6	71.7	54.1
12	Karnala Bird Sanctuary	55.3	49.5	48.7	51.8	48.7	44.3	56.5	40.5

Table 3
Annual Average Monthly Weather readings

Temperature ^{0} C	38.6
Wind speed (mps)	6.6
Pressure (mm-Hg)	1007.56

- Leq values recorded in the sensitive areas vary between 49.5 dBA to 71.0 dBA and during night time vary between 48.7 dBA to 60.1 dBA. This increase in noise level is due to close proximity of the highway to these areas. The noise levels at M.E.S school also exceeded the prescribed limit due to school buses and other transport vehicles near the premises.

- It is observed that aircraft noise adds very little amount to the noise level in the existing status at various receptor locations. Aircraft noise level decreases as per the inverse square law so it does not contribute significantly. Above results show that the increment in the baseline status varies between 0.02 dBA to 2 dBA which is significantly low.

Acknowledgement
The authors are thankful to Dr Nitin Tripathi, Professor, A.I.T. Bangkok and Dr. Mukesh Sharma, Professor, Civil Engineering Department, I.I.T. Kanpur (U.P.), India for their valuable guidance and suggestions.

Table 4
Flight Operations at Navi- Mumbai Airport

Departure		**Opening year(2014/15)**			**Arrivals**		**Opening year(2014/15)**		
AC TYPE	Day	Evening	Night	Total	AC TYPE	Day	Evening	Night	Total
A300	0	0	1	1	A300	0	0	1	1
A310	3	1	3	7	A310	3	2	3	8
A319	4	1	2	7	A319	6	2	0	8
A320	31	9	14	54	A320	29	14	10	53
A321	7	2	1	10	A321	7	2	1	10
A330	2	0	5	7	A330	1	2	3	6
A340	1	0	0	1	A340	1	0	1	2
ATR-42	3	1	1	5	ATR-42	3	1	0	4
ATR-72	4	0	1	5	ATR-72	3	0	1	4
B737	37	7	11	55	B737	34	14	5	53
B747	2	0	3	5	B747	2	1	4	7
B757	0	0	0	0	B757	0	0	1	1
B767	0	0	1	1	B767	1	0	2	3
B777	2	1	6	09	B777	2	2	4	8
CRZ	0	0	0	0	CRZ	0	0	1	1
Grand Total	96	22	49	167	Grand Total	92	40	37	169

Local and Foreign Standards

Table 5
Ambient Noise Quality standards (CPCB, India)

S. N.	**Category of Area**	**Limits in dB (A) L_{eq}**	
		Day Time	**Night Ti me**
1.	Industrial area	75	70
2.	Commercial area	65	55
3.	Residential area	55	45
4.	Sensitive area	50	40

Table 6
British Recommended Criteria for the control of development in areas affected by Aircraft Noise

Establish Noise	**Level of Aircraft Noise which is expected to be exposed**			
	>72 dB(A) Leq	**66-72 dB(A) Leq**	**60-66 dB(A) Leq**	**57-60 dB(A) Leq**
Dwellings	Refuse	Permitted with sound insulation	Permitted with sound insulation	Permission to develop should not be refused on noise ground alone
Schools	Refuse	Most undesirable and only under exceptional circumstances. Insulation required	Undesirable. Insulation required	Permission to develop should not be refused on noise ground alone. Insulation required
Hospitals	Refuse	Undesirable. Insulation required	Each case to be considered on its own	Permission to develop should not be refused on

			merit. Insulation required	noise ground alone. Insulation required
Offices	Undesirable. Full insulation required.	Permit. Full insulation required.	Permit but require insulation in special rooms (e.g. conference room)	Permit
Factories and Ward houses	Permit by taking all necessary Precautions.			

Table 7
Predicted Noise Level due to Aircrafts operations along with Ambient Noise Level

Receptor Name	**Baseline Noise Level in dB(A)**		**Combined Noise Levels in dB(A) (Baseline + Air Craft Noise)**			**Permissible Limits**	
						CPCB	
	Leq (d)	Leq (n)	Aircraft at take-off point	Aircraft at center of runway	Aircraft at landing point	Leq (d)	Leq (n)
Paragon School(S)	69.6	71	69.62(d) 71.02(n)	69.67(d) 71.05(n)	69.66(d) 71.04(n)	50	40
Panvel CIDCO Office(R)	65.3	65.7	65.31(d) 65.71(n)	65.32(d) 65.72(n)	65.36(d) 65.77(n)	55	45
MGM Hospital Kalamboli(S)	67.2	63.6	67.23(d) 63.62(n)	67.25(d) 63.65(n)	67.24(d) 63.64(n)	50	40
CIDCO office Kharghar(R)	65.9	62.2	65.92(d) 62.25(n)	65.93(d) 62.27(n)	65.92(d) 62.25(n)	55	45
Panchsheel Guest House(R)	65.9	61	65.94(d) 61.11(n)	65.93(d) 61.09(n)	65.02(d) 64.05(n)	55	45
MES School(S)	65.2	65.4	65.21(d) 65.43(n)	65.41(d) 65.44(n)	65.33(d) 65.92(n)	50	40
CIDCO Bhawan Belapur CBD (C)	56.6	53.3	60.75(d) 56.96(n)	60.67(d) 56.79(n)	60.64(d) 56.69(n)	65	55
Palaspa Junction (C)	72.2	72.4	72.21(d) 72.42(n)	72.21(d) 72.41(n)	72.21(d) 72.40(n)	65	55
Teen Tank Gavanphata (C)	64.1	62.9	64.17(d) 62.99(n)	64.13(d) 62.94(n)	64.12(d) 62.92(n)	65	55
Swapna Nagri (R)	48.7	46.4	48.99(d) 46.87(n)	48.05(d) 46.87(n)	48.08(d) 46.91(n)	55	45
Karnala Bird Sanctuary (S)	49.5	48.7	49.72(d) 48.93(n)	49.74(d) 48.98(n)	49.65(d) 47.93(n)	40	50
Ambuja Cement Ltd.(I)	61.6	59.2	63.88(d) 62.63(n)	62.95d) 59.90(n)	61.72(d) 59.09(n)	75	70

References

1. WHO Community noise, World Health Organization, Geneva, Berglund B., and Lindvall T., Online at http://www.who.int/docstore/peh/noiseold. html. **(1995)**

2.Bugliarello G., Alexandre A., Barnes J. and Wakstein C., *The impact of noise pollution: A socio technological introduction*, Pergamon Press Inc., New York **(1976)**

3. Canter, L.W, *Environmental Impact Assessment*, McGraw Hill Book Company, International Edition **(1991)**

4. Garg N.K., Gupta V.K. and Vyas R.K., Noise Pollution and its impact on urban life., *J. Environ. Res. And Develop.*, **2** (1), **(2007)**

5. Haines M.M., Brentnall S.l., Stansfeld S.A. and Klineberg E., Qualitative responses of children to environmental noise, *Noise Health*, **5,** 19-30 **(2003)**

6. Ising H. and Kruppa B., Health effects caused by noise: evidence in the literature from the past 25 years, *Noise Health*, **6,** 5-13 **(2004)**

7. Kryter K.D.,(1985), *The Effects of Noise on Man*, 2nd edn, Orlando, FL:Academic Press.

8. Nijland H.A., Van Kempen, E.E., Van Bee, G.P and Jabbben J. Cost and Benefits of Noise Abatement Measures, *Transport Policy*, **10**, 131-140 **(2003)**

9. Thangadurai N., Venkateswaran P. and Jeevanraj S., Evaluation and Analysis of noise quality of Ambur, Tamil Nadu, India, *Journal of Environmental Science and Engineering*, **47,** 7-12 **(2005)**

10. WHO., Environmental Health Criteria of noise., 12 World Health Organizations **(1980)**

11. Vidyasagar T. and Rao G.N., Noise Pollution Levels in Vishakhapatnam City (India)., *Journal of Environmental Science and Engineering*, **48,** 139-142 **(2006).**

(Received 25th March 2013, accepted 28th July 2013)

The Influence of a Newly Synthesized Zn (II) and Cu (II) Complexes based on Pyrazole Derivatives on the Inhibition of *Phomopsis Viticola* Sacc. (Sacc.) under Laboratory Conditions

Jaćimović Željko[1*], Latinović Nedeljko[2], Bošković Ivana[1] and Tomić Zoran[4]
1. University of Montenegro, Faculty of Metallurgy and Technology, Džordža Vašingtona bb, 81000 Podgorica, MONTENEGRO
2. University of Montenegro, Biotechnical Faculty, Center for Plant Protection, Mihaila Lalica 1 81000 Podgorica, MONTENEGRO
3. Institute of Nuclear Sciences, Laboratory of Theoretical Physics and Condensed Matter Physics ,11001 Belgrade, SERBIA
*zeljkoj@ac.me

Abstract
Chemical inhibition of Phomopsis cane and leaf spot disease of grapevine (Phomopsis viticola) has an important practical significance, and it is mainly focused on winter season treatment and beginning of vegatation period of grapevine. Its purpose is to reduce infectious effects of the fungus and to prevent primary infections at the beginning of the vegetation process. This research analysed fungicide activity of the newly synthesized Zn(II) complex with 4-acetyl-3(5)-amino-5(3)-methylpyrazole(Pz1) as ligand and Cu(II) complex with 3,5-dimethyl-1-thiocarbox - amidepyrazole(Pz-CS) as ligand on already mentioned pathogenic fungus that causes Phomopsis cane and leaf spot disease. Observed results are compared with fungicide product Cabrio Top (active substance piraclostrobin belongs to pyrazole derivatives).

Keywords: 3,5- dimethyl-1-thiocarboxamidepyrazole, 4-acetyl-3(5)-amino-5(3)-methyl pyrazole, biochemical role of Zn and Cu, *Phomopsis viticola*, biological researches, active fungicide substances, Phomopsis cane and leaf spot disease of grapevine.

Introduction

Phomopsis cane and leaf spot disease of grapevine [*Phomopsis viticola* Sacc. (Sacc.)] is known as a disease of European grapevine and it is in particular important for Mediterranean. This disease is widespread and very damaging. Its suppression is complicated and complex. It is assumed that Phomopsis cane and leaf spot disease, like the gray mold disease of grapevine, is a typical disease of high standard grapevine and nowadays mode of cultivation.

Although this disease was observed in the Montenegrin vineyards even in 1955, an intense epidemy[1] was identified in 1975 and today it is one of the most important diseases of grapevine. Montenegrin varieties Vranac and Kratošija are very susceptible to the disease[2].

Small, light green, chlorotic, irregular circular spots with dark center appear on the infected parts of the grapevine. The spots are scattered over the leaf and distributed along the main and lateral leaf nerves. The above spots also occur on leaf petioles. Sometimes the necrotic part of spots turn out, so holes of leaf occur. In strong infections, leaf becomes yellow and it falls down[3].

In the winter *Ph. viticola* is a saprophyte that develops in wooden parts of vines and in the spring it becomes a parasite on young parts of the grapevine. *Ph. viticola* attacks the variety of grapevine *Vitis vinifera*, which is intended for the production of wine in Montenegro[4] and it is a significant disease in Montenegrin vineyards[5,6].

Chemical inhibition of Phomopsis cane and leaf spot disease of grapevine has important practical significance and it is mainly focused on winter season treatment and beginning of grapevine vegetation with the purpose to reduce infectious effects of the fungus and to prevent primary infections at the beginning of the vegetation period. Literature data[8-22] show synthesis and characterisation of some pyrazole derivatives and some significant transition metal complexes which have practical application in pharmacy[23], agriculture[24-26] and environmental protection[1, 27].

Having regard that some pyrazole derivatives show fungicide activity, [$CuCl_2$Pz-CS] and [Zn $(NO_3)_2$Pz1] complexes have been synthesized and their biological efficiencies on inhibition of pathogenic fungal mycelium *Ph. Vitticola* are analysed. The structural formula Pz-CS ligand is presented in figure 1.

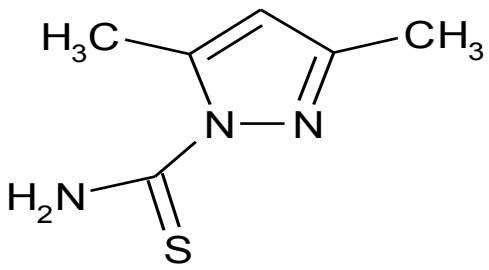

Figure 1: The structural formula Pz-CS ligand (3,5 dimethyl - 1 – thiocarboxamide pyrazole, $C_6H_9N_3S$)

The structural formula Pz1 ligand is presented in figure 2

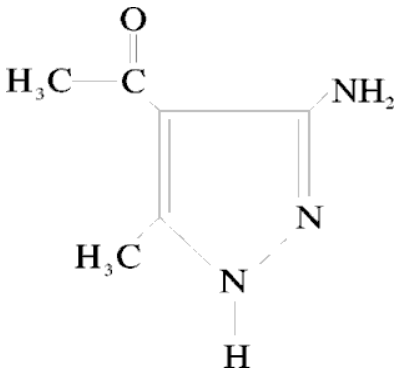

Figure 2: The structural formula Pz1 ligand (4-acetyl-3 (5)-amino-5 (3)-methylpyrazole)

In order to select the control sample for determining the biological efficiency of the synthesized complexes, a commercial fungicide Cabrio Top[24] was taken which has its active ingredient pyraclostrobin, the only active substance that is on the list of active substances permitted in plant protection products on the territory of Montenegro. Except pyraclostrobin, the compound contains metiram which belongs to dithiocarbamate fungicides.

Material and Methods

Synthesis of [$CuCl_2$Pz-CS] complexes: Solution obtained by the reaction of hot ethanol solution ($5cm^3$) $CuCl_2 \cdot 2H_2O$ and Pz-CS ligand in 1:2 molar ratio was left to crystallize. After 3 days microcrystals complex was filtered and washed with ethanol.

Synthesis of [Zn $(NO_3)_2$Pz1] complexes: Solution obtained by the reaction of hot ethanol solution ($5cm^3$) Zn $(NO_3)_2$ and Pz1 ligand in 1:2 molar ratio was left to crystallize. After 3 days microcrystals complex were filtered and washed with ethanol.

Materials to determine biological activity: [$CuCl_2$Pz-CS] and [Zn $(NO_3)_2$Pz1] complexes, potato-dextrose agar (PDA), a commercial fungicide Cabrio Top, grapevine shoots.

Potato-dextrose agar (PDA): 200g potatoes, 17-20g dextrose (d-glucose), 17-20g agar and 1L distilled water.

Method of obtaining colonies of *Ph. Viticola*: The grapevine shoots with typical symptoms of Phomopsis cane and leaf spot were used as starting materials in the study. Sampled materials were transferred from the locality of Lješkopolje to Phytosanitary laboratory at the Plant Protection Centre of the Biotechnical Faculty, University of Montenegro and were left in a humid chamber in which the temperature was maintained at 25 ° C. After 2-3 days there were swelling pycnidia and excreting of pycnospores from pycnidia in the form of curvy- mucous mass. Tendrils of pycnospores were abstracted with pin and they weres own in potato dextro seagar (PDA).

This isolated fungus was incubated in a thermostat (at 25 °C) in the alteration of natural light and darkness. After 4-5 days mycelium formed began to take on a greyish color.

Preparation of selected products samples: Following were prepared having initial concentrations:

• The complex [$CuCl_2$Pz-CS] ($C_1 = 2.9 \cdot 10^{-2}$%) •The complex [Zn $(NO_3)_2$ Pz1] ($C_1 = 3.9 \cdot 10^{-2}$%)

• Cabrio Top commercial fungicide (piraclostrobin) ($C_1 = 12.4 \cdot 10^{-4}$%)

The previous solution was double diluted in five series of synthesized Cu complexes and five series of synthesized Zn complexes. Four series of dilution of commercial fungicides Cabrio Top were made for biological studies. Thus prepared samples of these products (10ml) were poured into the previously prepared PDA (100ml) in ratio 10:1 Mixture was spilled in the 90mm diameter Petri dishes. When substrate became solid, fragments of fungal colonies were sown in the form of 7mm diameter discs and left in the incubator at a temperature of 25°C for 8 days. Each sample has the control which represented Petri dishes.

Results and Discussion

In the phase of biological research the measurements of fungal mycelium diameter of *Ph. viticola* were performed as a result of influence:

• Cabrio Top commercial fungicide, in prepared range of four concentrations (12.4 - $1.5 \cdot 10^{-4}$%) (Table 1)

• Newly synthesized [$CuCl_2$Pz-CS] complexes in the range of concentrations (2.9 - $0.2 \cdot 10^{-2}$%) (Table 2) and

• Complex compound [Zn $(NO_3)_2$Pz1] in the range of concentrations ($C_1 = 3.9 \cdot 10^{-2}$%, $C_2 = 1.9 \cdot 10^{-2}$%, $C_3 = 0.9 \cdot 10^{-2}$%, $C_4 = 0.5 \cdot 10^{-2}$%;$C_5 = 0.2 \cdot 10^{-2}$%) (Table3)

Statistically significant concentration values of synthesized complex compounds [$CuCl_2$Pz-CS] ($C_1 = 2.9 \cdot 10^{-2}$%, $C_2 = 1.4 \cdot 10^{-2}$%, $C_3 = 0.7 \cdot 10^{-2}$%, $C_4 = 0.4 \cdot 10^{-2}$% (Table 2) and all concentration of the commercial fungicides Cabrio Top (Table 1) were determined by applying the analysis of variance and LSD test (0.01) = 0.41. These concentrations showed an inhibitory effect on mycelium growth compared to the control sample.

Statistically significant values influenced by concentration values of synthesized complex compounds [Zn$(NO_3)_2$Pz1] ($C_1 = 3.9 \cdot 10^{-2}$%; $C_2 = 1.9 \cdot 10^{-2}$%; $C_3 = 0.9 \cdot 10^{-2}$%; $C_4 = 0.5 \cdot 10^{-2}$ %) (Table 3) were determined using analysis of variance. LSD test (0.01) = 0.27 also showed an inhibitory effect on mycelium growth compared to the control sample.

Table 1
The influence of samples of commercial Fungicide Cabrio top on *Ph. viticola* mycelium

Fungal mycelium diameters (cm) after the effects of commercial fungicide Cabrio top in given concentrations				**Mycelium diameter (cm) (control sample)**
$C_1 = 12.4 \cdot 10^{-4}$ %	$C_2 = 6.2 \cdot 10^{-4}$ %	$C_3 = 3.1 \cdot 10^{-4}$ %	$C_4 = 1.5 \cdot 10^{-4}$ %	
2.7	**3.5**	**4.6**	**5.1**	**7.9**

Table 2
The influence of samples of synthesized Cu (II) complex on *Ph. viticola* mycelium

Fungal mycelium diameters (cm) after the effect of samples of the synthesized [$CuCl_2$Pz-CS] complex in given concentrations					**Mycelium diameter (cm) (control sample)**
$C_1=2.9 \cdot 10^{-2}$%	$C_2=1.4 \cdot 10^{-2}$%	$C_3=0.7 \cdot 10^{-2}$%	$C_4=0.4 \cdot 10^{-2}$%	$C_5=0.2 \cdot 10^{-2}$%	
5,1	**5,2**	**5,3**	5,6	5,8	**5,8**
LSD 0,01= 0,41					

Table 3
The influence of synthesized complex [Zn $(NO_3)_2$Pz1] on *Ph. viticola* mycelium

Fungal mycelium diameters (cm) after the effect of samples of the synthesized [Zn $(NO_3)_2$Pz1] complex in given concentrations					**Mycelium diameter (cm) (control sample)**
$C_1=3.9 \cdot 10^{-2}$%	$C_2=1.9 \cdot 10^{-2}$ %;	$C_3=0.9 \cdot 10^{-2}$ %;	$C_4=0.5 \cdot 10^{-2}$ %;	$C_5=0.2 \cdot 10^{-2}$ %	
2.7	**3.1**	**3.8**	**5,1**	5,7	**5,8**
LSD 0,01=0,27					

Conclusion

The results of biological research [$CuCl_2$Pz-CS] complexes indicate significant reduction of the diameter of fungal mycelium: 5.2 cm with regard to Cabrio top and 0.7cm, 0.6cm, 0.5cm with regard to the mean diameter of the control sample i.e. identified concentrations of following products:

- Cabrio top ($C_1 = 12.4\% \cdot 10^{-4}$, $C_2 = 6.2 \cdot 10^{-4}$%, $C_3 = 3.1 \cdot 10^{-4}$%, $C_4 = 1.5 \cdot 10^{-4}$%),

- [$CuCl_2$Pz-CS] complex (($C_1 = 2.9 \cdot 10^{-2}$%, $C_2 = 1.4 \cdot 10^{-2}$%, $C_3 = 0.7 \cdot 10^{-2}$%, $C_4 = 0.4 \cdot 10^{-2}$%)

The results of biological research [Zn $(NO_3)_2$Pz1] complexes indicate significantly reduction the diameter of fungal mycelium with regard to the mean diameter of the control sample i.e. identified concentrations of following products

▪ Cabrio top ($C_1 = 12.4\% \cdot 10^{-4}$, $C_2 = 6.2 \cdot 10^{-4}$%, $C_3 = 3.1 \cdot 10^{-4}$%, $C_4 = 1.5 \cdot 10^{-4}$%)

▪ [Zn $(NO_3)_2$Pz1] complex ($C_1 = 3.9 \cdot 10^{-2}$%, $C_2 = 1.9 \cdot 10^{-2}$%, $C_3 = 0.9 \cdot 10^{-2}$%, $C_4 = 0.5 \cdot 10^{-2}$%)

The results of inhibition effect of newly synthesized [$CuCl_2$Pz-CS] and [Zn $(NO_3)_2$Pz1] complexes indicate their fungicide effect on *Ph. viticola* . Inhibition effect of Cu (II) complexes concentration C_1 is 12.07%.

The complex [Zn $(NO_3)_2$Pz1] concentration C_1 is $3.9 \cdot 10^{-2}$% showing the highest inhibition effect of 53.45%.

Statistical investigations LSD_{50} (0.01) = 0.78 showed that concentration C_1 of [$CuCl_2$Pz-CS] complex had a low inhibition effect on fungal mycelium of *Ph. viticola* compared to the control sample and the selected standard. Statistical investigations LSD_{50} (0.01) = 0.27 showed that concentrations C_1 C_2, C_3, C_4 of [Zn $(NO_3)_2$Pz1] complex have significant inhibition effect on the mycelium of fungus *Ph. viticola* compared to the control sample and the selected standard.

References

1. Radović Ana, Latinović Nedeljko and Jaćimović Željko, "The Influence of Some Pyrazole Derivatives and matching Newly Synthesized Ni(II) Complexes in the Inhibition of Phomopsis viticola (Sacc.) Sacc.," *Res. J. Chem. Environ* , **16 (1)**, 07-15 **(2012)**

2. Latinovic N., Latinovic J. and Zindović J., Susceptibility of grapevine to casual agent of dead arm disease *Phomopsis viticola* (Sacc.) Sacc. depending on growth form, *Natura Montenegrina*, **3**, 207-211 **(2004)**

3. Ivanović M. and Ivanović D., Bolesti voćaka i vinove loze i njihovo suzbijanje. Univerzitet u Beogradu, Poljoprivredni fakultet. 400 **(2005)**

4. Sl list CG 36/07 Zakon o vinu **(2007)**

5. Mijuškovic M., Proučavanja mogućnosti suzbijanja *Phomopsis Viticola* Sacc., značajnog parazita vinove loze u Crnoj Gori, *Zaštita bilja*, **31(3),** 153, 205-221(1980)

6. Latinović N., Model zaštite vinove loze od ekskorioze u uslovima podgoričkog vinogorja (doktorska disertacija). Univerzitet u Beogradu, Poljoprivredni fakultet **(2006)**

7. Kim Bulit, Bulit B. J. and Bugaret Y., The production of antifungal metabolites by *Bacillus subtilis*. *Journal of Applied Bacteriology*, **74,** 119–126 **(1997)**

8. Jaćimović Ž. K., Sinteze i strukture kompleksa Zn(II), Cd(II), Hg(II) i Cu(II) sa nekim di i trisupstituisanim derivatima pirazola (doktorska disertacija) Prirodno matematičku Fakultet, Novi Sad , Institut za hemiju **(1998)**

9. Pavlov S., Uvod u hemiju heterocikličnih jedinjenja, Grafofan, Beograd **(2001)**

10. Snežana Jokanović, Sinteza i kristalizacija Cu(II) i Ni(II) kompleksa sa 3,5dimetil-1tio karboksamid pirazolom, Diplomski rad, Podgorica Metalurško Tehnološki fakulter, Univerzitet Crne Gore **(2003)**

11. Matović Tanya Sinteza, Kristina i molekulska struktura novog Co(II) $Co_2L_2Cl_4$ (L=3,5dimetil-1 tiokarboksamid parasol) kompleksa, Diplomski rad, Podgorica Metalurško Tehnološki faultier, Univerzitet Crne Gore **(2004)**

12. Đurović Brana, Sinteza, kristalna i molekulska struktura novog Cu(II) $Cu_2L_2Br_2$ kompleksa (L=3,5dimetil-1 tiokarboksamid pirazol) u obliku nitratne soli Diplomski rad, Podgorica Metalurško Tehnološki fakulter, Univerzitet Crne Gore **(2004)**

13. Jacimovic Ž. K., Giester G., Tomic Z. D. and Leovac V. M., "Crystal and molecular structure of the 3,5-dimethyl -1-thiocarboxamidepyrazole," 3rd International Conference of the Chemical Societies of the South-Eastern European Countries," Bucharest, Romania, Book of Abstract, 178 **(2002)**

14. Mészáros Szécsényi K., Leovac V. M., Jacimovic Ž. K. and Pokol G., "Transition metal complexes with pyrazole-based ligands. Part 15 Cobalt (III)-, nickel (II)-, and copper (II) – complexes with 3,5-dimethyl-1-thiocarboxamidepyrazole", *J. Thermal. Anal. Cal.*, **74**, 943-952 **(2003)**

15. Evans R., Howard J. A. K., Mészáros Szécsényi K., Leovac V. M. and Jacimovic Ž. K., " Synthesis characterization and crystal structure of a novel Ni(II) complex, Ni(L-H)2 (L= 3,5-dimethyl -1- thiocarboxamide pyrazole, " *J. Coord. Chem.*, **57 (6),** 469-476 **(2004)**

16. Evans R., Howard J. A. K., Jacimovic Ž. K., Jeftovic V.S. and Leovac V. M., " Transition metal complexes with 3,5-dimethyl-1-thiocarboxamide pyrazole: Synthesis, structural and magnetic studies", British Crystallographic Associations (BCA), Manchester, 68 **(2004)**

17. Tomic Z. D., Jacimovic Ž. K., Giester G., Leovac V. M. and Zaric S. D., "Analiza intermolekulskih kontakata u 3,5-dimetil-1-tiokarboksamid pirazolu I tris (3.5-dimetil-1-tiokarboksamidpirazolato) kobalt (III); poredenje sa rezultatima dobijenim analizom relevantnih Para meter u strukturama organskih molecule koji sadrže pirazolni prsten", X Konferencija Srpskog kristalografskog društva, Sokobanja, Izvodi radova, 13 (**2002**)

18. Evans Radosavljević et al, Transition metal complexes with pyrazole based ligands, Part 18, new binuclear Cu(I), Cu(II) and Co(II) complexes with 3,5-dimethyl-1-thiocarboxamide pyrazole: synthesis, structural and magnetic studies, *Inorg. Chim. Acta*, **357,** 4528-4536 **(2004)**

19. Kovács A., Nemcsok D., Pokol G., Mészáros Szécsényi K., Leovac V. M., Jacimović Ž., Radosavljević Evans I., Howard J. A. K., Tomić Z.D. and Giester G., Structural, spectroscopic and computational studies of the Hg*L*2Cl2 complex (*L* = 3,5-dimethyl-1-thiocarboxamide pyrazole) and the crystal structure of *L*, *New J. Chem.*, **29,** 833-840 **(2005)**

20. Nemcsok D., Kovács A., Mészáros Szécsényi K. and Leovac V. M., Vibrational spectroscopic and theoretical study of 3,5-dimethyl-1-thiocarboxamide pyrazole (*L*) and the complexes Co2*L*2Cl4, Cu2*L*2Cl4 and Cu2*L*2Br2, *Chem. Phys.*, **328,**85-92 **(2006)**

21. Jaćimović Ž K., Tomić Z. D., Giester G. and Leovac V. M., Tris(3,5-dimethyl-1*H*-pyrazole-1-thiocarboxamidato-2*N*2,*N*) cobalt(III), *Acta Crystallogr.*, C**59,** m381-m383 **(2003)**

22. Jaćimović Ž., Radović A., Leovac V. M., Tomić Z. D. and Evans I.R., "Binuclear Ni(II) complex with 3,5-dimethyl-1-thiocarboxamide pyrazole," *Zeitschrift für Kristallographie - New Crystal Structures*, **222**(**4**) , 430 **(2007)**

23. Furka A., Szerves hemia, Tankonyvkiado, Budapest, **(1988)**

24. Trofimenko S., *Chem. Rev.*, ***72***, 447 **(1972)**

25. Liang Ying and He Hong Wu, Progresses on the Pyrazole Derivatives as Agrochemical Fungicides, *Chinese Journal of pesticides,* **44(11),** 491-495 **(2005)**

26.Sl list Crne Gore br. 70/09, Lista aktivnih materija dozvoljenih za upotrebu u sredstvima za zaštitu bilja **(2009)**

27. Barik A. K., Paul S., Butcher R. J. and Kar S. K., Synthesis and characterization of two tris-chelate complexes of cobalt (III) with 3,5 dimethyl-1- (*N* methyl/ethyl)thiocar bamylpyrazole (H*L*1, H*L*2) – biologically important bidentate ligands with one ambidentate donor site, *Polyhedron,* **19,** 2651-2655 **(2000).**

(Received 15th April 2013, accepted 20th July 2013)

Immobilization of Hazardous Cr(VI) in blended cement: XRD and Leaching Studies

Jain Neeraj
CSIR-Central Building Research Institute, Roorkee, INDIA
neerajest@rediffmail.com

Abstract

Marble dust from gang saw industries is generated as wastes in million tonnes and is an environmental hazard due to disposal problems. The marble dust is a filler material having similar properties like limestone and takes part in early hydration reactions due to the presence of high amount of calcium carbonate. In the present study, 40 % of marble dust (CM) blended with Portland cement (C0) has been utilized to immobilize (solidify) hazardous Cr (VI) (1000-3000 mg/l) and the effect on parameters like setting time, compressive strength and leachability of Cr (VI) has been investigated as a function of curing time. It is observed that the initial and final setting times of these cements increase with increase in Cr (VI) concentration. The effects of Cr (VI) addition on the physical, chemical and engineering properties of solidified samples (C0 and CM with Cr (VI)) were studied and the results revealed that the compressive strength reduced with addition of Cr (VI).

The samples of C0 and CM containing Cr (VI) were also tested for leachability of Cr (VI) in acidic solution (pH=~3) using Toxicity Characteristics Leaching Procedure (TCLP) tests. The leached Cr (VI) concentration was under the allowable limit (5 mg/l) of U.S. EPA at lower initial concentration. The hydration chemistry of the solidified samples has been studied by XRD which shows the formation of various phases like ettringite, Cr-ettringite, tobermorite, monocarboaluminate etc. The morphology of the hydration products was studied by Scanning Electron Microscopy (SEM) which also supports the formation of various hydrations phases as observed during XRD in the solidified cementitious binders.

Keywords: Hydration, Chromium, Solidification, Leaching, Compressive strength.

Introduction

Hazardous waste disposal is a major issue confronting the industrialized world because of limited sites, cost, technology and strict environmental standards for landfilling. The wide spread use of chromium has resulted in the contamination of soils and water. Chromium contamination is of great concern due to its toxic, mutagenic and carcinogenic nature. The chromium is generated from steel and other alloy's production, chrome plating, pigments and leather tanning industries. Among the various forms of chromium, Cr (VI) is the most important one because of its toxicity, solubility and mobility characteristics[1].

Solidification and stabilization (S/S) processes are waste treatments designed to improve the handling and physical characteristics of liquid or semisolids and decrease the release if hazard to the environment. These processes are based on hydraulic reactions of hydraulic cements or pozzolanic reactions between Portland cement or lime and pozzolanic materials such as pulverized-fuel ash, cement kiln dust and rice husk ash[2-7]. The chemical changes that take place as a result of the interaction between waste components and solidification binders play an important role in controlling the quality of cement based solidified products[8-11].

The limestone filler addition to Portland cement produces several effects on the mechanism and kinetics of cement hydration[12-18]. It has been observed that filler effect imparted by limestone filler causes a hydration acceleration of Portland clinker grains at early ages provides new nucleation sites for calcium hydroxide and produces the formation of calcium carboaluminates as results of the reaction between calcium carbonate from limestone and tricalcium aluminate from Portland clinker.

In India marble dust from gang saw industries is available as wastes in million tonnes and is an environmental hazard due to disposal problems. The marble dust is a filler material having similar properties like limestone and takes part in early hydration reactions due to the presence of high amount of calcium carbonate. In the present study, high amount of marble dust (40 %) blended with Portland cement has been utilized as filler to immobilize (solidify) Cr (VI) (1000-3000 mg/l) and the effect on parameters like setting time, compressive strength and leachability of Cr (VI) has been investigated as a function of curing time.

Material and Methods

Materials: Marble dust was collected in the form of slurry, dried and ground to a particle size of $< 300\mu m$. The physical and chemical analysis of ordinary Portland cement (OPC) cement was carried out as per IS 4031 (1999) and 4032 (1985) respectively. The results of cement analysis are given in table 1 along with marble dust analysis. The marble dust-blended cement was obtained by mixing 40 % marble dust with OPC using a mixer. A stock solution of 3000 mg/l of Cr (VI) was prepared using potassium dichromate. Table 2 shows the denominations

given to each sample during hydration of OPC and blended cement with and without Cr (VI).

Determination of Setting Times: The initial and final setting times of OPC and marble dust blended cement with and without Cr (VI) at different concentration (1000 mg/l to 3000 mg/l) were determined according to IS: 4031 (1999) using a Vicat needle.

Compressive Strength: To determine the effect of chromium on the compressive strength of the solidified samples, cubical molds (2.5cm x 2.5cm x 2.5 cm) of OPC and marble dust blended cement pastes were cast using water (distilled) to cement ratio of 0.35 as per IS 4031 (1999). The mixing was performed using automatic mortar mixer of ELE, U. K. After initial curing of 1 day, demolded specimens were stored at relative humidity of not less than 95% in airtight glass containers at 27±2^{o}C for different periods up to one year. The compressive strengths of these specimens were determined and the average value of three specimens is reported.

Leachability, Scanning Electron Microscopy (SEM) and XRD: Leaching test were carried out on the 28, 90, 180 and 360 day old hydrated pastes using the EPA Standard Toxicity Characteristics Leaching Procedure[12, 17] (TCLP). The sample was ground to a powder with a particle size <0.5 mm and leached in water (distilled) and acetic acid (pH =~3). 200 ml of water or acetic acid solution were added to the 10 g of sample in a high density polyethylene bottle. The bottle and its contents were agitated in a rotary shaker at 30 rpm for 18 h. The leachates were filtered through a 0.45 μm membrane filter to remove suspended solids and the leached solutions were used for determination of Cr (VI) by atomic absorption spectrometer (AAS). Each leachate was analyzed in triplicate and average values were reported to ensure the reproducibility of the data.

SEM was carried out using model LEO 438 VP, UK to study micro structural changes in the OPC and blended cement during hydration due to addition of Cr (VI). The hydrated samples were immersed in acetone to stop hydration at definite period of curing.

X-ray diffractometry (XRD) was used to study the hydration products of OPC and blended cement paste without and with addition of Cr (VI). The samples were immersed in acetone to stop hydration and grounded to a particle size of <45 μm for XRD. X-ray diffraction patterns were recorded on a Rigaku X-ray Diffractometer equipped with a rotating anode, utilizing CuK_a radiation at 40 kV and 30 mA.

Results and Discussion

OPC and marble dust blended cement samples containing Cr (VI) were investigated for change in setting time, compressive strength and leachability of Cr (VI)

Setting Time: The results of initial and final setting times of OPC and marble dust (40 %) blended cement with different concentration of Cr (VI) (1000-3000 mg/l) and without Cr (VI) are shown in fig.1. The control cement (C0) reaches initial and final set in 195 and 315 min respectively while control of blended cement (CM40) reaches initial and final set in 210 and 200 min. It is observed that addition of marble dust (40 %) in cement accelerates the final setting as compared to C0. It is also apparent that the addition of Cr (VI) retards the setting process of OPC (C0+1, C0+2 and C0+3) and blended cement (CM40+1, CM40+2 and CM40+3) and the retardation increases with increasing Cr (VI) concentrations. Further the results show that the initial and final setting times of marble dust blended cement samples (CM40 series) are comparable (± 15-20 min) to OPC samples (C0 series) and comply to the IS: 8112 (1989). The retardation in setting time of cement in presence of Cr (VI) may be due to the reaction between Ca^{2+} from Ca $(OH)_2$ and Cr (VI) to form $CaCrO_4$ which is a low solubility product (5.1 x 10^{-6}) as has been reported earlier[2,12].

Compressive Strength: Solidified samples with and without Cr (VI) were tested for compressive strength up to 360 days of curing at different time intervals and the results are shown in fig.2 and 3 for OPC and blended cement respectively. Samples of OPC (C0) and marble dust blended cement (CM40) without Cr (VI) served as controls for respective binder containing different concentration (1000-3000 mg/l) of Cr (VI). It is observed that in C0 and CM40 series samples containing Cr (VI), the rate of compressive strength development is very fast in early age upto 28 days of curing and decreases in later ages up to 360 days. Further, the compressive strength is a function of Cr (VI) concentration and decreases with increasing Cr (VI) concentrations.

Figure 2 depicts that the average strength of control (C0) is 59 and 73.8 MPa after 28 and 360 days of curing respectively. The samples of C0 series containing Cr (VI) exhibit a loss of compressive strength in the range of about 11-18 % and 8-14 % on 28 and 360 of curing respectively as compared to the control (C0). Figure 3 shows that samples of marble dust blended cement paste (CM40) exhibit a strength of 47.1 and 59.6 MPa after 28 and 360 days of curing respectively and is about 80 % of the strength of C0. The strength of CM40 series samples containing Cr (VI) decreases from 6-16 % and 10-19 % after 28 and 360 days of curing respectively as compared to the control (CM40).

The results also depict that the marble dust blended cement samples (CM40 series) exhibit low decrease in the percentage strength at an early age (28 days) as compared

to the OPC samples (C0 series) in the presence of Cr (VI). The possible reason for this may be the formation of phases like ettringite and associated phases like Cr-ettringite and Bentorite during hydration as reported earlier[14].

Leachability: The results of TCLP leaching tests for the hydrated OPC and blended cement paste samples containing Cr (VI) are depicted in table 3. The tests were performed at various curing time in water and acid (pH=~3) solution. The leaching of Cr (VI) with curing time decreases in all the samples and it may be due to the increase in compressive strength as a result of more hydration and densification of microstructure[3, 12]. The results also show that the leaching is a function of initial Cr (VI) concentration and increase in leaching is observed with increase in initial concentration.

However the retained percentage of Cr (VI) is independent of initial Cr (VI) concentration and is more than 99 % in acid as well as in water at all curing periods. It is also observed that the percentage Cr (VI) retained is slightly higher in water than in acidic solution. It is evident that the leached Cr (VI) concentration was under the allowable limits (5 mg/l) of US-EPA at 1ower concentration (1000 mg/l) of Cr (VI) for C0 and CM40 samples. The results show the affinity of marble dust to retain Cr (VI) is very high because the quantity of available cement in CM40 is very less as compared to C0 samples.

SEM and XRD Analysis: The scanning electron micrographs (SEM) of the hydrated cement samples with and without Cr (VI) are shown in figs 4-5 for C0 and CM40. After 1 day of hydration of cement, typical hydration products like calcium hydroxide (CH), tobermorite (T) and grain structure appear in the C0 paste together with short acicular and needle like crystals. After 7 days, the microstructure of the cement becomes much denser with pronounced formation of needle like crystals and acicular features. At 28 days, the hydrated grains are interconnected by outgrowth forming a continuous structure as shown in fig. 4 (a). The micrographs of hydrated OPC samples containing Cr (VI) for 28 days curing are shown in fig. 4 (b) which shows the formation of crystals of ettringite (E) and tobermorite (T).

The SEM of blended cement sample (CM40) hydrated for 28 days are shown in fig.5 (a-b). A perusal of fig. 5 (a) illustrates that at 28 days of hydration, dense structures containing ettringite subhedral to anhedral crystals of CSH agglomerated with cubic calcium hydroxide (CH) as well as prismatic and lath shaped crystals representing various hydration products are formed. Fig. 5 (b) shows the breakdown of the dense hydrated material by carbonation and formation of less crystal of calcium carbonate (CC).

The results of X-ray diffractograms evaluation show the formation of various crystalline phases after 28 days of curing which are more or less same for different Cr (VI) concentrations (1000 to 3000 mg/l). The most prominent peaks in the unhydrated cement were of tricalcium silicate (C_3S) at 29.4^o, 32.6^o, 34.3^o, 41.3^o, 51.7^o, 56.6^o and dicalcium silicate (C_2S) at 26.4^o and 32.2^o (Fig.6). The peaks of ettringite (E) were also observed at 28.6, 34^o and 50.7^o and calcium chromate peak was observed at 32.3^o along with peak of Calcium ettringite (Ca-E) at 44.9^o in samples of OPC with Cr (VI) as shown in fig.6.

The XRD pattern of marble dust blended cement (CM40) is almost similar to that of C0 at 28 days of hydration (Fig.7). Additionally, the peaks of calcium carbonate (CaC) at 29^o and 31.9^o and monocarboaluminate peaks at 23.2^o and 33.5^o were also observed. Addition of marble dust accelerates the formation of ettringite in early ages by the presence of calcium carbonate and also stops or delays the conversion of ettringite to monosulfoaluminate. This phenomenon occurs because some sulphate ions can be interchanged by carbonate ions during hydration of tricalcium aluminate (C_3A). Excess of calcium carbonate accelerates the hydration rate of C_3S in early ages and is also responsible for the transformation of mono-sulfoaluminate to monocarboaluminate because of low stability. Fig.7 shows the XRD pattern of CM40+1 after 28 days of curing. The peaks of chromium ettringite peak (Cr-E) and bentorite were observed at 44.9^o and 34.2^o along with other peaks similar to CM40.

Conclusion

The following conclusions can be drawn based on the investigation carried out:

(1) Addition of Cr (VI) retards the initial and final setting times of C0 and CM40 pastes and retardation increases with increase in Cr (VI) concentration.
(2) Samples of marbles dust blended cement (CM40 series) exhibit low decrease in the percentage strength at an early age (28 days) as compared to the OPC samples (C0 series) in the presence of Cr (VI). The possible reason for this may be the formation of various Cr-phases at an early age in presence of marble dust. The compressive strengths of all the series) tested were greater than the EPA compressive strength requirement (0.3 MPa) for S/S treatment of hazardous wastes.
(3) TCLP results reveal that OPC (C0) and marble dust blended cement (CM40) are the adequate binders to confine the hazardous Cr (VI) at low concentration for reduction of negative impact on land and ground water quality.
(4) The major hydraulic products like C_3S, C_2S, ettringite, Calcium chromate, Cr-ettringite, bentorite and monocarboaluminate were identified by XRD.

Acknowledgement

Authors are thankful to the Director, CBRI, Roorkee for his permission to publish the present work.

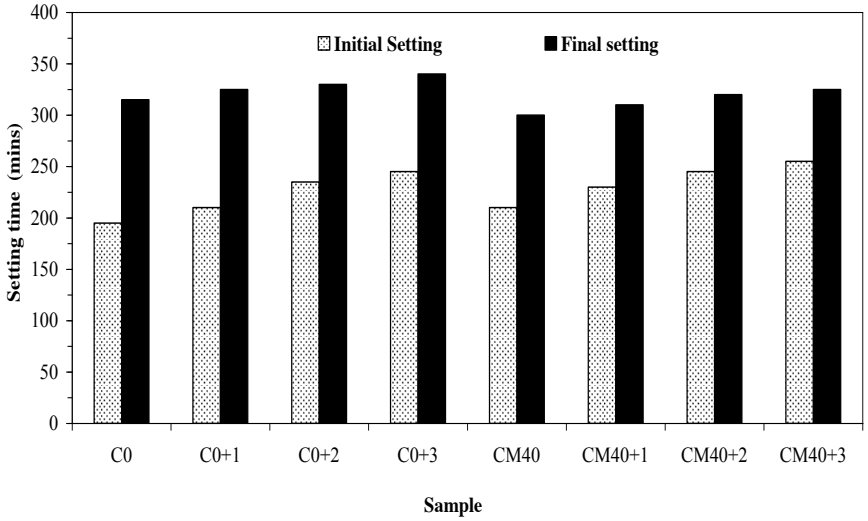

Fig.1: Setting time of OPC (C0 series) and marble dust blended cement (CM40 series) at various Cr (VI) concentrations

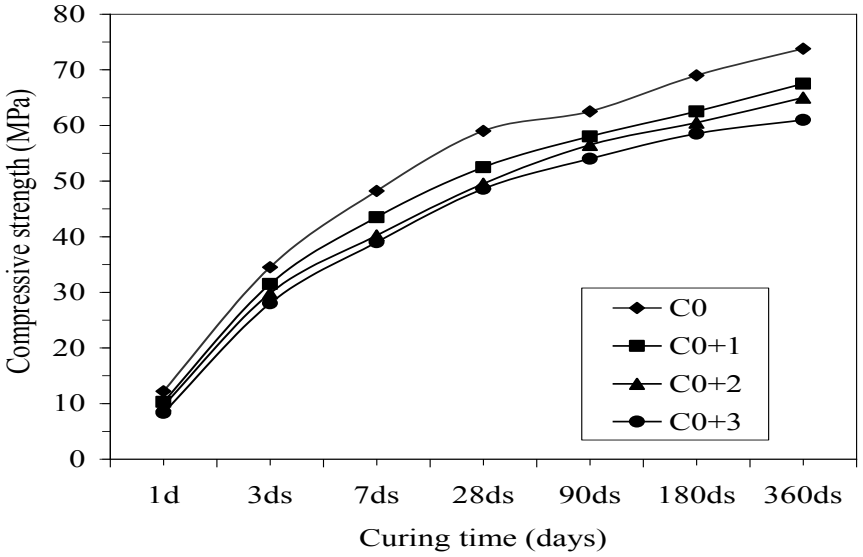

Fig.2: Effect of Cr (VI) concentration on compressive strength of OPC

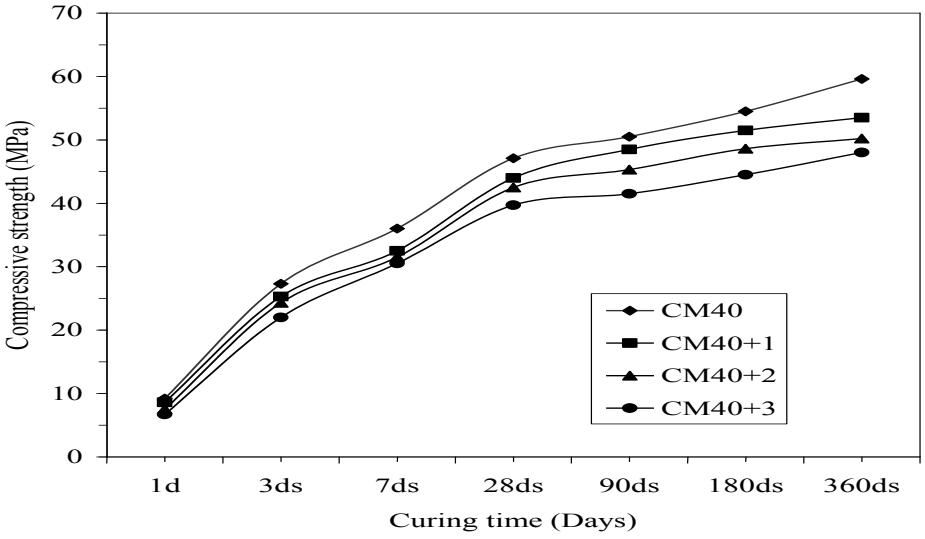

Fig.3: Effect of Cr (VI) concentration on compressive strength of blended cement

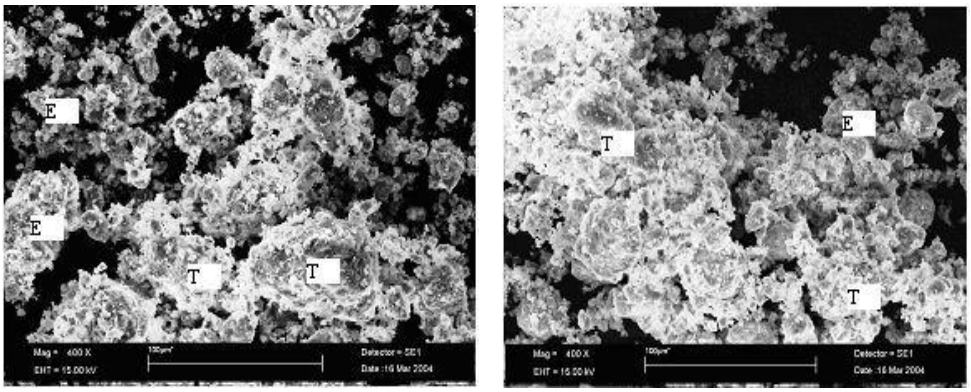

(a) **(b)**

Fig. 4: SEM of 28 days hydrated OPC without and with Cr (VI) (a) C0 (b) C0+1

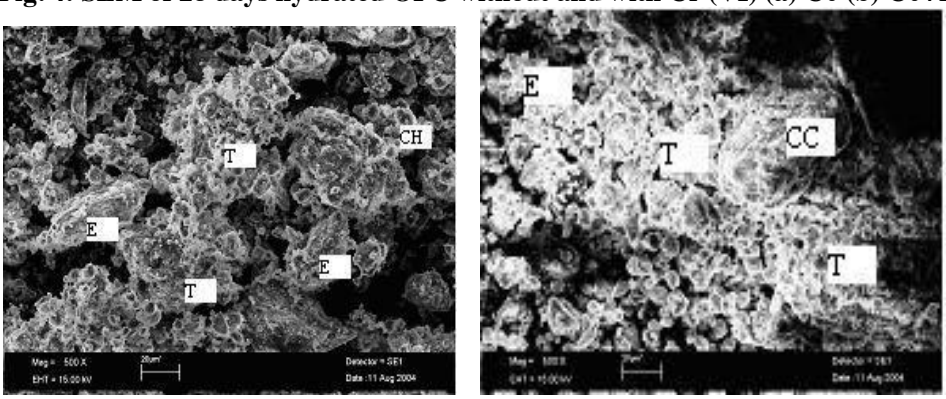

(a) **(b)**

Fig 5: SEM of marble dust blended cement without and with Cr (VI) (a) CM40 (b) CM40+1

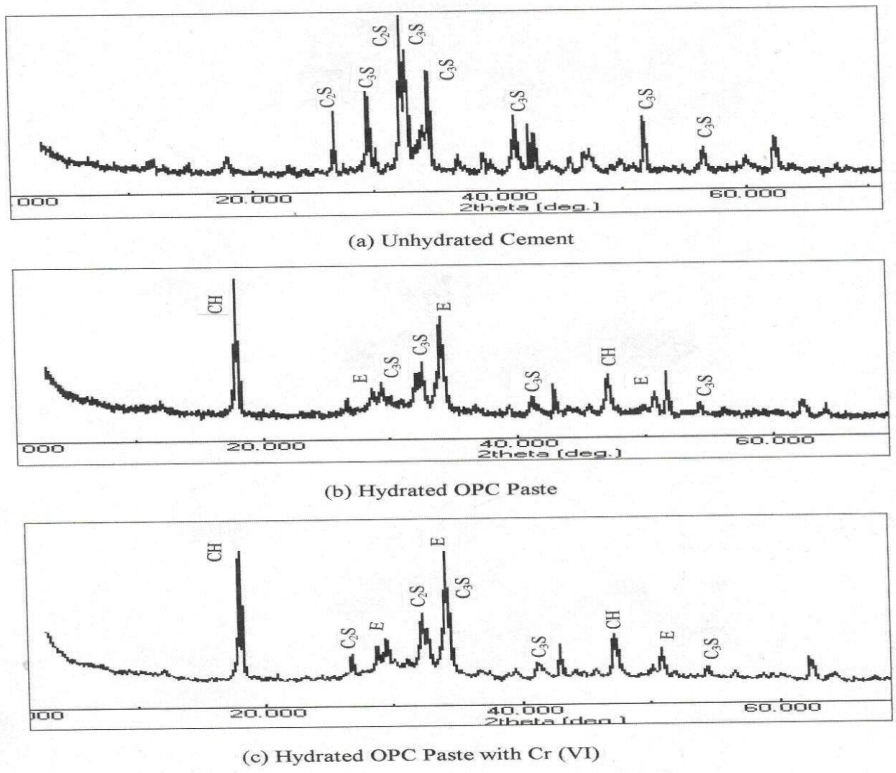

Fig.6: XRD of Unhydrated and hydrated cement paste without and with Cr (IV)

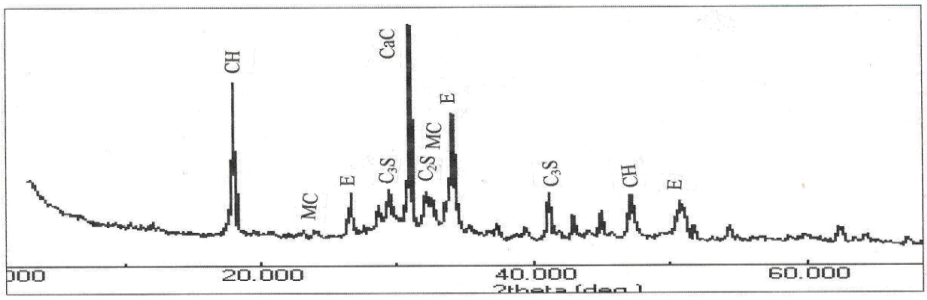

(a) Hydrated marble dust blended cement

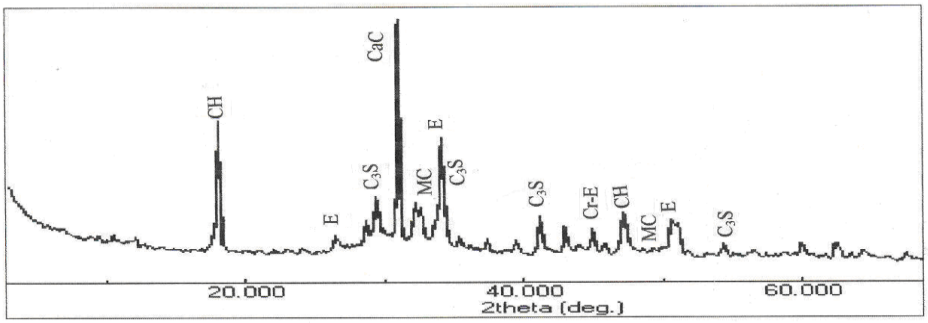

(b) Hydrated marble dust blended cement with Cr (VI)

Fig.7: XRD of hydrated marble dust blended cement without and with Cr (IV)

Table I
Physical and chemical analysis of Portland cement and marble dust

Properties	Portland Cement (43 G)	Marble Dust
Specific gravity	3.14	----
Insoluble residue (%)	1.30	----
Alkalies (%)	0.35	----
SO_3 (%)	2.10	----
Chloride (%)	0.012	----
LOI (%)	1.51	43.40
Surface area (m^2/kg)	308	310
Silica content (%)	21.6	3.01
CaO (%)	62.2	30.80
Magnesia (%)	1.40	19.27
Fe_2O_3+ Al_2O_3	----	2.70

Table II
Denominations given to samples during hydration studies

Sample	Denominations
OPC only (control)	C0
OPC + 1000 mg/l of Cr (VI)	C0+1
OPC + 2000 mg/l of Cr (VI)	C0+2
OPC + 3000 mg/l of Cr (VI)	C0+3
OPC + 40 % marble dust	CM40
OPC + Marble dust (40% + 1000 mg/l of Cr (VI)	CM40+1
OPC + Marble dust (40% + 2000 mg/l of Cr (VI)	CM40+2
OPC + Marble dust (40%)+ 3000 mg/l of Cr (VI)	CM40+3

Table III
Leaching Values of Immobilized Cr (VI) From Solidified Samples

Samples	Medium	Leached values of Cr (VI) in mg/l			
		28 days	90 days	180 days	360 days
C0+1	Acid	5	3	BDL	BDL
	Water	BDL	BDL	BDL	BDL
C0+2	Acid	22	15	17	12
	Water	15	13	12	8
C0+3	Acid	30	25	23	16
	Water	5	22	17	10
CM40+1	Acid	8	5	3	BDL
	Water	5	3	BDL	BDL
CM40+2	Acid	25	23	17	12
	Water	18	15	13	10
CM40+3	Acid	35	28	21	16
	Water	32	27	20	12

References

1. Katz S.A. and Salem H., The biological and environmental chemistry of chromium, VCH publications, New York **(1994)**

2. Wang S. and Vipulanandan C., Solidification/stabilization of Cr (VI) with cement leachability and XRD analyses, *Cem. Concr. Res.,* **30(3),** 385-389 **(2000)**

3. Jain N. and Garg M., Effect of Cr (VI) on the Hydration Behavior of Marble Dust Blended Cement: Solidification, Leachability and XRD Analyses, *Cons.Build. Mat.,* **22 (8),** 1851-1856 **(2008)**

4. Jain N., Solidification and Leachability of Cr (VI) in Rice Husk Ash Blended Cement, *ISRN Civil Engg., Article ID 183156***,** 1-6, doi:10.5402/2011/183158 **(2011)**

5. Park C. K., Hydration and solidification of hazardous wastes containing heavy metals using modified cementitious materials, *Cem.Concr. Res.,* 30**(3),** 429-435 **(2000)**

6. Minocha A.K., Jain N. and Verma C. L., Effect of inorganic materials on the solidification of heavy metal sludge, *Cem. Concr. Res.,* **33(10),** 695-701 **(2003)**

7. Asavapisit S. and Chotklang D., Solidification of electro-plating sludge using alkali activated pulverized fly ash as cementitious binder, *Cem. Concr. Res.,* **34(2),** 349-353 **(2004)**

8. Cullinane M. J. Jr. and Jones L. W., Solidification and stabilization of hazardous wastes, *Hazard. Mat. Cons.*, **2(1),** 9-17 **(1989)**

9. Rousekova I., Bajza A. and Zivica V., Silica fume-basic blast furnace slag systems activated by an alkali silica fume activator, *Cem. Concr. Res.,* **27(12)**, 1825-1828 **(1997)**

10. Zhang M. H., Lastra R. and Malhotra V. M., Rice-husk ash paste and concrete: some aspects of hydration and the microstructure of the interfacial zone between the aggregate and paste, *Cem. Concr. Res.,* **26(6)**, 963-977 **(1996)**

11. Pera J., Thevenim G. and Chabannet M., Design of a novel system allowing the selection of an adequate binder for solidification/stabilization of wastes, *Cem. Concr. Res.,* **27(10)**, 1533-1542 **(1997)**

12. Trezza M. A. and Ferraiuelo M. F., Hydration study of limestone blended cement in presence of hazardous wastes containing Cr (VI), *Cem. Concr. Res.*, **33(7)**, 1039-1045 **(2003)**

13. Bonavetti V. L., Rahhal V. F. and Irassar E. F., Studies on the carboaluminate formation in limestone filler-blended cements, *Cem. Concr. Res.,* **31(1)**, 853-859 **(2001)**

14. Ramachandran V. S., Thermal analysis of cement components hydrated in the presence of calcium carbonate, *Thermochim Acta,* **127(16)**, 385-394 **(1988)**

15. Tsivilis S., Kakali G., Chaniotakis E. and Souvaridou A., A study on the hydration of Portland limestone cement by means of TGA, *J. Thermal Anal.*, **52(3)**, 863-870 **(1998)**

16. Jain N., Effect of non pozzolanic and pozzolanic mineral admixtures on the hydration behavior of ordinary Portland cement, *Cons. Build. Mat.,* **27(1)**, 39-44 **(2012)**

17. Toxicity Characteristic Leaching Procedure (TCLP), 40 CFR 261, Appendix II, US Environmental Protection Agency, Washington DC **(1994)**

18. Lin C., Chen J. and Lin C., An NMR and XRD study of solidification/stabilization of chromium with Portland cement and β-C2S, *J. Hazard. Mat.*, **48(1-3)**, 137-147 **(1996)**.

(Received 05th March 2013, accepted 10th May 2013)

Influence of Pt on Structural and Morphologycal Properties of La_2O_3 / SnO_2Thick Film

Ehsani Maryam[1*], Hamidon Mohd Nizar[2] and Pah Lim Kean[3]
1. Electrical and Electronic Department, Engineering Faculty, University Putra Malaysia, 43400 UPM Serdang, Selangor, MALAYSIA
2. Functional Devices Laboratory, Institute of Advanced Technology, University Putra Malaysia, 43400 UPM Serdang, Selangor, MALAYSIA
3. Physics Department, Science Faculty, University Putra Malaysia 43400 UPM Serdang, Selangor, MALAYSIA
*fojan.1982@gmail.com

Abstract

In this study, the effect of La_2O_3/SnO_2 surface modification by Pt synthesized in the structural properties of SnO_2 was presented. Samples (2wt.% La_2O_3, SnO_2, 2 wt.% La_2O_3, SnO_2, 1 wt.% Pt)were prepared using the ball milling method with m-xylene medium and they were calcined under700 °C. The thick film resistive paste based on SnO_2 was fabricated on alumina substrate using screen printing technique. In order to prepare the printable thick film paste, the calcined resistive powders were mixed with organic vehicle and glass frit on alumina substrate with good rheology. Afterward, thermal treatment (drying and firing) was applied to dry the solvant from the printed paste and bonding the resistive paste on alumina substrate.

The particle size and crystallinity of samples were characterized using X-Ray Powder Diffraction (XRD)spectroscopy and Transmission Electron Microscopy (TEM). TEM results illustrate that the obtained material are nanoparticles in spherical shape and the size of particles decreases with addition of Pt. The XRD pattern results show that the prepared samples are the nanopowders with almost spherical crystalline structure. The thick film surface morphology was investigated by Field Emission Scanning Electron microscopy (FE-SEM) before and after Pt doping and Energy Dispersive X-Ray spectroscopy (EDX) was used to determine the elemental composition.The results proved the nanometric size of all particles and it illustrated that the particle size of materials decreased with the addition of Pt on La_2O_3/SnO_2.

Keywords: Nanocrystalline materials, Particle size, SnO_2, Catalytic additives.

Introduction

Tin oxide (SnO_2)is n-type metal oxide with a wide band gap of (E_g =3.6 eV, at 26.85°C) and rutile (tetragonal) structure[1, 2]. Tin oxide is used for some applications such as electrodeandcatalyst materials [3], due to suitable catalytic and electrical properties of this metal oxide. Additionally it is widely used for gas sensor fabrication because of its inherent oxygen vacancies. Small size of SnO_2 particles plays an important role for mentioned applications.

The size of tin oxide particles can be controlled by small amount of additives such as metal oxides and noble metals. Xu el al[4] have investigated the effect of small amount of foreign oxides on SnO_2 microstructure and they observed that the size of particles can be controlled by the additives. Catalytic properties of SnO_2 are affected by acidic or basic characterization of metal oxides [5-8]. Among all metal oxides which are used as tin oxide dopants, rare earth elements and noble metals have an effective role to increase the catalytic properties of tin oxide [9]; these materials are suitable for providing high surface area, small particle size and other morphological characteristics [10, 11].

The catalytic properties of rare earth metal oxides such as La_2O_3 can be activated by the acidic site of tin oxide. Moreover the electronic distribution of materials is affected by rare earth chain of this material which acts as adsorbing center. La_2O_3 is one kind of rare earth metal oxides with hexagonal and cubic crystalline structure at low and high temperature respectively. Lanthanum oxide contains the lanthanum metal atoms that are surrounded by seven octahedral shapes of O^{2-} atoms and one oxygen ion which is located above one of the octahedral faces. Lanthanum oxide with p-type semiconductor properties has high potential to adsorb the moisture and produce lanthanum hydroxide[12]. In gas detection application by tin oxide as a base material, large scale surface area is the most important parameter that is achieved by the small particle size and the other excellent morphological characteristics [13-15].

To prepare the powders, m-xylene is preferred to ethanol or acetone as a medium due to non-polarity of m-xylene and symmetrical C-H arrangement as compared with acetone and ethanol. There are many studies and experiments on SnO_2, SnO_2/La_2O_3[16]that demonstrate use of rare earth cations such as lanthanum oxide and noble metals such as Pt, Pd, Au[17, 18] leading to high performance of SnO_2 for gas detection application[19, 20]. In this work, the effect of catalytic element of Pt was investigated, results illustrated that using Pt as an impurity not only leads to the reducing of crystalline size of tin oxide doped with lanthanum but also the film structure produced by this material was modified. The nanocrystalline size of tin oxide plays a main role in promoting material characteristics for gas sensor application [21].

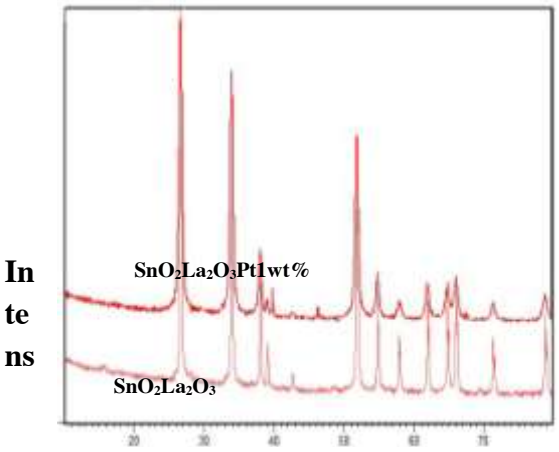

Fig.1: XRD patterns for the S1andS2 powders recorded at room temperature by ball milling process and drying at 150°C, calcined at 700°C for 2h

Material and Methods

The nano-powder samples include S1. 97 wt.%SnO_2, 2wt.% La_2O_{3and}S2. 95 wt.%SnO_2, 2wt.% La_2O_3 and 1wt.% Pt (Sigma Aldrich, 99.9%, average particle size of 100 nm) nano-powders were mixed together in m-xylene medium using ultrasonic bathandafter 24 h the component were dispersed homogenously. When the samples milled for almost 4 days (24h forward and 24 h reverse,450 rpm) inside planetary mono mill, with ceramic container (d=45mm) and ceramic balls (d=6mm) using m-xylene medium. In order to vaporize the solvent, samples were dried in normal oven at 50°C for about 1 h. Afterward the samples were milled using agate mortar to obtain the soft powder. Particle size analyzer was utilized to make sure about nano particle size less than 100 nm.

Then all samples were calcined in the air inside tube furnace at 700°C for almost 2 h, the final products had the grain grow and provided the desire sizeandXRD and TEM technique were used for characterization of samples. The final powders were utilized to make the resistive thick film paste for investigation of the film morphology and porosity. Droplet of organic vehicle made by alpha_terpineol, m-xylene and ethyl cellulose with glass frits were mixed together for preparation of resistive paste. The ball miller for almost 15 minutes was used to obtain the desired paste with suitable rheology to print over alumina (Al_2O_3) substrate by screen printing technique. Final products were dried at 150 °C for 20 minutes to vaporize the organic vehicle from the paste. Then, both samples were put inside the box furnace to bond the film to substrate. FE-SEM and EDX analyses were used to investigate the change of film rheology before and after dopant addition and elemental composition respectively.

Results and Discussion

The particle sizes (nm) of nanocrystalline were evaluated by X- ray diffraction (XRD) and the average size were calculated by the Scherer's equation as follows:

$$D= k \lambda/ \beta \cos \theta$$

In this equation the shape factor k, λ, β, θ are dimensionless shape factor (0.94), X-ray wavelength, full width of diffraction line at half maximum intensity (FWHM) and the Bragg angle respectively. The crystallite size of products is evident in the nanometric range with tendency of a slight decrease with addition of Pt. The average crystallite sizes (D) of the samples are sorted in table 1. Fig. 1 depicts the XRD patterns of SnO_2/La_2O_3 and 1wt. % Pt modified SnO_2/La_2O_3 powders obtained by ball milling process. The most intense lines for SnO_2 powder doped with lanthanum correspond to 2θ =26.66 °, 33.93°,37.99 °,39.02 °, 42.65, 48.53, 51.84, 54.82, 57.89, 61.95, 64.80, 66.03, 71.34, 78.77 which are adapted with JCPDS files of 98-010-5764and98-006-6322. Similar result is obtained for $La_2O_3/SnO_2/Pt$ but the intensity of diffraction peaks decreased after addition of platinum.

The crystallite sizes of these nanocrystals were calculated by Scherrers equation and the average crystallite size for samples S1 and S2 nanocrystals are 11.82 nmand5.53nm respectively. The other analysis method that is applied in this work for characterization of nanocrystalline powder in order to XRD results confirmation is TEM analysis. The precursors of samples S1 and S2 nanocrystalline powders which were prepared by high energy ball milling method can be affected by many parameters such as time of milling and amount of La_2O_3 and Pt doping over the reaction quality between the molecules structure of prepared samples[22]. Hence, the morphology of nanocrystalline powders was obtained by using TEM technique. Fig. 2a, 2b show TEM image of samples S1and S2 respectively.

The particle size of samples is reported in fig. 2(c) and 2(d). The results were summarized in table 2. As TEM results, the average of particles size for S1 and S2 is 42.43 and 11.29 nm. Consequently, the particle size for S2 is smaller than S1 and variable between 6 to31 nm. Fig. 2c shows the plots of particles size distribution. The most significant difference between both samples is in their particle sizes. The average particle sizes of the crystallite by XRD are smaller than the particles size of them.

Polycrystalline structure of samples also can be seen in the figures of 2(a) and (b), after doping of 1wt. % Pt the elongated shape of crystals becomes spherical and the size of them decreases. Reduction of particles after doping level has been presented by the other researchers[23].TEM image of SnO_2/ La_2O_3 powders shows that the doping of Pt causes decrease of the particle size to less than 10 nm. FE-SEM micrographs were taken to compare the morphology of printed thick film pastes using S1 and S2 nanosized

powders. FE-SEM images taken from the surface of printed paste on alumina substrate at firing temperature of 700°C are shown in fig.3.

Fig.3a shows the average grain sizes as compared with TEM results are larger because they were surrounded with melted glass frits with a homogeneous dimensional distribution. Fig.3b illustrates the uniform distribution of Pt in the surface of thick film which is distinguished by the EDX analysis. The surface porosity of samples is almost same with porosity average size ranges about 63.55 nm. The FE-SEM image shows the presence of angular hexagon structure for S1 that is changed to granular structure with hexagonal features after Pt doping. Particle distribution in both samples is almost uniform on the surface.

Elemental analysis in this work was obtained by energy dispersive X-ray spectroscopy.The EDX spectrum of samples illustrates that the Sn and O have more sharp peak than low concentration of La and Pt elements. A homogenous distribution of lanthanum and platinum into SnO_2 can be seen in fig. 5.

The specific area was chosen to collect the qualitative and quantitative of elements properties. The first peaks of La and Pt observed were around 1 and 1.6 keV while the highest peak of La and Pt are located at 4.2 and 1.5 keV respectively. The most significant peak of tin is identified around 3.5 keV. The EDX elemental composition results of SnO_2/La in pure form and loaded with 1wt. % Pt have been sorted in table 3.

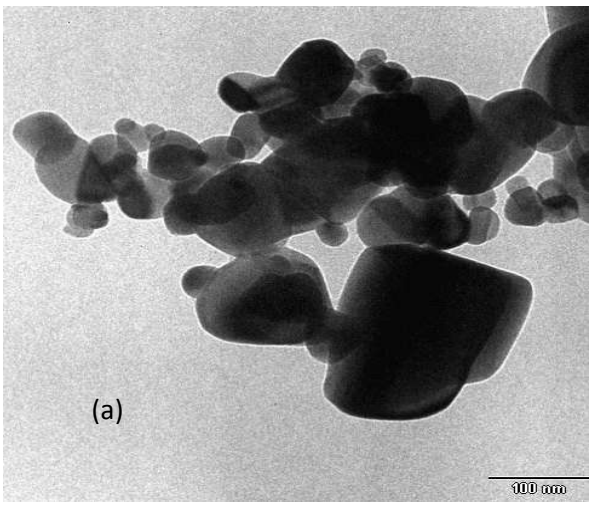

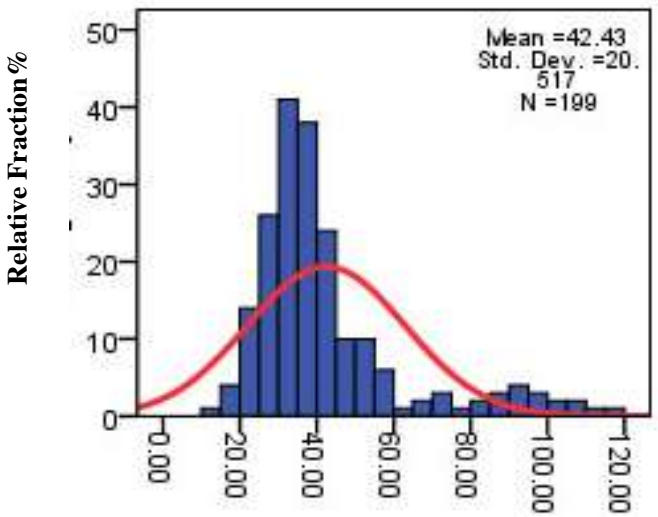

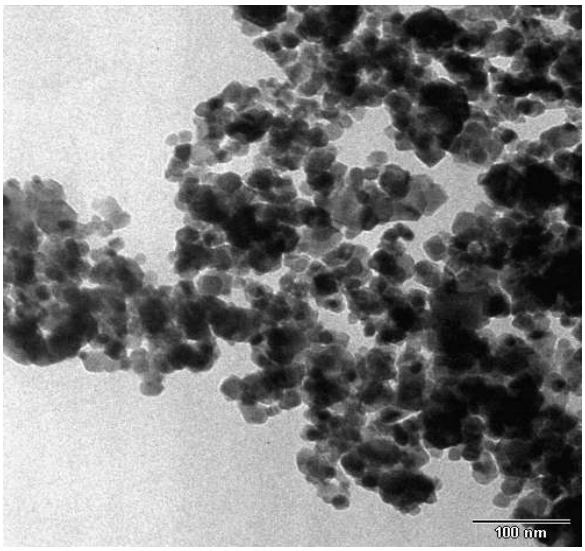

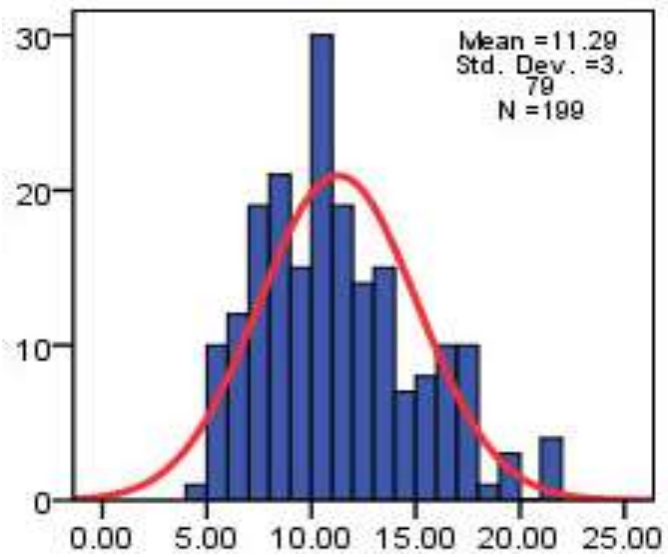

Fig.2: TEM micrograph of (a) S1, (b) S2andparticle size distribution graphs for (c) S1 and (d) S2

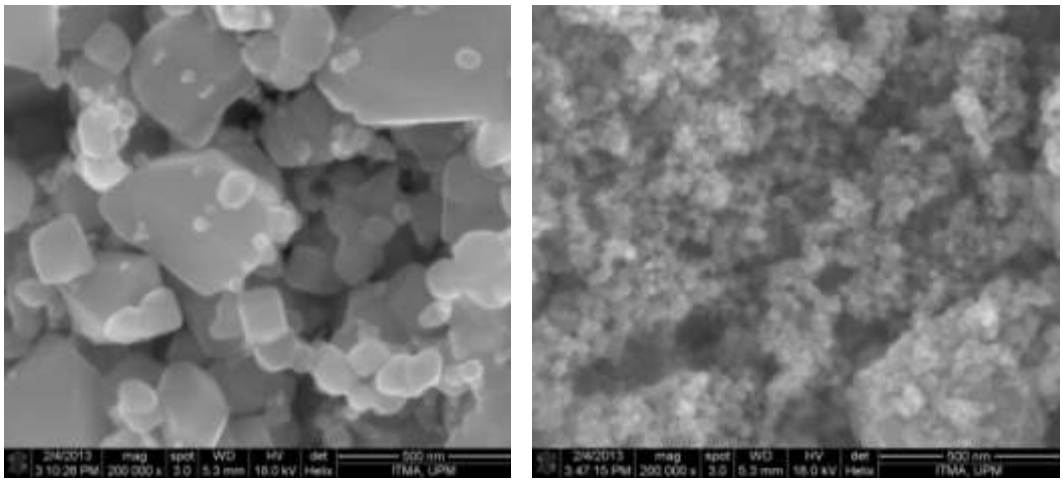

Fig.3: FESEM micrographs of thick films (a) SnO_2/La_2O_3 (b) SnO_2/La_2O_3/1wt.% Pt fired at 700°C

(a) (b)

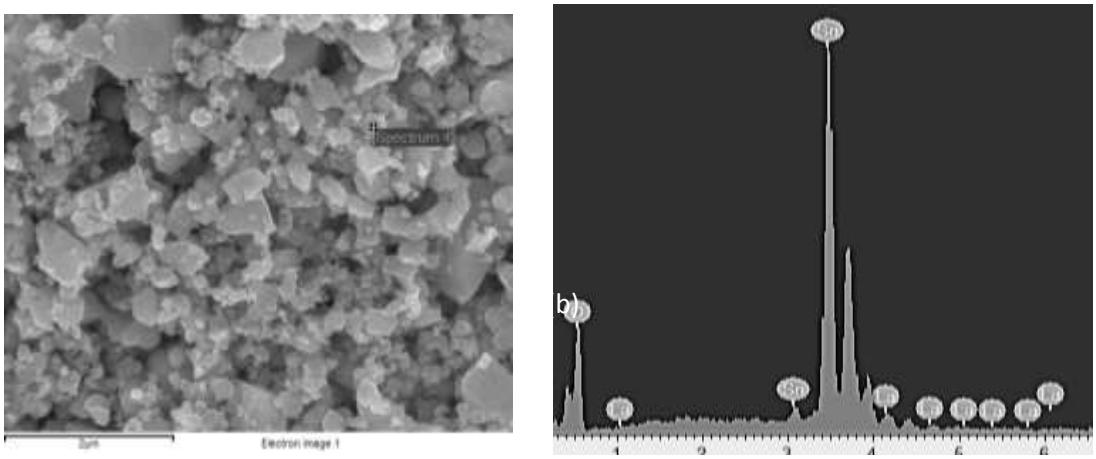

Fig.4: EDX spectrum of SnO_2/La_2O_3 fired at 700°C (a) chosen area and (b) response of elemental composition for chosen area

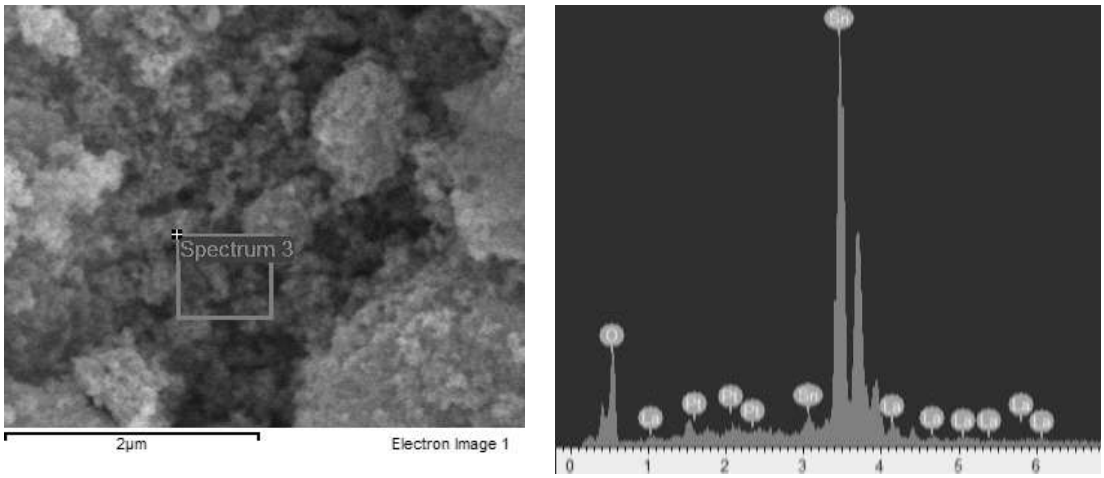

Fig.5: EDX spectrum of SnO_2/La_2O_3/1wt% Ptfired at 700°C (a) chosen area and (b) response of elemental composition for chosen are

Conclusion

La_2O_3/SnO_2 and Pt $/La_2O_3/SnO_2$ nanocrystalline powder for gas sensor application were prepared using ball milling method. The calcinations of composite occurred at 700ºC during 2 h. The TEM and XRD results achieved the particle size for La_2O_3/SnO_2 and Pt $/La_2O_3/SnO_2$ nanocrystalline powder as 11.82 and 5.53 nm respectively. Consequently, the particle size was decreased with presence of Pt. The powders were applied to prepare the resistive thick film paste for investigation of the film morphology and porosity. As a result, the distribution of Pt in the surface of thick film was uniform and the EDX analysis distinguished the chemical component such as Sn and O have sharper peak than La and Pt.

Acknowledgement

The present work was supported by the University Putra Malaysia (UPM). The authors thank the UPM for funding the nanotechnology research.

Table 1
Crystallite and particle sizes of samples demonstrated by XRD

Samples	Crystallite size (nm)		
	min	average	max
S1: SnO_2/La_2O_3	9.23	11.82	18.12
S2: SnO_2/La_2O_3/1wt. % Pt	3.104	5.53	11.78

Table 2
Average particle size of S1 and S2 calcined at 700°C observed in TEM

Samples	Minimum size	Average particle size	Maximum size
S1: SnO_2/La_2O_3	19.05	42.43	89.90
S2: SnO_2/La_2O_3/ 1wt. % Pt	4.95	11.29	21.15

Table 3
Analysis of EDX elemental composition of sensitive films of S1 and S2

Element	S1(Sn/La)		S2(Sn/La/Pt)		
	Sn	La	Sn	La	Pt
Weight %	67.95	1.21	70.18	1.55	0.76
Atomic %	22.81	0.35	25.43	0.48	0.17

References

1. Lee S.W., Kim Y.W. and Chen H., *Appl. Phys. Lett.*, **78,** 350 **(2001)**

2. Mason M.G., Hung L.S., Tang C.W., Lee S.T., Wong K.W. and Wang M., *J. Appl. Phys.*, **86,** 1688 **(1999)**

3. Anuar Kassim, Ho Soon Min, Atan Shariff and Md Jelas Haron, The effect of the pH value on the growth and properties of chemical bath deposited SnS thin films, *Res. J. Chem. Environ,* **15 (3),**45-48 **(2011)**

4. Xu C., Tamaki J., Miura N. and Yamazoe N., *Chem. Letts.*, 441 **(1990)**

5. Wang C.B., Cai Y. and Wachs I.E., Reaction-induced spreading of metaloxides onto surfaces of oxides supports during alcohol oxidation: phenomenon, nature mechanism, *Langmuir*, **15**, 1223–1235 **(1999)**

6. Jinkawa T., Sakai G., Tamaki J., Miura N. and Yamazoe N., Relationshipbetween ethanol gas sensitivity and surface catalytic properties of tin oxide sensors modified with acidic or basic oxides, *J. Mol. Catal. A,* **155,** 193–200 **(2000)**

7. Teterycz H., Licznerski H., Nitsch H., Wisniewski K. K. and Golonka J. L., Anomalous behaviour of new thick film gas sensitive composition, *Sens. Actuators* B, **47(1-3)**, 153–157 **(1998)**

8. Fukui K. and Nakane N., CO gas based on Au–La2O3 loaded SnO2 ceramic, *Sens. Actuators* B, 25(1) 486–490 **(1995)**

9. Yamazoe N., New approaches for improving semiconductor gas sensors, *Sens. Actuators* B, **5(1-4)**, 7–19 **(1991)**

10. Weber I.T., Maciel A.P., Lisboa-Filho P.N., Paiva-Santos C.O., Schreider W.H., Maniette Y., Leite E.R. and Longo E., Synthesis and processing effects on the super-saturated are earth doped nanometric SnO_2 powders, *Nanoletters,* **2**, 969–973 **(2002)**

11. Leite E.R., Maciel A.P., Weber I.T., Lisboa-Filho P.N., Longo E., Paiva-Santos C.O., Schreider W.H., Maniette Y., Pascocimas C.A. and Andrade A.V.C., Development of metal oxide nanoparticle with high stability against particle growth using metastable solid solution, *Adv.Mater.*, **14(12),** 905–908 **(2002)**

12. Wells A.F., Structural Inorganic Chemistry, Oxford, Clarendon Press, 546 **(1984)**

13. Reed J.S., Principles of Ceramics, 2nd ed., Wiley, New York, **(1995)**

14. Weber I.T., Maciel A.P., Lisboa-Filho P.N., Paiva-Santos C.O., Schreider W.H., Maniette Y., Leite E.R. and Longo E. Synthesis and processing effects on the super-saturated rare earth doped nanometric SnO2 powders, *Nanoletters,* **2,** 969–973**(2002)**

15. Leite E.R., Maciel A.P., Weber I.T., Lisboa-Filho P.N., Longo E., Paiva-Santos C.O., Andrade A.V.C., Pakoscimas C.A., Maniette Y. and Schreiner W.H., Development of Metal Oxide Nanoparticles with High Stability Against Particle Growth Using a Metastable Solid Solution, *Advanced Materials*,**14(12)**, 905-908 **(2002)**

16. Gonçalves F.M., Medeiros P.R.S., Appel L.G., The role of cerium in the oxidation of ethanol over SnO_2-supported molybdenum oxides, Appl. Catal, A, **208,** 265–270 **(2001)**

17. Mizsei J., Activating technology of SnO2 layers by metal particlesfrom ultrathin metal films, *Sens*. *Actuators*, B, **16 (1-3),** 328–333 **(1993)**

18. Penza M., Martucci C. and Cassano G., NOx gas sensing characteristicsof WO_3 thin films activated by noble metals (Pd, Pt, Au) layers, *Sens.Actuators*, B, **50 (1)**, 52–59 **(1998)**

19. Reddy C. V. G., Manorama S. V.and Rao V. J., Influence of La_2O_3 loading on SnO_2 based sensors, *Journal of materials science*, **35(13)**, 3403-3407**(2000)**

20. Weber I. T., Valentini A. N., Probst L. F. D., Longo E. and Leite E. R., Influence of noble metals on the structural and catalytic properties of Ce-doped SnO< sub> 2</sub> systems, *Sensors and Actuators, B: Chemical*, **97(1)**, 31-38 **(2004)**

21. Cheng B., Russell J. M., Shi W. S., Zhang L. and Samulski E. T., Large-Scale, Solution-Phase growth of single-crystalline SnO_2 nanorods, *Journal of American Chemistry Society*, **126**, 5972−5973 **(2004)**

22. Hamedani N. F., Mahjoub A. R., Khodadadi A. A.and Mortazavi Y., CO and ethanol selective sensor of La_2O_3-doped ZnO nanostructures synthesized by microwave assisted fast method., IMCS 2012 – The 14th International Meeting on Chemical Sensors, 1641-1643 **(2012)**.

(Received 12th April 2013, accepted 15th July 2013)

Solubility of Carbon Dioxide in Aqueous Solution of 2-Amino-2-hydroxymethyl-1, 3-propanediol at Elevated Pressures

Murshid Ghulam*, Shariff Azmi Mohd. and Bustam Mohammad Azmi
Department of Chemical Engineering, Universiti Teknologi PETRONAS, Tronoh-31750, Perak, MALAYSIA
*ghulam.murshid@petronas.com.my

Abstract

The removal of acid gases such as carbon dioxide (CO_2) from various industrial streams is a significant step in gas processing industry. The removal of CO_2 by alkanolamines absorption process is the most frequently used process around the globe. The conventional amines such as DEA and MDEA suffer with low CO_2 loading capacity and high heat of regeneration. Recently, sterically hindered amines are proposed as potential solvents for acid gas removal due to their unique cyclic structure, high CO_2 loadings and low heat of regeneration. The investigated solvent in this paper, 2-Amino-2-hydroxymethyl-1,3-propoanediol (AHPD) is a sterically hindered amine. The kinetic studies show that AHPD is a good potential solvent for CO_2 removal from various industrial streams.

The knowledge of equilibrium solubility data of such solvents is important to design acid gas removal system. The objective is to provide the CO_2 solubility data in aqueous solutions of AHPD at high pressures which can be helpful in designing of high pressure absorption systems. Therefore the solubility of CO_2 in aqueous solutions of AHPD is experimentally measured from 5 to 60 bar at three industrially important temperatures i.e. 303.15, 313.15 and 333.15 K. The effect of pressure is found to be positive on solubility as CO_2 loadings are higher at elevated pressures. The solubility data is also represented using Kent-Eisenberg model and a good agreement is found between model predicted values and experimental results.

Keywords: Global warming, Carbon dioxide, sterically hindered amines, Solubility, High Pressure.

Introduction

Alkanolamines are used for the removal of acid gases such as carbon dioxide (CO_2) and hydrogen sulphide (H_2S) in the process of different industrial gaseous streams through absorption process. The major sources of CO_2 emission include the burning of fossil fuels, coal fired power plants, oil refining, hydrogen production, several industrial processes and sweetening of natural gas.[3] Carbon dioxide (CO_2) is one of the green house gases that contribute to the global warming.[4] The most industrially used alkanolamines include; mono-ethanolamine (MEA), di-ethanolamine (DEA) and *N*-methyldiethanolamine (MDEA).[5] Recently, sterically hindered amines are proposed as potential solvents for acid gas removal due to their unique cyclic structure and high CO_2 loading capacities at low pressure.[1] The investigated solvent 2-Amino-2-hydroxymethyl-1,3-propoanediol (AHPD) is a sterically hindered amine.[2]

The solubility data and kinetic studies show that AHPD is a good potential solvent for acid gas removal from industrial streams of our interest.[6] The knowledge of equilibrium solubility data of such solvents is important to design acid gas removal systems.[10] This equilibrium data has significant importance for such systems as immense literature has been published within a decade.[8] Several researchers have reported the solubility data of aqueous solutions of AHPD.[7,9] The objective of this paper is to provide the solubility data of CO_2 in AHPD aqueous solutions at high pressures. Therefore in this research work, the solubility of aqueous solutions of AHPD is measured from 5 to 60 bar. The measurements are reported at three different temperatures 303.15. 313.15 and 333.15 K and for various AHPD concentrations.

Material and Methods

Materials: Carbon dioxide with a purity of 99.99 % was purchased from Malaysian Oxygen Behrad (MOX Gases) and AHPD of reagent grade (99.99 %) was purchased from Merck, Malaysia. The bi-distilled water was used to prepare aqueous solutions of AHPD. All the solutions were prepared gravimetrically using analytical balance (Mettler Toledo AS120S) within ± 0.0001 g.

Apparatus and Procedure: The solubility measurements were conducted in a high pressure solubility cell (SOLTEQ BP -22) shown in figure 1.[11] The set up consist of two vessels, pressurizing vessel (3 L) to raise the gas pressure up to 6000 kPa and equilibrium cell (50 mL) for solubility measurements.

Initially both vessels were purged with nitrogen and then mixing vessel was pressurized from 500 to 6000 kPa. The pressure of the system was measured using digital pressure indicator (Druck DPI 150) with a precision of ± 1.0 kPa for a range of 0 kPa to 10,000 kPa. The temperature of the system was controlled by thermostat water bath Julabo by ± 0.1 ^{o}C and the inside temperature of mixing vessel and

solubility cell was measured with Yokogava (7653) digital thermometer with an accuracy of ± 0.01 ^{o}C.

The solubility measurement method was similar as reported.[12.] Vacuum was created in equilibrium cell and 5 mL of the aqueous solution was introduced using metering pump. The temperature of the cell was then adjusted to the desired value and pressure was noted. At this stage, solvent exists under its own vapor pressure P_v. The CO_2 was transferred from mixing vessel to the equilibrium cell and the stirrer was turned on. The moles of CO_2 $_{nCO2}$ transferred were calculated using drop in pressure, volume of vessel and temperature by the following eq.:

$$n_{CO2} = \frac{V_T}{RT_a}\left(\frac{P_1}{z_1} - \frac{P_2}{z_2}\right) \quad (1)$$

where V_T is the volume of the gas container (mixing vessel), z_1 and z_2 are the compressibility factors for each pressure (P_1 and P_2), R is the real gas constant and T_a is the ambient temperature. The compressibility factors were calculated using Peng Robinson equation of state (EOS).[12] When there was no further drop in pressure inside equilibrium cell indicating thermodynamic equilibrium is achieved, pressure value was recorded. The equilibrium pressure (P_{CO2}) was calculated by the following eq.:

$$P_{CO_2} = P_T - P_V \quad (2)$$

where P_T represents the total pressure and Pv represents vapor pressure of solutions. The remaining moles of CO_2 in the gas phase n^g were calculated by equilibrium pressure (P_{CO2}), temperature and overhead gas volume by using the following eq.:

$$n^g_{CO_2} = \frac{V_g P_{CO_2}}{Z_{CO_2} RT} \quad (3)$$

where V_g is the gas volume in the equilibrium cell and T is the operating temperature. The moles of CO_2 in the liquid phase were then calculated from:

$$n^l_{CO2} = n_{CO_2} - n^g_{CO2} \quad (4)$$

The solubility was then calculated as mol of CO_2 per mol of amine by using the following equation:

$$\alpha = \frac{n^l_{CO_2}}{n_{AM}} \quad (5)$$

where n_{AM} represents the moles of AHPD in the liquid and calculated by the following eq.:

$$n_{AM} = \frac{\rho V_l m_{AHPD}}{M_{AHPD}} \quad (6)$$

where ρ is the density of the aqueous solution of AHPD, V_l is the liquid volume in the cell, m_{AHPD} is the mass fraction of AHPD and M_{AHPD} is the molecular weight of AHPD.

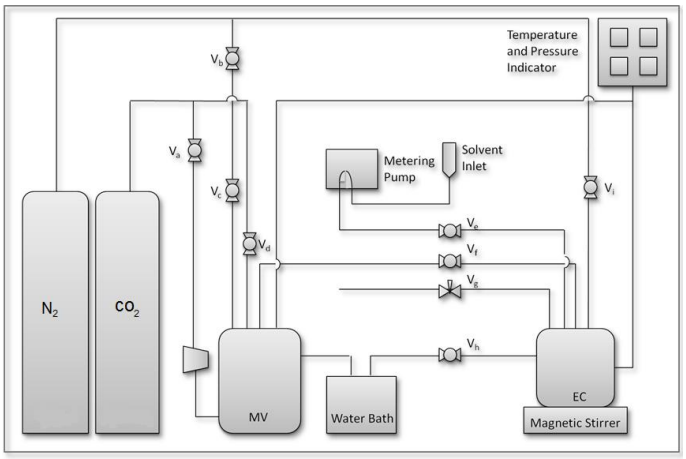

Figure 1: High pressure solubility cell

Results and Discussion

To validate the experimental method and solubility data, the solubility of 10 mass % AHPD aqueous solutions at 323.15 K was measured and compared with the literature. These results along with the literature[7] values are presented in table 1. The measured data was in good agreement with the literature with average absolute deviation (AAD) of less than 3 %. The AAD was calculated using the following eq.:

$$\%AAD = \frac{1}{n}\sum\left|\frac{X_{exptl} - Y_{lit.}}{Y_{lit.}}\right| * 100 \quad (7)$$

where n is the number of data points, X_{exptl} is measured physical property and Y_{lit} is physical property value from literature.

Table 1
Solubility of CO_2 in 10 % mass AHPD and comparison with literature

Park and Lee		Present work	
P/kPa	**A**	**P/kPa**	**α**
127.3	0.749	151.5	0.896
167.6	0.918	345.6	0.974
342.8	0.992	610.3	1.101
602	1.12	1045	1.113
1052.2	1.21	1500	1.271
1506.6	1.286	1985	1.385

The solubility of CO_2 in aqueous solutions of AHPD with concentrations (13, 19, 25) wt% was experimentally measured for a wide range of pressure at three important temperatures of industrial interests i.e. 303.15 K, 313.15 K and 333.15 K and the results were modeled using Kent-

Eisenberg approach. The overall reaction of CO_2 with AHPD can be explained through the following equation:

$$AHPD + CO_2 + H_2O \leftrightarrow AMPH^+ + HCO_3^- \quad (8)$$

The above equation shows that hydrolysis of carbamates enhances the formation of bicarbonate ion species and consequently releases free amine to absorb more CO_2.[9] The solubility increases with increasing pressure up to a certain point i.e. up to 30 bar and then curve gets steeper which shows that saturation point is achieved and no more CO_2 can be absorbed as shown in figures 2 (a, b) and 3 respectively. However, the relatively higher increase in CO_2 loading after increasing pressure shows that CO_2 was absorbed initially as a result of chemical reaction between aqueous solutions of AHPD (AHPD+water).

The following reaction mechanism of aqueous solutions of AHPD with CO_2 was considered to model the solubility data:

$$RNH_3^+ \xleftrightarrow{K_1} H^+ + RNH_2 \quad (9)$$

$$H_2O + CO_2 \xleftrightarrow{K_3} H^+ + HCO_3^- \quad (10)$$

$$HCO_3^- \xleftrightarrow{K_5} H^+ + CO_3^{-2} \quad (11)$$

$$H_2O \xleftrightarrow{K_4} H^+ + OH^- \quad (12)$$

Equation 9 represents the amine protonation reaction where free amines are released to attract more CO_2 molecules. Formation and dissociation of bicarbonates is represented by equations 10 and 11 respectively. Hydrolysis of water is represented by equation 12. The physical solubility of CO_2 in aqueous solutions of AHPD is represented by Henry's Law:

$$P_{CO_2} = H_{CO_2}[CO_2] \quad (13)$$

where P_{CO_2} represents the partial pressure of CO_2 in the gas phase and H_{CO_2} is the Henry's law constant respectively. In addition to the above equations, the material and charge balance holding on above equations is presented:

$$[AMP] = [RNH_2] + [RNH_3^+] \quad (14)$$

$$\alpha[AMP] = [CO_2] + [HCO_3^-] + [CO_3^{-2}] \quad (15)$$

$$[RNH_3^+] + [H^+] = [OH^-] + [HCO_3^-] + 2[CO_3^{-2}] \quad (16)$$

where α represents the CO_2 loading per mole of amine and [AMP]. All above equations were solved simultaneously for CO_2 loading (α) and equilibrium constant values (k) were calculated by applying Kent and Eisenberg correlations[14] and the error was minimized using the following loop:

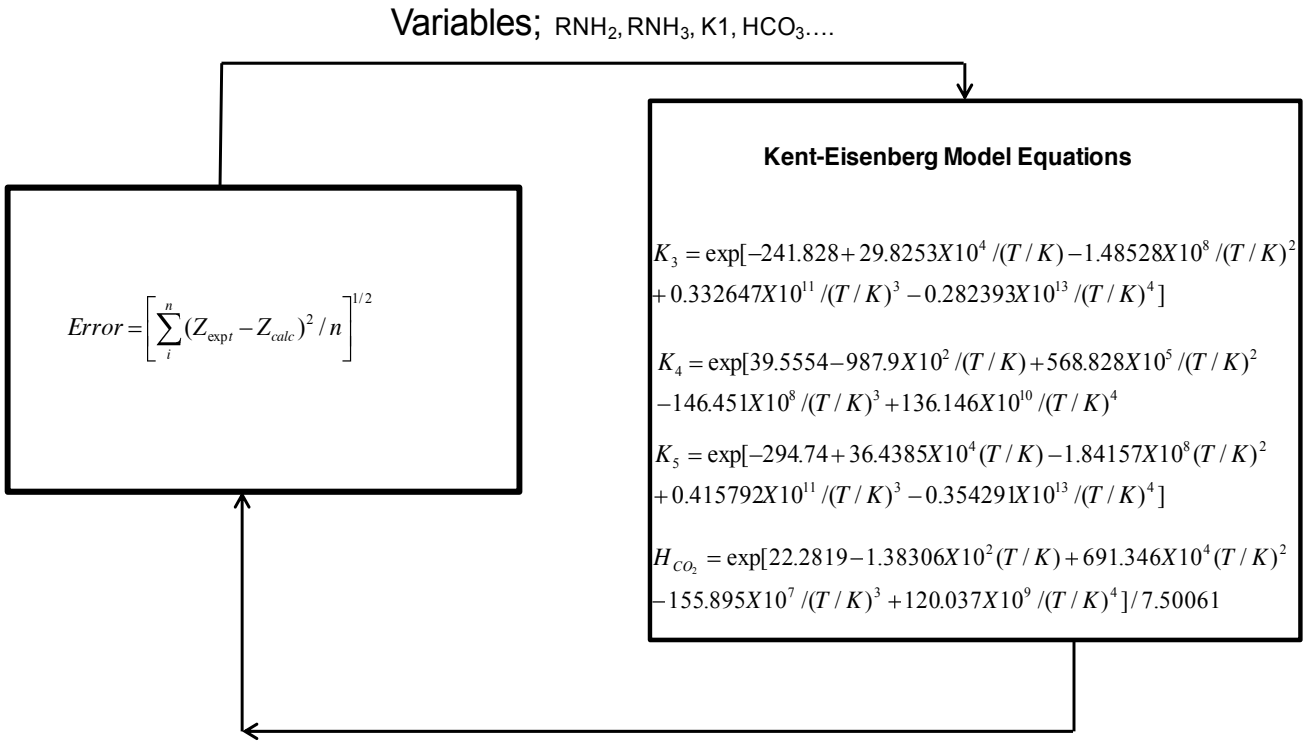

Schematic representation of solubility modeling

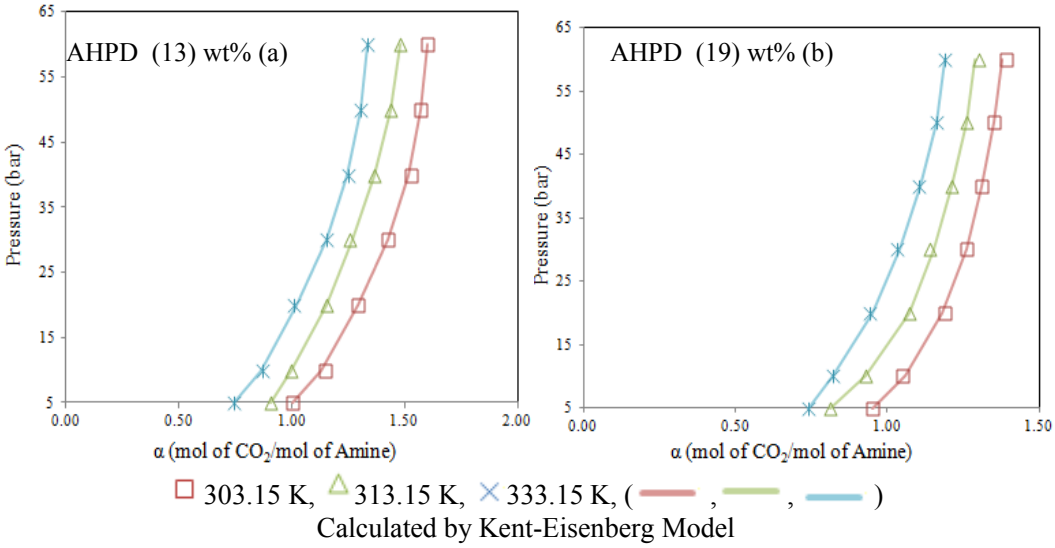

Figure 2: Solubility of CO_2 in aqueous solutions of AHPD at various temperatures

Using these parameters, the solubility was calculated by solving above equations by MATLAB fmincon function. The solid lines in the figures (2 to 4) show the results calculated by model at various temperatures.

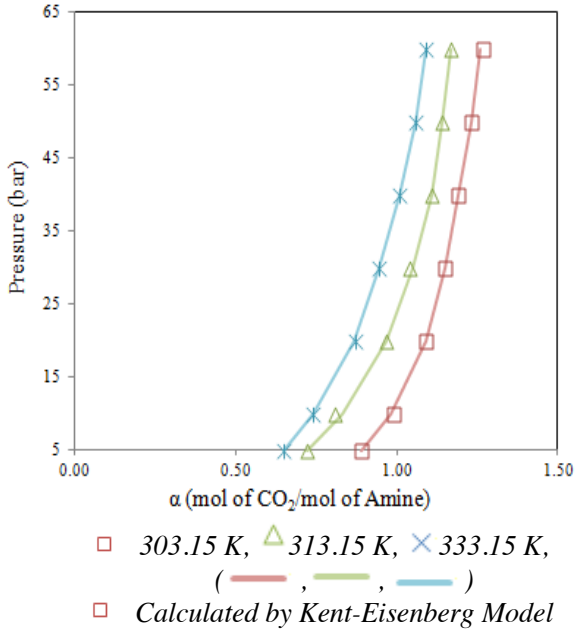

Figure 3: Solubility of CO_2 in aqueous solutions of AHPD (25) wt% at various temperatures

Moreover, temperature has shown the decreasing trend on solubility loading i.e. by increasing temperature, CO_2 loading tends to decrease which could be due to higher vapor pressure of solvents at higher temperatures as shown in figure 4. There were few solubility studies reported in literature and most of the work was conducted from lower to moderate range of pressure conditions. The following figure 5 shows the comparison between this work and Bougie et al work[6].

Although the concentrations of aqueous solutions of AHPD are different but the trend of CO_2 loading is similar i.e. by increasing pressure the loading capacity of solvents increases which could be associated with the physical solubility of CO_2 at higher pressure ranges. This is also shown that at the loading capacity of 25 wt % aqueous solution of AHPD is higher than of 30 wt % which is in agreement with the fact that at higher concentrations, loading capacity of solvents decreases due to higher viscosity or due to the lesser formation of bicarbonate species i.e. hydrolysis of carbamates.

Conclusion

Solubility measurements of CO_2 in aqueous solutions were experimentally conducted over a wide range of pressure from lower to elevated range in order to cover most of the CO_2 processing plants. There were three concentrations of aqueous solutions of AHPD considered for three temperatures at which the absorber is normally operated.

It has been found that at the high pressure sterically hindered amine (AHPD) gives better CO_2 loadings which could be helpful in capturing CO_2 from high pressure gaseous streams without reducing the pressure to the downstream process.

However, at higher temperatures and concentrations CO_2 loadings trend to decrease due to higher vapor pressure of solvents and possible evaporation of aqueous solutions. The model (Kent Eisenberg) calculated CO_2 loading values also show good agreement with the experimental data which can be useful to predict the CO_2 loadings at any operating conditions. The findings can be useful in the development of high pressure CO_2 removal absorption processes for better CO_2 capture and to minimize the emissions.

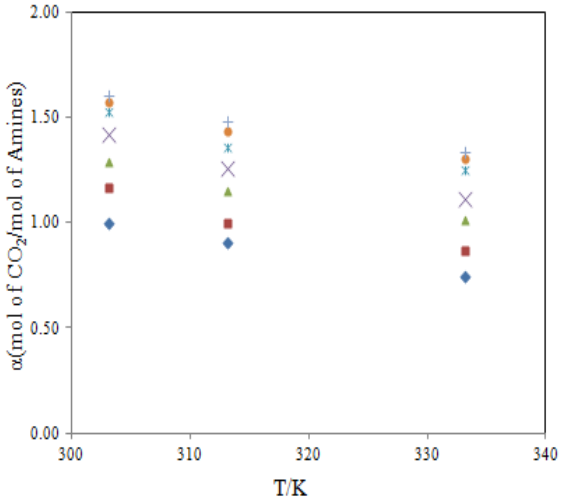

◆ *5 bar,* ■ *10 bar,* ▲ *20 bar,* × *30 bar,*
✳ *40 bar, 50 bar,* + *60 bar*

Figure 4: Effect of temperature on CO_2 loadings at all pressures

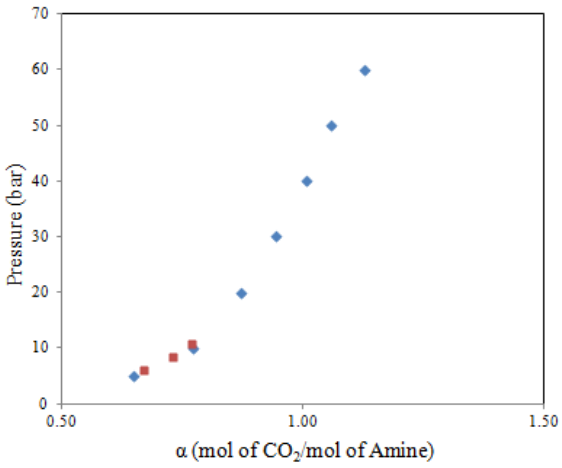

■ *Bougie et al*[6] *(30 wt%).,*
◆ *This work(25 wt%)*

Figure 5: Comparison of Solubility data

References

1. Paul S. and Mandal B., Density and Viscosity of Aqueous Solutions of (2-Piperidineethanol + Piperazine) from (288 to 333) K and Surface Tension of Aqueous Solutions of (N-Methyldiethanolamine + Piperazine), (2-Amino-2-methyl-1-propanol + Piperazine) and (2-Piperidineethanol + Piperazine) from (293 to 323) K, *Journal of Chemical & Engineering Data*, **51**, 2242-2245 **(2006)**

2. Sartori G. and Savage D.W., Sterically hindered amines for carbon dioxide removal from gases., *Industrial and Engineering Chemistry Fundamentals*, **22**, 239-249 **(1983)**

3. Puraba E. and Taharuddin T., CO_2 reduction using microalgae nanochloropsis oculata and Production of oil algae, *Chemical Engineering Transactions*, **21**, 397-402 **(2010)**

4. Gomez Castro F., Rico Ramirez V., Segovia Hernandez J. G. and Hernandez Castro S., Reducing costs and CO_2 emissions on the production of biodiesel by the super critical methanol method, *Chemical Engineering Transactions*, **19**, 143-148 **(2010)**

5. Collodi G. and Wheeler F., Hydrogen production via steam reforming with CO2 capture, *Chemical Engineering Transactions*, **19**, 37-42 **(2010)**

6. Bougie F. and Iliuta M. C., CO_2 Absorption into Mixed Aqueous Solutions of 2-Amino-2-hydroxymethyl-1,3-propanediol and Piperazine, *Industrial Engineering Chemistry and Research*, **49(3)**, 1150-1159 **(2010)**

7. Park J.Y., Yoon S. J. and Lee H., Density, Viscosity and Solubility of CO_2 in Aqueous Solutions of 2-Amino-2-hydroxymethyl-1,3- propanediol, *Journal of Chemical and Engineering Data*, **47**, 970-973 **(2002)**

8. Sairi N.A., Yusoff R., Alias Y. and Aruoa M. K., Solubilities of CO_2 in aqueous N-methyldiethanolamine and guanidinium trifluoromethanesulfonate ionic liquid systems at elevated pressures, *Fluid Phase Equilibria*, **300**, 89-94**(2011)**

9. Park J.Y., Yoon S.J. and Lee H., Effect of Steric Hindrance on Carbon Dioxide Absorption into New Amine Solutions: Thermodynamic and Spectroscopic Verification through Solubility and NMR Analysis, *Environmental Science and Technology*, **37**, 1670-1675 **(2003)**

10. Tourneux Le, Iliuta D. L., Iliuta M.C., Fradette S. and Larachi F., Solubility of carbon dioxide in aqueous solutions of 2-amino-2-hydroxymethyl-1,3-propanediol, *Fluid Phase Equilibria*, **268**, 121-129 **(2008)**

11. Harris F., Kurnia A. K., Mutalib M. I. and Thanapalan M., Solubilities of Carbon Dioxide and Densities of Aqueous Sodium Glycinate Solutions before and after CO2 Absorption. *Journal of Chemical and Engineering Data*, **54**, 144-147**(2008)**

12. Jenab H. M., Abdi M. A., Najibi S. H., Vahidi M. and Matin N. S., Solubility of Carbon Dioxide in Aqueous Mixtures of N-Methyldiethanolamine + Piperazine + Sulfolane, *Journal of Chemical and Engineering Data*, **50**, 583-586 **(2005)**

13. Chakraborty A.K., Astarita G. and Bischoff K.B., CO_2 absorption in aqueous solutions of hindered amines, *Chemical Engineering Science*, **41**, 997-1003 **(1986)**

14. Hu W. and Chakma A., Modelling of equilibrium solubility of CO_2 and H_2S in aqueous diglycolamine (DGA) solutions, *The Canadian Journal of Chemical Engineering*, **68**, 523-525 **(1990).**

(Received 19th April 2013, accepted 22nd July 2013)

Extraction of Rubber (*Hevea brasiliensis*) Seed Oil using Supercritical Carbon Dioxide and Soxhlet Extraction

Nian-Yian Lee [1], Siti Hamidah Mohd-Setapar[1 *], Nur Syahirah Mohd Sharif [1], Che Yunus Mohd Azizi[1] and Muhamad Ida-Idayu[2]

1. Centre of Lipid Engineering and Applied Research (CLEAR), Department of Chemical Engineering, Faculty of Chemical Engineering, Universiti Teknologi Malaysia 81310 Skudai, Johor, MALAYSIA
2. Department of Bioprocess Engineering, Faculty of Chemical Engineering, Universiti Teknologi Malaysia 81310 Skudai, Johor, MALAYSIA
*sitihamidah@cheme.utm.my

Abstract

This study involved the extraction of rubber (Hevea brasiliensis) seed oil using supercritical carbon dioxide (SC-CO_2) and Soxhlet techniques. The main aim of this study is to compare the extraction method between SC-CO_2 and Soxhlet extraction. The arrays of operating parameters for supercritical carbon dioxide are temperature and pressure conducted at 40°C, 60°C and 80°C and 20MPa, 25MPa and 30MPa respectively. The extraction was also processed under dynamic condition of 180min and carbon dioxide at constant flow rate of 4mL/min. The parameters studied for Soxhlet extraction are due to different solvents and extraction time.

Observation was done on the physical characteristics of oil obtained by these two methods where the oil obtained by SC-CO_2 was clean with pleasant smell while the oil produced by Soxhlet method was near to brownish color with white when extracted with polar solvents. The experiment results showed that the extraction of rubber seed oil by SC-CO_2 and Soxhlet extraction gave 33.652% g and 7-12% g respectively. In addition, the extraction time of SC-CO_2 is also shorter than Soxhlet extraction that needs the further process to evaporate solvent. This finding proves that the rubber seed oil produced by SC-CO2 has superior characteristics and better quality compared to Soxhlet extraction.

Keywords: Rubber seed oil, supercritical carbon dioxide, Soxhlet extraction.

Introduction

Rubber scientifically known as *Hevea brasiliensis* was initially cultivated at Amazon Rainforest but now mostly the plantation of rubber is in South and Southeast Asia. Malaysia has an estimated average of 1,229,940 hectares of rubber plantation in 2007 according to the report of Malaysian Rubber Board on 2009. There are ongoing researches developed to dismantle this major asset of Malaysia for its maximum utility as it is known to be very beneficial and profitable crop. In addition, ruber tree is also being applied in many industries such as furniture manufacturing. The most important use of rubber tree is the production of latex which had been modified and improved for many years to be used widely in industry.

As reported by several researches[1-3], rubber seed oil had shown its potential in oleochemical applications in paints, surface coatings, soap, alternative to diesel[4] and vulcanized vegetable oil production[2]. Rubber seed oil contains about 40-50% of oil[1, 4- 6]. Its high content of fats and protein can be consumed in human food and animal feed as well as in production of soap, cosmetics and biofuel[3]. Furthermore, the rubber seed has been fermented and is used in curries and condiments in Jerantut, Pahang in Malaysia[7]. Therefore, rubber seed had been found to have plenty of industrial potentials.

The most common method for the extraction of oilseeds is Soxhlet extraction while the solvent used is the organic solvent such as n-hexane or pentane. This extraction can be defined as transporting material from one phase to another for separation of one or more compounds from mixtures[8]. To date, n-hexane had been commercialized as a standard practice in industry. Most of this extraction is done in the Soxhlet extractor as shown in the figure 1. There are several factors which affect the oil yield like choices of solvent, extraction time, particle size, solid to solvent ratio, moisture content and temperature.

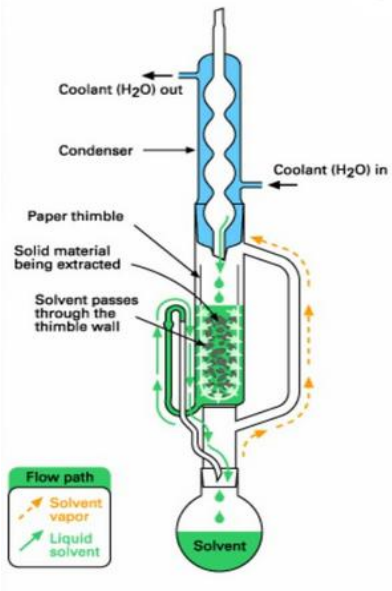

Figure 1: Soxhlet extractor used in the solvent extraction

It is important to make sure the safe and hygiene of the oil obtained. Moreover, million tons of chemical solvent had been used for this traditional extraction method in many industries causing pollution and environmental problems. The use of organic solvents will cause adverse effect to human health. Hence, it is significant to have the alternative method to extract the oilseeds. Supercritical carbon dioxide is one of the alternatives and attractive method to extract oilseeds because the solvent used which is carbon dioxide is generally recognized as safe to be used as a direct food ingredient and is regulated by the U.S. Food and Drug Administration [Code of Federal Regulation 21.184.1240 (C)][9]. In addition, there is no organic solvent residual inside the extracted sample since carbon dioxide is easier to be separated by decompression and also it has high recovery percentage. Therefore, supercritical carbon dioxide extraction can be applied in different industries.

In this study, the Supercritical 24 fluid extractor (SSI, State College Pennsylvania, US) was used to perform the supercritical carbon dioxide extraction experiments. This instrument had been implemented at the Centre of Lipid Engineering and Applied Research (CLEAR) laboratory. One of the components in this instrument is constant flow pump where the pressure can be set from 0 to 10,000 psi while the flow rate is 0.00 to 24.00 ml/min. The pump used is the high performance liquid chromatography (HPLC) pump because this type of pump can be modified easily for analytical and semi preparative techniques.

In addition, CLEAR supercritical carbon dioxide instrument also has the programmable back pressure regulator (Model BP-2080, JASCO, Japan) which controls the pressure by changing the time interval between valve opening and closing. Hence, extracted components are forced to push the valve and this can reduce the possibility of blocking of the flow pass. Therefore, the highly reproducible results can be obtained. The set up of supercritical carbon dioxide instrument in CLEAR laboratory is shown in the figure 2.

According to Floegel et al[10], antioxidant is described as the capability of redox molecules in foods and biological systems to scavenge free radicals. Antioxidants are divided into two groups which are primary and secondary group. Vitamin A, E, D, C and beta-carotene are generally classified as antioxidants. One of the most preferable methods is 2, 2-Diphenyl-1-Picrylhydrazyl (DPPH) in assay which DPPH is free radical. It is extensively used because DPPH reacts directly and rapidly with antioxidant compounds. This method measures the ability of an antioxidant compound to donate hydrogen, reducing or scavenging stable DPPH radicals to non-radicals[11]. The remaining DPPH radicals present in the sample will be measured by ultraviolet-visible (UV-VIS) spectrometer at 517nm.

The main objective of this study is to extract rubber (*Hevea brasiliensis*) seed oil by using supercritical carbon dioxide and Soxhlet extraction methods as well as to compare the characteristics and quality of the oil extracted using these both methods.

Material and Methods

Preparation of rubber seed sample: The fresh rubber (*Hevea brasiliensis*) seeds were obtained from Malaysia local company. The large quantity of rubber seeds had been purchased in order to make sure the profiling of the sample maintain the same throughout the experiment. First, the seeds were slightly crushed and separated from the shell to get the seeds. Then, the seeds were washed with tap water thoroughly. Next, the cleaned seeds were sliced to approximately the same size for drying. The seeds were dried at 105ºC ± 2ºC for 18 hours before grinding process.

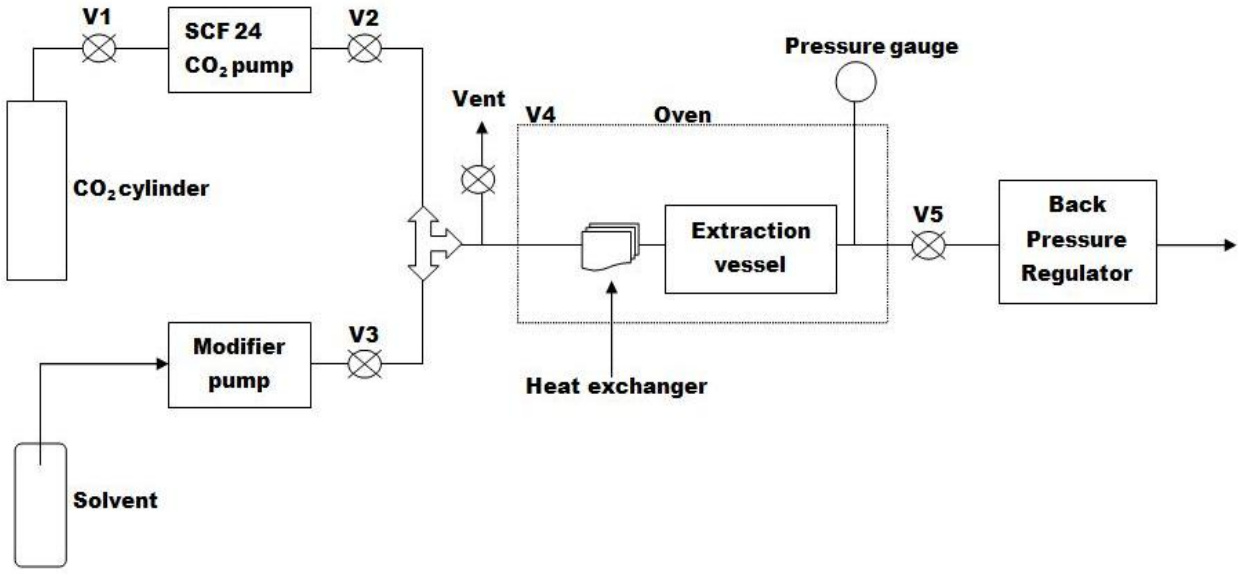

Figure 2: The schematic diagram of supercritical carbon dioxide instrument in CLEAR laboratory

The conventional sun drying is not suitable because the temperature is not consistent as oven drying, so drying is not uniform for all the samples. Then, the dried rubber seeds were ground to a fine powder using the blender (Philips) and sieved to a uniform particle size of 0.5mm. Lastly, the dried rubber seeds were kept in the air tight container and stored in the freezer at the temperature about -20°C to maintain the freshness of the seeds.

Supercritical carbon dioxide (SC-CO_2) extraction: In this extraction method, ground rubber seeds were put into the extraction vessel. The rubber seeds sample kept in the freezer had been put at the room temperature to make sure the trapped water vapor in the sample being released. Extraction is performed at range of temperature and pressure shown in the table 1. The amount of extracted oil obtained by supercritical carbon dioxide is calculated using direct measures of the extracted oil as shown below:

Percentage of overall extracted oil yield, % = (W_{oil}/W_s) x 100%

In this equation, the W_{oil} represents the weight of extracted oil in gram while W_s represents the weight of sample used in gram.

Table 1
The range of temperature and pressure for supercritical carbon dioxide extraction

Parameters	Unit	Range	Increment
Temperature, T	°C	$40 \leq T \leq 80$	$\Delta T = 20.00$
Pressure, P	MPa	$20 \leq P \leq 30$	$\Delta P = 5.00$

Soxhlet Extraction: 10g of the ground rubber seeds were transferred into a thimble and 150mL of solvent was poured into the round bottomed flask. Then, the Soxhlet's apparatus containing the sample and solvent was heated for a time interval using heating mantle. The oil was recovered from the solvent by evaporation of the solvent in a rotary vacuum evaporator under reduced pressure. In the experiment, there are different solvents used which are n-hexane, water, petroleum ether and ethanol: water (70:30, v:v). In addition, the extraction process was repeated using each proposed solvent for 4, 6 and 8 hours.

The mixture of the oil and excess solvent was poured into a weighed round bottomed flask. The flask was fitted to the rotary evaporator and immersed in the heating medium until all the mixture was totally immersed. The temperature of the rotary evaporator was set slightly above the boiling point of the solvent. Then, the mixture was rotated slowly to prevent the mixture to evaporate out from the instrument. The vacuum pump was switched on to suck the evaporated volatile solvent. After 30 minutes of evaporation, the heating system was switched off and left to cool down for another 30 minutes. Finally, the flask was weighed and the concentrated extract was taken out.

Antioxidant Analysis: In order to analyze the antioxidant inside the rubber seed oil, 0.025g of oil was diluted with 10mL of methanol in a 15mL sample bottle. Then, the required amount of 77µL of the diluted sample was pipette out into another sample bottle and 3mL of diluted 2, 2-Diphenyl-1-Picrylhydrazyl (DPPH) was added into the sample. The sample was triplicate and labeled followed by homogenization process and stored in a dark place for 30 minutes. Next, the samples were analyzed using Ultraviolet-Visible (UV-VIS) spectrometer at the wavelength of 517nm.

The scavenging activity represents the ability to inhibit the oxidation process. The expression of the percentage of scavenging activity is as below:

Scavenging Activity, % = $(1- A_E /A_D) \times 100$

In this equation, A_E represents the absorbance of the DPPH solution mix with the sample while A_D represents the absorbance of solution DPPH (control).

Results and Discussion

Physical Characteristics of Rubber (*Hevea brasiliensis*) Seed Oil: The rubber seed oil obtained by using supercritical carbon dioxide gives a very pleasant smell and the oil is the golden yellowish color even the extraction being done at different temperature and pressure.

However, the extraction by Soxhlet gives different physical characteristics based on the solvents used. The oils extracted using n-hexane and petroleum ether give golden-yellowish colour[5] with pleasant nut-like odor. Ultimately, no adverse observations were monitored from these two non-polar solvents.[12, 13]

On the other hand, the extracts of water and water: ethanol (70:30, v: v) were pale yellow in color at the first two cycles of Soxhlet extraction to dark brown at end of process. The white particles were also extracted together with the oil during the process. In some studies ethanol has the capability to co-extract other compounds in oilseeds which are insoluble in non-polar solvents[14-16] and this explains the different traits of the extracts. The oil extracted from water and ethanol: water (70:30, v: v) has unpleasant smell. According to Hron et al[15], water is a poor solvent for its immiscibility in oil. The proper grinding of seeds and pH of water used also affect the oil recovery as well as the appearance of the extracted oil[15].

Supercritical Carbon Dioxide (SC-CO_2) Extraction

Effect of temperature on the extraction yield: There is significant difference for the extraction yield between the temperature of 80°C and another temperature chosen. At highest temperature of 80°C at constant operating pressure of 30MPa as shown in the figure 3, the oil yield is the lowest which is 26.736% g oil/sample followed by 27.072% and 33.562% g oil/sample at 40°C and 60°C

respectively. Moreover, the extraction also shows the highest value of 9.778% g oil/sample at 60°C while 80°C give the lowest yield of 1.746% g oil/sample at the low operating pressure condition. Therefore, this finding shows that 60°C is more effective to extract the rubber seed oil. This is because at the constant pressure, the increasing of temperature will reduce the density of the supercritical fluid and will lead to the reduction of the supercritical fluid solvency power.

In addition, the diffusion of the compound into the solvent in fluid phase becomes favorable due to the increase of the vapor pressure of the compound to be extracted. The solubility is affected by two factors which are the solvating effect and the volatility of the solute. Therefore, increasing the temperature resulting in the maximum solubility of the solute in the fluid increases the oil yield. Furthermore, the temperature of the extraction should be controlled to prevent the structure alteration of the interest compound and the risk of being destroyed at high temperature. In fact the result is considered acceptable because in the study of the extraction of antioxidants from sweet Thai tamarind, the oil yield decreased when the temperature is being increased from 40°C to 80°C[17].

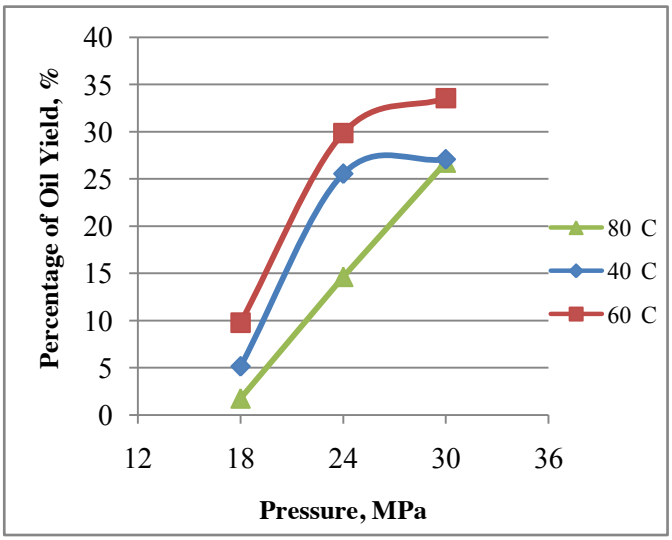

Figure 3: The effect of temperature at constant pressure on extraction yield

Effect of operating pressure on the extraction yield: In the figure 4, it shows that increasing the operating pressure results in the increase of oil yield obtained. The extraction oil yield increases from 9.778% to 33.562% g oil/sample when pressure increases from 20MPa to 30MPa at constant temperature of 60°C while the flow rate was fixed at 4mL/min and the experiment was performed using dynamic extraction. In fact, many studies showed that increasing pressure will increase the extraction yield. In the research of Peretti et al[18], highest yield of 4.93g of rice bran oil (24.65%) was given when the extraction was conducted at 68.96MPa in order to improve the value of rice. In addition, the extraction of vernolic acid (ranging from 48.5 to 56.8%) is higher at 34.5MPa extraction pressure than those found in the 13.8MPa extracts[19].

The reason is the solvent density is being increased when the operating pressure is increased resulting in greater solvating power causing higher solubility of oil. Hence, more oil will be transported to the surface of the seeds giving higher oil yield. When increasing the operating pressure in this study, carbon dioxide which acts as the solvent can dissolve the oil at the surface of the seeds easily because high pressure favours the transport of oil to the surface of seeds. Furthermore, extraction will be considered achieving equilibrium when the surface of the seeds is concentrated with oil thus limiting the mass transfer of the oil. Therefore, the concentration of the oil in the supercritical fluid will remain constant.

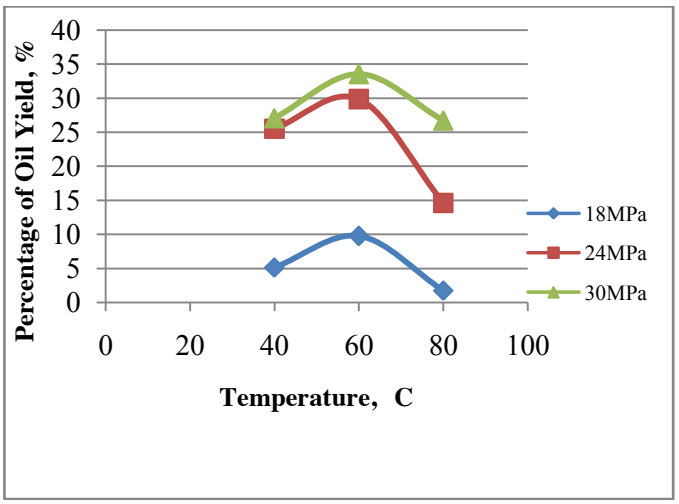

Figure 4: The behavior of pressure of its effect on extraction yield

Soxhlet Extraction

Effect of solvents used on oil yield: Based on the figure 5, it can be obviously seen that using n-hexane and petroleum ether gave a higher oil yield than conducting solvent extraction using water and a mixture of ethanol: water (70:30, v: v). The yield from both n-hexane and petroleum ether extracts was in close agreement to 40-50% oil content in rubber seed oil in literature[3, 4, 20, 21]. This obvious gap explains the polarity theory of solvent and oilseeds in solvent extraction. Since the polar lipid dissolves and is soluble in polar solvent, it can be said that rubber seed oil is a non-polar lipid[22]. This is because water is known to be universal solvent and ethanol: water has high polarity, where both are immiscible in oil[15]. This explains the 10-18% yield of rubber seed oil using these polar solvents.

Although the oil is reported to be soluble in ethanol at its boiling point, but it decreases with the decreasing of alcohol concentration in the presence of water[15]. Since the mixture of ethanol: water is 70:30 by volume, the solvent gradually inherits the characteristics of water, resulting in low oil yield. Furthermore, the differences in dielectric constant of solvent also give the effect to the oil yield obtained. This is because the solubility of solvent in oil

decreases with the increasing dielectric constant value, thus increasing its polarity. In this study, the dielectric constant values of the solvents used which are n-hexane, petroleum ether, water and ethanol:water are 1.8, 2.0, 80 and 24.3 respectively. In addition, solid to solvent ratio will give effect on the oil yield because the concentration gradient between the solid and liquid phase becomes greater and this favours the mass transfer to occur easily. Hence, increasing the solid to solvent ratio will also increase the oil yield.

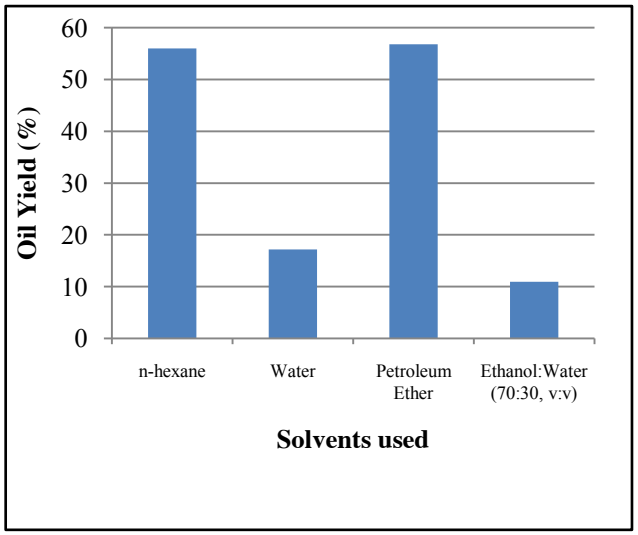

Figure 5: The effect of solvents used on oil yield using Soxhlet method

Effect of extraction time on oil yield: In this research, the Soxhlet extraction of rubber seed oil was performed at different time frame which are 4, 6 and 8 hours to examine the effect of extraction on oil yield. Based on the figure 6 shown, the maximum oil yields produced by four different solvents are at 6 hours of extraction. It can be observed that the extraction using petroleum ether gave the highest oil yield at 56% whole mixture of water and ethanol only gave 7-12% of oil yield. The amount of oil yield extracted using non-polar solvents which are water and ethanol does not change significantly after 6 hours in the study of Jatropha seed extraction by Sayyar et al[23]. The rubber seed oil can be said to be fully extracted from the seed after 6 hours although the maximum oil yield was achieved only after 8 hours. The best duration of extraction is 6 hours because the diffusion rate is decreasing when the concentration of oil is increasing. Therefore, when the maximum amount of extractable oil is achieved, even extending the reaction time will not cause any effect on the oil yield obtained.

Antioxidant activity: The antioxidant capacity value of rubber seed oil is -21.3×10^{-2}% which is the highest among the extraction. This result indicates that the overall antioxidant capacity of the rubber seed oil is very low or none. This is during the pre-treatment process, the rubber seed being dried at 105°C which may destroy the antioxidant inside the seed. The antioxidant component such as Vitamin E and beta-carotene may get destroyed by prolonged heating and become inactive, therefore there is negative result of the antioxidant capacity.

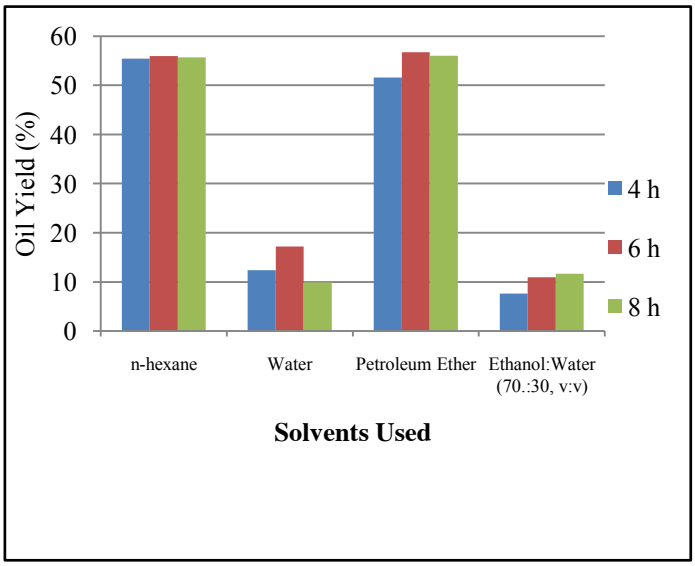

Figure 6: The effect of extraction time on oil yield using Soxhlet method

Comparison of SC-CO_2 and Soxhlet method: Soxhlet is the most common and traditional method used for extraction of oilseeds in industry. Meanwhile, the green technology SC-CO_2 extraction is not widely applied nowadays. In this research, the extraction of rubber seed oil is done by using different solvents by Soxhlet method while carbon dioxide is used as the solvent in SC-CO_2 extraction. The extraction using mixture of water and ethanol which is generally regarded as safe (GRAS) which is 7-12% of oil yield compared to the extraction using SC-CO_2 is about 33.562% of oil yield at operating pressure of 30MPa and 60°C. The efficiency of the method is that the density of the supercritical fluid is higher than the chemical solvent. In addition, the characteristics of diffusivity and viscosity of the supercritical fluid enable it to penetrate faster and deeper than a liquid into the oilseeds containing the components to be extracted.

Besides that, the extraction time of SC-CO_2 is shorter compared to Soxhlet method which is 3 hours and 8 hours respectively. In addition, the extraction using Soxhlet method required further process and time to evaporate the chemical solvent from the extract. Therefore, Soxhlet required more energy and is very time consuming.

Furthermore, the physical characteristics of the oil extracted using SC-CO_2 and Soxhlet method are different. Therefore, the difference in term of quality is very obvious. This is because the properties of selectivity of the supercritical fluid cause the final extract free from pigments compared to Soxhlet extraction. Lastly, the extract of SC-CO_2 has very pleasant smell because the extract is free from chemical solvent and is pure and clean.

Conclusion

The supercritical carbon dioxide (SC-CO_2) which is known as green technology is used to extract the rubber (*Hevea brasiliensis*) seed oil. In addition, the traditional Soxhlet is also used to perform the extraction experiments. From the results, the oil yield obtained from the Soxhlet method using petroleum ether is 56% oil/sample while the mixture of water and ethanol only produces 7-12% g oil/sample. Meanwhile, the extraction using supercritical carbon dioxide, the highest oil yield is 33.562% g oil/sample at the pressure of 30MPa and 60°C.

However, petroleum ether will cause adverse effect to human and pollution while the carbon dioxide is inert, non-flammable and also suitable for food consumption. In addition, the extract of supercritical carbon dioxide is of better quality, free from solvent, pleasant odor and is pure. Furthermore, the extraction time of supercritical carbon dioxide is shorter than Soxhlet method, thus it can save time and cost. The extract of rubber seed oil contains many valuable compounds such as omega-3 fatty acids and the high content of oil inside the seeds can be applied into different industries such as food, pharmaceutical, oleochemical and cosmetics.

Acknowledgement

The authors gratefully acknowledge the Centre of Lipid Engineering and Applied Research (CLEAR) and also Universiti Teknologi Malaysia, Johor for the laboratory experiment and instruments provided. Acknowledgement is also extended to Malaysia Government (Escience Fund) Vot 4S020 for the financial support.

References

1. Abdullah B.M. and Salimon J., Physicochemical Characteristics of Malaysian Rubber (*Hevea Brasiliensis*) Seed Oil, *European Journal of Scientific Research*, **31(3)**, 437-445 **(2009)**

2. Ebewele R. O., Iyayi A. F. and Hymore F. K., Considerations of The Extraction Process and Potential Technical Applications of Nigerian Rubber Seed Oil, *International Journal of the Physical Sciences*, **5(6)**, 826-831 **(2010)**

3. Eka H. D., Tajul Aris Y. and Wan Nadiah W. A., Potential Use of Malaysian Rubber (*Hevea Brasiliensis*) Seed as Food, Feed and Biofuel, *International Food Research Journal*, **17**, 527-534 **(2010)**

4. Ramadhas A.S., Jayaraj S. and Muraleedharan C., Biodiesel Production from High FFA Rubber Seed Oil, *Fuel*, **84**, 335-340 **(2004)**

5. Ikwuagwu O. E., Ononogbu I. C. and Njoku O. U., Production of Biodiesel Using Rubber [*Hevea Brasiliensis* (Kunth. Muell.)] Seed Oil, *Industrial Crops and* Products, **12**, 57-62 **(2000)**

6. Morshed M., Ferdous K., Khan M. R., Mazumder M.S.I., Islam M.A. and Uddin Md.T., Rubber Seed Oil As a Potential Source for Biodiesel Production in Bangladesh, *Fuel*, **90**, 2981 **(2011)**

7. Mohd-Setapar S.H., Nian-Yian L. and Mohd-Sharif N.S., Extraction of Rubber (*Hevea brasiliensis*) Seed Oil Using Soxhlet Method, Proceeding Regional Annual Fundamental Science Symposium **(2012)**

8. Johnson L. A. and Lusas E.W., Comparison of Alternative Solvents for Oils Extraction, *Journal of the American Oil Chemists' Society*, **60(2)**, 229-242 **(1983)**

9. Taylor L.T., Supercritical Fluid Extraction, A Willey-Interscience, United States of America, 155 **(1996)**

10. Floegel A., Kim D., Chung S., Koo S. and Chun O. K., Comparison of ABTS/DPPH Assays to Measure Antioxidant Capacity in Popular Antioxidant-Rich US Foods, *Journal of Food Composition and Analysis*, **24**, 1043-1048 **(2011)**

11. Wei A. and Shibamoto T., Antioxidant Activities and Volatile Constituents of Various Essential Oils, *Journal of Agricultural and Food Chemistry*, **55**, 1737-1742 **(2007)**

12. Iyayi A. F., Akpaka P. O. and Ukpeoyibo U., Rubber Seed Processing for Value-Added Latex Production in Nigeria, *African Journal of Agricultural Research*, **3(7)**, 505-509 **(2008)**

13. Njoku O. U., Ononogbu I. C. and Eneh F. U., Measurement of Lipase Activity in Rubber (*Hevea brasiliensis*) Seed, *Journal of the American Oil Chemists'* Society, **73**, 1471-1473 **(1996)**

14. Sharma M. and Ganguly M., Shaddock (Citrus grandis) seed oil as an alternative feedstock for the production of biodiesel, *Res. J. Chem. Environ.* **14(3)**, **(2010)**

15. Hron R. J., Koltun S. P. and Graci A. V., Biorenewable Solvents for Vegetable Oil Extraction, *Journal of the American Oil Chemists' Society*, **57(9)**, 674A-684A **(1982)**

16. Hron R. J., Kuk M. S., Abraham G. and Wan P. J., Ethanol Extraction of Oil, Gossypol and Aflatoxin from Cottonseed, *Journal of the American Oil Chemists' Society*, **71(4)**, 417-421 **(1994)**

17. Luengthanaphol S., Mongkholkhajornslip D., Douglas S., Douglas P., Pengsopa L. and Pongamphai S., Extraction of antioxidant from sweet Thai tamarind seed coat-preliminary experiments, *J. Food Engineering*, **63**, 247-252 **(2004)**

18. Perretti G., Miniati E., Montanari L. and Fantozzi P., Improving the value of rice by products by supercritical fluid extraction, *J. of Supercritical Fluids*, **26**, 1-9 **(2003)**

19. King J.W., Mohamed A., Taylor S.L., Mebrahtu T. and Paul C., Supercritical fluid extraction of *Vernonia galamensis* seeds, *Industrial Crops and Products*, **14**, 241-249 **(2001)**

20. Attah J.C. and Ibemesi J.A., Solvent Extraction of the Oils of Rubber, Melon, Pumpkin and Oilbean Seeds, *Journal of the American Oil Chemists' Society*, **67(1)**, 25-27 **(1990)**

21. Gandhi V.M., Cherian K.M. and Mulky M.J., Nutritional and Toxicological Evaluation of Rubber Seed Oil, *Journal of the American Oil Chemists' Society*, **67(11)**, 883-886 **(1990)**

22. Wildan A., Ingrid A. D. and Hartati I., Oil Extraction Process

from Solid Waste Rubber Seed by Soxhletation and Extraction Solvent by Stirring Methods, International Conference on Chemical and Material Engineering, 1-4 **(2012)**

23. Sayyar S., Zainal A., Z., Yunus R. and Muhammad A., Extraction of Oil from Jatropha Seeds-Optimization and Kinetics, *American Journal of Applied Sciences*, **6(7)**, 1390-1395 **(2009)**

(Received 28th March 2013, accepted 12th July 2013)

Synthesis and characterization of Dental Nanocomposite based on Hydroxyl Apatite/ZnO-MgO by Ultrasonic Method

Khani Arezoo Mohamad[1*], Farhadyar Nazanin [1,2] and Soltanian Mohamad Jafar[1]
1. Department of Chemistry, Firoozabad , Islamic Azad University, Firoozabad, IRAN
2. Department of Chemistry,Varamin –pishva Branch , Islamic Azad University, Varamin, IRAN
*nfarhadyar@gmail.com

Abstract
Hydroxyapatite ($Ca_{10}(PO_4)_6(OH)_2$, HA), is close to that of bone and this teeth mineral is commonly used as a dental nanocomposite due to its biological properties. In this work, Hydroxyapatite (HAp) crystals were prepared via an in situ biomimetic process in the presence of polyviny l pyrrolidone. The hydroxya-patite, HAP nanoparticles were prepared using $CaCl_2$ and KH_2PO_4 in the presence of polyviny l pyrrolidone (PVP). In an aqueous solution. ZnO -MgO were obtained with particle sizes of 30–50 by the reaction of $Zn(CHCOO_3)_2$ and $Mg(CHCOO_3)_2$ in the presence of HA-PVP. Characterization was performed using X-ray diffraction (XRD), Scanning electron microscopy (SEM) and Fourier transform infrared spectroscopy (FT-IR). The characterisation results indicate that PVP has been appended to the nano HAP forming regular crystals of nano sized HAP.

Keywords: Nanocomposite, PVP-HA, Dental composite, MgO-ZnO.

Introduction

The combination of polymers with nano-materials displays novel and often enhanced properties compared to the traditional materials. In recent years, researchers have focused more on the nanocomposite due to their applications in advanced technologies. The metal oxides are extremely important technological materials for use in active materials of dental nanocomposite and ceramic. The use of ceramics can be dated back to 19th century. Nowadays, the commonly used bioceramics are metallic oxides (e.g. Al_2O_3, MgO), calcium phosphate [e.g. hydroxyapatite (HA), tricalcium phosphate (TCP), octacalcium phosphate (OCP)] and glass ceramics (e.g. Bioglass, Ceravital).

Among the bioactive ceramics, synthetic hydroxyapatite with a chemical composition $Ca_{10}(PO_4)_6(OH)_2$ has been extensively studied as a bone replacement and nanocomposite dental material. Some of the more recent attempts in the in situ technique have made use of polymeric additives such as poly (lactic acid) (PLA), poly (acrylic acid) (PAAc), collagen and gelatin due to their calcium binding properties[1-6]. Another polar polymer with potential biomedical application is poly (vinyl alcohol) (PVA) or incorporating various fillers into the zinc-containing powder using aluminium compounds, silicon dioxide[7], magnesium oxide[8] etc. According to the literature[9], ZnO is very popular in the daily dental practice because it is the main substitute of some polycarboxylates in temporary dental cement powders or in the formula of dental impression materials[10-14].

In the present work hydroxyapatite/pvp /ZnO -MgO nanocomposites were synthesized and characterized. This nanocomposite system was developed for dental composite. For this purpose, ultrasonic waves were applied to formation of nanoparticles. In addition, polyvinyl pyrrolidone (PVP) was used as a structure director additive. In situ preparation method of nanohydroxyapatite was carried out in the presence of polyvinylpyrrolidone Hap-PVP named HAP. Microstructure characterization and morphology analysis on the nano-composites was conducted using Scanning electron microscope (SEM), Mechanical properties, X-ray diffractometer (XRD) and Fourier transform infrared spectrometer (FT-IR). Nanocomposite HAP-PVP/ ZnO-MgO generally seems as a promising way for producing HA-composite biomaterials with a potential in dental nanomaterials.

Material and Methods

Materials : Analytical reagent grade of magnesium acetate tetrahydrate, zinc acetate dehydrate, NaOH and polyvinyl pyrrolidone (PVP) were obtained from Merck. All solutions were prepared with double-distilled water. $CaCl_2$ (99% pure), KH_2PO_4 (99% pure) were supplied by Merck.

Synthesis of nanocomposite HAP-PVP: 2 ml of ammonia was added to 20 ml of 0.30 M $CaCl_2$ solution at room temperature. The pH value of the solution was between 9 and 11. PVP (0. 3 g) was completely dissolved in 10 ml water at 40 C. 2 ml of the prepared gelatin solution was then added to the above mixture. The mixture was sonicated with 30 kHz ultrasonic irradiation source rated at a power of 50 W. B). 60 ml of 0.20 M KH_2PO_4 was slowly added drop wise to the above mixture. The whole solution was kept under ultrasonic irradiation for 1 h.

The resultant white precipitate was filtered by centrifugation. It was heat treated in furnace for 2 h at a specific temperature of 300^0C. This produced Gel–HAP powders in granular form. The final PVP–HAP products were grinded to a fine powder.

Preparation of ZnO /MgO nanocomposite: In a typical process, the precursor solutions were prepared by mixing 3.2g ZnO nanopowder and 1g/L (PVP) stirred slowly on a magnetic stirrer for 1 h. After this stage, NaOH 0.1 M) was slowly added drop wise to the above mixture. The mixed solution was sonicated for about 60 min with a rotational speed of 1000 rpm and then heated at 95°C for 2 h. Finally, the products were washed three times with distilled water and ethanol and then dried at room temperature.

To form the ZnO/MgO nanocomposite, the obtained precipitate was dehydrated at 300 ºC for 4 h.

Preparation of nano composite HAP-pvp/ZNO-MgO: In this stage, 3.44 g of ZnO –MgO nano-powder solved at water was sonicated for 30 min and then 7.5 mL of HAP-GEL solution was slowly added. The mixture was additionally sonicated for 30 min., the obtained precipitate was dehydrated at 300 ºC for 4 h.

Results and Discussion

Fourier transmitter infra spectroscopic analysis: Characteristic double split bands at around 508 cm^{-1} and a band around 1046 cm^{-1} are due to the bending and stretching modes of P–O vibrations in the phosphate network respectively[12,13]. The absorption bands observed in the range of 1300 – 1650 cm^{-1} are due to the stretching and bending modes of C–O and P–O bonds and air carbonate $(CO3)^{2-}$ ions[3,4,17]. The presence of the carbonate peaks in this study could be due to contamination from the air. The FT-IR spectrum for the PVP polymer is displayed in fig. 1a. The comparison of the FT-IR spectrum for the HAp particles synthesized in the presence of polymer (Fig. 1b) with the spectra shown in fig. 1a and b shows that there is an increase in the intensity of the absorption bands associated with the OH^- suggesting the contribution from the similar groups in the PVP polymer[13].

There are no obvious broadening of the absorption PO_4^{3-} and OH^- bands in the IR spectra for the polymer mediated synthesized samples, indicating the crystalline nature of the HAp crystallites. The slight shift in the position of absorption bands for the Hap prepared in the presence of polymer is indicative of dissociation and interactions of polymer with the nucleating HAp crystals. The peak at 563.76 cm^{-1} is the characteristic absorption of Zn–O bond and the broad absorption peak at 3414.86 cm^{-1} can be attributed to the characteristic absorption of hydroxyls. The frequencies of heteropolar diatomic molecules of MgO are confirmed by the peak at 932 cm^{-1}.

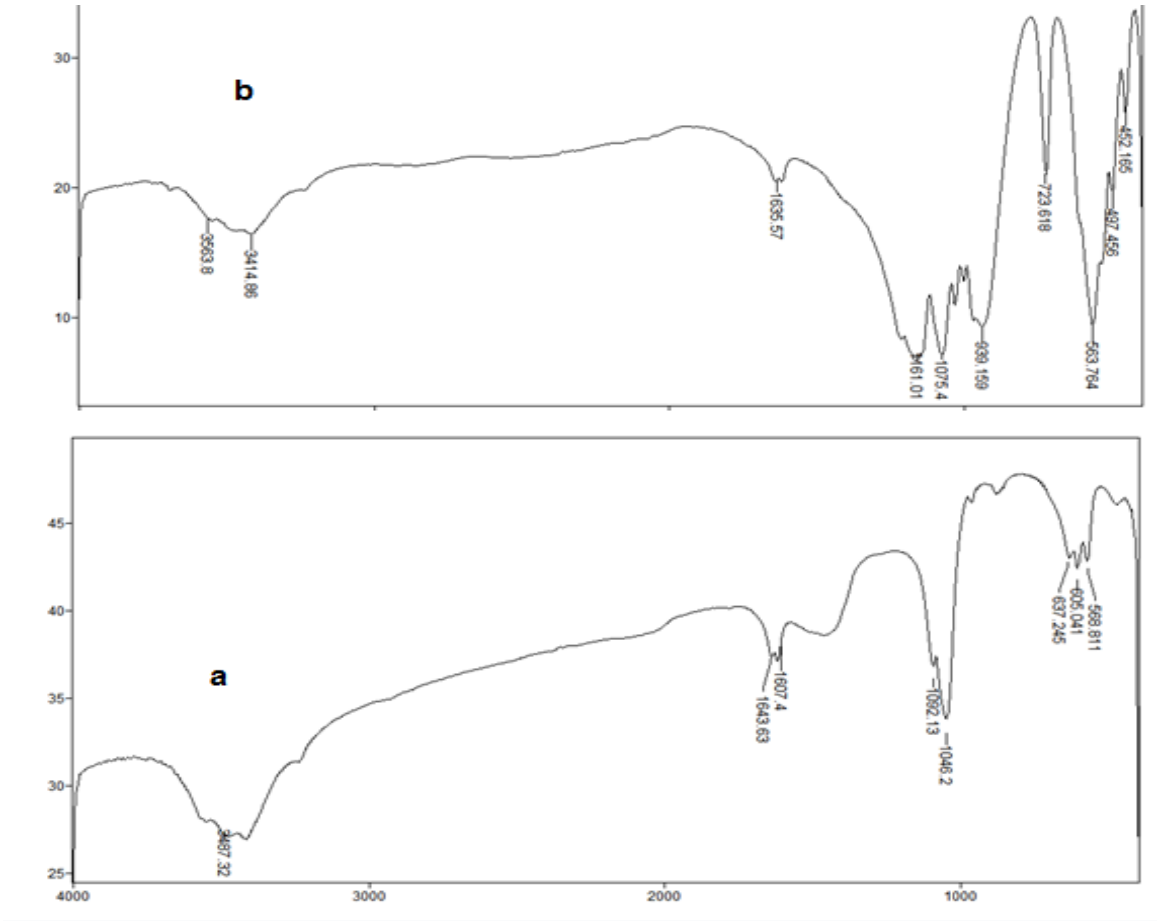

Fig.1: FTIR spectra of (a) hydroxyl apatite /pvp, (b) Hap/pvp/MgO-ZnO nano composite.

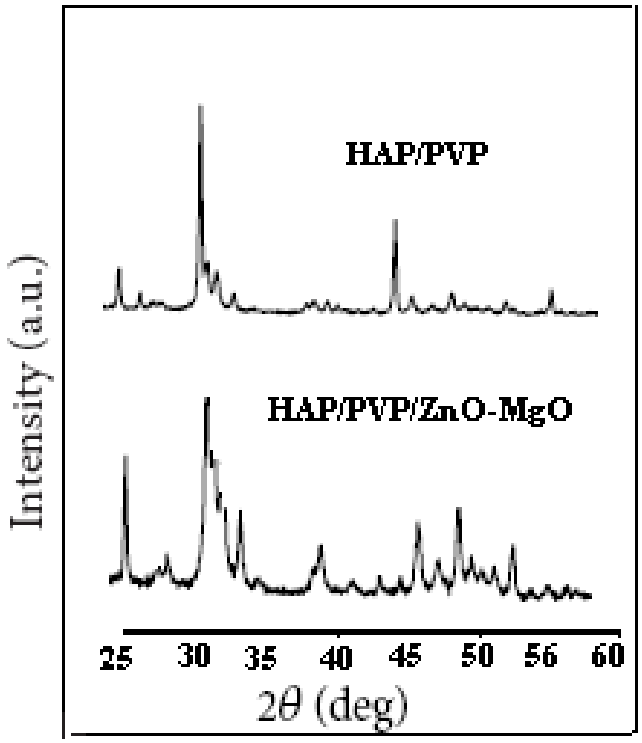

Fig.2: XRD spectra of (a) hydroxyl apatite /pvp, (b) Hap/pvp/MgO-ZnO nano composite

X-Ray diffraction analysis: The XRD pattern of HA/PVP composite obtained the characters peaks of hydroxyapatite structure 2Θ; 31.7°, 32.9° and 32.1°. These features corresponded well to those expected from the hydroxyapatite structure. Fig. 2b shows the XRD pattern of Hap-PVP/ZnO/MgO nanocomposite showing the characters of some peaks of hydroxyapatite structure beside the peaks of ZnO and MgO obtained from X-ray diffraction. Data are consistent with the JCPDS data of hydroxyapatite, ZnO and MgO. There is a little shift of peaks due to the PVP.

Scanning electron microscopy (SEM): Morphology of the powders was determined using electron microscopy. Figure 3 shows SEM micrographs of hydroxyl apatite /PVP (a,b), Hap/PVP/MgO-ZnO nano composite (c,d). Fig. 3a shows the morphology of HA/ZnO/ composite. Hap-PVP composites were observed as graphite like morphology about 2–5 μm in length on the surface as well as the inner walls of the scaffolds. The surfaces of the composites were rough and nanopowder crystals were homogeneously dispersed in the polymer matrix. MgO and ZnO crystals were partially embedded within the hydroxyapatite/PVP matrix throughout the walls. Results revealed that the calcination of ZnO-MgO nanocomposite at 300 °C resulted into rice like nano HAp nanocomposite having particle size in the range of 35-50 nm in diameter.

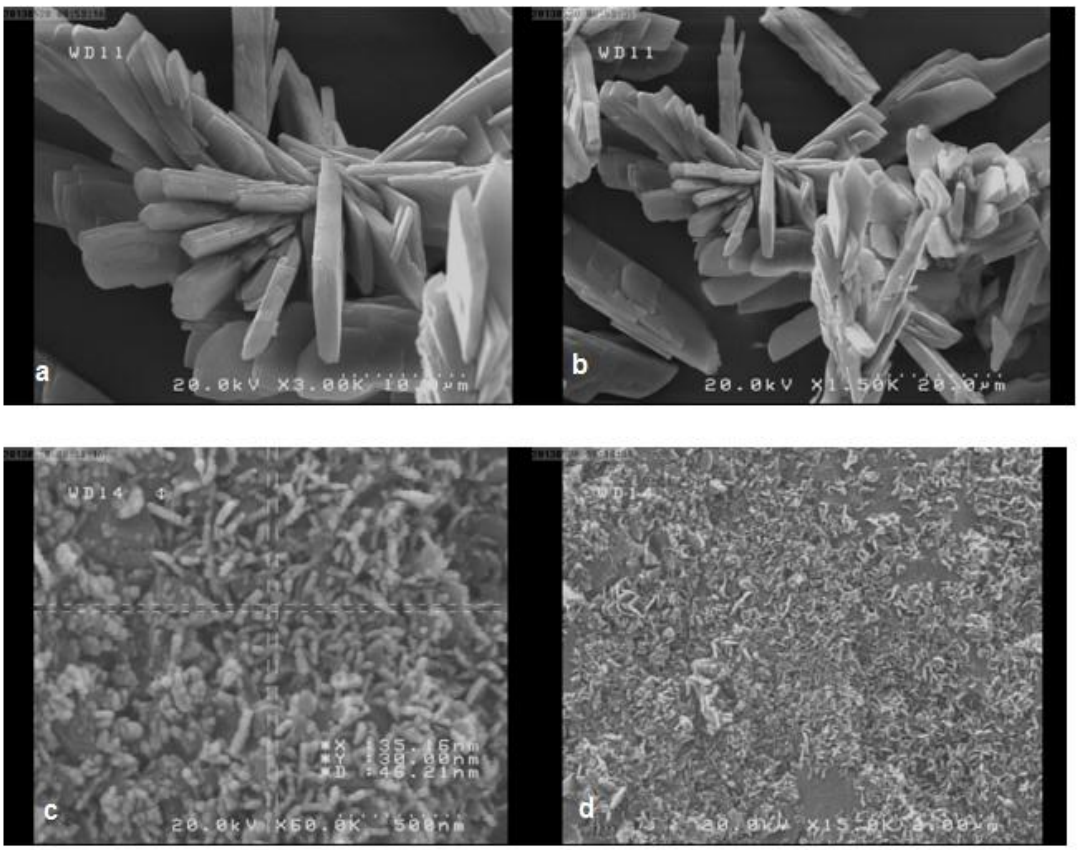

Fig.3: SEM micrographs of (a,b) hydroxyl apatite /pvp, (c,d) Hap/pvp/MgO-ZnO nano composite

Conclusion

The main result of this research is that the HAP/PVP-ZnO-MgO Nano composite with high quality and appropriate structural and morphological features was successfully produced via novel and simple thermally ultrasonic method. Crystallite size, lattice strain and crystallinity in the absence and presence of Mgo-ZnO were examined. SEM observations revealed that the experimental outcome had a graphite-like structure which consisted of several small particles with the average size of about 35 nm. Moreover the presence of ZnO-MgO within the nanocompsoite HAP-PVP was detected.

The results suggest that the presence of ZnO-MgO has undesirable effects on the structural features but also can promote the morphological properties. FT-IR and SEM confirmed that polymeric composites lead to the formation of apatite onto their surfaces especially this composite containing Mgo-Zno nanostructure. Finally, novel biocomposites having special properties could be used in bone substitutes and tissue engineering applications.

References

1. Radder A. M. and van Blitterswijk C. A., Abundant post-operative calcification of an elastomer matrix calcium phosphate-polymer compositee for bone reconstruction a preliminary study, *J. Mater. Sci., Mater in Med*., **5,** 320-331 **(1994)**

2. Chang M. C., Ko C. C. and Douglas W. H., Preparation of hydroxyapatite–gelatin nanocomposite, *Biomaterials*, **24**, 2853–2862 **(2003)**

3. Katti K. and Gujjula P., Control of mechanical responses in in-situ polymer/ hydroxyapatite composite for bone replacement, Proceedings of the 15th ASCE Engineering Mechanism Conference, Columbia University, New York, NY, June 2–5 **(2002)**

4. Ciftcioglu N. and Mckay D. S., Overview of biomineralization and nanobacteria, *Lunar Planet Sci*., XXXVI **(2005)**

5. Liou S.C., Chen S.Y. and Liu D. M., Synthesis and characterization of needlelike apatitic nanocomposite with controlled aspect ratios, *Biomaterials*, **24,** 3981–3988 **(2003)**

6. Spanos N., Deimede V. and Koutsoukos P.G., Functionalization of synthetic polymers for potential use as biomaterials: selective growth of hydroxyapatite on sulphonated polysulphone, *Biomaterials*, **23,** 947–953 **(2002)**

7. Soong Yee and Gamwo Isaac K., Particle Monitoring via an Ultrasonic Technique in Three-Phase Dense Silicon Slurries at Elevated Temperatures, *Res. J. Chem. Environ.,* **9(1),** 40-48 **(2005)**

8. Willems G., Lambrechts P., Braem M., Celis J.P. and Vanherle G., *Dent. Mater*, **8,** 310 **(1992)**

9. de Lima I. R., Andrea M. C., Ivan N. B., Granjeiro J. M. and de Almeida S. G., Development and characterization of 5% mol Zn bioceramic in granular form, *Material Research*, **9(4),** 399-403 **(2006)**

10. Binulal N., Deepthy M., Selvamurugan N., Shalumon K., Suja S., Mony U., kumar R. and Nair S., *Tissue Engineering Part A*., **16(2),** 393-404 **(2010)**

11. Meng H., Chen L., Zhaoyang Y., Wang S. and Zhao X., *Biomed J., Mater. Res. B Appl. Biomaterials*., **89B**,379-391 **(2009)**

12. Jones J., Ehrenfried L., Saravanapavan P. and Hench L., *J. Mater. Sci Mater. Med*., **17,** 989–996 **(2006)**

13. Theivasanthi T. and Alagar M., *Annals of Biological Research*, **2(3),** 82-87 **(2011)**

14. Abarrategi A. et al, *Biomaterials*, **29,** 94 – 102 **(2008)**.

(Received 15th April 2013, accepted 25th June 2013)

Synthesis, crystal structure and spectroscopic characterization of an oxalato bridged silver-deficient chromium(III) salt with water-filled nanochannels

Gouet Bebga[1], Signé M.[2], Nenwa J.[2*] and Fokwa B.P.T.[3]
1. Chemistry Department, Higher Teacher Training College, P.O. Box 47, University of Yaounde 1, Yaounde, CAMEROON
2. Coordination Chemistry Laboratory, Inorganic Chemistry Department, Faculty of Science, POB 812, University of Yaounde 1, Yaounde, CAMEROON
3. Institute for Inorganic Chemistry, RWTH Aachen University, D-52056 Aachen, GERMANY
*jnenwa@yahoo.fr

Abstract
The reaction of $K_3[Cr(C_2O_4)_3].3H_2O$ with $AgNO_3$ in water afforded the non-stoichiometric nanostructured silver salt, $\{Ag_{0.26}K_{0.24}[Ag_{2.5}Cr(C_2O_4)_3].3H_2O\}_n$ (1) which was characterized by elemental analysis, EDX, IR and UV-VIS spectroscopies and single crystal X-ray diffraction. Compound (1) crystallizes in a monoclinic space group C2/c, with unit cell parameters a = 18.2556(5), b = 14.6784(3), c = 12.2823(3) Å, β = 113.527(3)°, V = 3017.78(13) Å^3, Z = 8. The Cr(III) centers in the crystal structure are hexacoordinated by the oxalato-O atoms in a distorted octahedral geometry.

Compound (1) is a new member of the broad family of silver-deficient oxalatometalate(III) salts with water-filled nanochannels generally formulated as $[(M_xAg_{0.50-x})(H_2O)_3]@[Ag_{2.50}Cr(C_2O_4)_3]$, with $0 \leq x \leq 0.50$; M = K, Cs, Ag. The structure is best described as a non-molecular coordination polymer where the host lattice is constructed by the three-dimensional interconnectivity of the metallic centers through the O atoms of the oxalates and waters.

Keywords: Non-stoichiometric silver salt, nanochanneled lattice, coordination polymer, Cr(III) complex, solvent water molecules, crystal structure.

Introduction

Metal-organic frameworks (MOFs) have undergone revolutionary growth over the past few years owing to their intriguing architectures and potential applications as functional materials in catalysis, magnetism, non-linear optics, gas storage and separation[1-5]. In this respect, the family of materials with a variable Ag-Cr-oxalate channel lattice, formulated generally as $[(M_xAg_{0.50-x})(H_2O)_3]@[Ag_{2.50}Cr(C_2O_4)_3]$ ($0 \leq x \leq 0.50$; M = K, Cs, Ag), has been at the focus of interest in contemporary research and development[6]. These silver salts generally crystallize in a nonmolecular polymer framework preferentially with flexible deficiencies x of Ag^+ ions, thus generating a negatively charged lattice grid. They share in their crystal structures the one-dimensional channel lattice as their characteristic feature. Yet, these compounds exhibit a diversity of structures with varying connectivity, chemical composition, porosity and level of hydration[7-9].

Some closely related channel lattice networks[7-9] with respective chemical compositions: $[Ag_{2.90}Cr(C_2O_4)_3]^{0.10-}$, $[Ag_{2.50}M(C_2O_4)_3]^{0.75-}$ (M = Co^{III}, Cr^{III}) and $[Ag_{2.30}Cr(C_2O_4)_3]^{0.70-}$ have been reported recently. The present work is an effort to expand the known family of silver-deficient oxalatometalate(III) salts with water-filled nanochannels. Herein, we report the synthesis, crystal structure and spectroscopic characterization of the new non-molecular coordination polymer $\{Ag_{0.26}K_{0.24}[Ag_{2.5}Cr(C_2O_4)_3].3H_2O\}_n$. Its lattice grid is characterized by the chemical composition $[Ag_{2.50}Cr(C_2O_4)_3]^{0.50-}$ where the excess negative charge is compensated by the equivalent fraction of cationic pair $[Ag_{0.26}K_{0.24}]^{0.50+}$.

Material and Methods

Commercially available reagents were used as purchased from Prolabo (oxalic acid and silver nitrate) and Riedel-de Haën (dipotassium dichromate and dipotassim oxalate monohydrate). The precursor salt, $K_3[Cr(C_2O_4)_3].3H_2O$, was prepared by following the reported method[10]. The melting point was taken in open capillary tubes using Electrothermal 9100 apparatus. The EDX spectrum was carried out using scanning microscope JDX-7000F X-ray spectrometer. The IR spectrum in the range 4000-400 cm^{-1} was recorded with an Alpha-P spectrophotometer using KBr pallets. The UV–VIS spectrum was recorded on an AQUALYTIC spectrophotometer in water solution in the range 200–800 nm. Elemental analysis (C, H) was performed on a VARIO EL (Heraeus) CHNS analyzer.

Synthesis: The precursor salt $K_3[Cr(C_2O_4)_3].3H_2O$ (1.00 g, 2 mmol), freshly prepared and purified to analytical grade as reported[10], was dissolved in warm water (50 mL), called as solution A. Commercial $AgNO_3$ (1.01 g; 6 mmol, Riedel-de Haën, 99.5%) was dissolved in water (50 mL) and added dropwise in solution A. The mixture was stirred at 60 °C for 2 h. The resulting violet solution was filtered and left to stand in the hood at room temperature. After three days, violet needle-shaped crystals were harvested. Yield: 1.00 g (73.41%) based on $K_3[Cr(C_2O_4)_3].3H_2O$. M.P.: > 250 °C. Elemental analysis: Calc. for $C_6H_6Ag_{2.76}CrK_{0.24}O_{15}$ (676.53 g mol^{-1}) C, 10.64; H, 0.88. Found: C, 10.42; H, 0.80. The complex is soluble in water. IR (KBr,

cm^{-1}): 3424 (broad), 1625 (w), 1251 (sharp) and 407 (sharp). UV-VIS (H_2O solution, nm): 423; 573.

Crystal structure determination and Data collection: Crystal evaluation and X-ray data collection were performed on a model Xcalibur 3 diffractometer, equipped with Mo Kα (λ=0.71073 Å) radiation. A shinning violet crystal with approximate dimensions 0.45 x 0.30 x 0.20 mm^3 was selected on the oil at room conditions and attached to the tip of a nylon loop. It was mounted in a stream of cold nitrogen and countered in X-ray beam by using a video camera.

The initial cells constants were obtained from three series of ω scans and different starting angles. Each series consisted of 34 frames collected in the intervals of 0.75° about ω, with the exposure time of 16 seconds per frame. A total of 193 reflections were collected. The reflections were successfully indexed by an automated indexing routine built in the SMART program[11]. The highly redundant data sets were corrected for Lorentz and polarization effects. The collected data were reduced with SAINT[12] and an empirical absorption correction was carried out by using the SADABS[13] program. The crystal structure was solved by direct methods and refined by full-matrix least squares refinement[14], based on F^2. Crystal data and structure refinement parameters for compound (1) are given in table 1 and selected bond lengths in table 2.

Results and Discussion

Elemental and full X-ray structure analyses converge to support the formulation of compound (1) as $\{Ag_{0.26}K_{0.24}[Ag_{2.5}Cr(C_2O_4)_3].3H_2O\}_n$. It is a silver-deficient oxalatochromate(III) salt with water-filled nanochannels generally formulated as $[(M_xAg_{0.50-x})(H_2O)_3]@[Ag_{2.50}Cr(C_2O_4)_3]$[6], with $0 \leq x \leq 0.50$; M = K, Cs, Ag.

Compound (1) is an air-stable dark-violet material which does not melt up to 250 °C. The EDX spectrum (Figure 1) provides clear evidence for the presence of elements C, O, K, Cr and Ag in compound (1). The FTIR spectrum shows a broad absorption band around 3424 cm^{-1} which is assigned to coordinated and crystallization water. The bands centered at 1625 cm^{-1} and 1251 cm^{-1} are attributed to ν(C=O) and ν(C–O) stretches respectively[7-9]. The sharp band observed at 407 cm^{-1} can be assigned to the Cr–O vibration[7,8].

The UV-VIS spectrum displays two absorption bands centered at 423 and 573 nm, which are due to d-d electronic transitions within the octahedral complex ions $[Cr(C_2O_4)_3]^{3-}$ contained in compound (1)[7,8]. It is obvious that the present electronic absorption spectrum is virtually superimposable with that reported since the spectral informations thus obtained solely relate to the $[Cr(C_2O_4)_3]^{3-}$ species.

Compound (1) is a nonmolecular material whereby the host lattice network with chemical composition $[Ag_{2.50}Cr(C_2O_4)_3]^{0.5-}$ carries an overall excess negative charge and defines nanochannels, encapsulating water molecules and charge-balancing fractions of cations from Ag^+ and K^+ (0.24 Ag^+ is replaced by 0.24 K^+). This is closely reminiscent of the results reported by Dean et al[6].

The ORTEP[17] constitutive ionic building blocks of the structure of compound (1) – the $[Cr(C_2O_4)_3]^{3-}$ complex, the Ag and K atoms are depicted in figure 2. The anionic building stone, $[Cr(C_2O_4)_3]^{3-}$, functions as a metalloligand or else, as an internetting bridge. Hence, this internetting bridge interconnects, across its O atoms, the four independent sites Cr1, Ag1, Ag2/K2 and Ag3 (Figure 2) into a three-dimensional polymeric host lattice network that surrounds water-filled channels which contain additional fractions of cationic pairs, $[Ag_{0.26}K_{0.24}]^{0.50+}$, pasted at the internal wall periphery of the tube.

The Cr1 center (Figure 2a) is pseudo-octahedrally chelated by three oxalato ligands with helical orientation, coordination to the metal occurring across the six deprotonated "internal"(hydroxylato) O atoms (O2, O3, O6, O7, O9, O12) and giving rise to Cr1–O bond lengths and O–Cr1–O bond angles which fit well within the ranges of previous results[8].

Coordination geometry around Ag1 (Figure 2b) is severely distorted octahedron involving three "external" carbonyl O atoms (O1, O4, O11) and one "internal" O atom (O12) in the equatorial plane and two O atoms (O6, O10) – one "internal" and one "external" respectively in the axial positions. The Ag1–O lengths of this octahedron are different with the values ranging from 2.328(3) to 2.559(4) Å.

The Ag2 site (Figure 2c) experiences pentacoordination, not tetracoordination like in the structures reported by Dean et al[6] due to one chelation via the "external" O atoms (O10, O11) and to three monodentate linkages i.e. one across an O atom of a water molecule (OW3), one across an "external" O atom (O8) and one across an "internal"O atom (O7) from the internetting bridges. OW1 and OW2 are solvent water molecules. Bond lengths and bond angles for the coordination sphere around Ag2 diverge markedly from one another just as previously reported[8,9].

The K2 site is heptahedrally coordinated (Figure 2d). The atoms Ag2 and K2 share a mixed-site with the real occupancy of 0.759:0.241 ratio (Table 3) with bond distances K2–O7 = 2.344(9), K2–O11 = 2.374(8), K2–O5 = 3.168(9), K2–O8 = 3.179(9) and K2–OW3 = 2.066(12) Å. The atom Ag2 is disordered in the coordination sphere over four positions in a 0.2 (AgA):0.1 (AgB):0.1 (AgC):0.1 (AgD) ratio (Table 3) whilst in the previous results by Dean et al[6], Ag2 is disordered in the outer sphere over three positions in a 0.033:0.069:0.121 ratio.

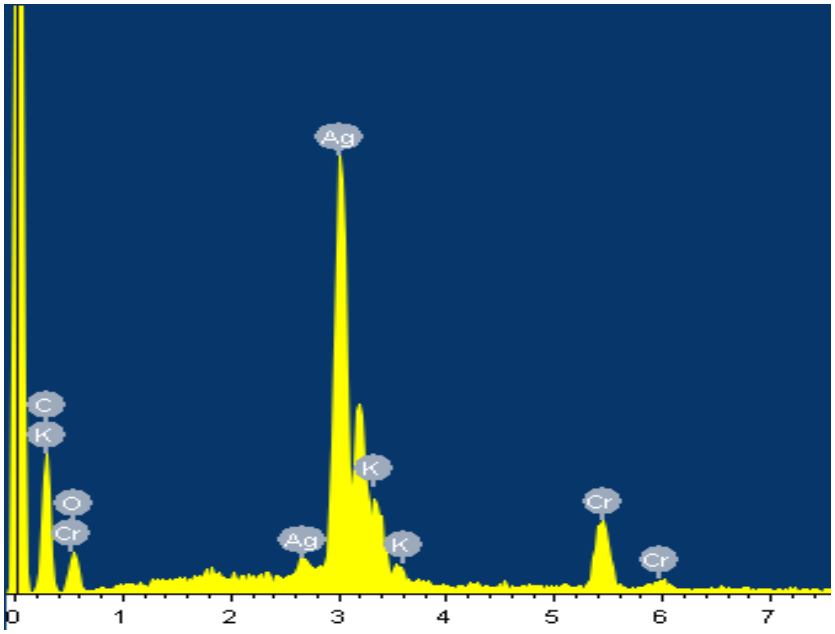

Figure 1: EDX spectrum of compound (1) showing the nature of its different heavy chemical elements.

Table 1
Crystal data and structure refinement parameters for compound (1)

Empirical formula	**$C_6H_6Ag_{2.76}CrK_{0.24}O_{15}$**
Formula weight	676.53
Temperature (K)	293(2)
Wavelength (Å)	0.71073
Crystal system	monoclinic
Space group	C2/c
a (Å)	18.2556(5)
b (Å)	14.6784(3)
c (Å)	12.2823(3)
β (°)	113.527(3)
Volume (Å^3)	3017.78(13)
Z	8
D_{calc} (Mg/m^3)	2.978
Absorption coefficient (mm^{-1})	4.372
F(000)	2470
Crystal size (mm)	0.45 x 0.30 x 0.20
θ Range for data collection (°)	3.69 – 32.22
Index ranges	$-27 < h < 27$, $-20 < k < 15$, $-18 < l < 17$
Reflections collected	14140
Independent reflections (R_{int})	4892 (0.0431)
Completeness to $\theta = 32.22°$ (%)	98.9
Absorption correction	Multi-scan with SADABS
Max. and min. transmission	0.4666 and 0.2664
Refinement method	Full-matrix least squares on F^2
Data / restraints / parameters	2703/1/275
Goodness-of-fit on F^2	0.870
Final *R* indices [$I > 2$sigma(I)]	$R_1 = 0.0431$, w$R_2 = 0.0933$
R indices (all data)	$R_1 = 0.0448$, w$R_2 = 0.1134$
Largest diff. peak and hole (eÅ^{-3})	1.199 and -0.813

Table 2
Selected bond lengths in compound (1)

Bond lengths (Å)			
Cr1–O2	1.968(3)	Ag2–OW3	2.470(8)
Cr1–O3	1.958(3)	Ag3–O5	2.370(3)
Cr1–O6	1.979(3)	AgA–OW3	2.567(11)
Cr1–O7	1.959(3)	AgB–O10	2.427(10)
Cr1–O9	1.979(3)	AgB–OW3	1.066(11)
Cr1–O12	1.965(3)	AgC–O7	2.354(9)
Ag1–O6	2.328(3)	K2–O7	2.344(9)
Ag1–O4	2.328(3)	K2–O11	2.374(8)
Ag1–O1	2.559(4)	K2–O5	3.168(9)
Ag1–O11	2.413(3)	K2–O8	3.179(9)
Ag2–O7	2.351(3)	K2–OW3	2.066(12)
Ag2–O10	2.440(4)		

Table 3
Atomic positions and equivalent thermal agitation parameters in compound (1)

Atome	**Wyckoff.**	**S.O.F.**	**x/a**	**y/b**	**z/c**	**Ueq [Å^2]**
Ag1	8f		0.24553(3)	0.30224(3)	0.24477(3)	0.0547(2)
Ag2	8f	0.759	0.92299(7)	0.31192(7)	0.13172(10)	0.0515(3)
K2	8f	0.241	0.9262(6)	0.2928(5)	0.0936(7)	0.037(2)
Ag3	4e		0	0.54394(5)	1/4	0.0506(2)
Cr1	8f		0.71098(4)	-0.00487(5)	0.02562(6)	0.0287(2)
C1	8f		0.3118(3)	0.1451(3)	0.1337(4)	0.033(1)
C2	8f		0.2234(3)	0.1527(3)	0.0429(4)	0.035 (1)
O1	8f		0.1807(2)	0.2121(2)	0.0515(3)	0.0499(9)
O2	8f		0.29618(18)	0.4077(2)	0.0402(3)	0.0383(8)
O3	8f		0.35046(18)	0.0794(2)	0.1131(3)	0.0337(7)
O4	8f		0.3381(2)	0.1992(3)	0.2150(3)	0.056(1)
C3	8f		0.5815(3)	0.0464(3)	0.0751(4)	0.0291(9)
C4	8f		0.1124(3)	0.4559(3)	0.1429(3)	0.0291(9)
O5	8f		0.52600(18)	0.0884(2)	0.0833(3)	0.0339(7)
O6	8f		0.17322(18)	0.4235(2)	0.1296(3)	0.0329(7)
O7	8f		0.61820(18)	0.06984(19)	0.0091(3)	0.0304(7)
O8	8f		0.0787(2)	0.4211(2)	0.2007(3)	0.0407(8)
C5	8f		0.7908(3)	0.1459(3)	-0.0029(4)	0.033(1)
C6	8f		0.8126(3)	0.1385(3)	0.1314(4)	0.034(1)
O9	8f		0.78211(19)	0.0694(2)	0.1609(3)	0.0355(7)
O10	8f		0.8557(2)	0.1958(2)	0.2005(3)	0.0481(9)
O11	8f		0.6842(2)	0.2897(2)	0.0427(3)	0.0442(9)
O12	8f		0.75541(19)	0.4163(2)	0.0653(3)	0.0335(7)
OW1	8f		0.4440(5)	0.5252(7)	0.0917(11)	0.196(4)
OW2	8f		0.3957(5)	0.4486(8)	0.3380(9)	0.214(6)
OW3	8f		-0.0068(4)	0.1933(5)	0.4039(6)	0.114(2)
AgA	8f	0.2	0.0176(6)	0.2372(5)	-0.0992(10)	0.229(5)
AgC	8f	0.1	-0.0460(7)	0.2372(6)	-0.1273(7)	0.120(3)
AgB	8f	0.1	-0.0534(5)	0.2153(9)	0.4292(9)	0.151(5)
AgD	8f	0.1	0.0738(2)	0.1569(4)	0.7953(4	0.062(1)

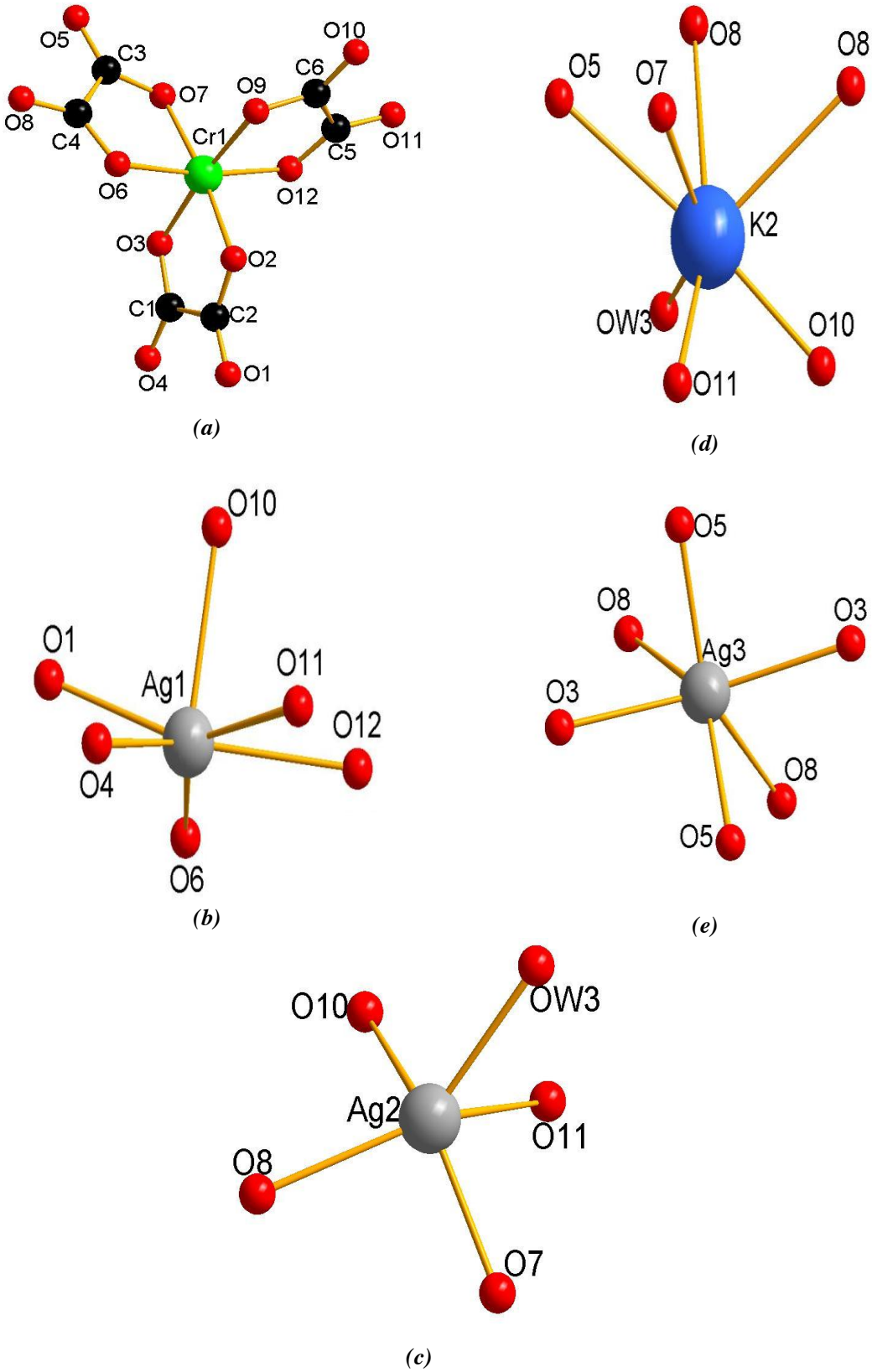

Figure 2: The ORTEP[17] plot of the coordination polyhedra around the different metallic centers in compound (1): Cr *(a)*, Ag1 *(b)*, Ag2 *(c)*, K *(d)* and Ag3 *(e)*

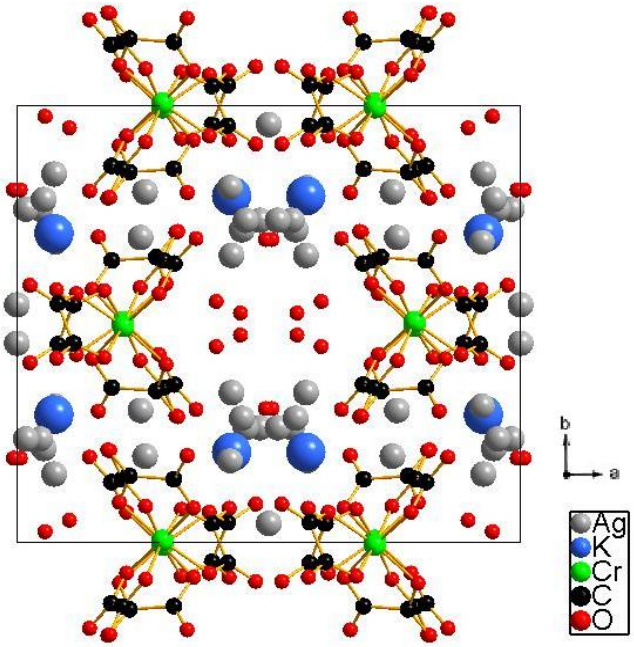

Figure 3: Lattice packing of the unit cell of compound (1) projected down [001] highlighting the water molecules within the tubular channel

The Ag3 atom is octahedrally coordinated with four "external" carbonyl O atoms (O5, O8, $O5^{i}$, $O8^{i}$) lying in the equatorial plane and two "internal" O atoms (O3, $O3^{i}$) in the axial position. All the Ag3–O distances of this octahedron are comparable with reported values[7-9].

A lattice packing of the unit cell of compound (1) (Figure 3) highlights the water molecules within the tubular channels oriented parallel to [001]. The structural framework in fact is exclusively the result of 3D interconnectivity between Ag^{+} cations and $[Cr(C_2O_4)_3]^{3-}$ complex anions. In figure 3, the H_2O molecules inside the channels are shown to be essentially of two types: those coordinated to the Ag2 atoms (or K2 atoms) located at the wall periphery of the tube (dangling water molecules) and those located at the center of the tube (free water molecules).

Conclusion

In summary, the compound $\{Ag_{0.26}K_{0.24}[Ag_{2.5}Cr(C_2O_4)_3].3H_2O\}_n$, isolated from aqueous solution as dark-violet needles is a novel non-stoichiometric nanostructured silver salt hosting H_2O-guest molecules. It crystallizes in the monoclinic space group *C*2/c and the chemical composition of its lattice grid is $[Ag_{2.50}Cr(C_2O_4)_3]^{0.50-}$ where the excess negative charge is offset by the equivalent fraction of cationic pair $[Ag_{0.26}K_{0.24}]^{0.50+}$. This work confirms the great flexibility of synthetic manoeuvres for the construction of supramolecular assemblies. One could consider with serenity the development of new systems where the deficiency in Ag^{+} ions could in the best of the cases, be solely compensated by hydronium (H_3O^{+}) ions. Materials of this type, no doubt, could be well-adapted models in the exploration of the concept of one-dimensional proton conducting solid (ID-PCS)[7,8,18].

Acknowledgement

The authors would like to thank Dr. Simeon Ponou for Single Crystal X-ray diffraction measurement and structure determination during his stay at Lund University (Sweden).

References

1. Lee J. Y., Farha O. K., Roberts J., Scheidt K. A., Nguyen S. T. and Hupp J. T., Metal–organic framework materials as catalysts, *Chem. Soc. Rev.*, **38**, 1450–1459 **(2009)**

2. Zhang X. M., Wang Y. Q., Wang K., Gao E. Q. and Liu C. M., Metamagnetism and slow magnetic dynamics in an antiferromagnet composed of cobalt (II) chains with mixed azide–carboxylate bridges, *Chem. Commun.*, **47**, 1815–1817 **(2011)**

3. Coe B. J., Foxon S. P. and Harper E. C., Evolution of linear absorption and nonlinear optical properties in V-shaped ruthenium(II)-based chromophores, *J. Am. Chem. Soc.*, **132**, 1723–1723 **(2010)**

4. Yaghi O. M., O'Keeffe M., Ockwig N., Chae H. and Eddaoudi M., Reticular synthesis and the design of new materials, *Nature*, **423,** 705–714 **(2003)**

5. Lim C. S., Schnobrich J. K., Wong-Foy A. J. and Matzger A. J., Metal-dependent phase selection in coordination polymers derived from a C_{2v}-symmetric tricarboxylate, *Inorg. Chem.*, **49**, 5271–5275 **(2010)**

6. Dean P. A. W., Craig D., Dance I., Russell V. and Scudder M., A variable Ag–Cr–oxalate channel lattice: $[M_xAg_{0.5-x}(H_2O)_3]@[Ag_{2.5}Cr(C_2O_4)_3]$, M = K, Cs, Ag, *Inorg. Chem.*, **43**, 443–449 **(2004)**

7. Bélombé M. M., Nenwa J., Mbiangué Y. A., Gouet Bebga, Majoumo-Mbé F., Hey-Hawkins E. and Lönnecke P., Water-filled pseudo-Nanotubes in $Ag_{11.60}H_{0.40}[Cr(C_2O_4)_3]_4.15H_2O$: synthesis, characterization and X-Ray structure, *Inorg*. *Chim*. *Acta*, **362**, 1–4 **(2009)**

8. Bélombé M. M., Nenwa J., Tene O. T. and Fokwa B. P. T., Synthesis, X-ray structure and thermal behavior of isomorphous silver-deficient channel lattice frameworks with general formula $[(Ag_{0.25}/M_{0.25})(H_2O)]@[Ag_2M(C_2O_4)_3].4H_2O$ (M = Co^{III}, Cr^{III}), *Glob*. *J*. *Inorg*. *Chim*., **1**, 34–41**(2010)**

9. Nenwa J., Gouet Bebga, Djonwouo P. L. and Fokwa B. P. T., Synthesis, X-ray structure and spectroscopic characterization of a non-stoichiometric nanostructured silver salt hosting water-guest molecules, *Res*. *J*. *Chem*. *Environ*., **16(4)**, 111–115 **(2012)**

10. Bailar J. C. and Jones E. M., Tris(oxalato) salts, *Inorg*. *Synth*, **1**, 35–38 **(1939)**

11. SMART: Version 5.624a. Bruker AXS Inc., Madison, Wisconsin, USA **(1998)**

12. Siemens Inc.: SAINT Area-Detector Integration Software, Version 6.01, Siemens. Industrial automation, Inc., Madison, Wisconsin, USA **(1997)**

13. Sheldrick G. M., SADABS, Program for Empirical Absorption Correction of Area Detector Data, University of Göttingen, Göttingen, Germany **(2010)**

14. Sheldrick G. M., A Short History of SHELX, *Acta Cryst*., A**64**, 112–122 **(2008)**

15. Brandenburg K., DIAMOND, Release 2.1c, Crystal Impact, Bonn, Germany **(1999)**

16. Farrugia L. J., Win GX publication routines, *J*. *Appl*. *Cryst*., **32**, 837–838 **(1999)**

17. Johnson C. K., ORTEP-II, A Fortran Thermal-Ellipsoid Plot Program. Report ORNL-5138, Oak Ridge National Laboratory, Oak Ridge, Tennessee, USA **(1976)**

18. Bélombé M. M., Nenwa J., Mbiangué Y. A., Majoumo-Mbé F., Lönnecke, P. and Hey-Hawkins E., Hydrogen-bonded pillars of alternating chiral complex cations and anions:1. Synthesis, characterization, X-ray structure and thermal stability of catena $\{[Co(H_2oxado)_3][Cr(ox)_3].5H_2O\}$ and of its precursor $(H_3oxado)[Co(H_2oxado)_3](SO_4)_2.2H_2O$, *Dalton Trans*., 4519–4525 **(2009).**

(Received 15th March 2013, accepted 22nd July 2013)

Characterization of Oil Palm Shell Activated Carbon and ZSM-5 Supported Cobalt Catalysts

Izirwan I.*, Mohd A. and Saidina Amin N.A.
Chemical Reaction Engineering Group (CREG), Energy Research Alliance, Faculty of Chemical Engineering, Universiti Teknologi Malaysia, 81310 Johor Bahru, Johor, MALAYSIA
*izirwan@ump.edu.my

Abstract

In this paper we are reporting the preparation and characterization of supported cobalt catalysts using a wetness impregnation method. Different cobalt catalysts loading of 0 and 10 wt% were prepared by dissolving cobalt nitrate hexahydrate in distilled water and dried in an oven at 100 °C overnight. Two selected supports of oil palm shell (OPS) activated carbon and ZSM-5 zeolite were employed and compared. Catalysts characterizations of both supports were performed by Thermogravimetric analysis (TGA), X-ray diffraction (XRD) analysis and Scanning electron microscope analysis (SEM). Using Scherrer equation, the cobalt metallic size was calculated.

OPS activated carbon supports were further analyzed for CHNOS elemental analysis. Both supports of OPS activated carbon and ZSM-5 zeolite exhibited the successful loading of cobalt catalysts and have potential to be utilized in catalytic reactions.

Keywords: Activated carbon, cobalt catalyst, oil palm shell**,** zeolite, ZSM-5.

Introduction

Cobalt based catalysts are widely employed for catalytic reactions [1-2] due to their high activity [3-5], less side reactions such as low water-gas shift activity [6] and high selectivity of desired products.[7-11] Other available metal catalysts especially the transition metals such as Ru, Pd, Pt are superior in their reaction performances but higher costs hinder their utilization in the large scale for industrial production. Cobalt catalysts are comparatively cheaper and reasonable in price [12] than the transition metals with good reaction performances .

In order to improve the catalyst activity and selectivity, the cobalt precursor is dispersed onto the surface of the porous supports to enhance the catalytic surface area for the successive reactions. Various methods of catalysts loading such as ultrasound impregnation,[13] incipient wetness co-impregnation [14] are employed for loading the catalysts onto the supports. The porous supports such as ZSM-5 zeolite, activated carbon, alumina, titania, bentonite and silicon carbide [15] are selected for the augmentations of the catalysts surface area, pore diameter, pore volume and metal-support interaction that have a great effect on the size, dispersion and catalytic performance of cobalt catalysts.The objective of this study is to prepare and characterize the cobalt catalysts based on the different supports of ZSM-5 zeolite and OPS activated carbon with various loadings of cobalt catalysts.

Material and Methods

Chemicals: Zeolite and activated carbon were used as supports for catalysts. Zeolite ammonium ZSM-5 powder was purchased from Zeolysts International. Activated carbon of Oil Palm Shell (OPS) was supplied by Multi Filter Sdn Bhd. The precursor of cobalt catalyst was cobalt (II) nitrate hexahydrate Co $(NO_3)_2$. $6H_20$ from Friendemann Schmidt.

Catalysis Synthesis: The oil palm shell (OPS) activated carbon was rinsed with distilled water to remove impurities and dried in an oven at 110 °C overnight. The cobalt precursor was added onto the supports of OPS activated carbon by wetness impregnation method after dissolving in distilled water. The mixtures were stirred on a magnetic stirrer plate overnight. Then, the sample was dried in the oven at 110 °C for 3 days. As for support of ZSM-5, this zeolite was utilized without further treatment and using the aforementioned method of catalysts loading. Only ZSM-5 zeolite supported cobalt catalysts were calcined at 550 °C for 5 h at a heating rate of 10 °C/min in a furnace. Both supported cobalt catalysts were prepared at different cobalt loadings of 0 and 10 wt% and denoted as AC(0), AC(10), ZSM-5(0) and ZSM-5(10) respectively.

Elemental Analysis: The elemental analysis of activated carbon was performed by CHNOS Elemental Analyzer Vario MACRO Cube using an oil method.

Thermalgravimetric Analysis (TGA): Perkin Elmer TGA7 and Perkin Elmer Thermal Analysis Controller TAC7/DX were used for the thermalgravimetric analysis (TGA). The equipment conditions were set at temperature 29-950 °C, heating rate 10 °C/min and nitrogen flow rate 20 ml/min.

X-Ray Diffraction (XRD): X-Ray Diffraction (XRD) analysis was conducted by using a benchtop X-Ray Diffractometer Rigaku Miniflex II with $Cu_{K\alpha}$ radiation (λ_a = 0.1541 nm), step size 0.02 and scan speed 0.3 s/ step. The X-ray tube was operated at 10 kV and at 50pA.

Scanning Electron Microscopy (SEM): The surface morphology of the catalysts was observed with a Scanning Electron Microscope (SEM, Zeiss EV050). The images were captured in SEM mode at 5,000 times magnification.

Results and Discussion

The elemental contents of Oil Palm Shell (OPS) activated carbon were analyzed and the obtained data were shown in table 1. The major elemental content was carbon (C) with the highest percentage of 81.06 wt%. However, the oxygen (O) was calculated at 15.88 wt% by the difference of overall contents. There was minimal sulfur found at 0.16 wt%.

Figure 1 displays the TGA/DTG of OPS activated carbon and activated carbon supported catalyst under N_2 atmosphere. Generally, a weight loss below 100 °C as exhibited in figure 1 (a) is considered due to the evaporation of the absorbed water in the sample. The activated carbon sample is stable below 650 °C. However, approximately 5% weight loss can be detected when the activated carbon supported cobalt catalyst is heated at 650-700 °C. This may be due to the loss of the carbon by oxidation reaction.

Figure 2 shows the TGA/DTG of ZSM-5 zeolite and ZSM-5 zeolite supported catalyst under N_2 atmosphere. Both curves exhibit a weight loss below 100 °C due to the release of the absorbed water in the samples. The ZSM-5 zeolite sample is thermally unstable with the weight loss of 10 wt% after 650 °C. On the contrary, the ZSM-5 zeolite supported cobalt catalyst sample shows greater stability than the former sample.

Figure 3 presents the XRD patterns of the ZSM-5 zeolite with and without loading of cobalt catalysts. The major magnitude of the peak was observed at 23 degree (2Θ) with the intensity of 1800 cps. After the impregnation of cobalt catalysts, the magnitudes of ZSM-5 zeolite peaks were reduced to almost half indicating that the cobalt catalysts have been successfully coated onto the surface of ZSM-5 zeolite. In addition, the spinel phase of cobalt oxide (Co_3O_4) was observed at 2Θ of 30.2, 37.0, 45.2, 58.3 and 65.4. The crystallite diameters of cobalt particles were calculated using Scherrer equation taken from the most intense cobalt oxide, Co_3O_4 peak at 2Θ of 37.0 as shown below:

$$d = 0.89\lambda / B\cos\theta \times 180/\pi \quad (1)$$

where d is the mean cobalt crystallite diameter, λ is the X-ray wave length (1.541 A°) and B is the full width half maximum (FWHM) of the Co_3O_4 diffraction peak. The mean crystallite diameter of the cobalt catalyst was calculated by using (1) and the crystallite diameter was about 0.34 ηm.

Figure 4 displays the XRD patterns of the OPS activated carbon with the loading 0 and 10 wt% cobalt catalysts. The major magnitude of the broadening peak was observed at 23 degree (2Θ) with the intensity of 650 cps. This magnitude of the broadening peak was reduced to 200 cps suggesting that the impregnation of cobalt catalysts has been successfully coated onto the surface of OPS activated carbon. However, the spinel phase of cobalt oxide was not obvious due to the broadening of the XRD peaks. Therefore, calculating the size of the cobalt catalyst crystallites using the most intense peak of cobalt oxide may not be accurate for the OPS activated carbon.

The SEM images of OPS activated carbon with and without the addition of cobalt catalysts are presented in figure 5. As shown in figure 5 (a), the pores are obviously discovered on the surface of OPS activated carbon in different sizes. After the impregnation with the cobalt catalysts, the pores of OPS activated carbon were completely covered with cobalt particles as shown in figure 5 (b). Furthermore, the cobalt particles of the catalysts were found to be partly agglomerated on the surface and showed non-uniform distributions.

Figure 6 exhibits the SEM images of ZSM-5 zeolite for 0 and 10 wt% cobalt catalyst loadings. The dense surface morphology was caused by the aggregation of zeolite particles. The existence of cobalt catalyst particles was hardly differentiated but the aforementioned decrease in intensity of XRD peaks suggested the impregnation of cobalt catalysts.

Conclusion

Further characterizations of the catalysts are required for the full understandings of the physical and chemical properties of the catalysts. The catalyst supports of OPS activated carbon and ZSM-5 demonstrated the successful loading of cobalt catalysts. In the extensions of this work, both supports of OPS activated carbon and ZSM-5 will be utilized in the catalytic reactions of Fischer-Tropsch synthesis or carbon dioxide reforming of methane.

Acknowledgement

The authors are grateful to Zainab Salleh from the Faculty of Chemical Engineering, Universiti Teknologi Malaysia for conducting catalyst analyses. This work was supported by Research Energy Alliance of Universiti Teknologi Malaysia under Grant GUP05J02. One of the authors is gratefully acknowledged to the Malaysia Ministry of Higher Education for the scholarship during his study period.

Table 1
Ultimate analysis of activated carbon

Elemental Analysis (wt.%)				
C	**H**	**N**	**S**	**O**
50.10	6.85	1.90	ND*[16]	41.15
81.06	1.78	1.12	0.16	15.88

*ND, not detectable

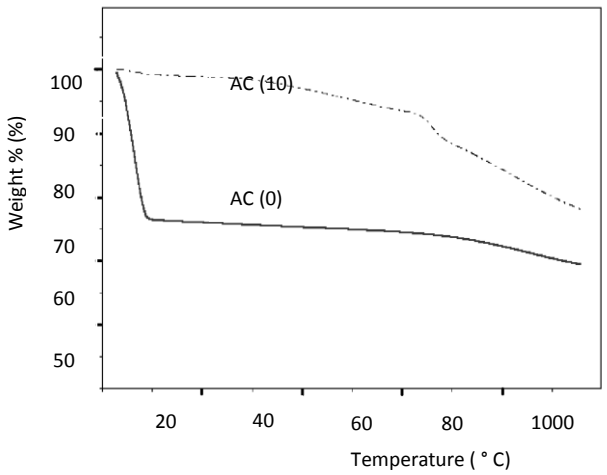

(a)

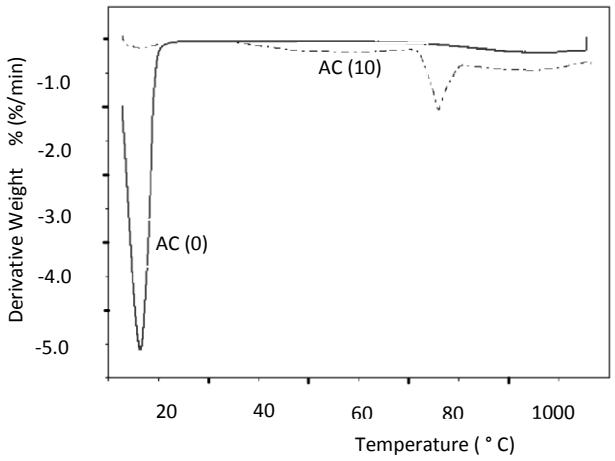

(b)

Fig.1: TGA/DTG curves of activated carbon: (a) TGA; (b) DTG.

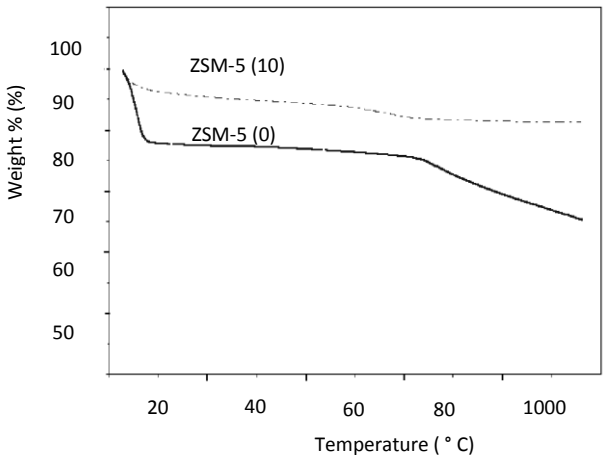

(a)

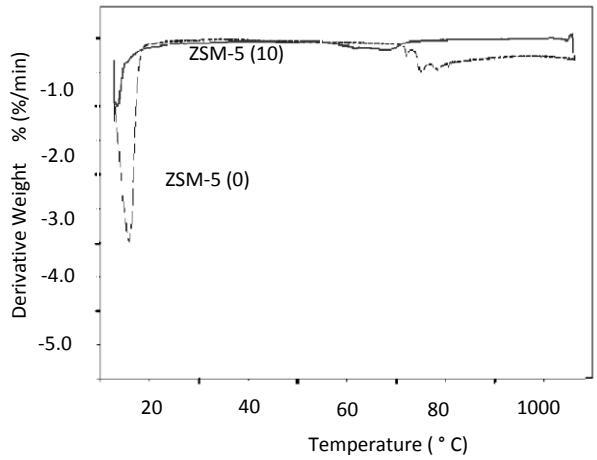

(b)

Fig. 2: TGA/DTG curves of Zeolite ZSM-5: (a) TGA; (b) DTG.

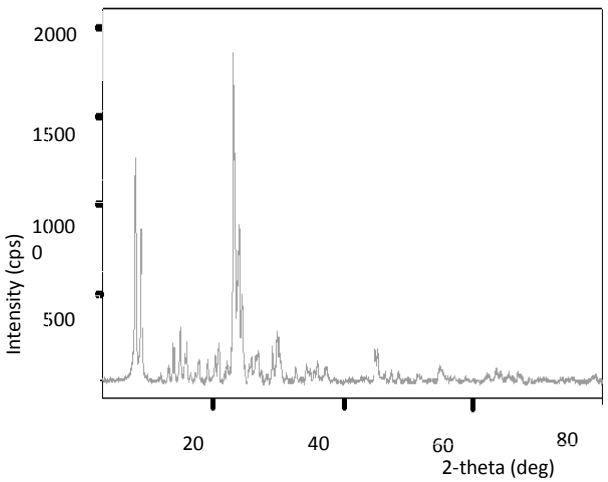

(a)

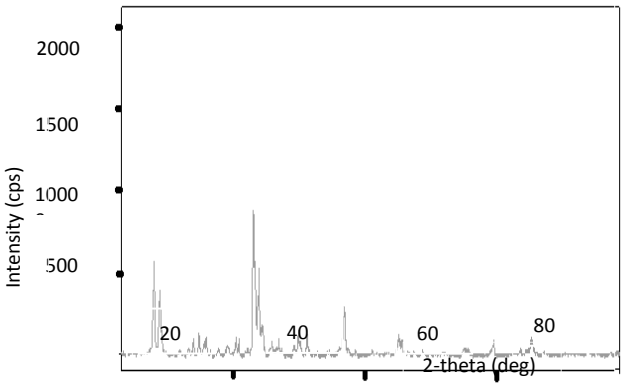

(b)

Fig. 3: XRD patterns of Zeolite ZSM-5: (a) ZSM-5(0); (b) ZSM-5 supported cobalt catalyst, ZSM-5(10).

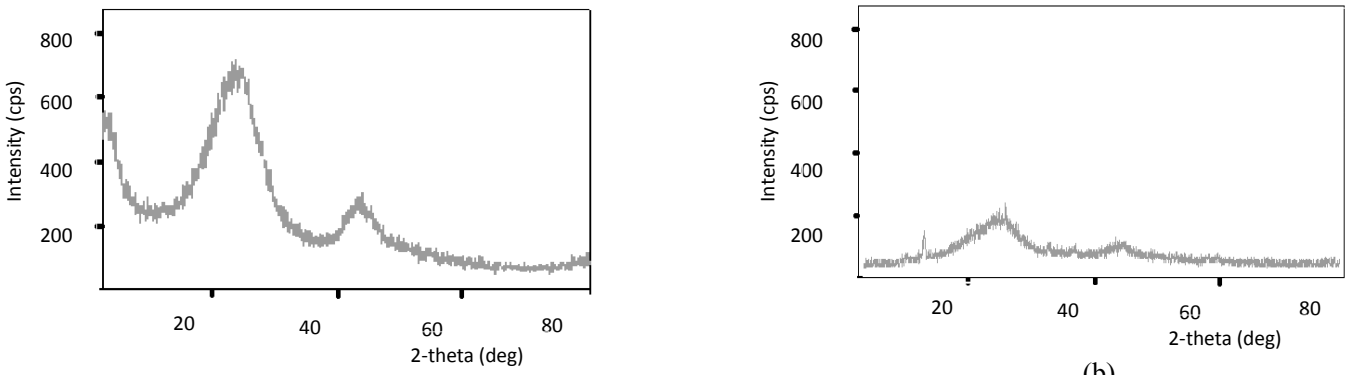

(a) (b)

Fig. 4: XRD patterns of: (a) activated carbon, AC (0); (b) activated carbon supported cobalt catalyst, A C (10).

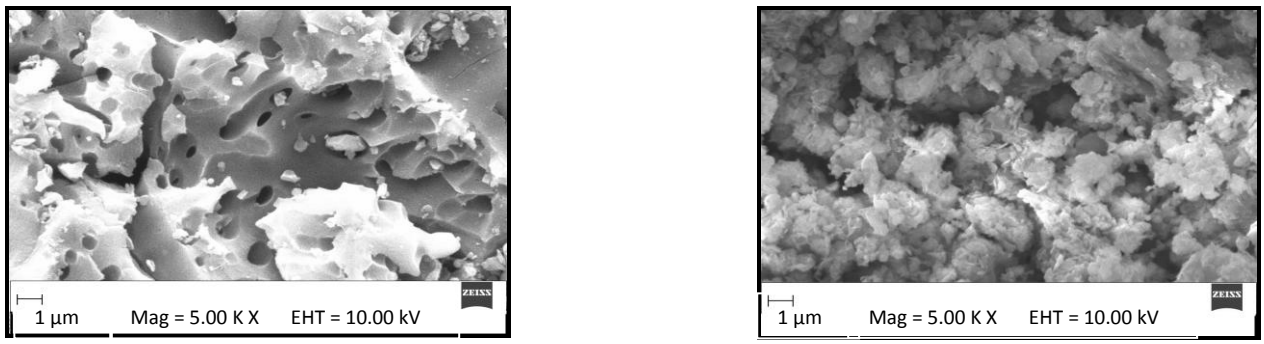

(a) (b)

Fig. 5: SEM images of activated carbon at 5000x magnification: (a) activated carbon; (b) activated carbon supported cobalt catalyst.

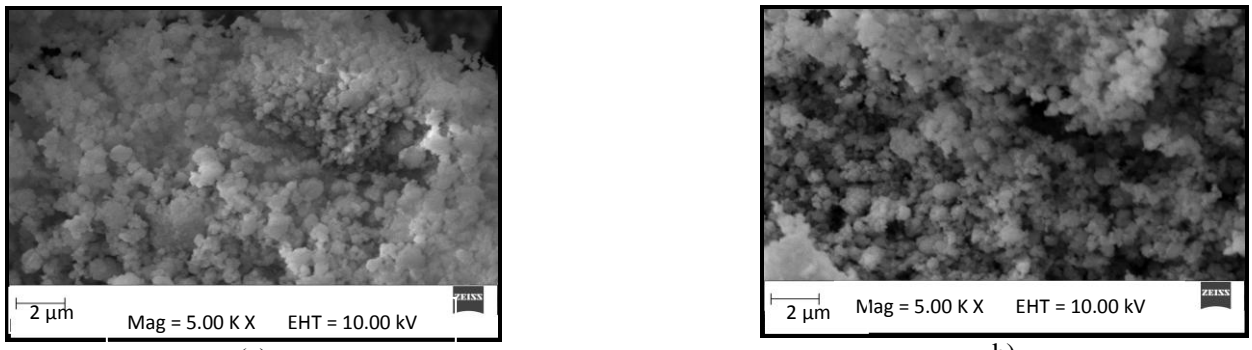

(a) b)

Fig. 6: SEM images of Zeolite ZSM-5 at 5000x magnification: (a) ZSM-5; (b) ZSM-5 supported cobalt catalyst

References

1. Tao C., Li J., Zhang Y. and Liew K.Y., Effect of isomorphic substitution of zirconium on mesoporous silica as support for cobalt Fischer– Tropsch synthesis catalysts, *J. Mol. Catal. A: Chem.*, **331(1, 2)**, 50-57 **(2010)**

2. Knochen J., Güttel R., Knobloch C. and Turek T., Fischer–Tropsch synthesis in milli-structured fixed-bed reactors: Experimental study and scale-up considerations, *Chem. Eng. Process*, **49(9)**, 958-964 **(2010)**

3.Tan K.F., Chang J., Borgna A. and Saeys M., Effect of boron promotion on the stability of cobalt Fischer–Tropsch catalysts, *J. Catal.*, **280(1)**, 50-59 **(2011)**

4.Karimi A., Pour A.N., Torabi F., Hatami B., Tavasoli A., Alaei M. R. and Irani M., Fischer-Tropsch synthesis over ruthenium-promoted Co/Al_2O_3 catalyst with different reduction procedures, *J. Nat. Gas Chem.*, **19(5)**, 503-508 **(2010)**

5.de la Osa A. R., De Lucas A., Díaz-Maroto J., Romero A., Valverde J. L. and Sánchez P., FTS fuels production over different Co/SiC catalysts, *Catal. Today*, **187(1)**, 173-182 **(2012)**

6.Tehrani S., Irani M., Tavasoli A., Mortazavi Y., Khodadadi A. A. and Pour A. N., Studies on accelerated deactivation of ruthenium-promoted alumina-supported alkalized cobalt Fischer-Tropsch synthesis catalyst, *J. Nat. Gas Chem.*, **20(1)**, 65-71 **(2011)**

7. Bao A., Li J. and Zhang Y., Effect of barium on reducibility and activity for cobalt-based Fischer-Tropsch synthesis catalysts,

J. Nat. Gas Chem, **19(6),** 622-627 **(2010)**

8. Rahman M. M. and Yusof A. M., Preparation and Modification of Activated Carbon from Oil-Palm Shell and Its Adsorption Capacity Through Speciation of Chromium, *Res. J. Chem. Environ.*,**15(4),** 49-51 **(2011)**

9.Khobragade M., Majhi S. and Pant K.K., Effect of K and CeO_2 promoters on the activity of Co/SiO_2 catalyst for liquid fuel production from syngas, *Appl. Energy*, **94,** 385-394 **(2012)**

10. Jiao G., Ding Y., Zhu H., Li X., Li J., Lin R., Dong W., Gong L., Pei Y. and Lu Y., Effect of La_2O_3 doping on syntheses of C1–C18 mixed linear α-alcohols from syngas over the Co/AC catalysts, *Appl. Catal. A: Gen*, **364(1,2)** 137-142 **(2009)**

11.Cai Z., Li J., Liew K. and Hu J., Effect of La_2O_3-dopping on the Al_2O_3 supported cobalt catalyst for Fischer-Tropsch synthesis, *J. Mol. Catal. A: Chem*, **330(1,2)** 10-17 **(2010)**

12.Lögdberg S., Lualdi M., Järås S., Walmsley J.C., Blekkan E.A., Rytter E. and Holmen A., On the selectivity of cobalt-based Fischer–Tropsch catalysts: Evidence for a common precursor for methane and long-chain hydrocarbons, *J. Catal*, **274(1)**,**(2010)**

13. Zhou X., Chen Q., Tao Y. and Weng H., Influence of Ultrasound Impregnation on the Performance of $Co/Zr/SiO_2$ catalyst during Fischer-Tropsch Synthesis, *Chinese J. Catal*, **32(6,8),** 1156-1165 **(2011)**

14. Enger B. C., Fossan Å. L., Borg Ø., Rytter E. and Holmen A., Modified alumina as catalyst support for cobalt in the Fischer–Tropsch synthesis, *J. Catal*, **284(1),** 9-22 **(2011)**

15. de la Osa A. R., De Lucas A., Romero A., Valverde J. L. and Sánchez P., Influence of the catalytic support on the industrial Fischer–Tropsch synthetic diesel production, *Catal. Today*, **176(1)**, 298-302 **(2011)**

16. Daud W. M. A. W., Ali W. S. W. and Sulaiman M. Z., The effects of carbonization temperature on pore development in palm-shell-based activated carbon, *Carbon*, **38(14),** 1925-1932 **(2000).**

(Received 20th March 2013, accepted 22nd July 2013)

A kinetic insight into the oxidation of perfumery alcohols by inorganic oxidizing agents

Prabhu D.V.*, Tandel M. A., Parbat H. A. and Uchil Meera H.
Department of Chemistry, Wilson College (University of Mumbai) Mumbai 400007, INDIA
*dvprabhu48@gmail.com

Abstract

Literature survey shows that inorganic salts have rarely been used for the controlled oxidation of alcohols to the corresponding carbonyl compounds. The kinetics of oxidation of perfumery alcohols has been studied using $KBrO_3$ and KIO_3 in acidic medium. The primary acyclic alcohols, geraniol, nerol and citronellol and the secondary cyclic alcohols borneol, isoborneol and menthol are extensively used in the manufacture of perfumes and fragrances. Menthol is also used in medicine as local anesthetic and counter irritant.

The oxidation was carried out under pseudo first order kinetic conditions with respect to the inorganic oxidant. The progress of the reaction was monitored by iodometric estimation of the unreacted oxidant at regular time intervals and the pseudo first order rate constants were determined from the straight line plots of log (a-x) versus time. The oxidation rates increase with the alcohol concentration but decrease with increasing $KBrO_3$/KIO_3 concentration. The oxidation rate was found to be independent of ionic strength as borne out by the reaction mechanism suggested .The oxidation reaction was studied in the temperature range 303-318K and the thermodynamic activation parameters were evaluated and correlated with the dynamics of the oxidation process.

For both the oxidants, the oxidation rates of the alcohols under study follow the sequences:
1) Primary acyclic alcohols: nerol > citronellol > geraniol.

2) Secondary cyclic alcohols: borneol > isoborneol > menthol.

Keywords: Acyclic alcohols, cyclic alcohols, controlled oxidation, inorganic oxidants, reaction mechanism, steric factors, energy of activation, entropy of activation.

Introduction

In our laboratory, the kinetic investigations of the oxidation of a variety of alcohols and phenols have been carried out using different oxidizing agents [4-10]. This paper deals with the kinetics of the controlled oxidation of some acyclic and cyclic alcohols which are widely used in the manufacture of perfumes, fragrances and cosmetics. The acyclic terpenoid alcohol, geraniol is the chief constituent of essential oils and is also used as an insect repellent. $KBrO_3$ and KIO_3 are used as oxidizing agents in acidic medium. $K_2S_2O_8$ was used to study the effect of ionic strength on the oxidation rate of perfumery alcohols.

Material and Methods

Perfumery alcohols were procured from 1) S.H.Kelkar and Co., Mumbai and 2) Shaivi Industries, Lucknow and purified by distillation. The controlled oxidation of alcohols was studied under pseudo first order kinetic conditions with respect to the inorganic oxidants $KBrO_3$ and KIO_3 containing halogen in the +5 oxidation state.

Aliquots of the reaction mixture were withdrawn at regular time intervals, the reaction was quenched using ice and the unreacted oxidant was subjected to iodometry. The pseudo first order rate constants (k) were determined from the linear plots of log (a-x) versus time. The effect of ionic strength on the oxidation rate was studied in dilute solution in the range μ =5.0 to 25.0 x 10^{-2} mol dm^{-3} using K_2SO_4. From the Arrhenius plots of logk versus 1/T, the energy of activation and other thermodynamic activation parameters were evaluated and interpreted.

Results and Discussion

The primary acyclic alcohols, geraniol, nerol and citronellol were oxidized to the corresponding aldehydes by $KBrO_3$/KIO_3. Similarly the secondary cyclic alcohols, borneol, isoborneol and menthol were oxidized to the corresponding ketones.

Effect of alcohol and oxidant concentrations on oxidation rate of alcohols: For all the alcohols studied, the oxidation rate increased with alcohol concentration but decreased with oxidant concentration.

Reaction Mechanism of oxidation of alcohols: In acidic medium, the inorganic oxidants $KBrO_3$ and KIO_3 quickly form the halic acids $HBrO_3$ and HIO_3 respectively which are strong acids as well as strong oxidizing agents[2, 11]. The oxidation of alcohols results in the formation of the corresponding hypohalite ions OBr and OI respectively.

Primary alcohols

$$R\text{-}CH_2\text{-}OH + BrO_3 + 2H^+ \longrightarrow R\text{-}CHO + OBr + 2H_2O$$

$$R\text{-}CH_2\text{-}OH + IO_3 + 2H^+ \longrightarrow R\text{-}CHO + OI + 2H_2O$$

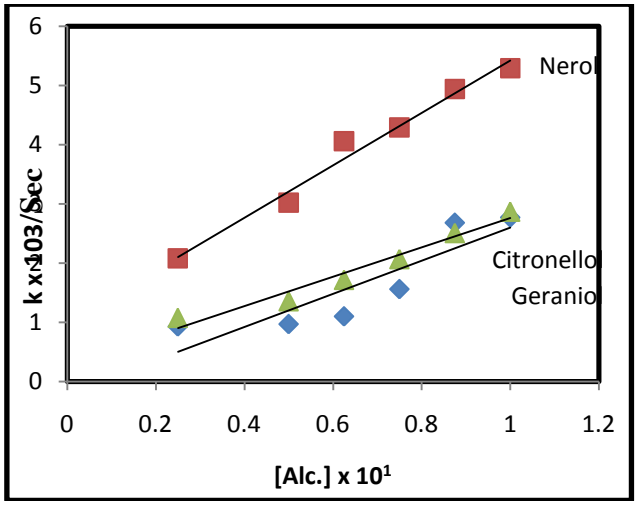

Fig. 1a: Variation of rate constant of oxidation of primary acyclic alcohols by $KBrO_3$ with [Alc.]

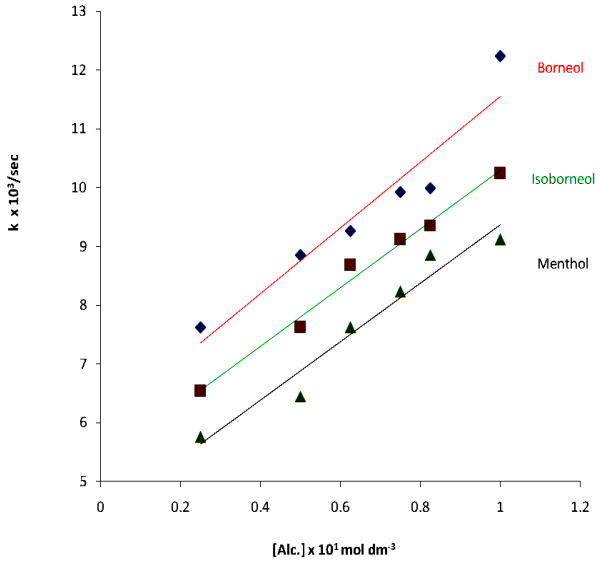

Fig. 1b: Variation of rate constant of oxidation of secondary cyclic alcohols with [Alc.]

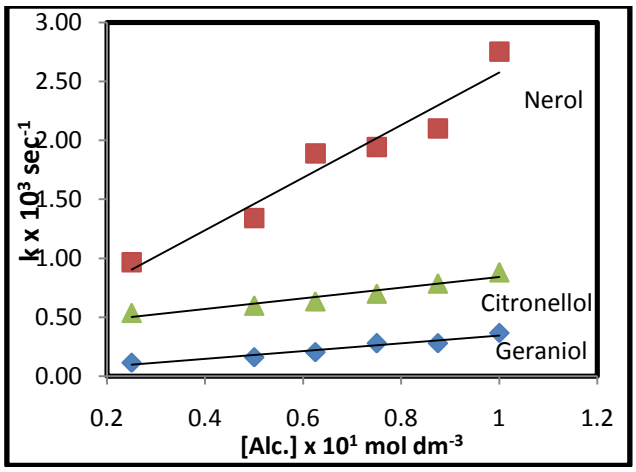

Fig. 2a: Variation of rate constant of oxidation of primary acyclic alcohols by KIO_3 with [Alc.]

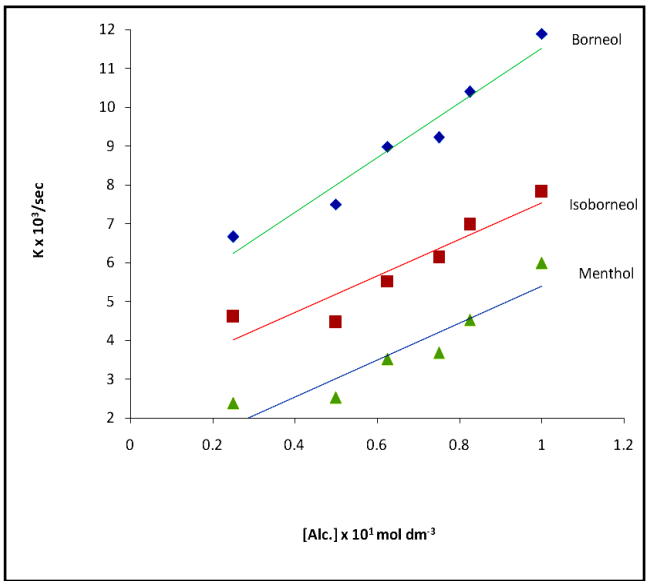

Fig. 2b: Variation of rate constant of oxidation of secondary cyclic alcohols with [Alc.]

The unreacted $KBrO_3$ / KIO_3 was estimated by treatment with ice cold KI in dil. H_2SO_4 and subsequent titration of the liberated iodine against standard $Na_2S_2O_3$ solution.

$$BrO_3^- + 6I^- + 6H^+ \longrightarrow 3I_2 + Br^- + 3H_2O$$

$$IO_3^- + 5I^- + 6H^+ \longrightarrow 3I_2 + 3H_2O$$

Secondary alcohols:

$$R_2\text{-}CH\text{-}OH + BrO_3 + 2H^+ \longrightarrow R_2\text{-}C{=}O + OBr + 2H_2O$$

$$R_2\text{-}CH\text{-}OH + IO_3 + 2H^+ \longrightarrow R_2\text{-}C{=}O + OI + 2H_2O$$

The unreacted oxidants were estimated iodometrically. The product of the reaction i.e. aldehyde/ketone was identified by 2, 4-dinitrophenyl hydrazone test and confirmed by TLC. The oxidation rates follow the same sequence for both oxidants:

Primary acyclic alcohols: nerol > citronellol > geraniol (Tables 1a and 2a, Figures 1a and 2a). The relative oxidation rates of the primary acyclic alcohols under study are consistent with their steric effects on the oxidation. Thus nerol undergoes fastest oxidation and geraniol is least susceptible to oxidation.

Secondary cyclic alcohols: borneol > isoborneol > menthol (Tables 1b and 2b, Figures 1b and 2b).

Borneol has the least hindered α hydrogen, hence its oxidation is the fastest whereas menthol has the most hindered α hydrogen, hence it undergoes slowest oxidation. For all the alcohols studied, $KBrO_3$ is a stronger oxidizing agent than KIO_3.

Table 1
Rate constant data for the oxidation of perfumery alcohols by $KBrO_3$ in 0.05 M H_2SO_4 Temperature = 303 K.

A: Primary acyclic alcohols

[Alc.]x10^1 mol dm^{-3}	**[$KBrO_3$]x10^3 mol dm^{-3}**	**Nerol**	**Citronellol**	**Geraniol**
		k x 10^3 s^{-1}	k x 10^3 s^{-1}	k x 10^3 s^{-1}
1.00	2.50	5.52	3.93	3.13
1.00	5.00	5.29	2.86	2.79
1.00	10.00	4.64	2.67	0.99
1.00	15.00	1.25	2.57	0.97
1.00	20.00	0.91	2.20	0.95
1.00	25.00	0.68	3.29	0.87
0.25	5.00	2.08	1.08	0.93
0.50	5.00	3.02	1.36	0.97
0.63	5.00	4.06	1.72	1.10
0.75	5.00	4.29	2.07	1.56
0.88	5.00	4.94	2.51	2.68
1.00	5.00	5.29	2.87	2.77

B: Secondary cyclic alcohols

[Alc.] x 10^1 mol dm^{-3}	**[$KBrO_3$] x 10^3 mol dm^{-3}**	**Borneol**	**Isoborneol**	**Menthol**
		k x 10^3 s^{-1}	k x 10^3 s^{-1}	k x 10^3 s^{-1}
1.00	2.50	12.90	10.91	10.17
1.00	5.00	10.24	9.58	9.35
1.00	10.00	9.64	9.46	7.62
1.00	15.00	9.02	8.94	7.72
1.00	20.00	8.38	9.34	6.91
1.00	25.00	7.27	7.66	6.08
0.25	5.00	7.62	6.54	5.76
0.50	5.00	8.85	7.62	6.45
0.63	5.00	9.26	8.68	7.62
0.75	5.00	9.92	9.12	8.23
0.88	5.00	9.99	9.36	8.86
1.00	5.00	12.24	10.24	9.12

Table 2
Rate constant data for the oxidation of perfumery alcohols by KIO_3 in 0.05M H_2SO_4 Temperature = 303 K.
A: Primary acyclic alcohols

[Alc.] x 10^1 mol dm^{-3}	[KIO_3] x 10^3 mol dm^{-3}	Nerol	Citronellol	Geraniol
		k x 10^3 s^{-1}	k x 10^3 s^{-1}	k x 10^3 s^{-1}
1.00	2.50	3.92	0.92	0.66
1.00	5.00	2.80	0.88	0.37
1.00	10.00	1.43	0.77	0.42
1.00	15.00	0.74	0.21	0.39
1.00	20.00	0.48	0.28	0.24
1.00	25.00	3.92	0.92	0.66
0.25	5.00	0.97	0.54	0.11
0.50	5.00	1.34	0.60	0.16
0.63	5.00	1.89	0.64	0.20
0.75	5.00	1.94	0.70	0.28
0.88	5.00	2.10	0.79	0.28
1.00	5.00	2.75	0.88	0.37

B: Secondary cyclic alcohols

[Alc.]x10^1 mol dm^{-3}	[KIO_3]x 10^3 mol dm^{-3}	Borneol	Isoborneol	Menthol
		k x 10^3 s^{-1}	k x 10^3 s^{-1}	k x 10^3 s^{-1}
1.00	2.50	10.06	7.29	8.06
1.00	5.00	9.78	6.91	5.07
1.00	10.00	7.68	6.21	1.84
1.00	15.00	6.56	5.91	1.61
1.00	20.00	5.76	5.09	1.61
1.00	25.00	3.47	4.61	1.38
0.25	5.00	6.67	4.61	2.38
0.50	5.00	7.51	4.47	2.53
0.63	5.00	8.99	5.53	2.76
0.75	5.00	9.23	6.13	3.68
0.88	5.00	10.40	7.23	5.53
1.00	5.00	11.90	7.83	5.99

Table 3
Effect of Ionic Strength on the oxidation rates of perfumery alcohols by $KBrO_3$ in 0.05 M H_2SO_4
A: Primary acyclic alcohols
[Alc] = 0.1 M, [H_2SO_4] = 2.5 x10^{-2}M, [$KBrO_3$] = 2.5 x10^{-3} M, Temperature = 313 K

[K_2SO_4] μ x 10^2 mol dm^{-3}	Nerol	Citronellol	Geraniol
	k x 10^3 s^{-1}	k x 10^3 s^{-1}	k x $10^3 s^{-1}$
0.00	4.97	2.10	2.79
5.00.	5.16	2.28	2.70
10.00	4.93	2.04	2.52
15.00	5.15	2.10	2.86
20.00	5.10	2.15	2.52
25.00	4.97	2.10	2.57

B: Secondary cyclic alcohols
[Alc] = 0.1 M, [H_2SO_4] = 2.5 x10^{-2}M, [$KBrO_3$] = 2.5 x10^{-3} M, Temperature = 313 K

[K_2SO_4] μ x 10^2 mol dm^{-3}	Borneol	Isoborneol	Menthol
	k x 10^3 s^{-1}	k x 10^3 s^{-1}	k x $10^3 s^{-1}$
0.00	10.20	9.26	6.91
5.00.	10.24	9.24	6.58
10.00	10.14	9.26	6.59
15.00	10.12	9.24	6.91
20.00	10.32	9.24	6.08
25.00	10.24	9.42	6.08

Table 4
Effect of Ionic Strength on the oxidation rates of perfumery alcohols by KIO_3 in H_2SO_4
[Alc] = 0.1 M, [H_2SO_4] = 2.5 x10^{-2}M, [KIO_3] = 2.5 x10^{-3} M, Temperature = 313 K
A: Primary acyclic alcohols

[K_2SO_4] μ x 10^2 mol dm^{-3}	Nerol	Citronellol	Geraniol
	k x 10^3 s^{-1}	k x 10^3 s^{-1}	k x $10^3 s^{-1}$
0.00	1.34	0.79	0.39
5.00.	1.32	0.79	0.41
10.00	1.33	0.78	0.39
15.00	1.38	0.77	0.42
20.00	1.38	0.79	0.39
25.00	1.38	0.81	0.40

B: Secondary cyclic alcohols
[Alc] = 0.1 M, [H_2SO_4] = 2.5 x10^{-2}M, [KIO_3] = 2.5 x10^{-3} M, Temperature = 313 K

[K_2so_4] μ x 10^2 mol dm^{-3}	Borneol	Isoborneol	Menthol
	K x 10^3 s^{-1}	K x 10^3 s^{-1}	K x 10^3s^{-1}
0.00	7.82	5.52	2.76
5.00.	7.84	5.51	2.84
10.00	7.12	5.52	2.76
15.00	7.25	5.03	2.84
20.00	7.68	5.67	2.69
25.00	7.68	5.67	2.81

Table 5
Thermodynamic activation parameters for the oxidation of perfumery alcohols by $KBrO_3$ in H_2SO_4
A: Primary acyclic alcohols

	Temp. K	Rate constant k x 10^3 s^{-1}	E_a kJ mol^{-1}	K* x10^{16}	ΔH* kJ mol^{-1}	ΔG* kJ mol^{-1}	ΔS* kJ $K^{-1}mol^{-1}$
NEROL	303	4.97	2.01	7.81	0.64	87.63	—0.2909
	308	5.04	2.01	7.82	0.59	89.08	—0.2910
	313	5.10	2.01	7.86	0.55	90.54	—0.2912
	318	5.17	2.01	7.87	0.51	91.99	—0.2913
CITRO NELLOL	303	2.86	11.73	4.53	9.22	89.02	—0.2634
	308	3.02	11.73	4.70	9.17	90.39	—0.2637
	313	3.46	11.73	5.30	9.13	91.55	—0.2633
	318	3.52	11.73	5.31	9.09	93.01	—0.2639
GERANIOL	303	2.89	53.83	1.39	51.31	94.79	—0.1435
	308	2.93	53.83	1.41	51.27	96.36	—0.1464
	313	6.72	53.83	3.23	51.22	95.81	—0.1425
	318	7.02	53.83	3.37	51.18	97.27	—0.1449

B: Secondary cyclic alcohols

	Temp. K	Rate constant k x 10^3 s^{-1}	E_a kJ mol^{-1}	K* x10^{16}	ΔH* kJ mol^{-1}	ΔG* kJ mol^{-1}	ΔS* kJ $K^{-1}mol^{-1}$
BORNEOL	303	10.24	11.30	1.62	8.78	85.80	—0.2542
	308	10.96	11.30	1.71	8.74	87.09	—0.2544
	313	12.55	11.30	1.92	8.70	88.19	—0.2540
	318	15.82	11.30	2.70	8.65	88.71	—0.2518
ISO BORNEOL	303	9.23	11.72	1.46	9.20	86.06	—0.2537
	308	9.74	11.72	1.52	9.16	87.39	—0.2540
	313	11.30	11.72	1..73	9.12	94.46	—0.2726
	318	12.89	11.72	1.95	9.08	95.66	—0.2723

MENTHOL	303	6.58	12.14	1.04	9.42	86.91	—0.2551
	308	8.61	12.14	1.34	9.58	87.71	—0.2537
	313	10.00	12.14	1.53	9.54	94.78	—0.2723
	318	12.13	12.14	1.82	9.50	95.82	—0.2715

Table 6
Thermodynamic activation parameters for the oxidation of some perfumery alcohols by KIO_3 in H_2SO_4
A: Primary acyclic alcohols

	Temp. K	Rate constant k x 10^3 s^{-1}	E_a kJ mol^{-1}	K* x10^{16}	ΔH* kJ mol^{-1}	ΔG* kJ mol^{-1}	ΔS* kJ $K^{-1}mol^{-1}$
NEROL	303	2.80	7.94	7.81	5.42	87.63	—0.2713
	308	3.03	7.94	7.82	5.38	89.08	—0.2718
	313	3.16	7.94	7.86	5.34	90.54	—0.2722
	318	3.25	7.94	7.87	5.29	91.99	—0.2726
CITRO NELLOL	303	0.598	13.27	0.95	10.75	92.96	—0.2713
	308	0.624	13.27	0.97	10.71	94.43	—0.2718
	313	0.668	13.27	1.02	10.67	95.83	—0.2721
	318	0.780	13.27	1.18	10.63	96.99	—0.2716
GERANIOL	303	0.291	58.53	0.46	56.02	94.78	—0.1279
	308	0.349	58.53	0.54	55.97	95.92	—0.1297
	313	0.669	58.53	1.03	55.93	95.82	—0.1274
	318	0.831	58.53	1.25	55.89	96.82	—0.1287

B: Secondary cyclic alcohols

	Temp. K	Rate constant k x 10^3 s^{-1}	E_a kJ $mol^{—1}$	K* x10^{16}	ΔH* kJ $mol^{—1}$	ΔG* kJ mol^{-1}	ΔS* kJ $K^{-1}mol^{-1}$
BORNEOL	303	5.76	29.83	0.91	27.31	93.05	—0.2170
	308	7.85	29.83	1.22	27.27	93.84	—0.2162
	313	10.16	29.83	1.56	27.23	94.73	—0.2152
	318	15.59	29.83	2.35	27.19	95.15	—0.2143
ISO BORNEOL	303	5.51	33.52	0.87	31.00	93.16	—0.2052
	308	7.12	33.52	1.11	30.95	94.09	—0.2050
	313	9.03	33.52	1.38	30.91	95.04	—0.2049
	318	10.18	33.52	1.54	30.87	96.28	—0.2057
MENTHOL	303	1.38	53.91	2.19	51.39	96.65	—0.1494
	308	1.84	53.91	2.87	51.34	97.55	—0.1500
	313	2.77	53.91	4.24	51.31	98.12	—0.1496
	318	3.69	53.91	5.56	51.27	98.47	—0.1500

Effect of ionic strength on oxidation rate of alcohols: K_2SO_4 was used in the range μ= 5.0 to 25.0 x 10^{-2} mol dm^{-3} at 313K to study the effect of ionic strength on oxidation rate of alcohols [Tables 3a and 3b ($KBrO_3$), 4a and 4b (KIO_3)]. The graphs of log k versus √μ were found to be straight lines parallel to the √μ axis indicating that the

oxidation rate is independent of ionic strength. This observation is supported by the reaction mechanism of the oxidation of alcohols by inorganic oxidants.

Effect of temperature on oxidation rate of alcohols: The oxidation was carried out in the temperature range 303-318K and the thermodynamic activation parameters were calculated [Tables 5a and 5b ($KBrO_3$), 6a and 6b (KIO_3)].

The important findings from the thermodynamic study are:

1) The rate constant of oxidation (k) is inversely proportional to the energy of activation (E).
2) The equilibrium constant (K*) for the formation of the activated complex from the reactants, increases with temperature. Hence like k, K* is a function of temperature.

3a) For a given alcohol, the entropy of activation (Δ S*) is constant at all temperatures indicating that the site of oxidation of alcohol remains the same at all temperatures.

3b) The negative values of (Δ S*) indicate a decrease in the degrees of freedom due to the formation of a rigid activated complex during the course of the reaction and reorientation of the solvent molecules around the activated complex[1,3]. This can be explained by a model in which the solvent molecules are tightly held to the -OH bond which is the site of oxidation of alcohols.

Conclusion

For both oxidants $KBrO_3$ and KIO_3, the oxidation rates follow the sequences:

Primary acyclic alcohols: nerol > citronellol > geraniol
Secondary cyclic alcohols: borneol > isoborneol >menthol.

For all the perfumery alcohols, $KBrO_3$ is a stronger oxidizing agent than KIO_3. The oxidation rates increase with alcohol concentration but decrease with oxidant concentration. Ionic strength has no effect on the oxidation rates of the perfumery alcohols under investigation.

Acknowledgement

Authors wish to acknowledge the valuable help rendered by Himanshu Gupta, Asiya Kasmani and Sangeeta Yadav in the kinetic study of oxidation of perfumery alcohols.

References

1. Amis E.S., Kinetics of chemical change in solution, The Macmillan Co., New York (**1949**)

2. Ananda S. and Gopalan R., *J. Ind. Chem. Soc.*, **62**, 216 (**1985**)
3. Eichhorn G. L. and Trachtenberg I. M., *J. Am. Chem. Soc.*, **76**, 5184 (**1954**)

4. Prabhu D.V., Kinetics and reaction mechanism of the controlled oxidation of some Industrial alcohols, *J. Ind. Chem. Soc.*, **84**, 1135 **(2007)**

5. Prabhu D.V., Reaction kinetics and mechanism of the transition metal ion catalysed oxidation of some cyclic alcohols, Proceedings of the Third International Congress of Chemistry and Environment (Research Journal of Chemistry and Environment), Kuwait City, 126-132 **(2007)**

6. Prabhu D.V., Tandel M.A. and Tandel Parbat H. A., Oxidation studies of some acyclic and cyclic alcohols, Proceedings of the Fourth International Congress of Chemistry and Environment, Ubonratchathani, Thailand, *Res. J. Chem. Environ.*, 169-172 **(2010)**

7. Prabhu D.V., Parbat H. A. and Tandel M.A., A kinetic approach to the oxidation of some perfumery alcohols by N-Bromosuccinimide in alkaline medium, *Asian J. Chem.*, **23(12),** 5495 **(2011)**

8. Prabhu D.V., Tandel M.A. and Parbat H.A., Kinetic and thermodynamic studies of the oxidation of eugenol and isoeugenol by Sodium-N-chlorotoluene-p-sulphonamide in NaOH, *Asian J. Chem.*, **23(12),** 5503 **(2011)**

9. Prabhu D.V., Tandel M.A., Parbat H.A. and Uchil Meera H., Kinetic aspects of the oxidation of perfumery phenols, *Asian J.Chem.,* **24(12),** 5691 **(2012)**

10. Prabhu D.V., Parbat H. A. and Tandel M.A., Kinetic studies of the transition metal ion catalysed oxidation of some fragrance alcohols, *J. Indian Council of Chemists* **(2012)**

11. Shukla P.S. and Mehrotra R.N., *J. Inorg. Nucl. Chem.*, **35**,891 **(1973).**

(Received 15th March 2013, accepted 25th July 2013)

The role of threshold inhibitors on water scale precipitation from tap water

Danijela Dobersek* and Darko Goricanec
University of Maribor, Faculty of Chemistry and Chemical Engineering, Smetanovaul 17, 2000 Maribor, SLOVENIA
*danijela.dobersek@um.si

Abstract
This paper presents research results on how threshold inhibitors influence on water-scale precipitation and morphology. The inhibitory effect was evaluated from observing two experiments in regard to water-scale precipitation. The first experiment was conducted on heaters from a boiler for hot water and outflow pipes. The second experiment was carried-out on washing machine heaters. In both cases, tap water was used that contained Mg^{2+} and Zn^{2+} ions. In all the samples the hard, compact water scale was in the shape of aragonite.

Keywords: Scale control, threshold inhibitors, morphology, crystallisation.

Introduction

Water-scale precipitation is a serious problem in many industrial processes as well as within households, in fact literally everywhere regarding natural water usage. The supplied water is usually oversaturated with calcium carbonate. The conditions for over saturation are very often achieved during industrial operations and that is why the water scale precipitates on heat-transfer surfaces within cold water systems as well as in high temperature systems. The accumulation of scale deposits is a common and costly problem during many industrial processes.

The consumption of drinking and industrial water is increasing. The whole world is searching for new ways of ensuring suitable amounts of water and accordingly thinks about how to use energy more efficiently, so it is reasonable to search for a solution regarding scale-reduction[1-3]. The concept of water hardness occurs due to different inorganic salts that are composed of earth–alkaline metal ions[4]. Natural waters contain some ions (Fe^{2+}, Mg^{2+}, Zn^{2+}, etc.) in very small concentrations which are capable to retarding the formation of calcite and consequently provide the priority for aragonite precipitation even at room temperature[5,6].

This study presents the results of various experiments for water-scale elimination from tap water. Water with relatively high hardness was used, together with some other metal ions in very small concentrations. The results from all the different experiments were the same. The water scale was very hard and compact but was in the shape of aragonite. It has been considered for a long time that aragonite precipitates within a porous, easily removable structure whilst the calcite is hard and difficult to remove scale[7-9].

Precipitation and crystal structures of calcium carbonate: In most cases, $CaCO_3$ is a dominant component because natural waters are rich with Ca^{2+} ions and carbonic species (CO_2, HCO_3^-, CO_3^{2-}). CO_2 from the air dissolves in water where a weak carbonic acid is formed which dissociates in two steps[10]:

$$H_2CO_3 \leftrightarrow H^+ + HCO_3^- \quad (1)$$

$$HCO_3^- \leftrightarrow H^+ + CO_3^{2-} \quad (2)$$

Carbonate ions react with Ca^{2+} ions and a very slightly soluble calcium carbonate is precipitated according to equation (3):

$$Ca(HCO_3)_{2\,(aq)} \leftrightarrow CaCO_{3\,(s)} + CO_{2\,(g)} + H_2O \quad (3)$$

The relationship between the Ca^{2+} concentration (5), depending of the pH, is derived from the term of the solution´s electro-neutrality and by considering equations (1), (2) and (4).

$$2c_{Ca^{2+}} + c_{H^+} = 2c_{CO_3^{2-}} + c_{HCO_3^-} + c_{OH^-} \quad (4)$$

$$c_{Ca^{2+}} = \frac{K_w - c_{H^+}^2 + \sqrt{\left(c_{H^+}^2 - K_w\right)^2 + 8K_s\, c_{H^+}^2 \left(2 + \frac{c_{H^+}}{K_2}\right)}}{4c_{H^+}} \quad (5)$$

where $c_{Ca^{2+}}$ is concentration of Ca^{2+} [mol/l], c_{H^+} is concentration of H^+ [mol/l], K_w is water ionic product and K_s is solubility product of $CaCO_3$.

$CaCO_3$ starts to precipitate when the concentration of Ca^{2+} ions is grater than the equilibrium. The precipitated $CaCO_3$ may be a mixture of crystalline phases, amorphous and hydrated phases. The crystalline phases are[11]:

- Calcite (rhomboedral structure) (Fig. 1a),
- Aragonite (orthorhombic structure) (Fig. 1b),
- Vaterit (hexagonal structure) (Fig. 1c).

Their stabilities are falling according to the listed order. Very often aragonite precipitates first, more rarely vaterit, which then crystallises into more stable calcite.

The role of thresholds inhibitors on scale formation: In water processes, which are usually supplied from tap water containing different ions, the nucleation is important as the first step of the crystallisation. Crystallisation mostly occurs on the surfaces of the dispersed particles and especially on the walls of pipelines and heating equipment. The composition and structure of precipitated scale also depends on the material on which the nucleation had started. The more important threshold inhibitors for water scale precipitation are definitely Mg^{2+} and Zn^{2+} ions.

The effect of Mg^{2+} ions: Inhibition of $CaCO_3$ crystallisation by magnesium ion has been studied by number of investigators. Gutjahr et al[6] reported about the efficient inhibition of aragonite to calcite transformation in the presence of Mg^{2+} ions even at very low concentrations. The experiments were done on pure solutions where Mg^{2+} ions were added in different concentrations. The results showed that the calcite growth was inhibited at a concentration greater than 10^{-3}mol/l.

Kiatmura[12] has reported that magnesium ions suppress the transformation of vaterite by inhibiting the growth of the calcite. Magnesium ion is selectively included within calcite, causes an increase of the attained concentration and a remarkable change in the morphology of calcite, especially in 0.05 mol/l solution. An experiment was done with a prepared solution from $CaCl_2$ and Na_2CO_3 by adding Mg^{2+} ions.

The results of researchers indicate that Mg^{2+}cations slow the rate of calcite dissolution by adsorbing on mineral surface in competition with Ca^{2+} ions, so reducing the number of empty sits in order to receive dissolving lattice Ca^{2+} ions[13].

Reddy and Wang[14] had experimentally confirmed that at 10^{-3}mol/l Mg^{2+} ion greatly reduced the calcite crystallisation, yet at10^{-5}mol/l it had almost no effect. At Mg^{2+} concentrations greater than 10^{-3}mol/l separate magnesium – rich phase may form and may become a significant kinetic factor[14].

The effect of Zn^{2+} ions: Since $CaCO_3$ precipitation reaction is known to be extremely sensitive to impurity ions, even at ultra - trace concentration levels. Zn^{2+} could be released from the devices' surfaces (pipes, heater, etc.) in very small concentrations and effect the crystal morphology changes and the reduced nucleation rate. Cotzzee at al[15,16] have showed that the emission of zinc from three different types of physical water treatment devices can affect the rate of $CaCO_3$ crystallisation and also cause changes to the crystal morphology and promote crystallisation in the aragonite rather than calcite even under conditions where calcite would be preferred in crystalline form.

The fact that ionic impurities can influence crystallisation reactions is very well known. Meyer[5] has studied the effect of impurities on the crystal growth rate of calcite and has reported that 2×10^{-7}mol/l Zn^{2+} ions can reduce the crystal growth rate in calcite by 80%.

(a) (b) (c)

Fig. 1: Crystals of (a) calcite, (b) aragonite and (c) vaterit[11]

Material and Methods

The causes of intensity of scale precipitation on washing machine heaters and in boilers for hot water were examined with a view to investigate the phenomena of scale formation from tap water.

The tap water used during the experiments had a total hardness of 14.7 °n and pH 7.5. The results from the chemical analysis for this water are presented in table 1.

Scale on washing machine heaters: The experiment regarding water scale precipitation from tap water without washing powders or any other additives was done in four washing machines where 2,000 W heaters were built in. Testing included 300 washing cycles with tap water at 95°C. Figure 2 shows heaters from washing machines after the experiment.

Table 1
Results of chemical analysis for tap water

Parameter	Value
Carbonate hardness (KT)	12.5°n
Noncarbonated hardness (NKT)	2.2°n
Calcium hardness (CaT)	10.7°n
Magnesium hardness (MgT)	4°n
Ca^{2+}	2 mmol/l
Mg^{2+}	0.75 mmol/l
Fe^{2+}	< 0.0018 mmol/l
Zn^{2+}	< 0.0015 mmol/l

First machine

Second machine

Third machine

Fourth machine

Fig. 2: Precipitated scale in the heaters after the experiment

.

The water-scale samples from the heaters were analysed using X – ray diffraction[17]. It was determined from the spectra (Figure 3) that all the water-scale samples were in the shape of aragonite. Additionally, micro structure analyses were done for the scale samples. The results are presented in figure 4 where the needles of aragonite can be seen.

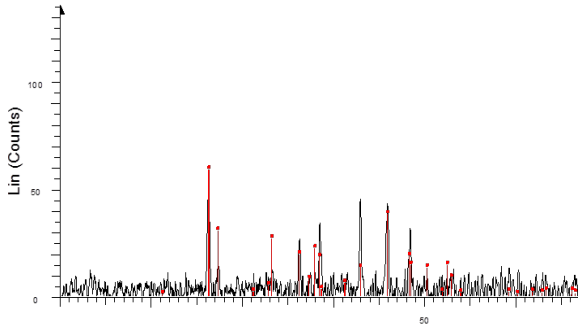

Fig 3: Spectra from X – ray diffraction

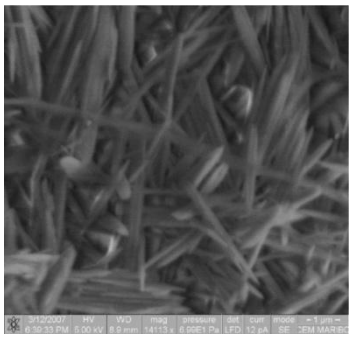

Fig. 4: Snapshot of scale sample with laser electronic microscope

Scale on a heater within the boiler for hot water: The experimental line in figure 5 was installed for studying the scale-precipitations on the heaters in the boiler for hot water and the outlet pipes. The line was supplied by tap water at an adjusted input (0.2 l/min) running continuously for three weeks at 70°C.

The scale precipitated on the heater within the boiler started to crack after the lining had reached a particular thickness and husks were accumulated on the bottom of the boiler (Fig. 6 a). The scale also precipitated within the outlet Zn – coated steel pipes (Fig. 6 b).

The samples data were collected using X – ray diffraction. The spectres for both samples were practically identical to figure 3 and identified as aragonite. In addition, the micrographs of the scale samples observed by the laser electronic microscope were the same as in figure 4.

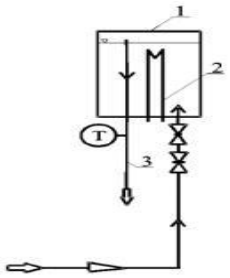

Fig. 5: The experimental line (1 – boiler, 2 – heater, 3 - outlet Zn coated pipe)

(a)

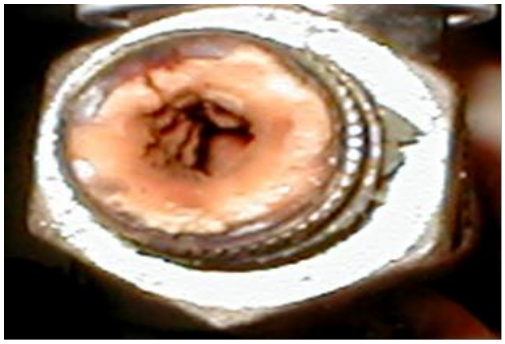

(b)

Fig. 6: Photographs of scales after the experiment: a) sediment in the boiler b) Zn- coated steel pipes

Results and Discussion

Very often a less stable phase occurs at first which is subsequently transformed into a more stable one. The kinetics of such transformation may be hindered or even suppressed by additives, so that less stable phase is found under conditions that are incompatible with its thermodynamic stability[18]. The tap water during our experiment had a concentration Fe^{2+} ions of less than 2×10^{-6}mol/l, the concentrations of Mg^{2+} and Zn^{2+} ions were higher than the minimal concentration required for efficient calcite inhibition.[6,12,15,16,19] According to the magnesium concentration and high – temperature conditions, all samples were identified as aragonite.

In literature[7-9], there is a general opinion that calcite is responsible for hard scales because it forms rhombohedra crystals which are highly adhesive whilst the presence of needle like crystals of aragonite is the main factor for the formation of softer, porous and more soluble deposits. The results of our experiments did not confirm the before-mentioned fact. All the samples of water-scale were identified as aragonite although the structure was very hard and difficult to remove from the heaters` surfaces.

Conclusion

Water scale precipitation from tap water was observed within different experiments at high temperature. All the scale samples were analysed by X – ray diffraction and an electronic laser microscope. The results have shown that in all the scale samples were aragonite and not calcite. This presented fact confirms that the presence of Mg^{2+} and Zn^{2+} ions in very small concentrations affects the crystallisation process and inhibits calcite precipitation which is in accordance with the research results of other authors.[5,6,12,15,16,19]

The very hard and compact structure of the participated water-scale in the shape of aragonite was mostly the result of parallel arranged crystals. The experimental results proved that also aragonite can also form hard and difficult to remove structures and not only calcite[7-9].

References

1. Dobersek D. and Goricanec D., Influence of water scale on thermal flow losses of domestic appliance, *International Journal of mathematical models and methods in applied sciences*, **1(2),** 55-61 (**2007**)

2. Jamsek M., Dobersek D., Goricanec D. and Krope J., Determination of optimal district heating pipe network configuration, *WSEAS transactions on fluid mechanics*, **5 (3),** 165-174 (**2010**)

3. Krope J., Dobersek D. and Goricanec D., Economic evaluation of possible use of heat of flue gases in a heating plant, *WSEAS transactions on heat and mass transfer*, **1,** 75-80 (**2006**)

4. Harris D. C., Quantitative chemical analyses, Freeman, New York (**1995**)

5. Meyer H. J., The influence of impurities on the growth rate of calcite, *Journal of Crystal Growth*, **66,** 639–646 (**1984**)

6. Gutjahr A., Dabringhaus H. and Leemannm R., Studies of the growth and dissolution kinetics of CaC_{O3} polymorphs calcite and aragonite, II, The influence of divalent cations additives on the growth and dissolution rates, *Journal of Crystal Growth*, **158**, 310–315 (**1996)**

7. Higashitani K., Kage A., Katamura S., Imai K. and Hatade S., Effects of magnetic field on the formation $CaCO_3$ particles, *Journal of Colloid and Interface Science*, **156**, 90–95 (**1993**)

8. Barret R.A. and Parsons S.A., The influence of magnetic fields on calcium carbonate precipitation, *Water Research*, **32(3),** 609–612 (**1998**)

9. Coey J.M.D. and Cass S., Magnetic Water Treatment, *Journal of Magnetism and Magnetic Materials*, **209**, 71–74 (**2000**)

10. Lpez Lara T., Hernndez Zaragoza J. B., Prez Rea M. L., Lpez Cajn C. and Castao V. M., Reaction Kinetics of an Expansive Soil Stabilized with Calcium Oxide, *Res. J. Chem. Environ.*, **10(1)**, (**2006**)

11. Reede R. J., Carbonates mineralogy and chemistry, Book Crafters, Michigan (**1983**)

12. Kitamura M., Crystallization and transformation mechanism of calcium carbonate polymorphs and the effect of magnesium ion, *Journal of Colloid and Interface Science*, **236**, 318–327 (**2001**)

13. Compton R. G. and Brown C. A., The inhibition of calcite dissolution/precipitation; Mg^{2+}cations, *Journal of colloid and interface science,* **165**, 445–449 (**1994**)

14. Reddy M. M. and Wang K. K., Crystallization of calcium carbonate in the presence of metal ions, *Journal of crystal growth,* **50**, 470 – 480 (**1980**)

15. Coetzee P. P., Yacoby M. and Howell S., The role of zinc in magnetic and other physical water treatment methods for the prevention of scale, *Water SA,* **22(4),** 319 – 326 (**1996**)

16. Coetzee P.P., Yacoby M., Howell S. and Mubenga S., Scale reduction and scale modification effects induced by Zn and other metal species in physical water treatment, *Water SA,* **24 (1),** 77-84 (**1997**)

17. Kristl M., Hojnik N., Gyergyek S. and Drofenik M., Sonochemical preparation of copper sulfides with different phases in aqueous solutions, *Mater. res. bull.*, **48,** (**2013**)

18. Reddy M.M. and Nancollas G.H., Crystalization of calcium carbonate, Isotopic exchange and kinetics, *Journal of Crystal Growth,* **35**, 33–38 (**1976**)

19. Kitano Y., Kanamori N. and Yoshioka S., Adsorption of zinc and cooper ions on calcite and aragonite and its influence on the transformation of aragonite and calcite, *Geochemical journal,* **10**, 175– 79 (**1976**).

(Received 18th March 2013, accepted 28th July 2013)

Modelling of Dilution of Thermal Discharges in Enclosed Coastal Waters

Balas Lale[1], İnan Asu[2*] and Numanoğlu Genç Aslı[3]
Gazi University, Coastal and Marine Sciences Application and Research Center 06570, Ankara, TURKEY
*asuinan@gazi.edu.tr

Abstract
In enclosed coastal areas, such as estuaries and bays, where water exchange is limited, the discharges of industrial and power plant facilities result in change in the temperature of water. This change threats significantly living organisms in the water. For this reason, the effects of heated discharges must be investigated prior to discharging, considering its near field and far field dilutions. The near field and far field dilutions of thermal discharges are simulated by HYDROTAM-3D which is an unsteady three-dimensional baroclinic hydrodynamic and transport model that has been developed to simulate the transport processes in coastal water bodies. It has hydrodynamic, transport, turbulence and wave model components.

The model computes the full spatial distribution of velocities of unsteady flow induced by wind, tide or water density differences solving full Navier-Stokes equations with only Boussinesq approximation. The transport model component consists of the pollutant transport model, the water temperature and salinity transport models and the suspended matter transport. The numerical model includes thermohaline forcing due to changes in the sea water density.

To consider the large scale turbulence caused by the horizontal shear, horizontal eddy viscosity is simulated by the Smagorinsky algebraic subgrid scale turbulence model. The pollutant transport model can simulate the near and far field dilutions of sea outfalls with a dynamic coupling. Pollutant may be bacteria or heated water. HYDROTAM-3D is integrated with GIS. In the model, wind and wave climate analyses of Turkish coast line exist. Turkish coastline and most of the Turkish Bay bathymetries are provided on GIS mapping. Effect of a thermal discharge rate of 56000 m^3/hour is investigated with its coupled near field and far field dilution modelling.

Keywords: Modelling, thermal discharge, dilution, hydro-dynamics, wind climate, wave climate.

Introduction

The discharge of heated water into the sea environment is an important reason for the water pollution since the whole ecosystem is under the risk of change. Addition of warmer water into a cooler water results in the change of bio life significantly, therefore it is crucial to reduce the amount of heat rejected and to control its impacts.

One of the biggest sources of thermal pollution in the sea environment is power plants where water passes through the condenser and returns to the sea water at an elevated temperature. 1000 MW electricity generating plant with once through cooling typically discharges to the sea environment nearly 30-60 m^3/s, if the maximum allowable temperature rise across the condenser is limited to $\Delta T=10$ C^o. In the last decade there has been an extensive engineering study on increasing the efficiency of power plants for economic reasons, so a considerable amount of heated water will be discharged into waters in the near future. Heated water is mostly discharged into the sea environment by a submerged pipeline system having a diffuser with one or more discharge ports lying at the sea bottom.

Once heated water is discharged, for the purpose of analysis, the physical processes may be categorized as near field and far field. Port velocities are usually in the range of 2-3 m/s. These high port velocities induce rapid entrainment of ambient sea water into the plume and cause the reduction in the plume temperature. So, heated water plume is several times diluted by mixing with the ambient cooler water till it reaches the sea surface.

This dilution is called as the near field dilution. The conditions in the near field are strongly dependent on the thermal emission rate i.e. the rate at which excess heat contained in the cooling water is discharged. Other factors are: the temperature of cooling water, the discharge designs i.e. the water depth, pipe diameter, initial velocity of the jet, port diameters, number of ports etc.

On the other hand, conditions in the far field depend on the ambient water hydrodynamics i.e. currents, turbulence, stratifications, surface heat exchange etc[1]. It is very important to predict the extent of the impacted area which can be defined by criteria such as $\Delta T=1$ ^oC or 3 ^oC i.e. near field and far field analysis, to understand whether discharge system satisfies the regulations or not. According to the Turkish regulations;

a) whatever the dilution in the ambient water is, the maximum allowable temperature of the discharged water could be 35 ^oC.

b) at the end of near field dilution, the maximum increase in the ambient water temperature can be at most 1^0C during June to September and at most 2 ^{0}C in the other months. If the ambient water temperature is above 28 ^{0}C, without any limitation in the temperature of the heated water discharged, the maximum increase in the ambient water temperature is allowed to be 3^0C.

c) near field dilution of heated discharges should be at least 40 and preferably 100.

d) diffuser should be at least at a water depth of d=-20 m.If it not possible due to bathimetry and/or topography, the length of the discharge pipe from the shoreline up to the starting point of the diffuser should be at least 500 m if heated water discharge rate is 200 m^3/day and population is less than 1000 and should be at least 1300 m if heated water discharge rate is in between 200 m^3/day and 2000 m^3/day and population is in between 1000 and 10000.

There are various methods to determine the effect of heated discharges, like physical modeling, empirical modeling, integral modeling and numerical modelling. Since actual turbulent jets are very complex, all of these methods are approximate in simulating the real environments but they could be used to predict the distribution of heated temperature plumes with a reasonable accuracy[2,3].

In this study a three dimensional hydrodynamic and transport numerical model, HYDROTAM-3D is used. Hydrothermal modeling study is necessary to characterize the circulation and temperature distribution in the coastal waters. The modeling study is applied to evaluate the potential effects of proposed increase on the temperature distribution in the coastal waters under the expected and worst-case conditions[4].

Theory

HYDROTAM-3D is an unsteady three-dimensional baroclinic circulation model that has been developed to simulate the transport processes in coastal water bodies. It has hydrodynamic, transport, turbulence and wave model components. The model computes the full spatial distribution of velocities of unsteady flow induced by wind, tide or water density differences solving full Navier-Stokes equations with only Boussinesq approximation. The transport model component consists of the pollutant transport model, the water temperature and salinity transport models and the suspended matter transport. The suspended sediment transport model simulates the advective and diffusive transport, settling, deposition and re-suspension of suspended matters. In coastal waters erosional and deposional areas can be identifed.

The numerical model includes thermohaline forcing due to changes in the sea water density. The density of sea water is a function of its salt content, its temperature and to a much lesser degree, its pressure. The two equation k-ε turbulence model is used for the turbulence modelling. To consider the large scale turbulence caused by the horizontal shear, horizontal eddy viscosity is simulated by the Smagorinsky algebraic subgrid scale turbulence model. The pollutant transport model can simulate the near and far field dilutions of sea outfalls. Pollutant type may be bacteria or heated discharges[5,6].

HYDROTAM-3D is integrated with GIS (http://hydrotam.com). In the model, wind and wave climate analyses of Turkish coast line exist. Turkish coastline and most of the Turkish Bay bathymetries are provided on GIS mapping. Wind and wave roses based on over 40 years of meteorological data(1970-2011) are also provided for all the Turkish coastal meteorological stations. According to the selected coastal location that the user wants to investigate the current pattern or the transport mechanisms, nearest meteorological stations wind and wave roses are served to the user[7-9].

Based on the predicted deep water wave height, its propagation to the coast line is numerically simulated as well by the wave model. In the wave model modified mild slope equations are solved. Model equations govern combined effects of shoaling, refraction, diffraction, reflection and breaking. Nonlinear and irrotational waves are considered and the effects of currents on the wave propagation are assumed to be negligible.

It is assumed that energy propagates along the wave crests, however, the wave phase function changes to handle any horizontal variation in the wave height. Model does not have the limitation that one coordinate should follow the dominant wave direction. Different wave approach angles can be investigated on the same computational grid[10,11].

Solution scheme is a composite finite element-finite difference scheme. The governing equations are solved by Galerkin Weighted Residual Method in the vertical plane and by finite difference approximations in the horizontal plane without any coordinate transformation. The water depths are divided into the same number of layers following the bottom topography. So, the vertical layer thickness is proportional to the local water depth. The model predictions were verified by using several experimental and analytical results published in the literature and its successful use for a variety of real life cases was demonstrated.

Near Field Dilution: The diffuser discharge momentum creates a head difference along the diffuser[3]. This head induces the flow to accelerate towards the diffuser from behind and away from the diffuser in front. Bernoulli equations for the approach flow and accelerating flow and a momentum equation for the pressure discontinuity across the diffuser axis were applied. Combining these equations, the dilution equation for coflowing diffusers in a near field was derived as:

$$\frac{S_c}{S_{ou}} = \sqrt{\frac{m_r}{2\cos\theta}} + \sqrt{\frac{m_r}{2\cos\theta} + 1} \quad (1)$$

where S_C is surface minimum dilution for coflowing diffuser; S_{0U} is surface minimum dilution for unidirectional diffuser in stagnant ambient condition; θ is angle between port and sea bed, which is usually taken as θ<45, mr is the momentum ratio of the ambient current to the effluent discharge which is expressed as:

$$m_r = \frac{u_a^2 H}{U_o^2 B} \quad (2)$$

where u_a is velocity of ambient current (Figure 1); H is depth of ambient water; U_0 is velocity of effluent discharge; B is A/*l* width of equivalent slot diffuser which is defined as where A is cross-sectional area of individual port; l is port spacing. The surface minimum dilution in stagnant ambient condition, S_{0U}, is defined as:

$$S_{ou} = \sqrt{\frac{H\cos\theta}{2B}} \quad (3)$$

Far Field Dilution: The region where the excess heat cloud is transported by ambient sea currents and diluted by turbulent diffusion is referred to as the "far field". In the near field and far field transition called as intermediate field, the dynamics depends on both the jet momentum and buoyancy and the ambient flow. To correctly simulate the dominant physical processes in this region, the dynamic near field effects of the discharge and the corresponding volume and mass fluxes need to be properly modelled in the far field model[12]. The equations of hydrodynamics of the far field model are as follows:

$$\frac{\partial u}{\partial x} + \frac{\partial v}{\partial y} + \frac{\partial w}{\partial z} = 0 \quad (4)$$

$$\frac{\partial v}{\partial t} + u\frac{\partial v}{\partial x} + v\frac{\partial v}{\partial y} + w\frac{\partial v}{\partial z} = -fu - \frac{1}{\rho_o}\frac{\partial p}{\partial y} + 2\frac{\partial}{\partial y}(\nu_y\frac{\partial v}{\partial y}) + \frac{\partial}{\partial x}(\nu_x(\frac{\partial v}{\partial x} + \frac{\partial u}{\partial y})) + \frac{\partial}{\partial z}(\nu_z\frac{\partial v}{\partial z}) \quad (5)$$

$$\frac{\partial u}{\partial t} + u\frac{\partial u}{\partial x} + v\frac{\partial u}{\partial y} + w\frac{\partial u}{\partial z} = fv - \frac{1}{\rho_0}\frac{\partial p}{\partial x} + 2\frac{\partial}{\partial x}(\nu_x\frac{\partial u}{\partial x}) + \frac{\partial}{\partial y}(\nu_y(\frac{\partial u}{\partial y} + \frac{\partial v}{\partial x})) + \frac{\partial}{\partial z}(\nu_z\frac{\partial u}{\partial z}) \quad (6)$$

$$\frac{\partial w}{\partial t} + u\frac{\partial w}{\partial x} + v\frac{\partial w}{\partial y} + w\frac{\partial w}{\partial z} = -\frac{1}{\rho_0}\frac{\partial p}{\partial z} - g + \frac{\partial}{\partial y}(\nu_y(\frac{\partial w}{\partial y} + \frac{\partial v}{\partial z})) + \frac{\partial}{\partial x}(\nu_x(\frac{\partial w}{\partial x} + \frac{\partial u}{\partial z})) + \frac{\partial}{\partial z}(\nu_z\frac{\partial w}{\partial z}) \quad (7)$$

Where *x,y* are Horizontal coordinates; *z* is Vertical coordinate; *t* is Time; *u,v,w* are Velocity components in x,y,z directions at any grid locations in space; ν_x, ν_y, ν_z are Eddy viscosity coefficients in x,y and z directions, respectively; *f* is Coriolis coefficient; ρ(x,y,z,t) is In situ water density; ρ_o is Reference density; *g* is Gravitational acceleration and *p* is Pressure.

The numerical model includes thermohaline forcing. Temperature and salinity variations are calculated by solving the three dimensional convection-diffusion equation which is written as:

$$\frac{\partial Q}{\partial t} + u\frac{\partial Q}{\partial x} + v\frac{\partial Q}{\partial y} + w\frac{\partial Q}{\partial z} = \frac{\partial}{\partial x}(D_x\frac{\partial Q}{\partial x}) + \frac{\partial}{\partial x}(D_y\frac{\partial Q}{\partial y}) + \frac{\partial}{\partial z}(D_z\frac{\partial Q}{\partial z}) + \theta_0 \quad (8)$$

where D_x,D_y and D_z are Turbulent diffusion coefficient in x,y and z directions respectively; Q is Temperature (T) or salinity (S) and θ_o is source of temperature and/or salinity

Estimation of the heat exchange through the water surface is important to simulate the water temperature distribution. It includes radiation transfer and diffusive processes. The boundary condition at the upper surface takes into account the heat flux through it. At the surface:

$$D_z\frac{\partial T}{\partial z} = \frac{K}{\rho C_p}(T_s - T_e) \quad (9)$$

where K is the surface heat transfer coefficient, ρ is fluid mass density, C_p is specific heat of water, T_s is surface temperature and T_e is equilibrium temperature.

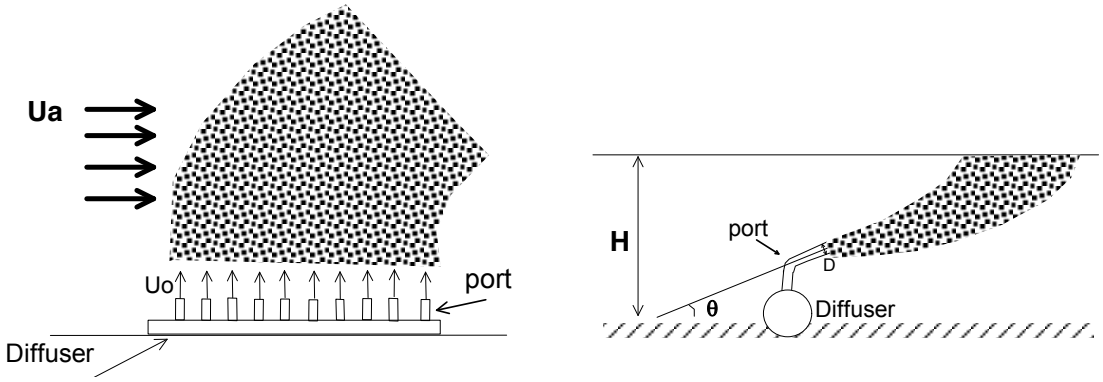

Figure 1: Diffuser and ports

The density of sea water changes as its temperature and salinity changes. The density of sea water is a function of its salt content (or salinity), its temperature and to a much lesser degree, its pressure. It is evident that the density distribution depends on the distribution of temperature and salinity. The average density of sea water is close to 1.0276 g/cm^3. The significant part of this number with respect to the density of other water samples is generally in (or beyond) the third decimal. Therefore, a simplifying convention has been adopted for sea water density which uses σt instead of the real density ρ. The relation between these two quantities is:

$$\sigma_t = (\rho - 1) \times 10^3 \quad (10)$$

Following formulae are used to calculate σt, as a function of salinity and temperature[5-7]:

$$S = 1.80655 Cl$$

$$\sigma_o = -6.9\times10^{-2} + 1.4708Cl - 1.57\times10^{-3}Cl^2 + 3.98\times10^{-5}Cl^3 \quad (10\text{-a})$$

$$A_t = 4.7867\times10^{-3}T - 9.8185\times10^{-5}T^2 + 1.0843\times10^{-6}T^3 \quad (10\text{-b})$$

$$B_t = 1.803\times10^{-5}T - 8.146\times10^{-7}T^2 + 1.667\times10^{-8}T^3 \quad (10\text{-c})$$

$$\sum_t = -(T-3.98)^2(T+283)(503.57(T+67.26))^{-1} \quad (10\text{-d})$$

where S is the salinity (%), Cl is the chlorinity (gr/kg) and T is the temperature (^{o}C). Pressure is not constant and changes with density:

$$p(x,y,z,t) = \int_z^{\eta} g\rho(x,y,z,t)\, dz \quad (11)$$

If Leibniz Rule is applied and independent variables are omitted, then:

$$\frac{\partial p}{\partial x} = \frac{\partial}{\partial x}\int_z^{\eta} g\rho\, dz = \int_z^{\eta} g\frac{\partial \rho}{\partial x}\, dz + g\rho_s\frac{\partial \eta}{\partial x} \quad (12)$$

Water elevation changes are calculated with the continuity equation:

$$\frac{\partial \eta}{\partial t} = -\frac{\partial}{\partial x}\left(\int_{-h}^{\eta} u.dz\right) - \frac{\partial}{\partial y}\left(\int_{-h}^{\eta} v.dz\right) \quad (13)$$

Eddy viscosity and turbulence diffusion coefficients are computed using 2 equations k-ε turbulence model. The equations of the kinetic energy and disappear velocity of the kinetic energy are:

$$\frac{\partial k}{\partial t} + u.\frac{\partial k}{\partial x} + v.\frac{\partial k}{\partial y} + w.\frac{\partial k}{\partial z} = \frac{\partial}{\partial z}\left(.\frac{\upsilon_z}{\sigma_k}.\frac{\partial k}{\partial z}\right) + P + B - \varepsilon + \frac{\partial}{\partial x}\left(D_x.\frac{\partial k}{\partial x}\right) + \frac{\partial}{\partial y}\left(D_y.\frac{\partial k}{\partial y}\right) \quad (14)$$

$$\frac{\partial \varepsilon}{\partial t} + u.\frac{\partial \varepsilon}{\partial x} + v.\frac{\partial \varepsilon}{\partial y} + w.\frac{\partial \varepsilon}{\partial z} = \frac{\partial}{\partial z}\left(.\frac{\upsilon_z}{\sigma_\varepsilon}.\frac{\partial \varepsilon}{\partial z}\right) + C_{1\varepsilon}.\frac{\varepsilon}{k}.(P + C_{3\varepsilon}.B) - C_{2\varepsilon}.\frac{\varepsilon^2}{k} + \frac{\partial}{\partial x}\left(D_x.\frac{\partial \varepsilon}{\partial x}\right) + \frac{\partial}{\partial y}\left(D_y.\frac{\partial \varepsilon}{\partial y}\right) \quad (15)$$

(σ_ε = 1.3); ($C_{1\varepsilon}$ = 1.44); ($C_{2\varepsilon}$ = 1.92); If $B>0$, $C_{3\varepsilon}$ = 1 and if $B<0$, $C_{3\varepsilon}$ = 0.2).

Change of velocity of kinetic energy produced due to density differentiation is:

$$B = \frac{g}{\rho_o}.\frac{\upsilon_z}{P_r}.\frac{\partial \rho}{\partial z} \quad (16)$$

where P_r is Prandtl or Schmidt coefficient and is considered as constant in the model (P_r = 0.7)[10]. Velocity of kinetic energy produced in turbulence:

$$P = \upsilon_h\left[2.\left(\frac{\partial u}{\partial x}\right)^2 + 2.\left(\frac{\partial v}{\partial y}\right)^2 + 2.\left(\frac{\partial w}{\partial z}\right)^2 + \left(\frac{\partial u}{\partial y} + \frac{\partial v}{\partial x}\right)^2\right] + \upsilon_z.\left[\left(\frac{\partial u}{\partial z} + \frac{\partial w}{\partial x}\right)^2 + \left(\frac{\partial v}{\partial z} + \frac{\partial w}{\partial y}\right)^2\right] \quad (17)$$

Vertical length scale is smaller than horizontal length scale in coastal waters, therefore accuracy of prediction of vertical eddy viscosity and turbulence coefficients is an important phenomena. Vertical eddy viscosity coefficients are calculated with eq. 12. (C_μ is an experimental constant, C_μ = 0.09):

$$\upsilon_z = C_\mu.\frac{k^2}{\varepsilon} \quad (18)$$

Horizontal eddy viscosity coefficients are calculated by the Smagorinsky subgrid scale turbulence model.

$$\upsilon_h = 0.01\times\Delta x.\Delta y.\left(\left(\frac{\partial u}{\partial x}\right)^2 + \left(\frac{\partial v}{\partial y}\right)^2 + \frac{1}{2}.\left(\frac{\partial u}{\partial x} + \frac{\partial v}{\partial y}\right)^2\right)^{1/2} \quad (19)$$

Dynamic Coupling of Near Field and Far Field: In the applied three dimensional hydrodynamic and transport model HYDROTAM-3D, far field is dynamically coupled with the near field analyses. The velocity and density profile throughout the depth (vertical) effect the near field plume trajectory. The heated plume effect on the ambient flow is modelled by a diluted source flow at the calculated terminal height of rise. The influence of the source characteristics decreases further away from the discharge point. The simulation of physical transport processes in the transition zone between the near and far field dilutions depends on the estimations of volume and mass fluxes[13,14].

HYDROTAM-3D Application

HYDROTAM-3D is applied to predict the impacted coastal area of natural gas combined cycle power plant heated water discharge system which is planned to be constructed at coastal waters in Marmara Sea, Turkey. The study area is in between the coordinates of 27.98187 E -40.99612 N and 28.01174 E – 41.02060 N as shown in figure 2. First, wind characteristics of the area are analyzed. The wind rose

which provides the directional distribution of wind speeds, is obtained using the measured wind data between the years 1970 and 2011 of the State Meteorological Station in Tekirdağ. Wind rose is given in figure 3. The dominant wind direction range to induce dominant currents is North NorthEast South SouthEast. In these directions, results of long term wind statistics show that the yearly average of the extreme values for the wind speed is 10 m/s and the mean monthly wind speed is 3.5 m/s. The percent of winds blowing with a speed of 1m/s and less is nearly 4%.

To investigate the long-term wave climate, the wave characteristics of the study area are estimated by the well known CEM method[8] utilizing the hourly averaged wind data of Tekirdağ Meteorological Station. Study area coastline lies in the north-south direction. Due to the location of the study area, the directions for the wind wave growth are in between (clockwise) north northeast and south (NNE-S). Yearly wave rose is presented in figure 4. The dominant wave direction for the site is south southeast (SSE) one for the project area. It is observed that the significant wave heights, H_s, to be exceeded for 1, 5 and 10 hours in a year for SSE, the dominant wave direction with a fetch length of 100 km, have been estimated as 2.2 m, 1.8 m and 1.6 m respectively. As a more general conclusion, however, it is seen that for the directions between NNE and S, the waves exceeded for 1 to 10 hours in a year having significant wave height values changing from 1.0 m to 2.2 m. The significant wave periods T_s are changing in between 1-5 sec.

Wind and wave induced water exchange patterns in Marmara Ereğlisi coastal waters are modeled by the three dimensional hydrodynamic transport model HYDROTAM-3D. The steady state circulation patterns at the surface and bottom layers under the shear forcing of wind blowing from SSE and NNE with a speed of 10 m/s are shown in figure 5, figure 6, figure 7 and figure 8 respectively. It is seen that under the effect of southerly winds, in the study area there occur surface currents from south to north direction whereas under the effect of northerly winds, surface currents are from the north to the south direction. Towards the sea bottom, current directions turn to the opposite of the surface currents due to the barotropic pressure gradient effect and the current speeds decrease almost 6 times in the bottom layer. It is seen that under the effect of northerly winds, there occurs a counterclock wise gyre in the bottom layer due to topography. Surface current speeds are about 20-25 cm/s.

The rate of heated water discharge is 59.000m^3/hour (16,4m^3/sec) and the maximum allowable temperature rise across the condenser is ΔT_o=10 C^o. The discharge pipe diameter is 3 m. The coflowing diffuser is at a depth of d=-22 m. The horizontal distance between the staggered ports is 5 m. The effects of different wind speeds (W), current speeds, number of ports and the port diameters on the near field dilution, $S = \frac{\Delta T_o}{\Delta T}$ are analyzed and are presented in table 1.

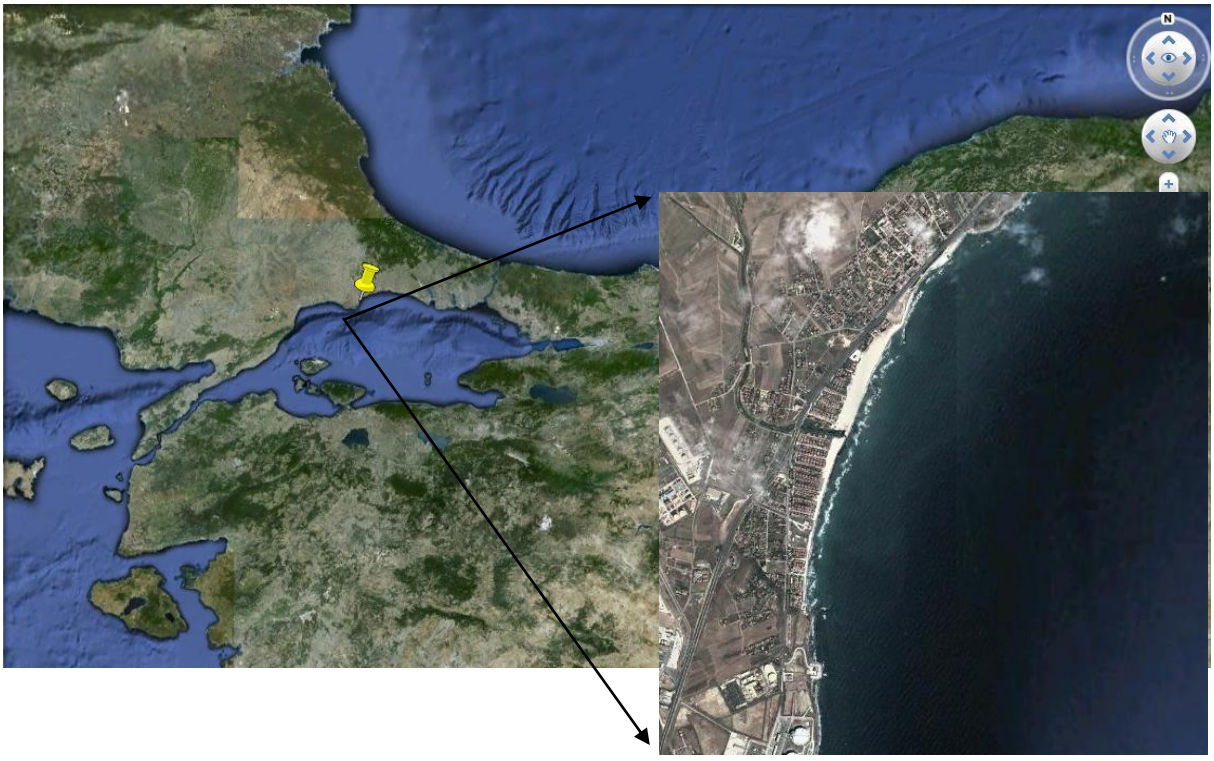

Figure 2: Study area (Google, 2012)

Table 1
Near field dilution(S) results for different wind speeds (W), number of ports in the diffuser pipe(n) and port diameters (D).

Port Diameter D (m)		n=35				n=45			
		W(m/s) >10	W(m/s) 7	W(m/s) 4	W(m/s) <1	W(m/s) >10	W(m/s) 7	W(m/s) 4	W(m/s) <1
0.7	S	97	73	38	25	122	91	47	36
0.5	S	118	87	53	42	150	112	71	53

The results of near field analyses show that for wind speeds greater than 1 m/s, 35 ports with diameters of D=0.5 m satisfy Turkish near field dilution requirements (S>40). The simulations show that at the end of near field dilution, the pollutant cloud reaches to the surface with a minimum temperature rise of ΔT=+0.45 ^{o}C. This amount is taken as the initial value (starting value) of the far field dilution analyses.

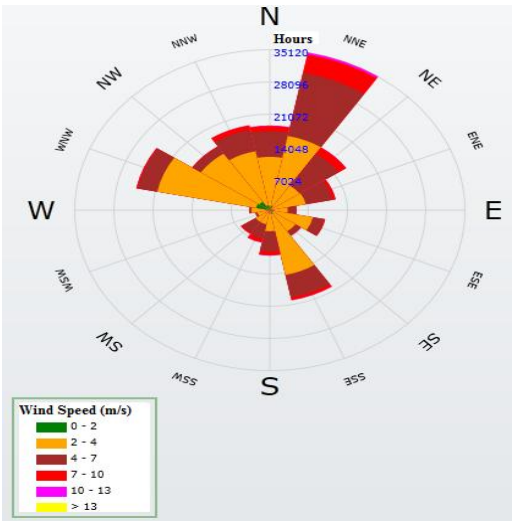

Figure 3: Wind rose of the study area based on hourly wind measurements between the years 1971-2012

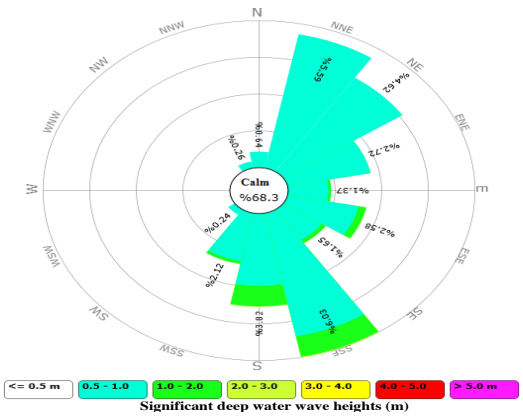

Figure 4: Yearly wave rose

In the far field analyses, the advection and diffusion of the heated discharge cloud is investigated by model HYDROTAM-3D under the effect of wind and wave induced currents. The surface layer and bottom layer distributions of excess heat for winds blowing from SSE and NNE with a speed of 10 m/s are shown in figure 5, figure 6, figure 7 and figure 8 respectively at the steady state reached after 4 hours. It is seen that at the surface, nearly, in an area with a diameter of 650 m., water temperatures are in between +0.45 ^{o}C and +0.1 ^{o}C. If wind speeds are less than 1 m/s, this decreases to 400 m.

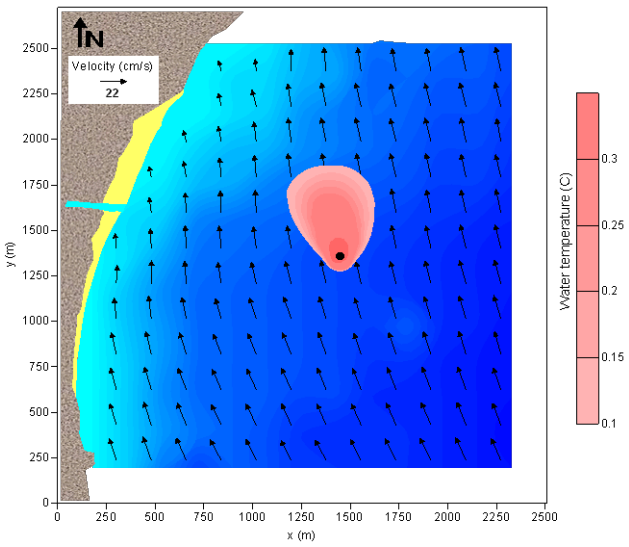

Figure 5: Current pattern and water temperature distribution at the sea surface layer for wind blowing from SSE with 10 m/s at the steady state (●: diffuser location)

Conclusion

Temperature increases in an enclosed coastal area due to the discharge of heat from a power plant simulated by, HYDROTAM-3D. It is a Geographic Information Systems (GIS) integrated three-dimensional baroclinic numerical model that has been developed to simulate the hydrodynamic and transport processes in coastal waters. In its transport model, three dimensional adjective diffusion equation is solved. Model is capable of simulating the near and far field dilutions of heated discharges. The equations

of hydrodynamics of the far-field model are completed by equations for heat and salt.

Special attention is paid to the parameterization of heat fluxes between water and atmosphere. In the near field area, the dilution of heated water is mostly due to inital momentum of the discharge. Away from the discharge location, the mixing becomes more random and the plume becomes more disperse. The near field dilution is coupled by far field dilution analyses so, the effect of near field plume mixing is properly represented in the far field model. A dynamic link is established between the near and far field models along with water and mass conservation. Model can be succesfully implemented in predictions of the near and far field dilution analyses for many environmental transport problems.

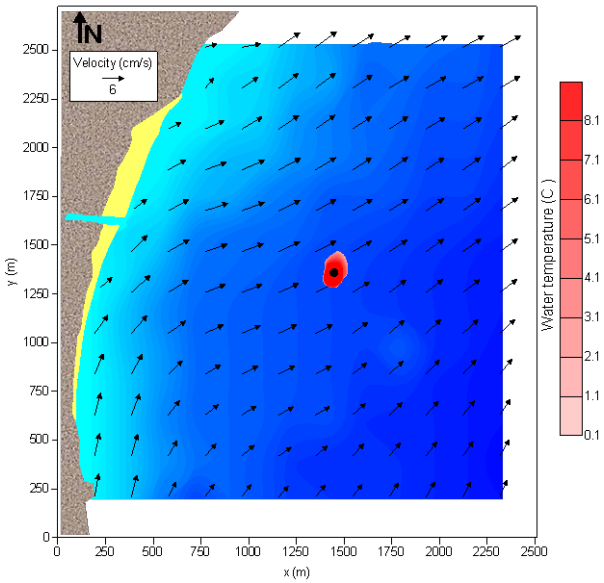

Figure 6: Current pattern and water temperature distribution at the bottom layer for wind blowing from SSE with 10 m/s at the steady state(●: diffuser location)

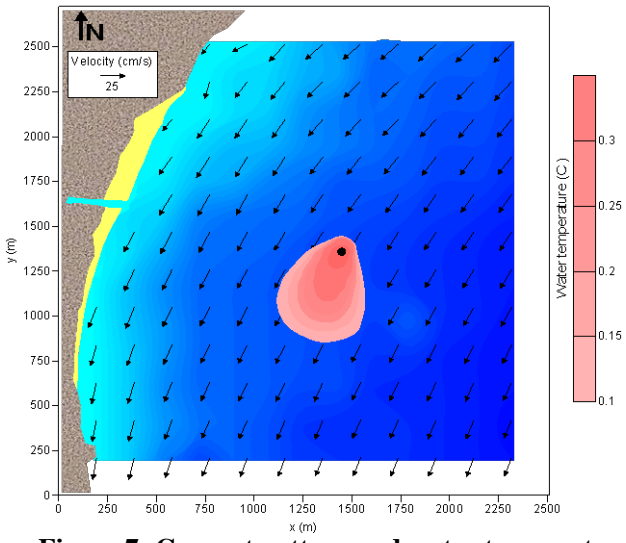

Figure 7: Current pattern and water temperature distribution at the sea surface layer for wind blowing from NNE with 10 m/s at the steady state (●: diffuser location)

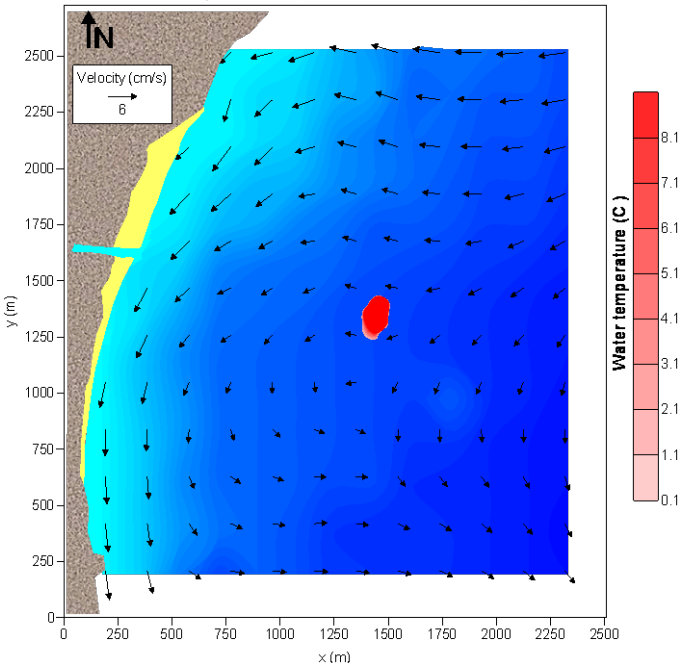

Figure 8: Current pattern and water temperature distribution at the bottom layer for wind blowing from NNE with 10 m/s at the steady state (●: diffuser location)

References

1.GESAMP, Thermal Discharges in the Marine Environment, UNEP Regional Seas Reports and Studies, No. 45 **(1983)**

2. Davis L.R., Thermal Pollution in Water, Environmental and Ecological Chemistry**,** Encyclopedia of Life Support Systems, editor, Aleksandar Sabljic, Croatia **(1991)**

3. Seo Il Won, Daeyoung Yu and Hong Sik Kim, Near Field Mixing of Submerged Multiport Diffusers in Shallow Water with Strong Currents, 4th International Conference on Hydroscience and Engineering, Seoul, Korea **(2000)**

4. Balas L. and Özhan E., An implicit three dimensional numerical model to simulate transport processes in coastal water bodies, *Int Journal of Numerical Methods in Fluids*, **34,** 307-339 **(2000)**

5. Balas L. and Özhan E., Applications of a 3-D numerical model to circulations in coastal waters, *Coastal Engineering Journal*, **43 (2),** 99-120 **(2001)**

6. Balas L., Simulation of Pollutant Transport in Marmaris Bay, *China Ocean Engineering*, **15(4)**, 565-578 **(2001)**

7. Balas L. and Özhan E., Three dimensional modelling of stratified coastal waters, *Estuarine, Coastal ve Shelf Science*, **56,** 75-87 **(2002)**

8. Balas L., Numanoglu Genc A. and İnan A., HYDROTAM, 3D Model for Hydrodynamic and Transport Processes in Coastal Waters, International Environmental Modelling and Software Society (IEMSS) International Congress on Environmental Modelling and Software**,** Leipzig, Almanya **(2012)**

9. Numanoglu Genç A., İnan A., Yılmaz N. and Balas L., Modeling of Coastal Erosion in Göksu Coasts, *Journal of Coastal Research* , **SI 65(2),** 2155-2160 **(2013)**

10. İnan A. and Balas L., Numerical Modeling of Mild Slope Equations with Finite Volume Method, *WSEAS Transactions on Mathematics*, **7(5)**, 234-243 **(2008)**

11. İnan A. and Balas L., Applications of a Numerical Model to Wave Propagation on Mild Slopes, *China Ocean Engineering*, **16(4)**, 569-576 **(2002)**

12. Fossati M., Santoro P., Urrestarazu S. and Piedra-Cueva I., Numerical Study of the Effect of a Power Plant Cooling Water Discharge in the Montevideo Bay, *Journal of Applied Mathematics*, 1-23 **(2011)**

13. Choi K.W. and Lee Joseph H.W., A New Approach To Effluent Plume Modelling, Proceedings of 31 th IAHR Congress, Korea, 4303-4311 **(2005)**

14. Kim D. G. and Cho H. Y., Modeling the buoyant flow of heated water discharged from surface and submerged side outfalls in shallow and deep water with a cross flow, *Environmental Fluid Mechanics*, **6(6)**, 501–518 **(2006)**.

(Received 22nd March 2013, accepted 29th July 2013)

Bioethanol production from oil palm trunk juice by different strains of yeast and bacteria

Norhazimah* A. H. and Faizal C. K. M.
Faculty of Chemical and Natural Resources Engineering, Universiti Malaysia Pahang, 26300 Gambang, Kuantan, Pahang, MALAYSIA
*aimc.azim@gmail.com

Abstract
Oil palm trunk (OPT) juice is one of the abundant agricultural wastes available as feedstock for bioethanol production. OPT juice is advantageous due to high levels of soluble sugars available. This paper presents a comparative study on the effect of using different strains of yeast and bacteria on OPT juice for bioethanol production. The study was performed using Saccharomyces cerevisiae, Scheffersomyces stipitis, Zymomonas mobilis and Zymobacter palmae. It was found that co-culture of S. cerevisiae Kyokai no. 7 and S. stipitis excellently produced the highest bioethanol up to 30.25 g/l and productivity of 0.252 g/l.h. The results obtained from the experiment also demonstrated that S. cerevisiae Kyokai no. 7 and S. cerevisiae JCM 2220 were good strains for producing bioethanol from OPT juice.

Keywords: Oil palm trunk, *Saccharomyces cerevisiae*, *Scheffersomyces stipitis*, *Zymomonas mobilis*, *Zymobacter palmae*.

Introduction

Selection of microbes for bioethanol production is important to choose the most suitable microbes for specific agricultural waste. This is because different waste contains certain inhibitor that can influence the production. Yeast is the preferred organisms for industrial scale ethanol production due to a wide variety of yeast species that can be utilized depending on the composition of raw material used[1]. In general, *S. cerevisiae* is the most common organism used in ethanol production. A wide variety of characteristics are also observed within *S. cerevisiae* species especially between the industrial and laboratory strain [2]. The industrial sake yeasts *S. cerevisiae* Kyokai no. 7 (K-7) and *S. cerevisiae* Kyokai no. 9 (K-9) are capable to produce more than 20% v/v of ethanol [3].

A gram-negative bacterium, *Z. mobilis*, is also considered an alternative organism for the large scale ethanol production fuel due to higher sugar uptake, higher ethanol yield and lower biomass production [4]. This bacteria is able to utilize glucose, fructoseand sucrose as the substrate for the ethanol production. Apart from that, *Z. palmae* is also a suitable candidate to be used for bioethanol production from oil palm trunk (OPT) juice as it can utilize sugar alcohols for bioethanol production. *Z. palmae* is a facultative anaerobe initially isolated from palm sap [5].Oil palm tree is a crop that is widely planted for cooking oil production purpose. Even though replantation of old oil palm tree is done in every 25–30 years interval, the total land planted with oil palm is enough to generate large amounts of agricultural waste in the form of OPT.

As OPT is one of the most abundant agriculture wastes in Southeast Asian countries, it could be used to produce commercial bioethanol production. There are several reports on the direct fermentation of OPT juice for bioethanol production. Early attempts are performed using single strains of *S. cerevisiae* Kyokai no. 7 and baker's yeast *S. cerevisiae* [6,7]. Some works on combination of *S. cerevisiae* and *Pichis stipitis* (*S. stipitis*) for bioethanol production find that co-culture is able to improve overall result as compared to using a single strain only [8,9].

Material and Methods

Raw Materials: OPT was collected from the local plantation area in Pahang, Malaysia. The leaves, fruits and roots were removed from the trunks. The trunks were crushed by sugar cane press machine to obtain their juice. The OPT juice had the following compositions (in g/l: sucrose, 40–45; starch, 5–10; fructose, 10–15; glucose, 20–25). Each fermentation medium contained 59.29 g/l of initial total sugars. The OPT juice was stored at –18 °C for storage purposes and sterilized for 10 min at 121 °C prior to use.

Strain: An industrial strain of *Saccharomyces cerevisiae* Kyokai no. 7 (ATCC 26622) was obtained from American Type of Culture Collection (ATCC). The strains of *Zymomonas mobilis* JCM 10190 (ATCC 29191), *Zymobacter palmae* JCM 21091 (ATCC 51623), *Saccharomyces cerevisiae* JCM 2220 (ATCC 9804) and *Scheffersomyces stipitis* JCM10742 (ATCC 58376) were obtained from Japan Collection of Microorganisms (JCM). A baker's yeast *Saccharomyces cerevisiae* was obtained from local market (Pahang, Malaysia). All strains were maintained in Petri plate and subcultured in every 5 weeks.

Inoculum Preparation: Seed cultures were prepared by transferring a loopful of colony directly into OPT juice. The culture was previously pre-adapted through two cycles of OPT juice medium before being subcultured into the inoculation medium. All inoculums were grown aerobically at 30 °C without shaking.

Fermentation: Fermentations were started with 10% v/v inoculums in 250 ml Erlenmeyer flasks (with 100 ml total working volume comprising pure OPT juice) without pH adjustment. For co-culture, 5% v/v of each culture was added into fermentation flask. The flasks were incubated at

30 °C without shaking for 120 h. All the experiments were performed in duplicates and data represented were average of the three replications.

Analytical Procedures: Fermentation broth was analyzed for bioethanol content, individual sugar and cell biomass. A UV-VIS spectrophotometer (Hitachi U-1800) was used to determine cell biomass. Samples were centrifuged at 10000 RPM for 7 min to separate the supernatant. The supernatant was used for determination of bioethanol concentration using GC-FID (HP-INNOwax column, oven temperature 70 °C, injector and detector temperature 250 °C, initial temperature 70 °C held for 4 min, rate of increase 20 °C/min until 120 °C min held for 2 min)and determination of sugar was done using HPLC-RID (Agilent Zorbax Carbohydrate Analysis Column, column temperature of 30 °C, mobile phase at flow rate of 1.4 ml/min with the ratio of 70:30 for acetonitrile and water).

Results and Discussion

Figure 1 and figure 2 show the bioethanol production and cell biomass changes in OPT juice in 120 h of fermentation.

It was observed that at the end of fermentation, the co-cultures of *S. cerevisiae* Kyokai no. 7 and *S. stipitis* JCM10742 were able to produce the highest bioethanol concentration of 30.25 g/l followed by a single strain of *S. cerevisiae* JCM 2220 (29.82 g/l). In this study, all strains of *Saccharomyces* genus produced more than 20 g/l of final bioethanol concentration. *Z. mobilis* and *Z. palmae* produced 8.072 and 11.566 of bioethanol respectively. The lowest final bioethanol concentration was achieved by *S. stipitis* which was 6.69 g/l/. All yeast cultures and co-cultures produced more than 19 g/l of bioethanol on the first day of fermentation (24 h) except single strain yeast *S. stipitis*. The highest bioethanol concentration of 25.949 g/l at 24 h was produced by co-culture of *S. cerevisae Kyokai* no. 7 and *S. stipitis* JCM10742. This was contributed by the highest increase of cell biomass in the total 120 h of fermentation.

For the first 24 h, considering only single strain, *S. cerevisiae* Kyokai no. 7 showed the highest increase of cell biomass followed by *S. cerevisiae* JCM220 and *S. cerevisiae* (local). *S. stipitis* produced the lowest cell biomass followed by *Z. palmae* and *Z. mobilis* after 24 h of fermentation. The maximum cell biomass changes for *S. cerevisiae* Kyokai no. 7 were achieved at 24 h fermentation; *Z. mobilis*, *S. cerevisiae* (local) and *S. cerevisae* JCM220 at 48 h fermentation and *Z. mobilis* at 96 h fermentation.

Cell biomass was calculated as the total changes i.e. cell biomass reading at that particular time was subtracted with initial reading of cell biomass. The selected *S. cerevisiae* showed several advantages over bacteria (*Z. palmae* and *Z. mobilis*). A comparative study done by Behera et al[10] using *S. cerevisiae* and *Z. mobilis* for bioethanol production from mahula flowers also shows that *S. cerevisiae* is able to produce 21.2% more bioethanol than *Z. mobilis*.

The main components of OPT juice were sucrose, glucoseand fructose. The sucrose concentration decreased rapidly during fermentation of yeast. The sucrose fermented by *S. cerevisiae* Kyokai no. 7 and *S. cerevisiae* JCM 2220 was depleted within 24 h. During fermentation by yeast, sucrose was hydrolyzed to the glucose and fructose, thus no sucrose was detected at the end of the fermentation.

For the fermentation by bacterial strains, there was a large amount of sucrose still available at the end of fermentation. This might be due to the inability of this bacteria to produce enzyme that can hydrolyze sucrose to its monomer. All glucose nearly exhausted before 72 h in fermentation by bacterial strains. Substrate exhaustion should be avoided as it would lead to production of organic acids and consumption of ethanol. Table 1 shows the summary of bioethanol production from the OPT juice by different strains of microorganism.

From the results, a single strain of *S. stipitis* was unable to produce a good amount of bioethanol. When paired with *S. cerevisiae* Kyokai no. 7, the strain was able to improve the bioethanol yield. Different from co-culture of *S. cerevisiae* (local), the bioethanol obtained was lower as compared to using single strains of *S. cerevisiae* (local).

S. cerevisiae Kyokai no. 7 and *S. cerevisiae* JCM220 have been proven as very versatile yeast species to be used for bioethanol production from OPT juice. They have high capacity to produce a good amount of biomass and bioethanol. Further study should be carried out to identify physical and chemical factors that affect bioethanol fermentation of OPT juice using *S. cerevisiae* Kyokai no. 7 and *S. cerevisiae* JCM220.

Conclusion

The *S. cerevisiae* species can be considered as a more reliable strain compared to bacterial strains such as *Z. palmae* and *Z. mobilis* in terms of productivity and bioethanol production.

References

1. Shuler M.L. and Kargi F., Bioprocess Engineering Basic Concepts, 2nd ed., Prentice Hall International Series **(2000)**

2. Pereira F.B., Guimaraes P.M.R., Teixeira J.A. and Domingues L., Selection of *Saccharomyces cerevisiae* strains for efficient very high gravity bio-ethanol fermentation process, *Biotechnol Lett,* **32(11),** 1655-1661 **(2010)**

3. Ohbuchi K., Ishikawa Y., Kanda A., Hamachi M. and Nunokawa Y., Alcohol dehydrogenase I of sake yeast *Saccharomyces cerevisiae* Kyokai, No. 7, *Journal of Fermentation and Bioengineering*, **81(2)**, 125-132 **(1996)**

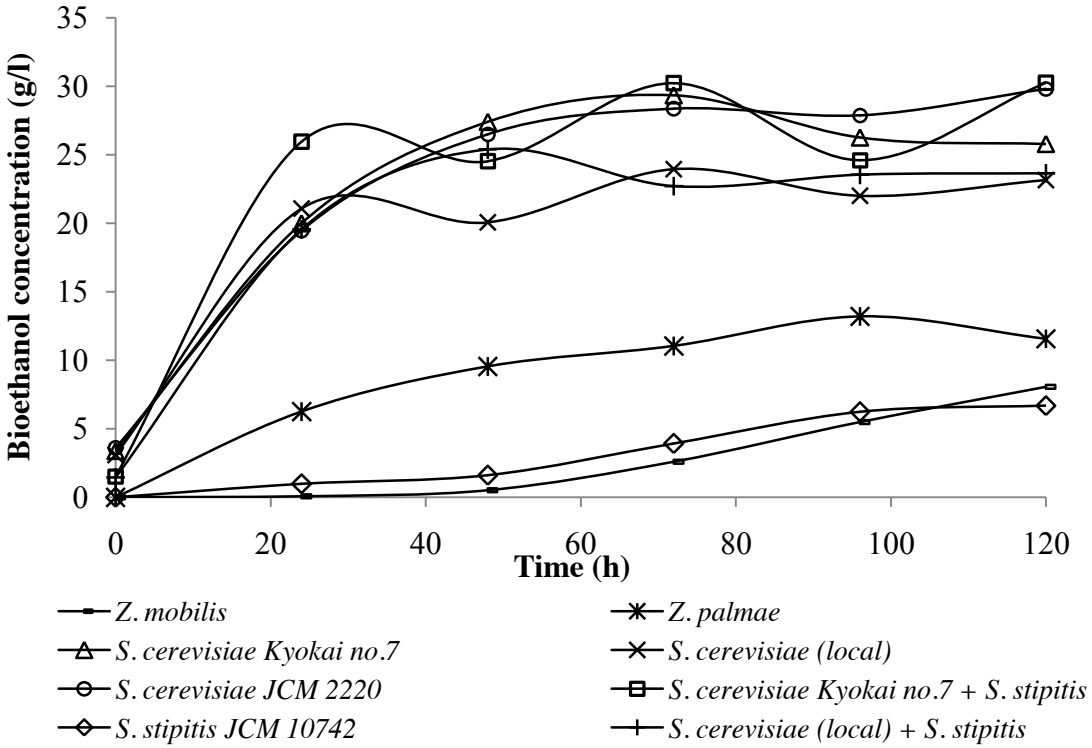

Fig. 1: Bioethanol production within 120 h of fermentation

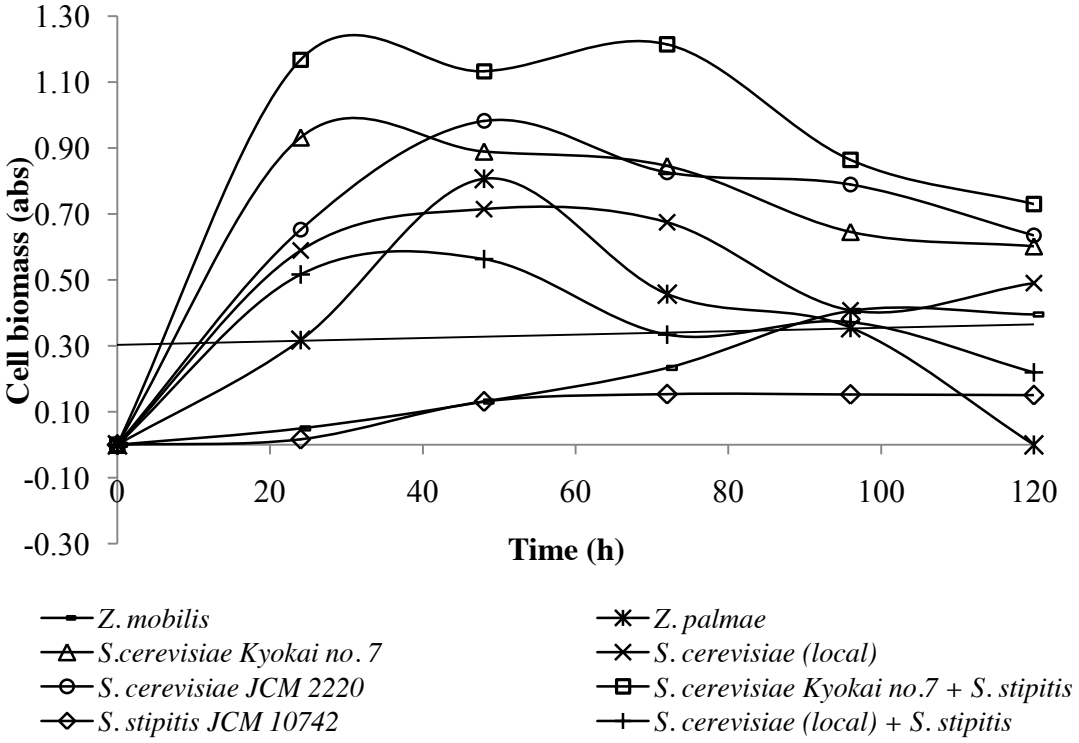

Fig. 2: Cell biomass changes within 120 h of fermentation.

Table 1
Effects of different strains to the production of bioethanol from OPT juice

	***Zymomonas mobilis* JCM10190**		***Zymobacter palmae* JCM21091**		***Scheffersomyces stipitis* JCM10742**		***Saccharomyces cerevisiae (local)***	
Time (h)	Ethanol (g/l)	Productivity (g/l.h)	Ethanol (g/l)	Productivity (g/l.h)	Ethanol (g/l)	Productivity (g/l.h)	Ethanol (g/l)	Productivity (g/l.h)
0	0.00	0.000	0.00	0.000	0.00	0.000	3.09	0.000
24	0.08	0.003	6.26	0.261	0.98	0.041	21.08	0.878
48	0.51	0.011	9.55	0.199	1.61	0.034	20.07	0.418
72	2.59	0.036	11.05	0.153	3.92	0.054	23.95	0.333
96	5.50	0.057	13.22	0.138	6.24	0.065	22.01	0.229
120	8.07	0.067	11.57	0.096	6.69	0.056	23.16	0.193
	***Saccharomyces cerevisiae* JCM 2220**		***Saccharomyces cerevisiae* Kyokai no. 7**		***Saccharomyces cerevisiae* (local) and *Scheffersomyces stipitis* JCM10742**		***Saccharomyces cerevisae Kyokai no. 7* and *Scheffersomyces stipitis* JCM10742**	
Time (h)	Ethanol (g/l)	Productivity (g/l.h)	Ethanol (g/l)	Productivity (g/l.h)	Ethanol (g/l)	Productivity (g/l.h)	Ethanol (g/l)	Productivity (g/l.h)
0	3.60	0.000	3.39	0.000	1.45	0.000	1.53	0.000
24	19.46	0.811	20.01	0.834	19.56	0.815	25.95	1.081
48	26.51	0.552	27.41	0.571	25.39	0.529	24.52	0.511
72	28.36	0.394	29.35	0.408	22.72	0.316	30.23	0.420
96	27.88	0.290	26.25	0.273	23.54	0.245	24.61	0.256
120	29.82	0.249	25.79	0.215	23.65	0.197	30.25	0.252

4. Maiti B., Rathore A., Srivastava S., Shekhawat M. and Srivastava P., Optimization of process parameter for ethanol production from sugar cane molasses by *Zymomonas mobilis* using response surface methodology and genetic algorithm, *Appl Microbiol Biotechnol*, **90(1),** 385-395 **(2011)**

5. Okamoto T., Taguchi H., Nakamura K., Ikenaga H., Kuraishi H. and Yamasato K., *Zymobacter palmae* gen. nov., sp. Nov., a new ethanol-fermenting peritrichous bacterium isolated from palm sap, *Arch Microbiol*., **160**, 333-337 **(1993)**

6. Kosugi A., Tanaka R., Magara K., Murata Y., Arai T., Sulaiman O., Hashim R., Hamid Z.A.A., Yahya M.K.A.Y., Yusof M.N.M., Ibrahim W.A. and Mori Y., Ethanol and lactic acid production using sap squeezed from oil palm trunks felled for replanting, *Journal of Bioscience and Bioengineering*, **110(3),** 322- 325 **(2010)**

7. Norhazimah A.H. and Faizal C.K.M., Production of bio-ethanol from oil palm trunks sap waste as new substrate by baker's yeast *Saccharomyces cerevisiae*, *Res. J. Chem. Environ*., **15(2),** 205-208 **(2011)**

8. Yadav K.S., Naseeruddin S., Prashanthi G.S., Sateesh L. and Rao L.V., Bioethanol fermentation of concentrated rice straw hydrolysate using co-culture of *Saccharomyces cerevisiae* and *Pichia stipitis*, *Bioresource Tech*., **102(11),** 6473-6478 **(2011)**

9. Chandel A.K., Chandrasekhar G., Narasu M.L. and Rao L.V., Simultaneous saccharification and fermentation (SSF) of aqueous ammonia pretreated *Saccharum spontaneum* (wild sugarcane) for second generation ethanol production, *Sugar Tech*., **12(2),** 125-132 **(2010)**

10. Behera S., Mohanty R.C. and Ray R.C., Comparative study of bio-ethanol production from mahula (*Madhuca latifolia L.)* flowers by *Saccharomyces cerevisiae* and *Zymomonas mobilis*, *Appl. Energ*., **87**, 2352-2355 **(2010).**

(Received 23rd March 2013, accepted 29th July 2013)

Assessing the inhibitory potential of natural silicon oil on brass degradation in 1M H_2SO_4

Fayomi O. S. I.* and Popoola A. P. I.
Department of Chemical, Metallurgical and Material Engineering, Tshwane University of Technology, P.M.B. X680, Pretoria, SOUTH AFRICA
*ojosundayfayomi3@gmail.com

Abstract
Assessment of silicon oil as natural inhibitor on brass in 1 M H_2SO_4 acid solution has been studied using linear potentiodynamic polarization and gravimetric method in the inhibited concentration variation between 2% to 10% range. Tafel extrapolation techniques were used to obtain corrosion potential (Ecorr) and corrosion current density (Icorr). From all indication, the inhibitor is of mixed type. The adsorption behavior occurs on the surface of brass due to the presence of the absorbed complex atom from the oil. The calculated portion of the surface covered from the corrosion process follows Langmuir adsorption Isotherm.

Keyword: Adsorption, SEM/EDX, Silicon oil, Corrosion rate,OPM.

Introduction

The constant use of acid solution in metal finish industries, metal heat exchanger, rust cleaning and contaminated oil spill equipment are enormous. One of these strong acid solutions is tetraoxosulphate IV acid[1-5].The use of inhibitors for protection against corrosion especially in acid solutions to prevent metal degradation has been a promising technique[1-14]. Inhibitors are chemical-inorganic or organic which react with corroding surfaces or the environment, to give the surface a level of protection. This may be by forming a film thereon or forming an inert compound[6-10].Brass corrosion occurrence has become vital predominantly in acidic and acid-chloride solution due to the accelerated engineering applications of acid solutions.

Corrosion inhibitors additions are known to protect the metal against an acid outbreak. Numerous investigations in this respect using organic inhibitors have been performed. Plant oils have become important inhibitors that are considered cheap, safe and non-toxic for a wide range of corrosion prevention and control[2-3]. In this work, the potential of silicon natural oil as a corrosion inhibitor on brass in one molar sulphuric acid (1 M H_2SO_4) has been studied using gravimetric and potentiodynamic polarization techniques.

Material and Methods

Materials and sample preparation: Brass specimen of dimension 20 x 20 x 3 mm with chemical composition shown in table 1 was used as coupons for the corrosion study in 1M sulphuric solution. The coupons were mechanically polished with different grade of emery papers, degreased in ethanol, dried and stored in a desiccator. The initial weights of each sample were recorded. The natural silicon oil used was obtained from chemical shop in Pretoria, South Africa. Corrosion studies were conducted at room temperature 298^{o}K.

Weight loss measurement: The weight loss corrosion test was carried out on the previous weighed samples with and without inhibitor at 298^{o}K. The volume of the solution was 10 mL with and without the addition of silicon oil inhibitor. The silicon oil inhibitor concentration was varied from 2, 5 and 10%v/v in 50 ml of 1M H_2SO_4 acidic solution. After each weight loss measurement, the samples were washed, dried and weight taken at interval of 48, 120, 168, 216, 264 and 312 h of exposure time. The weight loss, corrosion rate and inhibitor efficiency were examined along with the degree of surface coverage for each inhibitor concentration at 298^{o}K.

Electrochemical measurement: The linear polarization was used to study the corrosion rate of the brass in silicon oil acidic media. In the electrochemical test, a glass corrosion cell kit with a platinum counter electrode, a saturated Ag/Ag reference electrode and aluminum sample as working were used. The working electrodes samples were positioned at the glass corrosion cell kit, leaving 1 cm^2 surfaces in contact with the solution in line. Polarization tests were carried out in H_2SO_4 solution at room temperature using a potentiostat. The linear polarization curves were determined by using potential scan rate of 0.0012V/sec from -1.5 to +1.5V.

Surface morphology: The interface degradation trends of as-corroded uninhibited and inhibited brass sample were characterized with the help of high magnification OPM.

Results and Discussion

The weight loss data for brass in 1 M H_2SO_4 medium with the variation in percentage inhibitor concentration is shown in tables 2, figures 1, 2 and 3. From the experimental results obtained corrosion rate (CR) of brass decreased with addition of silicon oil as an eco-friendly natural green corrosion inhibitor for both environments and exposure time. It was observed that at various exposure times, corrosion rate decreased, though with lower percentage inhibitor efficiency (% IE).

Specifically, the acid test solution with all % concentration of silicon oil addition showed good behaviour corrosion inhibition effect, although at different individual immersion

time. In general, averagely weight losses were minimal at the end of the 312h immersed specimens with 100% extracts concentration addition. The potential of silicon oil at all grade of concentration was excellent within immersion time of 216-264h. This indicates that the adsorption atom and activities of this silicon compound could still withstand SO_4^{2-} penetration within this period.

However, another important observation is the inconsistence and fluctuation trend behavior of adsorption of silicon oil efficiency in 48h and 264h. The silicon oil at lower concentration inhibits well than the 100% concentration addition within that immersion time, this in turn makes it difficult to explain why the lowest concentration of 20% oil concentration addition had the best corrosion inhibition effect. In general, an appreciable and apparent corrosion inhibition of the specimen was achieved when the results of the tests were compared without oil addition and with oil additon.

Considering an exposure time of 216 h where the corrosion process could be seen to be more, higher % IE was calculated to be 82% at 20%v/v silicon oil addition. While at 50%v/v and 100%v/v inhibitor concentration for the same exposure time, corrosion rate/IE were found to be 0.000386/87% and 0.000241/97% respectively. However, corrosion resistance of brass in H_2SO_4-silicon oil is much appreciated and these significant occurrences have been ascribed to the formation of thin oxides which make pits and their growths difficult.

Linear Potentiodynamic polarization

Table 3 and figure 4 show a linear polarization resistance data and curve obtained for electrochemical corrosion examination for brass in IM H_2SO_4 SO. In figure 4 the anodic and cathodic polarization curves for the brass in acidic media-SO and uninhibited conditions are shown. With critical consideration of the corrosion condition of 1M H_2SO_4 SO, it can be seen that the current density decreased with an increase in inhibitor concentration and corrosion potential (E_{corr}) increased for 2, 5 and 10% v/v SO additions respectively (Figure 4). Though, the improvement from the polarization trend might be seen to be minimal, however studies[2,13,14] verify that adsorption inhibition process is from activities and potentials of molecules and hetero-atom of the oil extract. Therefore, the significant minimal improvement thin film atom adsorbed on the interface is a strong indication to recommend the potential of SO as mixed inhibitor.

From the linear polarization resistance value, it shows that addition of the inhibitor resulted into an increase in the R_p of the brass from 30.444(uninhibited) to 53.022(inhibited) condition with an IE of 97%. The increase in R_p generally suggested an improvement in the corrosion resistance of the metal in the presence of the inhibitor. This demonstrated that the metal is secure within the immersion time measured.

The lower values of *I*corr in the presence of investigated compounds without causing significant changes in *E*corr values suggest that these compounds are mixed type inhibitors.

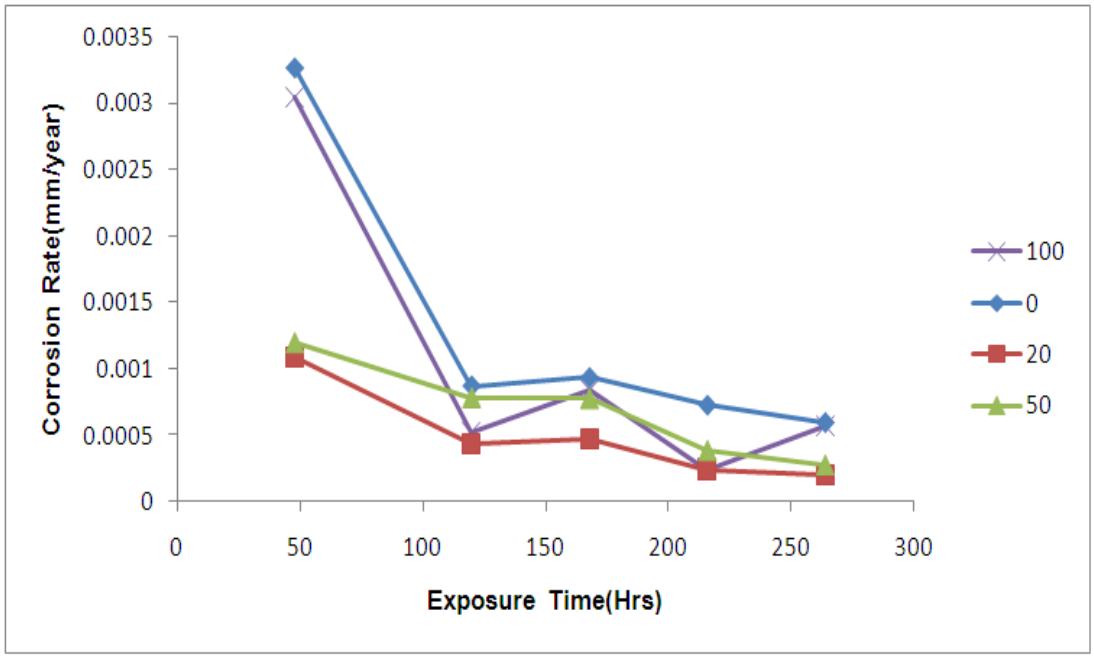

Figure 1: Variation of corrosion rate with exposure time of brass in 1 M H_2SO_4 solution with and without SO

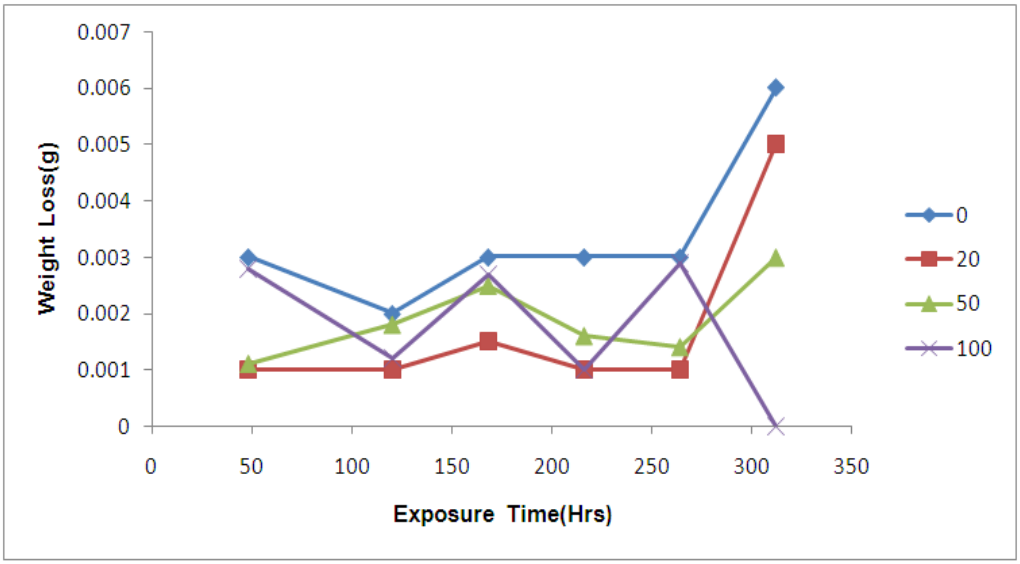

Figure 2: Variation of weight loss with exposure time of brass in 1 M H_2SO_4 solution with and without SO

Table 1: Chemical composition of the brass sample used

Element	Cu	Zn	Mn	Mg	Sr	Bi	Ca	Fe, C	Ti	P, Cr, Zr,Al,Si	B,Ni,Ag, Co
%	65.01	34.2	0.0035	0.001	0.0001	0.0034	0.0012	0.581, 0.032	0.0026	0.04	0.035

Table 2
Corrosion rate (CR), Inhibition efficiency and surface coverage (θ) for brass in 1M H_2SO_4 solution without and with varying concentration of silicon oil at 30°C

Samples(hrs)	Conc. of Inhibitor	weight loss (wt.)	corrosion rate (CR)	Inhibitor Efficiency (%IE)	Surface coverage
48	0	0.003	0.00326	-	-
	20	0.001	0.001086	96	0.9667
	50	0.0011	0.001195	86	0.8633
	100	0.0028	0.003042	33	0.333
120	0	0.002	0.000869	-	-
	20	0.001	0.000435	80	0.8
	50	0.0018	0.000782	72	0.721
	100	0.0012	0.000521	97	0.97
168	0	0.003	0.000931	-	-
	20	0.0015	0.000466	64	0.64
	50	0.0025	0.000776	92	0.92
	100	0.0027	0.000838	99	0.995
216	0	0.003	0.000724	-	-
	20	0.001	0.000241	82	0.82
	50	0.0016	0.000386	87	0.875
	100	0.001	0.000241	97	0.975
264	0	0.003	0.000593	-	-
	20	0.001	0.000198	75	0.75
	50	0.0014	0.000276	75	0.75

	100	0.0029	0.000573	50	0.5
312	0	0.006	0.001003	-	-
	20	0.005	0.000836	16	0.1667
	50	0.003	0.000201	40	0.4
	100	0.001	0.000167	65	0.65

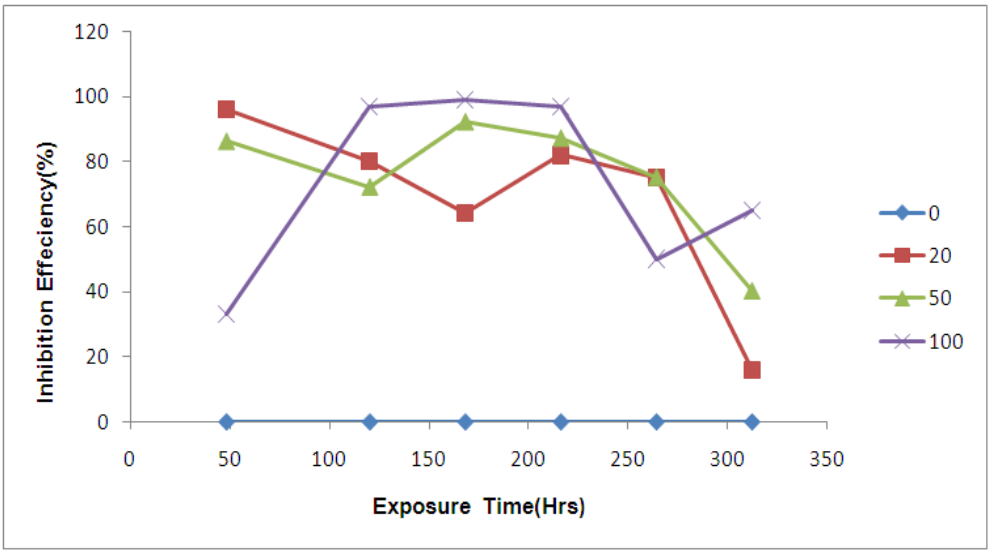

Figure 3: Inhibitory efficiency against exposure time trend of brass in 1 M H_2SO_4 solution with and without SO

Table 3
Electrochemical corrosion data obtained for aluminum in 3.5% NaCl varying concentration of *SO* environment at 30°C

Inhibitor conc.	ba (V/dec)	bc (V/dec)	Ecorr, Obs (V)	jcorr (A/cm^2)	icorr (A)	CR (mm/y)	Rp (Ω)
10ml inhibitors	0.01610	0.0258	-0.446	8.12E-05	8.12E-05	0.072749	53.022
2ml inhibitor	0.05972	0.0197	-0.4569	0.000164	0.000164	0.19758	39.264
5ml inhibitor	0.01226	0.0799	-0.4603	0.000153	0.000153	0.23226	37.172
Control	0.06058	0.0322	-0.4957	0.000244	0.000244	0.27548	30.444

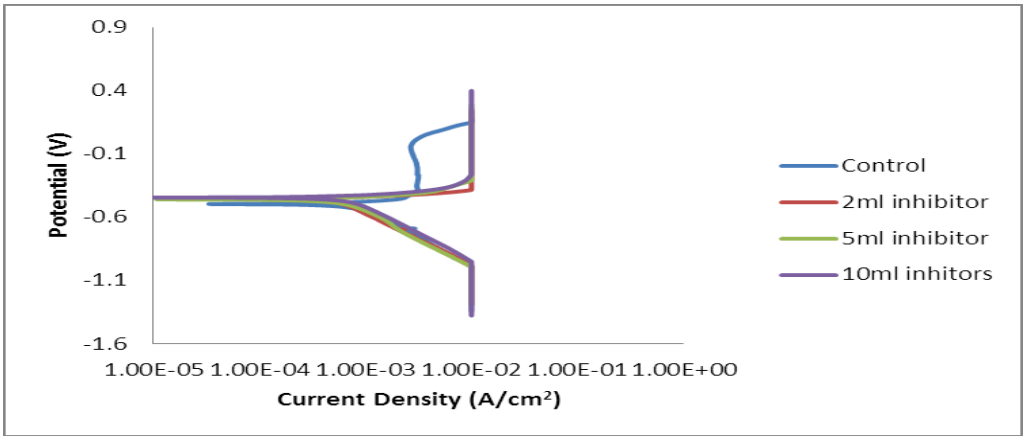

Figure 4: Linear polarization of brass in 1M H_2SO_4 solution *SO* environment at 30°C

Photomicrography studies (OPM)

The OPM micrographs of brass surfaces and its relative deterioration tendency are shown in figure 5. The uninhibited brass sample in 1M H_2SO_4 solution (Figure 5) indicates a severe surface uniform degradation as compared with the inhibited brass sample in figures 5b-d.The adsorption potential of the oil trend could be seen to perform effectively since stress initiation that is often seen during degradation was not visible.

Therefore, the little improved activities in the metal interface are mostly influenced by the chemo-physical properties[12-14] resulting in recrystallization on the microstructural homogeneity rather than the degradation behavior expected.

In view of this, a notable conclusion could be drawn that the *SO* natural oil was able to exhibit some degrees of inhibition which retarded the corrosion rate of the brass in IM H_2SO_4 solution. Subsequently, the inhibited samples can be observed to be covered with thin layer of the corrosion inhibitor resulting in the protection of the brass against degradation.

Inhibitor efficiency and adsorption behaviour

The inhibitor efficiency (% IE) of the brass-induced *SO* in 1M H_2SO_4 solution was calculated and computed using the equation reported.[2] The calculated and computed data for the IE using potentiodynamic polarization-corrosion rate (PP-CR), potentiodynamic polarization-corrosion density (PP-I_{corr}), linear polarization resistance (LPR) and gravimetric (GM) are presented in fig. 6 for 1M H_2SO_4 *SO*. From all indication, the % IE of the *SO* oil increases with an increase in the inhibitor concentrations especially at high concentration. Most importantly is the film formed which expressly acts as a formidable barrier between the brass and the corrosion environment interface as early mention. A wide spread of surface coverage was also seen with respect to the increase in inhibitor concentration which leads to higher IE as a result of associated SO complex compound/structural constituent which acts as passive film former on brass layer substrate.

Hence, *SO* oil can be said to exhibit a mixed-type corrosion inhibition because of the concurrent change at both anodic and cathodic region during the electrochemical reaction process. This is in conformation with previous studies[2,3]. The adsorption behavior mechanism was shown that the relationship between C/θ against C is linear at 30°C for both the environments (Figure 7). Hence, the linear regression coefficient/or correction factor (R^2) is PP (0.9973), with adsorption activities seem to have obeyed Langmuir isotherms adsorption system.

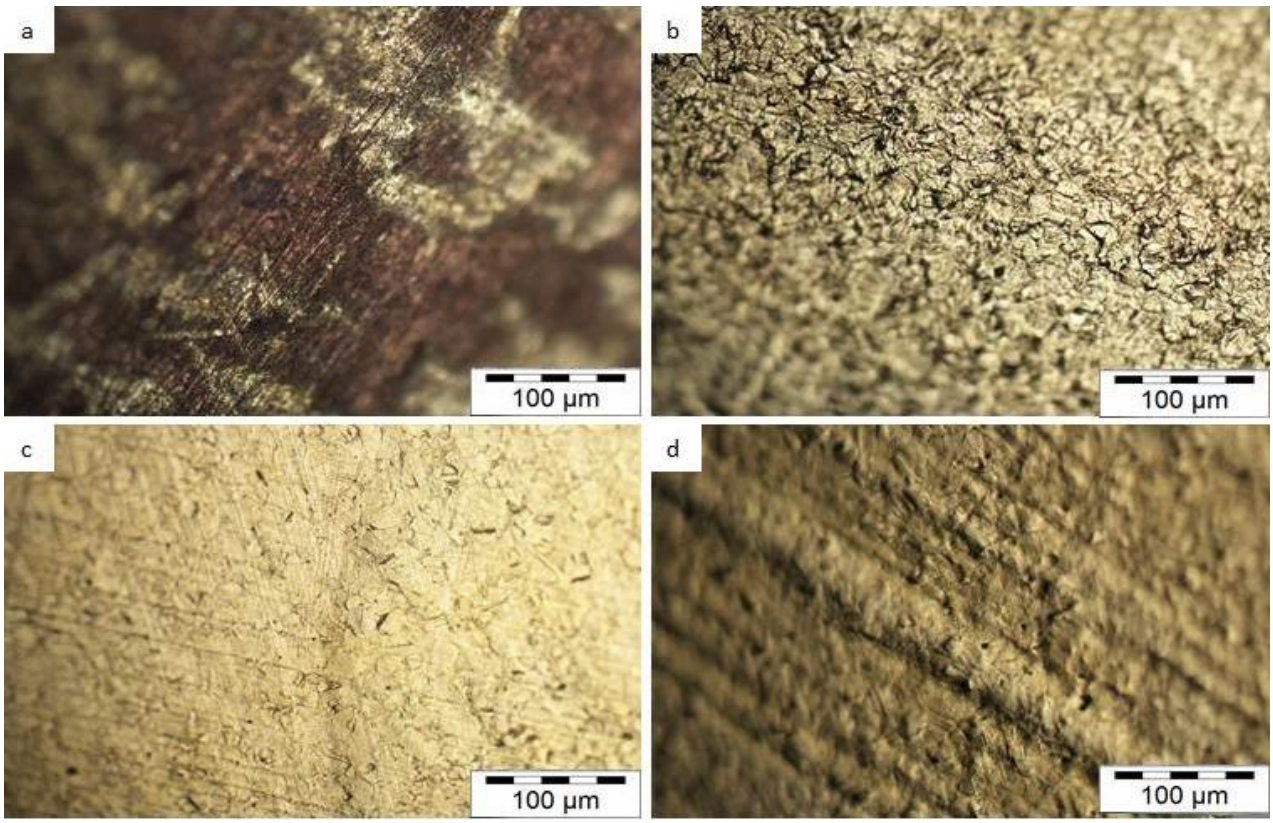

Figure 5: OPM micrograph of a) as-corroded uninhibited b) inhibited brass in 2% c) inhibited brass in 5% d) inhibited brass in 10% in 1M H_2SO_4 solution *SO* environment at 30°C

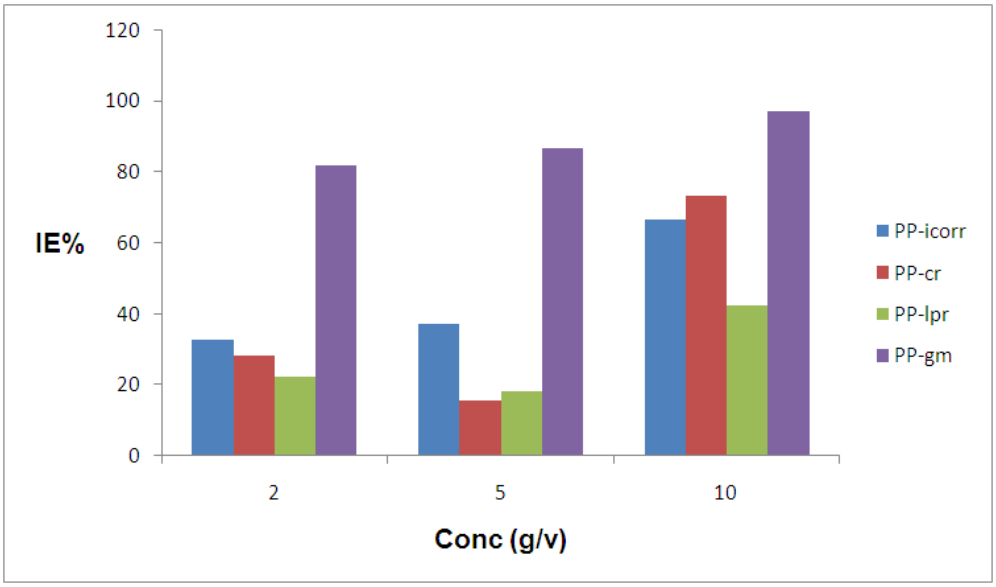

Figure 6: Comparative chart of inhibitor efficiency (IE) for 1M H_2SO_4 solution/*SO* concentration obtained by gravimetric (GM), potentiodynamic polarization-corrosion rate (PP-CR), potentiodynamic polarization-corrosion current (PP-Icorr) and linear polarization resistance (LPR)

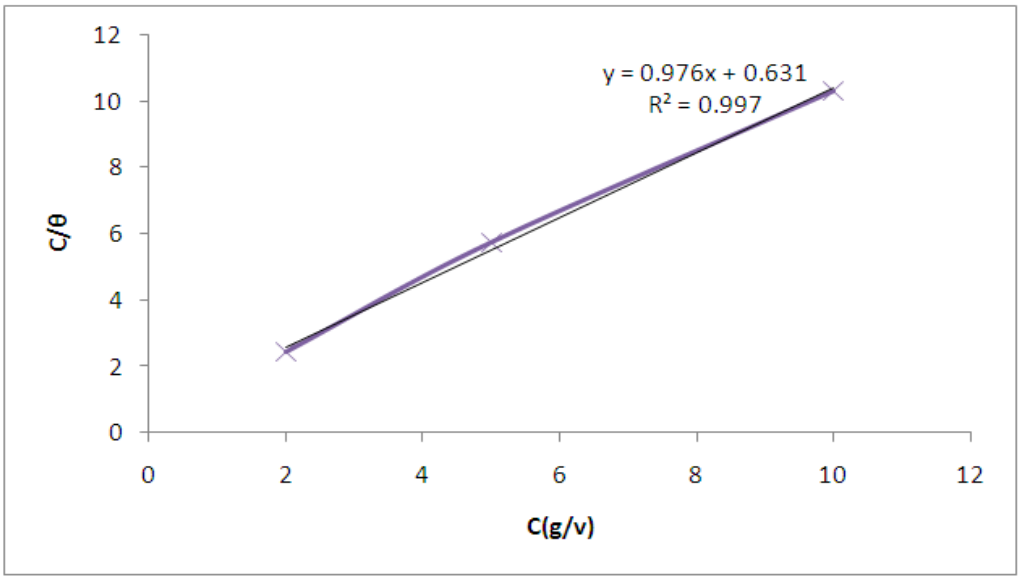

Figure 7: Langmuir isotherm for the adsorption of *SO* compounds on the brass surface in 1M H_2SO_4 solution at 30°C obtained by gravimetric and potentiodynamic polarization method

Conclusion

1. Addition of silicon natural oil decreases the corrosion rate of brass deterioration in 1 M H_2SO_4 solution.
2. The inhibitive action of silicon natural oil increases with percentage of concentration induced in the solution.
3. Inhibitor efficiency above 90 % was obtained at 10 ppm silicon natural oil addition and the Langmuir adsorption isotherm was proposed for the brass.
4. The active molecules and atom present in the silicon natural oil have effectively and efficiently inhibited corrosion of brass in 1 M H_2SO_4 at various concentrations by providing a protective barrier layer against pits.

Acknowledgement

This research is based upon work supported financially by the National Research Foundation (NRF), South Africa. The equipment support by Surface Engineering Research Centre (SERC) Tshwane University of Technology, Pretoria is deeply appreciated.

References

1. Bouyanzer A., Hammouti B. and Majidi L., Pennyroyal Oil from Mentha Pulegium as Corrosion Inhibitor for Steel in M HCl, *Materials Letters*, **60(23),** 2840-2843 **(2006)**

2. Abdulwahab M., Fayomi O. S. I., Popoola A. P. I., Asuke F. and Umoru L.E., Effect Of Avogadro Natural Oil on The

Corrosion Inhibition of Mild Steel In Hydrochloric Acid Solution, *Research on Chemical Intermediates,* **39(2),** 1025 **(2013)**

3. Popoola A.P.I. and Fayomi O.S.I., Electrochemical Study of Zinc Plate In Acid Medium: Inhibitory Effect Of Bitter Leaf (VerononiaAmygdalina), *International Journal of Electro chemical Science*, **6,** 4581- 4592 **(2011)**

4. Satapathy A. K., Gunasekaran G., Sahoo S.C., Kumar A. and Rodrigues P.V., Corrosion Inhibition By Justicia Gendarussa Plant Extract In Hydrochloric Acid Solution, *Corrosion Science*, **51(12),** 2848-2856 **(2009)**

5. Subhashini S., Rajalakshmi R. and Prithiba A., Corrosion Mitigating Effect of Cyamopsis Tetragonaloba Seed Extract on Mild Steel In Acid Medium, *E-Journal of Chemistry,* **7(4),** 1133-1137 **(2010)**

6. Da Rocha J. C., Da Cunha Ponciano J. A. and D'elia E., Corrosion Inhibition of Carbon Steel in Hydrochloric Acid Solution by Fruit Peel Aqueous Extracts, *Corrosion Science* **,52(7),** 2341-2348 **(2010)**

7. Ramesh S. P., Vinod Kumar K. P. and Sethuraman M. G., Extract of Andrographis Paniculata As Corrosion Inhibitor of Mild Steel In Acid Medium, *Bulletin of Electrochemistry,* **7(3),** 141-144 **(2001)**

8. Loto C. A. and Mohammed A. I., The Effect of Cashew Juice Extract on Corrosion Inhibition of Mild Steel in HCl, *Corrosion Prevention and Control,* **47(2),** 50-56 **(2000)**

9. Minhaj A., Saini P. A., Quraishi M. A. and Farooqi I. H., A Study of Natural Compounds as Corrosion Inhibitors for Industrial Cooling Systems, *Corrosion Prevention and Control,* **46(2),** 32-38 **(1999)**

10. Tadeja K., Ingrid M. and Boris Pihlar, Benzotriazole As An Inhibitor Of Brass Corrosion In Chloride Solution, *Applied Surface Science***, 253,** 8863–8873 **(2007)**

11. Lahhit N., Bouyanzer A. Desjobert J. M., Hammouti B., Salghi R., Costa J., Jama C., Bentiss F. and Majidi L., Fennel (FoeniculumVulgare) Essential Oil As Green Corrosion Inhibitor Of Carbon Steel In Hydrochloric Acid Solution, *Portugaliae Electrochimica Acta,* **29(2),** 127-138 **(2011)**

12. Bammou L., Mihit M., Salghi R., Bouyanzer A., Al-Deyab S. S., Bazzi L. and Hammouti B., Inhibition Effect Of Natural Artemisia Oils Towards Tinplate Corrosion In HCl Solution: Chemical Characterization And Electrochemical Study, *Int. J. Electrochem. Sci.,* **6,** 1454 - 1467 **(2011)**

13. Ezuber H. M., Corrosion behavior of copper alloys in contaminated seawater, *Res. J. Chem. Environ.,* **8(3),** 56-63 (**2004**)

14. Popoola A.P.I. and Fayomi O.S.I., Environmental Failure of 2m Acid Strength on Zinc Electroplated Mild Steel in the Presence of Nicotiana Tobacum, *Scientific Research and Essay*, **6(14),** 3079-3088 **2011**)

15**.** Fayomi O.S.I., Popoola A. P. I., Abdulwahab M. and Popoola O. M., Inhibitive Effect of SimmondsiaChinenis on 2M HCl Acid Corrosion of Mild Steel, *International Journal of Research in Engineering, IT and Social Sciences,* **2(10),** 13-24 **(2012)**

16. Abdulwahab M., Popoola A. P. I. and FayomI O. S. I., Inhibitive Effect by Ritinus Communis the HCl/H_3PO_4 Acid Corrosion of Aluminum, *International Journal of Electrochemical Science,* **6(7),** 11706- 11717 **(2012).**

(Received 26th March 2013, accepted 27th July 2013)

The effect of Copper Concentration on Morphology of Copper - PVP Nanostructured Composites

Sadjadi Mirabdollah Seyed* and Mashayekhi Parivash
Department of Chemistry, Science and Research Branch, Islamic Azad University, Tehran, IRAN
*m.s.sadjadi@yahoo.com

Abstract
Our aim in this work was low temperature preparation of copper nanoparticles embedded in PVP by wet chemical method. Copper (II) sulfate was taken as metal precursor, ascorbic acid at the presence of an appropriate amount of NaOH as reducing agent and polyvinylpyrrolidone k-30 (PVP K-30) as a protecting agent. The reaction was performed in high-speed stirring rate at room temperature. Characterization of the samples was carried out by using powder X-ray diffraction technique (XRD), Fourier transform infrared spectroscopy (FTIR) and Scanning electron microscopy (SEM). The results revealed the crucial role of copper (II) sulfate/surfactant molar ratio on the morphologies of the copper-PVP nanocomposites and homogeneous flower like nanostructured copper – PVP composite film mainly composed of face-centered cubic (fcc) copper with a crystalline size of 9.7 nm was obtained for $CuSO_4.5H_2O$ /surfactant molar ratio of 70/1.

Keywords: Low temperature synthesis, Embedded copper nanoparticle, Copper-PVP nanocomposite, Polyvinyl pyrrolidone K-30, Protecting agent.

Introduction

Many techniques, including chemical and physical means, were developed to prepare the metal nanoparticles such as chemical reduction[1–8], electrochemical reduction[9,10], photochemical reduction[11,12], heat evaporation [13,14] and so on[15,16]. The physical ways always need high temperature[16] (over 1000 ◦C), vacuum and expensive equipments but the conditions that the chemical methods needed are not so critical. The chemical reduction way is one of the commonest methods to synthesize colloidal metal particles, because of its convenient operation and simple equipment needed.

Recently research on the composite materials made of nanosize metal particles embedded in polymer matrix has received considerable attention because of the unique properties that they exhibit as a result of the presence of reduced size metal. Quantum size effects may arise and influence all the physical and optical properties of such materials[17-18]. In such nanocomposite materials, studying the morphology change will be of great interest in materials science due to their importance in basic scientific research and potential of technological applications[19, 20].

In this work, we attempted to study the effect of copper/PVP molar ratio on the morphology and optical properties of the materials synthesized of copper NPs embedded in PVP by wet chemical method. The results revealed crucial role of copper /PVP molar ratio on the morphologies of copper-PVP nanocomposites and homogeneous flower like nanostructured copper –PVP composite mainly composed of face-centered cubic (fcc) copper with a crystalline size of 9.7 nm was obtained for $CuSO_4.5H_2O$ /surfactant molar ratio of 70/1.

Material and Methods

Materials: All the chemicals were of analytical grade and used as purchased without further purification. Copper (II) sulfate pentahydrate salt ($CuSO_4.5H_2O$) of 98% purity (Merck) and polyvinylpyrrolidone K-30 (PVP-30) were purchased from Merck. Ascorbic acid ($C_6H_6O_6$) and sodium hydroxide (NaOH) were supplied by Sigma-Aldrich.

Table 1
Experimental parameters in preparation of nanostructured copper-PVP nanocomposites

Morphology	**Concentration of $CuSO_4.5H_2O$ ($MolL^{-1}$)**	**Concentration of ascorbic acid ($MolL^{-1}$)**	**$CuSO_4.5H_2O$ /surfactant molar ratio**	**Surfactant (the types and the concentration) ($MolL^{-1}$)**	**Sediment color**
Spherical Fig.3a	0.05	0.2	50/1	PVP-K30 0.001	Dark brown
Flower-like Fig.3b	0.07	0.2	70/1	PVP-K30 0.001	Gray
Mixture of Spherical and hexagonal Fig.3c	0.2	0.2	200/1	PVP-K30 0.001	Black

Results and Discussion

XRD characterization: Fig.1a,b,c represent powder XRD patterns of the nanocomposite samples prepared at the different molar ratio of copper/PVP. The peaks observed at $2\theta = 43.52^{\circ}$, 50.8° corresponding to the (111), (200) lattice planes can be well indexed to face-centered cubic (fcc) structure related to JCPDS card No.4-836. It was observed that the intensity of the diffraction peak at (111) plane is stronger than other peak indicating that the copper polycrystalline structure is mainly dominated by the crystal facet (111) and thus the crystal growth direction is favorably oriented parallel to the [111] direction. The mean crystalline size using Scherrer's equation was about 5.7-19.5 nm. Findings of the different values of crystalline size mean clearly size dependence of embedded nanoparticle with increased copper/ PVP molar ratio.

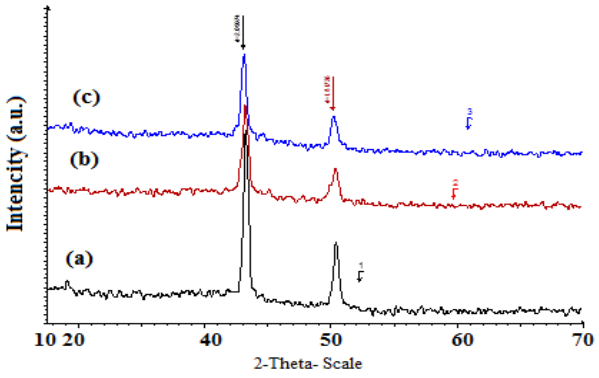

Fig.1: XRD pattern of as-prepared copper-PVP nanostructured composites in different molar ratio of Cu/PVP: a) 50/1; b)70/1 and c)200/1.

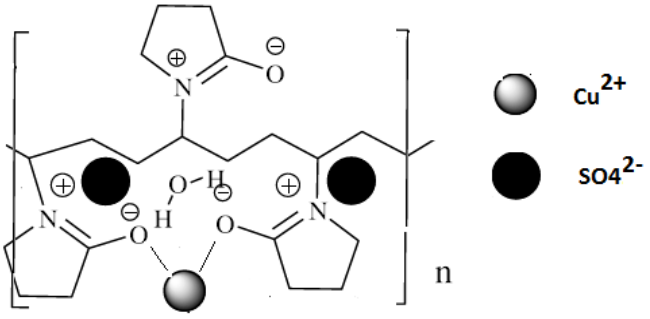

Fig. 2: Proposed mechanism for interactions between PVP and metal ions in the formation of copper nanoparticles.

FTIR Analysis: Fourier Transform Infrared spectroscopy is a very useful technique to examine the structure and structural transformation of materials using this technique. Here a detailed vibrational analysis was carried out for pure PVP and PVP nano copper composite. Fig.2a, b and c represent the FTIR spectra of superposed pure PVP with copper nanocomposites in different Cu/PVP molar ratio. In this figure, a main intense metal-oxygen band observed from 505 to 506 cm^{-1} for all the prepared Cu/PVP nanocomposites, corresponds to intrinsic stretching vibrations of the metal at the tetrahedral site[21-22], M ↔ O. The shift observed for carbonyl vibrational stretch from 1643 cm^{-1} to 1648-1669 cm^{-1} shows clearly modification of PVP in copper-PVP nanocomposites.

Interactions between the PVP as protecting agent[23] and metal ions represented schematically in figure 2 show that the Cu (II) ions are bound to the polymeric chain by strong ionic bonds between the metallic ions and the amide group. Therefore, PVP acts as a stabilizer to dissolve metallic salts through steric and electrostatic stabilization of the amide groups of the pyrolidine rings and the methylene groups. Initially, the PVP stabilizer may decompose to a limited extent, thereby producing shorter polymer chains that are capped when they are adsorbed onto the surfaces of metallic ions[24]. The metallic ions, which are well dispersed in the cavities and networks, have been then reduced to the well dispersed copper nanoparticles. In this condition, the peaks of N^{+} OH^{-} complex (at 1484-1444) were weakened greatly (1320-1363 cm^{-1}). These changes of intensity and stretching frequencies can be attributed to the coordination created between N-OH and metal copper[25].

Whereas the peaks of C N, at 1019, were strengthened and red shift to 1125 and 1100 for Cu/PVP= 50/1 and 200/1, but weakened (875) for Cu/PVP= 50/1. This behavior duality in CN frequency indicated that although the pyrrolidyl has steric effect on the coordination between N and Cu^{2+} but the electronegativity of N was lower than that of O and the capability of electron donating of N was higher than that of O. In this case N would be coordinated with copper ions. This result is in conformity with Zhang et al[26]. They analyzed the possible mode of PVP protecting particles with diameters of about 50 nm and made an assumption that the two reactions through O and N of PVP were equal. But, for the particles with the diameter shorter than 50 nm, the steric effect was not the main factor that influenced the reaction between PVP and silver. As a result, we can do the same assumption that coordination between PVP and copper was not on O, but on N when the particle size is shorter than a limit. Details of vibrational frequencies for PVP- copper nanostructures are given in table 2.

As a further investigation, the role of Cu/PVP in the synthesis of copper nanoparticles is taken in consideration via the SEM images. FT-IR spectra of the nanocomposites with various Cu/PVP molar ratio of 50/1, 70/1 and 200/1 revealed that when the molar ratio concentration of Cu/PVP was 200/1, the copper nanoparticles that were formed became more regular in shape than in the case without PVP. But, due to the low concentration of PVP, these nanoparticles can be aggregated because there were insufficient PVP to protect them and prevent their agglomeration. Due to the aggregation and increasing size of copper nanoparticles, the steric hindrance phenomenon became important and bonding between copper and PVP became weak (CO stretching frequency change from 1643 to1648).

The SEM image shows a no phase separation where PVP was segregated to the free surface (Fig. 3a). By decreasing molar ratio of Cu/PVP to 70/1, the copper nanoparticles formed did not agglomerate and a homogenous distribution of Cu NPs agglomerates in nanocomposite films was obtained (Fig. 3b). In this condition the size of copper nanoparticles formed is in a limited copper/PVP and the steric hindrance phenomenon was not the main factor that influenced the reaction between PVP and copper. As a result, coordination between PVP and copper was not on O, but on N when the particle size is shorter than a limit.

The optimum concentration of Cu/PVP was reached because of the fact that this concentration was the minimum concentration at which the nanoparticles were pure; also, this is the concentration at which the nanoparticles had the smallest particle size and a nearly uniform distribution of shapes (Fig. 3b). When, the molar ratio of Cu/PVP was 50/1, the copper nanoparticles formed did not agglomerate and homogenous distribution of Cu NPs agglomerates in nanocomposite films (Fig. 3c).

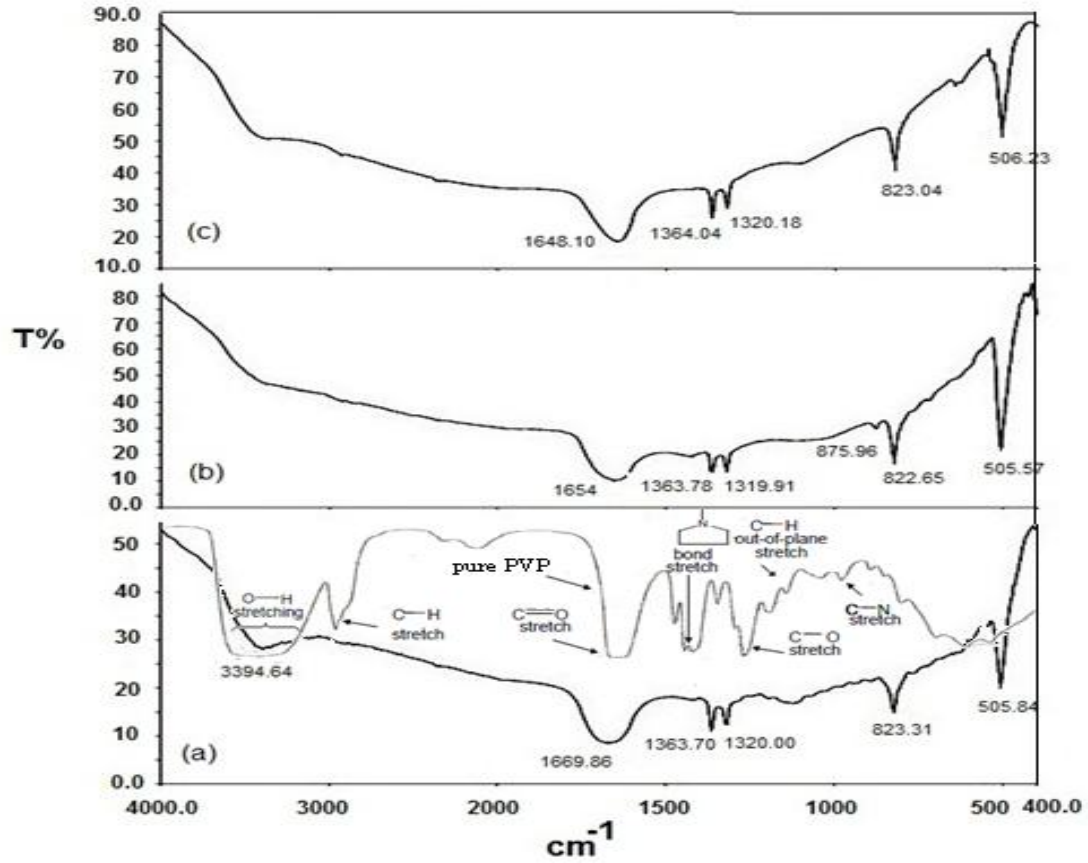

Fig.2: FTIR spectra of PVP and PVP-Cu nanocomposites in $CuSO_4.5H_2O$/PVP in a molar ratio of: a) 50/1; b) 70/1; c) 200/1

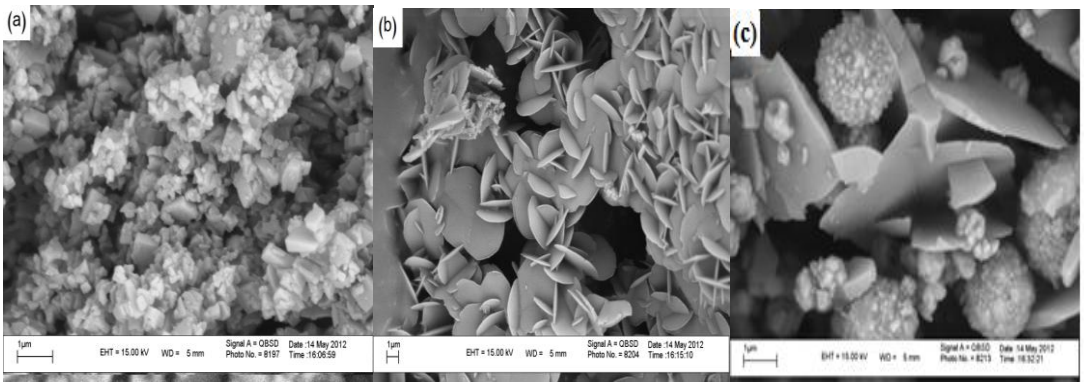

Fig.3: Typical SEM images of PVP copper nanostructures of as prepared nanocomposites in different Cu/PVP molar ratios: a) 50/1; b) 70/1 and c) 200/1

Table 2
FTIR vibrational spectra of PVP and Cu /PVP nanocomposites in different molar ratio and their assignments

Assignments	PVP/cm^{-1}	Cu/PVP=50 cm^{-1}	Cu/PVP=70 cm^{-1}	Cu/PVP=200 cm^{-1}
Cu-O		505 -506	505 -506	505 -506
C-N	1019	1125	875.96	1100
N-OH	1484-1444	1320.-1363	1319-1363	1320-1364
C=O	1643	1669.88	1654	1648.10

SEM characterization: Fig. 3a, b and c represent SEM images of PVP- copper nanostructured composites as ratios of copper (II) sulfate to PVP surfactant of 50/1, 70/1 and 200/1.These images show clearly that the copper (II) sulfate/surfactant molar ratio plays a crucial role on the morphologies of copper-PVP nanocomposites and a flower like nanostructured copper composite mainly composed of face-centered cubic (fcc) in a crystalline size of 5 nm was obtained.

Conclusion

In summary, copper nanoparticles embedded in PVP were successfully synthesized at low temperature by a chemical reduction method using $CuSO_4.5H_2O$ as metal precursor and ascorbic acid as reducing agent. The molar ratio of copper (II) sulfate/ PVP plays a crucial role on the morphology of nanostructured composites and a small size nanostructured composite was obtained when the molar ratio of $CuSO_4.5H_2O$/PVP was 70/1. PVP macromolecule in solution may take part in some form of association with the metal atoms and can increase the probability of nucleus formation.

Acknowledgement

The authors express their thanks to the research vice presidency of Science and Research Branch, Islamic Azad University, Iran for encouragement and financial supports.

References

1. Chou K.S. and RenMate C. Y., *Chem. Phys.* **64,** 241 **(2000)**

2. Christophe P., Patricia L. and Paule P. Marie, *J. Phys. Chem.* **97,** 12974 **(1993)**

3. Vorobyova S. A., Lesnikovich A. I. and Sobal N. S., *Colloid Surf.* A, **152,** 375**(1999)**

4. Zhang Z., Zhao B. and Hu L., *J. Solid State Chem*, **121,** 105 **(1996)**

5. Yakutik I.M. and Shevchenko G. P., *Surf. Sci.*, **414,** 566–568 **(2004)**

6. Huang H. and Yang X., *Carbohyd. Res.*, **339,** 2627**(2004)**
7. Zhang Z. and Han M., *Chem. Phys. Lett.*, **374,** 91–94 **(2003)**

8. Tan Y. et al, *J. Colloid Interface Sci.*, **249,** 336 **(2002)**

9. Liu Y.C. and Lin L.H., *Electrochem. Commun.*, **6,** 1163 **(2004)**

10. Sandmann G., Dietz H. and Plieth W., *J. Electroanal. Chem.*, **491,** 78 **(2000)**

11. Mallicka K., Witcombb M. J. and Scurrella M. S., *Mater. Chem. Phys.*, **90,** 221 **(2005)**

12. Keki S. et al, *J. Colloid Interface Sci.*, **229,** 550 **(2000)**

13. Bae C. H., Nam S.H. and Park S.M., *Appl. Surf. Sci.* **628,**197–198 **(2002)**

14. Smetana A. B., Klabunde K. J. and Sorensen C.M., *J. Colloid Interface Sci.*, **284,** 521**(2005)**

15. Wang X. L., Meng Y. Z. and Li R. K. Y., *Res. J. Chem. Environ.*, **10(3),** 38-43 **(2006)**

16. Jin Z. L. et al, *Shanghai Met.*, **23(2),** 37 **(2001)**

17. Carotenuto G., Pepe G. P and Nicolais L., *Eur. Phys. J.*, B**, 16,** 11-17 **(2000)**

18. Zimmermann L., Weibel M., Caseri W. and Suter U.W., *J. Mater. Res.*, **8,** 1742 **(1993)**

19. Khanna P. K. et al, *Materials Letters*, **61,** 4711**(2007)**

20. Gu A., Wang G., Zhang X. and Fang B., *Bulletin of Materials Science*, **33**, 17 **(2010)**

21. Niasari M.S., Davar F. and Mahmoudi T., *Polyhedron*, **28**, 1455–1458 **(2009)**

22. Naseri M. G., Saion E. and Khalil Zadeh N., *International Nano Letters*, **3**, 19 **(2013)**

23. Sivakumar P., Ramesh R., Ramanand A., Ponnusamy S. and Muthamizhchelvan C., *Mater. Lett.*, **65**, 483–485 **(2011)**

24. Koebel M. M., Jones L. C. and Somorjai G.A., *J Nanopart Res.*, **10**, 1063–1069 **(2008)**

25. Wang H., Qiao X., Chena J., Wang X. and Ding S., *Materials Chemistry and Physics*, **94,** 449–453 **(2005)**

26. Zhang Z., Zhao B. and Hu L., *J. Solid State Chem.*, **121,** 105 **(1996).**

(Received 25th March 2013, accepted 28th July 2013)

*****